MODEL SYSTEMS FOR STUDIES AT THE PLASMA MEMBRANE: INVESTIGATING LIPID PHASE BEHAVIOR AND PROTEIN-MEDIATED MEMBRANE REMODELING

A Dissertation

Presented to the Faculty of the Graduate School

of Cornell University

In Partial Fulfillment of the Requirements for the Degree of

Doctor of Philosophy

by

Shih Lin Goh

May 2013

MODEL SYSTEMS FOR STUDIES AT THE PLASMA MEMBRANE: INVESTIGATING LIPID PHASE BEHAVIOR AND PROTEIN-MEDIATED MEMBRANE REMODELING

Shih Lin Goh, Ph. D.

Cornell University 2013

The plasma membrane is a multicomponent mixture of lipids and proteins. Functional domains ("lipid rafts") that arise from nonrandom mixing of membrane components are believed to be important in governing the spatial organization of lipids and proteins. Proper compartmentalization of lipids and proteins is vital to facilitate cellular processes, such as signaling, endocytosis and trafficking. While evidence has shown that lipids play an integral role in protein-mediated processes, the chemical complexity of the plasma membrane and the dynamic nature of intermolecular interactions pose challenges for systematic investigations that aim to determine the interplay between lipids and proteins. Model membrane mixtures provide chemically simplified systems for studies of both lipid-lipid, and lipid-protein interactions.

In four-component lipid mixtures that model the outer leaflet of the plasma membrane, we observed a nanoscopic-to-macroscopic transition of domain size and morphology by tuning lipid composition. Using fluorescence microscopy imaging of giant unilamellar vesicles (GUVs), we found that this nano-to-macro transition exhibits a regime of patterned fluid domains within the liquid coexistence region of this four-component system. Temperature-dependent FRET and microscopy studies strongly suggest that the patterned domains are thermodynamically stable, lending support for the existence of nanoscopic domains with possibly complex morphology

in cellular plasma membranes. Together, our studies allude to a possible mechanism for cells to control domain size and morphology by merely changing lipid composition.

The importance of lipids in facilitating cellular processes is evident from examining protein-mediated membrane remodeling events. Using *in vitro* liposome deformation and liposome binding assays, we examined the activation mechanism of pacsin-1, an F-BAR domain protein enriched in neurons, by dynamin-1 PRD (proline-rich domain). While key basic residues in the PRD were vital to the activation of pacsin-1, we found that pacsin-1's membrane sculpting potential depends on membrane properties such as curvature and bending rigidity. In separate *in vitro* investigations of HIV-1 Gag-membrane associations, we found that lipid composition strongly affects Gag membrane affinity. These results highlighted the complex nature of protein-mediated membrane remodeling processes, which requires understanding both protein function and lipid phase behavior.

BIOGRAPHICAL SKETCH

Shih Lin (also known as Lynda) grew up on the tropical island of Penang, in Malaysia. After graduating at the top few percent of her class of ~800 students at Penang Chinese Girls' High School in 2000, she began her pre-university studies at the same high school, with the intention of eventually enrolling in a local public university to pursue her bachelor's degree. Encouraged by her supportive parents, Shih Lin ventured to apply for scholarships that were offered at several U.S. universities. A generous offer from Franklin & Marshall (F&M) College resulted in a change of career path for her.

Shih Lin earned her B.A. degree in chemistry and biochemistry from F&M College in Lancaster, PA. During her undergraduate training, she was fortunate to be involved in two different research projects. At F&M, she performed an independent study with Dr. Edward Fenlon on the synthesis of a polyethylene trefoil knot. But it was her summer research experience at Princeton University with Dr. Frederick Hughson on intercellular trafficking that confirmed her interest to pursue biochemistry at the doctoral level.

During her doctoral training at Cornell, Shih Lin's continued interest in the overlapping areas of chemistry and biochemistry led to her joint appointment as a member in the labs of Dr. Gerald Feigenson and Dr. Holger Sondermann. She intends to pursue a career of research in either academia or industry.

To David

ACKNOWLEDGMENTS

I would like to say a big Thank You to my co-advisors, Dr. Gerald Feigenson and Dr. Holger Sondermann. They have provided me with the invaluable opportunity to conduct research in their labs, and have offered much guidance and inspiration to me throughout my doctorate work. Both Jerry's and Holger's doors are always open for scientific discussions: they are easily approachable and always patient with me as I stumble through obstacles in my research works. I have been extremely lucky to have them as my mentors.

The execution of the various projects described in this dissertation would not have been possible without the direct help of my labmates and collaborators. I thank Jonathan Amazon for his contribution in performing Monte Carlo simulations for the work described in Chapter 2; Dr. Qi Wang and Laura Byrnes for experimental execution, data analysis and discussions for the work described in Chapter 4; and Robert Dick for experimental work and data analysis for the work described in Chapter 5.

I am also thankful for the support of many current and former members of both Feigenson and Sondermann labs, either through direct experimental help or stimulating discussions: Dr. Robin Petruzielo, Tatyana Konyakhina, David Ackerman, Susan Duan, Debashree Chatterjee, John O' Donnell, Dr. Petya Krasteva, Dr. Frederick Heberle, Nelson Morales-Penningston, Jing Wu, and Dr. Jiang Zhao. It was with their support that allowed me to smoothly perform experimental works in both labs throughout my doctorate work. I have also benefitted from valuable discussions with Dr. Volker Vogt, Kylan Szeto, and Sarah Shelby.

Many thanks to Dr. Boris Dzikovski at ACERT for assisting me in performing ESR experiments and data analysis. I thank committee members Dr. Barbara Baird and Dr. William Brown for critical reading of the dissertation.

I am grateful for the moral support of my classmates in the BMCB program, and all my friends at Cornell. It is helpful to balance work with play, and you have helped me achieved that during my stay in Ithaca.

Last but not least, I thank my parents, Yeang Liang and Ween Churn, who have always believed in me. I would never have gone this far in life without their support and I am deeply grateful for that. Thanks also to my siblings, Shih Han, Shih Yi and Shih Hui who have always been there for me. Finally, I would like to thank my husband, Dr. David Lee, who has been my number one supporter and has kept my chin up throughout this journey. I could never have done it without him.

TABLE OF CONTENTS

LIST OF FIGURES

LIST OF TABLES

LIST OF ABBREVIATIONS

16-DSA	16-DOXYL-stearic acid
BAR	Bin/Amphiphysin/Rvs
Bodipy-PC	2-(4,4-difluoro-5,7-dimethyl-4-bora-3a,4a-diaza-s-indacene-3-pentanoyl)-1-hexadecanoyl-sn-glycero-3-phosphocholine
bSM	brain-sphingomyelin
C12:0-DiI	1,1′-didodecyl-3,3,3′,3′-tetramethylindocarbocyanine perchlorate
C22:0-DiI	1,1′-didocosanyl-3,3,3′,3′-tetramethylindocarbocyanine perchlorate
CHOL	cholesterol
CTB	cholera toxin B
DHE	ergosta-5,7,9(11),22-tetraen- 3b-ol
DiPhyPC	diphytanoyl-phosphatidylcholine
DLPC	dilauroyl-phosphatidylcholine (12:0. 12:0 chains)
DOPC	dioleoyl-phosphatidylcholine (18:1, 18:1 chains)
DOPG	dioleoyl-phosphatidylglycerol (18:1, 18:1 chains)
DOPS	dioleoyl-phosphatidylserine (18:1, 18:1 chains)
DPPC	dipalmitoyl-phosphatidylcholine (16:0, 16:0 chains)
DPPS	dipalmitoyl-phosphatidylserine (16:0, 16:0 chains)
DRMs	detergent-resistant membranes
DSPC	distearoyl-phosphatidylcholine (18:0, 18:0 chains)
ESR	electron spin resonance
F-BAR	Fer/CIP homology-BAR
FPALM	fluorescence photoactivation localization microscopy
FRET	fluorescence resonance energy transfer
FT	freeze-thaw
Gag	group-specific antigen
GPI	glycosyl-phosphatidylinositol
GPMV	giant plasma membrane vesicles
GUVs	giant unilamellar vesicles
I-BAR	inverse-BAR
LUV	large unilamellar vesicles
MA	matrix domain
N-BAR	BAR with N-terminal amphipathic helix
NSOM	near-field optical microscopy
PC	phosphatidylcholine
PE	phosphatidylethanolamine
PI	phosphatidylinositol
$PI(4,5)P_2$	phosphatidylinositol-4,5-bisphosphate
PS	phosphatidylserine
PM	plasma membrane
PMS	plasma membrane spheres
POPC	palmitoyl-oleoyl-phosphatidylcholine (16:0, 18:1 chains)
POPE	palmitoyl-oleoyl-phosphatidylethanolamine (16:0, 18:1 chains)
POPS	palmitoyl-oleoyl-phosphatidylserine (16:0, 18:1 chains)

PRD	proline-rich domain
PSM	palmitoyl-sphingomyelin (16:0)
REE	region of enhanced FRET efficiency
RRE	region of reduced FRET efficiency
RSE	rapid solvent exchange
SAXS	small-angle X-ray scattering
SFT	sonicated and freeze-thaw
SH3	Src homology 3
SM	sphingomyelin
SOPE	stearoyl-oleoyl-phosphatidylethanolamine (18:0, 18:1 chains)
SP-FRET	steady-state probe-partitioning FRET
SSM	stearoyl-sphingomyeline (18:0)
STED	stimulated emission depletion
Tm	melting transition temperature
WASP	Wiscott-Alrich Syndrome protein

CHAPTER 1
Introduction

1.1 Overview

An overarching theme of the studies presented in this work relates to understanding the functional heterogeneity in animal cell plasma membranes, and how membrane properties and lipid-lipid interactions govern protein functions. The plasma membrane is a multicomponent mixture of lipids and proteins, with dynamic intermolecular interactions. The asymmetrical composition in its two monolayers introduces an additional level of complexity for studying protein-lipid associations in facilitating cellular functions. We seek to first understand lipid-lipid interactions by studying the phase behavior of model membrane mixtures consisting of chemically well-defined lipid compositions. Even in simple lipid mixtures mimicking the outer leaflet, rich phase behaviors are found, alluding to the active role of lipids in controlling the size and shape of domains that could be important in facilitating protein functions at the membrane. However, there is a disproportionately large number of model membrane studies on lipid mixtures that mimic the outer leaflet compared to the smaller number of models for the cytoplasmic leaflet; this precludes systematic investigations on the role of inner leaflet lipids in cellular processes such as endocytosis, exocytosis and retroviral budding.

The aim of this chapter is to give a unifying picture of the works presented in Chapters 2-5 from several distinct fields; more detailed background of each study is given in the individual chapters. I begin by providing background information on lipid bilayer phases, and the important developments in the identification and

characterization of plasma membrane rafts. Next, a brief overview of studies on outer leaflet membrane models is given, highlighting the need for a lipid-only model to investigate how cells might control a wide range of domain sizes (i.e. nanoscopic to micron-sized), and leading to specific questions to be addressed in Chapters 2 and 3. I then provide background information on the current view of lateral heterogeneity in the inner leaflet gathered from several model membrane studies, and of the two protein-mediated membrane binding and remodeling processes that occur on the cytoplasmic leaflet, studied in Chapters 4 and 5. I will end by describing problems to be addressed in Chapter 4, relating to membrane deformation mediated by F-BAR domain protein, pacsin-1; and in Chapter 5, relating to budding of HIV-1 protein, Gag.

1.2 Lipid phases in bilayers

Phosphoglycerolipids and sphingolipids are amphiphiles that form micelles or bilayer structures in the presence of water. Since the discovery of lipid bilayers in cells (1), understanding lipid phase behavior has become an important component towards understanding cellular processes. Phase behavior describes the interactions between different (or similar) molecules in a mixture, which is strongly affected by temperature. In bilayers, several types of lipid phases can form depending on the positional and conformational orders of the lipids. Positional order describes the two-dimensional (2D) spatial correlation between lipids within the bilayer. Bilayers with a high degree of positional order have a low lipid translational diffusion rate. Conformational order depicts the order of the lipid hydrocarbon chains, specifically the ratio of *trans* to *gauche* conformers. Lipids with all-*trans* conformers have acyl

chains that are fully extended, hence, high conformational order. Bilayers that have high positional and conformational orders are in the solid ordered, or gel phase (Lβ). At ambient temperature, phospholipids that have long and fully saturated acyl chains are usually in the Lβ phase. On the other hand, low positional and conformational orders are found in the liquid-disordered phase (Ld). In a pure lipid system, a phase transition from Lβ to Ld, which goes through a rippled gel phase ($P_{\beta'}$)-, can occur with increasing temperature, where complete phase transition occurs at the melting transition temperature, Tm. Saturated, long-chain phospholipids usually have a high Tm, whereas unsaturated or short-chain lipids have a low Tm.

In addition to the two phases mentioned, a third phase can exist when sterols such as cholesterol are added to a phospholipid bilayer: this is the liquid-ordered (Lo) phase. Due to the largely hydrophobic nature of cholesterol, it needs to be shielded by the head groups of phospholipids from exposure to water outside the bilayer, forcing the acyl chains of phospholipids in cholesterol mixtures to straighten out and assume higher *trans* conformations. Hence, lipid head groups act as umbrellas to shield the hydrophobic cholesterol molecules (2). However, even though conformational order is high, the Lo phase still preserves a high rate of lipid translational diffusion similar to that found in the Ld phase, resulting in a liquid phase that is high in acyl chain order.

1.3 Functional heterogeneity

1.3.1 Lipid rafts in animal cell plasma membrane

The plasma membrane (PM) is a quasi-2D barrier that surrounds a cell, and provides a well-controlled environment for the function of its organelles, away from the extracellular matrix. When the fluid mosaic model was proposed in 1972 (3), lipids in the membrane were pictured as a passive and fluid "sea" of molecules in which transmembrane and peripheral proteins diffuse and interact to drive cellular processes (Fig. 1.1 *A*). It was not until 16 years later that reports on lipid sorting into apical and basolateral areas of epithelial cell PM led to the notion that lipids could play a more active role along with proteins in the PM to mediate cellular functions (4). This resulted in an increasing appreciation for the possibility that lateral heterogeneities in the PM arising from nonrandom mixing of lipids and proteins could be important in governing cellular processes. Subsequently, the lipid raft hypothesis was proposed (5), postulating that functional domains within the PM with compositions that differ from the bulk "sea" of lipids, could influence the localization and function of proteins. These domains could serve to compartmentalize the quasi-2D bilayer, controlling the diffusion and local concentrations of particular proteins. A more current view of the PM is depicted in Fig.1.1 *B*. For the remaining of this chapter, the term "raft" refers to ordered regions in the PM, more enriched in cholesterol and saturated lipids.

Another important property of the mammalian cell PM is the asymmetric lipid composition of its monolayers, which is well documented in erythrocytes (7, 8). The lipid composition of the outer leaflet consists of mainly sphingomyelin (SM) and phosphatidylcholine (PC), whereas phosphatidylserine (PS), phosphatidylethanolamine (PE), and phosphatidylinositol (PI) mainly reside on the inner leaflet (9). Interestingly, almost all of the negatively charged phospholipids in

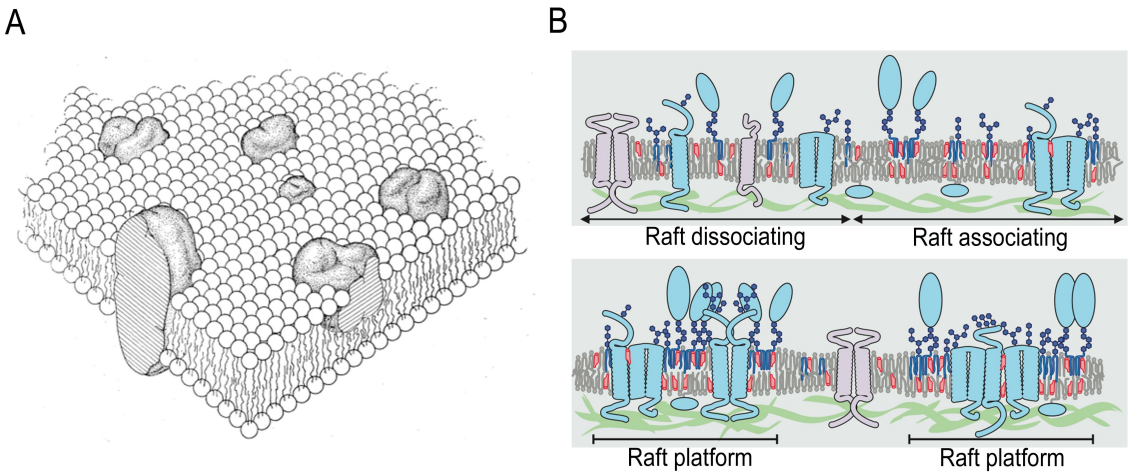

Figure 1.1 Evolving models of the animal cell plasma membrane. (A) The fluid mosaic model depicts the lipid bilayer as an overall uniform fluid matrix, where various integral proteins diffuse within (taken from (3)). (B) The current view of lipid rafts as nanoassemblies of ordered regions in the bilayer. Raft components such as GPI-anchored proteins (*dark and light blue*), acylated proteins (*light blue*), glycosphingolipids (*dark blue*) and cholesterol (*red*) can associate to form transient molecular assemblies (top panel) or more stable platforms (bottom panel), where non-raft transmembrane proteins (*light pink*) are excluded (modified from(6)).

the bilayer are located on the inner leaflet. Adding to this complexity is the variable distribution of transmembrane proteins, glycans, and peripheral membrane proteins throughout the bilayer. Despite that, the asymmetry in the lipid composition in plasma membranes allow researchers to study the lipid mixing behavior of each leaflet separately in model membrane mixtures (described later in this chapter), which is a good first step towards understanding overall membrane heterogeneity and its role in facilitating cellular functions.

Plasma membrane heterogeneity arises from nonrandom mixing amongst membrane components. One clue to a specific favorable interaction is that between long-chain sphingolipids and cholesterol; indeed, glycosphingolipids and cholesterol were enriched in the apical membranes of endothelial cells (4). Evidence for

compositionally distinct regions in the PM come from various studies. Reports on the diffusion dynamics of lipids and proteins obtained from single-particle tracking experiments revealed that particular lipids or membrane bound proteins undergo “hop diffusion”, where they were observed to diffuse more slowly within patches of small areas compared to the rest of the bilayer (10, 11). In other studies, altering or removing acylation on proteins involved in signaling cascades had dramatic effects on their localizations at the membrane, and resulted in loss of function of the proteins (12-14). Altogether, these observations are consistent with the presence of regions (domains) in the PM that have different compositions, which are affecting the movements and compartmentalization of proteins at the membrane.

The significance of membrane heterogeneity in governing protein functions can be gleaned from research conducted in the field of immune cell signaling (13). When FcεRI receptors are crosslinked by IgE, they form a stable patch on the PM outer leaflet, which recruits Lyn kinases to initiate phosphorylation of the receptors on the inner leaflet. Phosphatases were excluded from this patch. Furthermore, cholesterol depletion disrupted the co-localization of crosslinked receptors and Lyn, and subsequently, caused a loss of Lyn-mediated phosphorylation (15). This indicated that specialized compartments, distinct in compositions from the rest of the bilayer, could be formed in the PM based on favorable associations between particular lipids and proteins. Similar observations were reported in T cell signaling, where the regulation of adaptor protein phosphorylation events by kinases is dependent on their co-localization in specific regions within the PM upon stimulation of T cell receptors

(14). Disruption of proper protein localization results in disturbance of the entire signaling cascade.

1.3.2 Detergent-resistant membranes and the Lo phase

The sorting of glycosphingolipids and cholesterol to the *trans*-Golgi membranes and apical PM of epithelial cells raised questions on whether specific lipid-anchored proteins could be sorted based on preferential association with these "raft" lipids (4). Using a detergent-resistant assay, where cell membranes were treated with cold detergent and fractionated through a sucrose gradient, the same two lipids were recovered in the insoluble, low-density fraction, along with glycosyl-phosphatidylinositol (GPI)-anchored proteins (16). This biochemical assay was then used to probe other raft-associated proteins or membrane complexes (17, 18).

The properties of detergent-resistant membranes (DRMs) were also concurrently examined in model membrane mixtures. By comparing the differences in detergent solubility of several well-defined lipid mixtures, Schroeder *et al.* (19) revealed that the extent of detergent insolubility depends on the Tm of the lipids and the fluidity of the bilayers: the most insoluble lipids were long-chain saturated PC or sphingolipids with higher Tm's that can pack closely in the bilayer to result in high order, such as that found in Lo and Lβ phases. In addition, they were able to reproduce co-localization of GPI-anchored proteins in DRMs isolated from liposomes that contained sphingolipids and cholesterol, corroborating results from cellular DRMs. Separate studies employing electron spin resonance (ESR) determined that the rotational diffusion rates and order parameter of spin labels in DRMs extracted from rat basophil leukemia (RBL) cells were similar to that found in Lo bilayers (20).

Altogether, results from model membrane studies describe DRMs as ordered regions in the PM with Lo phase properties, probably coexisting with a more fluid Ld-like phase.

While the detergent-resistant assay had been widely used to identify cellular raft components, its consistency and reliability in correlating directly with pre-existing rafts in cells had been questioned (21). Mayor *et al.* (22) revealed that localization of GPI-anchored proteins to caveolae in cells only occurred after crosslinking the proteins with antibodies. In addition, cold detergent was also found to alter the distribution of several GPI-anchored proteins on the surface of cells (23) and induce the formation of ordered domains in model membrane mixtures (24). Indeed, this was not surprising because phase behavior is strongly affected by temperature. Moreover, different lipids and proteins were isolated if the assay was performed at higher temperatures (> 4°C) or if different detergents (besides Triton X-100) were used (25). Hence, the chemical interaction of components in DRMs may not reflect the *a priori* interactions between lipids and proteins in unperturbed cells, and DRMs are not synonymous to lipids rafts in cell plasma membranes (25). Additional methods are needed to aid the identification and characterization of functional domains in cell plasma membranes.

1.3.3 Biomembrane preparations from cells

Modeling PM rafts as coexisting Lo-like and Ld-like domains provides a clear physical basis for describing the underlying intermolecular interactions. However, the exclusion of many transmembrane proteins from the Lo phase in model membranes (26, 27), which have been previously thought to prefer rafts in cell PM-, raises the

question of whether the terms “Lo” and “rafts” can be used interchangeably. Recent studies on biomembrane preparations from cellular plasma membranes offer possible explanations for this discrepancy.

Giant plasma membrane vesicles (GPMV, (28)) or plasma membrane spheres (PMS, (29)) isolated from cellular PM contain lipids and proteins that are native to the cell PM, but do not include cytoskeleton elements. Hence, they could be better models for examining the potential of the PM to segregate into heterogeneous domains. Using fluorescent lipid analogs as phase indicators, membrane vesicles display micron-scale fluid phase separation (Ld + Lo) at ambient temperature (<25°C), or after crosslinking of GM1 by cholera toxin B (CTB) at 37°C (28, 29).

The partitioning of several transmembrane peptides, however, was observed to be variable, depending on the isolation conditions of the membrane vesicles. Paraformaldehyde and dithiothreitol (DTT) that are used to generate GPMV were found to disrupt palmitoylation of transmembrane proteins, which subsequently weakened their affinities for rafts (30, 31). Interestingly, some raft-preferring transmembrane peptides were observed to co-localize with the Lo-like phase in PMS, but not in that of GPMV, attributing to the variable properties of PMS and GPMV (29). Indeed, the use of paraformaldehyde in producing GPMV could cause crosslinking of components in the PM, and thus, affect phase properties of GPMV. A comparison of membrane order between phase-separated PMS, GPMV and model membrane mixtures led to distinct order differences between Ld-like and Lo-like phases (32): in PMS, where vesicles were obtained by osmotic swelling, the membrane order of its Lo-like phase was much lower compared to that in GPMV and

model membranes. This was proposed to be an explanation for why some transmembrane peptides partition out of the Lo phase in GMPV and model membranes, but prefer the Lo phase in PMS.

Both GPMV and PMS display macroscopic fluid phase separation, alluding to the presence of pre-existing raft nanoassemblies in cell PM. (In this chapter, "macroscopic" refers to size scales that are above the diffraction limit). However, comparison of the phase properties and protein partitioning behaviors in GPMV, PMS and model membranes led to the conclusion that properties of cellular lipid rafts are not the same as the Lo phase. While the Lo phase in model membranes have defined conformational and positional orders determined via spectroscopy methods, cellular rafts could have a variable range of properties that are dependent on more complex mixing of lipids and proteins (31). Hence, Lingwood and Simons (6) have proposed to only apply the terms Ld and Lo to model membrane mixtures, and not to describe rafts in living cells. However, since Ld and Lo phases in some model membrane mixtures could also be closer in composition and hence, in order, it remains to be determined whether model membranes can be used appropriately to describe lipid rafts.

1.4 Outer leaflet model membrane mixtures studied on giant unilamellar vesicles

Model membrane mixtures have proven to be invaluable in shedding light on the physical and chemical interactions that drive mixing/demixing of lipids. The complexity of the PM from multitudes of lipid-protein interactions hinders careful investigation of how membrane compartmentalization is controlled by cells. While the phase behavior observed in model membranes may not be directly correlated with

lipid rafts, phase diagrams of multicomponent lipid mixtures offer guides and predictions for the more complicated mixing behaviors in cell plasma membranes.

Several relatively complete phase diagrams of lipid mixtures that mimic the outer leaflet of a mammalian cell PM have been solved in the last decade. Mixtures containing a high Tm lipid, a low Tm lipid and cholesterol exhibit macroscopic phase separating regions of {Ld + Lo}, {Ld + Lβ}, and {Ld + Lo + Lβ}; these mixtures are deemed Type II mixtures (33, 34). Examples of Type II mixtures include dipalmitoyl-PC (DPPC)/dioleoyl-PC (DOPC)/ cholesterol (CHOL) (35, 36), brain-SM (bSM)/DOPC/CHOL (37), DPPC/ diphytanoyl-PC (DiPhyPC)/ CHOL (38), and distearoyl-PC (DSPC)/DOPC/CHOL (39). It turns out that the minimum requirement for obtaining coexisting Ld + Lo *in vitro* is the presence of cholesterol and two phospholipids with drastically different Tm. Within the coexisting Ld + Lo region of these mixtures, the Lo phase is enriched in the high Tm lipid and cholesterol, consistent with the umbrella model (2), and reminiscent of the close packing of long-chain glycosphigolipids and cholesterol that was observed in cellular rafts.

A description of model membranes studies would not be complete without mentioning one of the most important advances in the field that greatly aid phase behavioral investigation of model membranes. While Ld + Lo coexistence can be detected using infra-red spectroscopy and fluorescence quenching (40), it was the fluorescence microscopy imaging of coexisting domains on giant unilamellar vesicle (GUVs) that initiated an avalanche of model membrane studies (41). Using fluorescent lipid analogs that have preferential partitioning into different phases, macroscopic phase separation in lipid mixtures can be visualized with conventional fluorescence

microscopy methods. In addition to decisive determination of phase behavior upon visualization, the types of phases present could also be identified based on the dye partitioning behavior (42).

Preparation of GUVs is relatively straightforward; several different methods including gentle hydration (43, 44), and electroswelling (45) on conductive slides (indium tin-oxide or titanium) or on platinum wires (46) have been developed to allow preparation of GUVs from both net neutral and charged lipid mixtures, under low-salt to physiological conditions (47-49). In addition to the conventional methods that involve rehydration of a dried lipid film deposited on electrodes, several improvements have been introduced to prepare GUVs from pre-hydrated aqueous lipid samples (47, 48, 50), which can offer better compositional homogeneity in each sample (50).

Although fluorescence imaging of GUVs is useful for studying phase behavior of lipid mixtures, it does have several limitations. An inherent limitation is the resolution that can be acquired: all conventional microscopy methods are diffraction limited, and domains below ~ 200 nm cannot be clearly detected. This does not restrict investigations of macroscopic phase behavior, but is a problem if domains were nanoscopic. Second, lipid compositions are uniformly distributed across both leaflets in GUVs, and hence, do not mirror the asymmetry of cellular PM. Recent efforts have been made towards preparing asymmetric vesicles for more biologically relevant studies (51-53). Third, the method can give rise to artifactual light-induced phase separation, where chemical crosslinking can occur if fluorescent dyes are photo-oxidized upon intense fluorescence illumination (54-56). Usually, these occurrences

can be minimized by lowering the dye concentrations, and limiting the fluorescence exposure times and light intensity (56); but still many researchers ignore this major problem. A final weakness in using GUVs to study phase behavior relates to the phase preferences of the chosen fluorescent lipid analogs. Partitioning of fluorophores is not always predictable and can vary in different model membrane mixtures. For example, the long-chain saturated carbocyanine dye, C22:0-DiI, prefers the Lo phase in DSPC-containing mixtures, but partitions into the Ld phase in SM-containing mixtures (42). Also, in some mixtures, dyes could have only modest or equal partitioning preference into a phase, usually the Lo phase. Hence, care needs to be taken when selecting fluorescent lipid analogs for GUV phase studies as partitioning behavior of dyes depends on both the chemical structure of the dye and the lipid host system under study.

1.5 Nanoscopic Ld and Lo phase coexistence

1.5.1 Lipid rafts as nanoscopic assemblies in cells

The collective observations in cells, DRMs and biomembrane vesicles point to rafts as being nanoassemblies in cell plasma membranes (see Fig. 1.1 *B*). Indeed, unstimulated cells do not display macroscopic immiscible domains. Even GPI-anchored proteins, consistently identified as being raft-associated in various systems-, appeared to be uniformly distributed on the surface of cells, and only clustered into optically resolvable domains after crosslinking events or upon treatment with cold detergent (22, 23).

Reports on direct detection of nano-scale heterogeneities lend evidence for the existence of nanoscopic domains in cells. Sharma *et al.* ((57) used homo- and hetero-FRET (fluorescence resonance energy transfer) to detect clusters of various GPI-anchored proteins on the cell surface. They reported cluster sizes of < 5nm, and also observed that the clusters were sensitive to cholesterol and sphingolipid depletions. Antibody-mediated crosslinking resulted in formation of micron-size domains enriched in GPI-anchored proteins, consistent with many previous studies (18, 58). In a separate study, FRET between carbocyanine lipid analogs (markers of the PM outer leaflet) revealed nanoscopic heterogeneities in RBL cells, that were also dependent on cholesterol content (59). Additional comparison of FRET between the same dye pairs in model membranes confirmed that the heterogeneity detected in live cells were not results of nonrandom mixing, and represents coexisting nanoscopic phases (59).

Correlation between the nanoscopic heterogeneities in cells with Ld + Lo phase coexistence was demonstrated in an ESR study by Freed and colleagues (60). The order parameter and rotational diffusion coefficient reported by various spin-labeled lipids in four different cell lines revealed coexisting Ld and Lo environments. In addition, they also detected the Lo phase being the major component, consistent with other observations proposing that the bulk of the plasma membrane is in a more ordered (Lo-like) environment (61).

Advances in pushing the resolution limit in microscopy methods also aided in detection of nanoscopic heterogeneities in cells (6, 62). Fluorescence photoactivation localization microscopy (FPALM) was applied to resolve 40 nm-size clusters formed by influenza hemagluttinin proteins on cell membranes (63). Separately, stimulated

emission depletion (STED) far-field nanoscopy detected hindered diffusion of sphingolipids in nanoscopic domains in the plasma membrane of live cells (64). In T-cell signaling, van Zanten *et al.* (65) determined the nanoscale architecture of integrin (lymphocyte function-associated antigen-1, LFA-1) and GPI-anchored protein clusters prior to antigen stimulation using single-molecule near-field optical microscopy (NSOM). They revealed that LFA-1 forms separate nanoclusters near hotspots of GPI-anchored proteins, but upon ligand binding to LFA-1, co-localization of ligand-bound LFA-1 and GPI-anchored proteins formed a larger macromolecular assembly. Many of these studies also found that the integrity of the nanoassemblies depends on cholesterol concentrations in cells (64, 65), lending support for nanoscopic lipid rafts in cell PM.

The current view of lipid rafts as nanoscale assemblies leads to many questions regarding their lifetime and stability. If the PM is indeed phase-separated, what are the mechanisms in play that keep the domains from coalescing? Results from experimental and theoretical studies suggest that cytoskeletal attachments on the plasma membrane could play a role in regulating raft sizes (11, 13, 66, 67). In addition, transmembrane proteins could also be involved in compartmentalizing the PM (6, 11). On the other hand, there are speculations suggesting that the PM composition is close to or at a critical point, and that the nanoscopic domains detected in cells are merely critical fluctuations (68, 69). The lifetime and residency time of lipid rafts in cells are also not well described (reviewed in (70)).

1.5.2 Nanosopic domains in outer leaflet model membrane mixtures

The underlying complex multicomponent mixing behavior that gives rise to nanoscopic and possibly fleeting rafts in the PM is poorly understood. Since model membrane studies have provided the physical and chemical basis for describing large-scale phase separation in cell membranes, at least for mixtures that model the outer leaflet of the PM, we believe that model membranes are still invaluable for studying nanoscopic phase separation. Under steady-state conditions governed by the rules of equilibrium thermodynamics, where parameters such as temperature and lipid composition can be controlled, the phase behavior of lipid-only mixtures allows the study of how domain size (or shape) and mixing might vary with temperature and lipid composition. This information will provide a basis for understanding more complex interactions at the PM.

Coexisting nanodomains were detected in DPPC/dilauroyl-PC (DLPC)/CHOL mixtures as early as 2001, using FRET and dipyrene-PC excimer/monomer ratio (71). In Type II phase diagrams, where only macroscopic phase separation was observed, the canonical choices for lipids are largely unnatural lipids, such as DSPC, DOPC or DiPhyPC. Later, when more biologically relevant lipids (i.e. palmitoyl-oleoyl-phosphatidylcholine [POPC], bSM) were used instead in related three-component mixtures, such as DSPC/POPC/CHOL (72), bSM/POPC/CHOL (73), and palmitoyl-SM (PSM)/POPC/CHOL (74), nanoscopic Ld + Lo domains were reported. In all cases, the detection of nanodomains was done using methods sensitive to small length scales, such as FRET, ESR, and/or fluorescence quenching. These mixtures were grouped as Type I mixtures, which generally exhibit a {Ld + Lβ} region, but no macroscopic {Ld + Lo} regions (34).

Mixtures that have the potential for nanoscopic phase separation are superior models for studying similar interactions in cell PM. In particular, they provide good systems for nanodomain size estimations and also spurred several theoretical studies on examining the various opposing forces at work to maintain stably dispersed nanodomains (75-77). Despite that, the model membranes field still lacks an appropriate system for systematic studies of how (or if) domain size, and possible shape, can be controlled in lipid-only mixtures. Such investigations would require more than three components, based on studies of related Type I and Type II mixtures, such as DSPC/POPC/CHOL and DSPC/DOPC/CHOL (72). Furthermore, nanoscopic compartmentalization in presumably phase-separated PM could be achieved by controlling phase connectivity (or phase percolation). Percolation is affected by the fractions of two coexisting phases; a switch in phase percolation can change phase morphology without altering the compositions in each phase. Changing phase connectivity in cells can be achieved without drastic perturbations to local membrane composition, and can concentrate or co-localize particular proteins in one phase, while excluding antagonistic proteins in a different phase. In any cases, the mechanism of domain size and morphology control has yet to be revealed in detail.

1.6 Thesis aim 1: Investigating modulated phases in a four-component outer leaflet model

The transition from nanoscopic to macroscopic Ld + Lo coexisting domains can be obtained in the four-component mixture DSPC/DOPC/POPC/CHOL, when the biologically relevant lipid, POPC, is replaced with DOPC (Konyakhina, TM *et al.*,

unpublished). While GUVs abruptly go from appearing uniform (when domains are nanoscopic), to exhibiting macroscopic round domains, FRET detected a gradual narrowing in the Ld + Lo region (72). Hence, this system seems appropriate for examining the nature of nano-to-macro domain size transition.

Recently, we reported the occurrence of modulated phases at particular DOPC/POPC ratios (78), corresponding to an intermediate regime between the nanoscopic and macroscopic liquid coexisting regions of the tetrahedral phase diagram. In chapters 2 and 3, we proceeded to more clearly describe the occurrence of modulated phases in the Ld + Lo volume of DSPC/DOPC/POPC/CHOL (Chapter 2), and also to investigate the thermodynamic nature of modulated phases in bilayers (Chapter 3).

1.7 Lipid rafts in the inner leaflet?

The PM has an asymmetric distribution of lipid species on each leaflet, with PE, and negatively charged PS and PI located mostly on the inner leaflet, whereas PC and sphingolipids reside mainly on the outer leaflet (8, 9). The distribution of cholesterol in each leaflet has been hard to determine due to its high flip-flop rate, but the overall cholesterol content in the PM could be close to 50 mol % (79, 80). Since one of the main constituents of lipid rafts, long-chain sphingolipids, reside on the outer leaflet of the bilayer, all of the model membrane studies described above only explain the basis for heterogeneity on the outer leaflet of the PM. The majority of PE and PS lipids have unsaturated acyl chains, based on recent lipidomics studies (62, 81). So far, no coexisting Lo + Ld domains have been found in mixtures consisting of

only inner leaflet lipids (unsaturated PS, PE) and cholesterol (82). Furthermore, these mixtures are also soluble in cold detergent (82), raising questions about the potential of acidic phospholipids and PE to form cholesterol-rich rafts in the cytoplasmic leaflet.

Recently, the effect of negatively charged lipids on the formation of macroscopic immiscible fluid domains was studied in several mixtures containing PS (or phosphatidylglycerol, PG), PC and cholesterol. Shimokawa *et al.* (83) found that immiscible fluid domains occurred in DPPC/dioleoyl-PS (DOPS)/CHOL mixtures only in the presence of $CaCl_2$, where the presence of calcium-bound DOPS induced lateral de-mixing. Separately, Vequi-Suplicy *et al.* (49) examined egg-SM/dioleoyl-PG (DOPG)/CHOL mixtures and observed Ld + Lo coexistence occurring only in a very small region on the phase diagram. In the Feigenson lab, we observed that larger regions of Ld + Lo coexistence can be obtained in mixtures containing dipalmitoyl-PS (DPPS)/DOPC/CHOL (Nelson Morales-Penningston, personal communication), where DPPS has a Tm similar to DSPC (55°C). These studies indicate that unsaturated, negatively charged lipids do not have a strong tendency to drive Ld + Lo phase separation, even in the presence of saturated lipids.

From model membrane studies, the cytoplasmic leaflet of the PM may not form pre-existing lipid rafts on its own; but cellular studies indicate that outer leaflet rafts can be coupled to the inner leaflet and re-distribute inner leaflet proteins (18). Coupling between leaflets could occur via interdigitation from long-chained lipids, or from transmembrane proteins (84). Indeed, strong bilayer coupling was confirmed in two-photon imaging of GUVs displaying macroscopic phase separation (41). Another possible mechanism of coupling could involve the formation of coexisting phases in

one leaflet influencing phase separation in the opposite leaflet. Studies performed on supported lipid bilayer systems revealed that Lo + Ld phase separation can be induced in inner leaflet mixtures by an opposite phase-separated monolayer consisting of outer leaflet mixtures (85). However, possible artifacts imposed by the solid support and from photo-oxidation of fluorescent dyes warrant further investigations in such systems. On the other hand, binding of proteins on the cytoplasmic leaflet could result in lipid sorting and local phase separation, depending on the composition (86). Nevertheless, the detailed mechanism of leaflet coupling and the effect of protein binding on lipid mixing remain to be explored.

Valuable information on lipid-lipid mixing can be gleaned from outer leaflet model membrane studies to aid further investigations on protein-raft association in the outer leaflet of cell PM. The lack of a good "inner leaflet model" poses a challenge for researchers to effectively study membrane-protein interactions in processes that occur mainly on the cytoplasmic leaflet, such as endocytosis and viral assembly/ budding. In particular, we are interested in exploring the roles played by lipids in membrane remodeling events involving BAR (Bin/Amphiphysin/Rvs) domain proteins in receptor-mediated endocytosis, and retroviral HIV-1 Gag (human immunodeficiency virus-1 group-specific antigen) proteins in viral assembly and budding. Both systems are similar in that they involve a membrane binding event, followed by a membrane remodeling event upon recruitment of additional adaptor proteins and/or the formation of a local protein lattice, and finally, a membrane scission event. One main difference between endocytosis and retroviral budding relates to the change in local membrane topology during the processes: BAR domains aid in bending membranes towards the

cytoplasm, whereas HIV-1 Gag proteins bend the membrane outwards to release viral particles and sustain infectivity.

1.8 The BAR domain superfamily

1.8.1 BAR domains are curvature sensors and generators

The BAR domain superfamily includes a large number of proteins that are regulators of membrane curvature, and are involved in cellular trafficking and membrane fission events (87, 88). All BAR domain-containing proteins exist as stable dimers, with a six-helix bundle formed by the three helices in each BAR domain fold (Fig. 1.2). The majority of BAR domain proteins appear crescent-shaped, where the degree of their structural intrinsic curvatures can vary. Positively charged residues on the membrane-interacting surfaces on BAR domains bind electrostatically to acidic phospholipids on the inner leaflet of the PM (89, 90). Based on their structures and their membrane sculpting abilities, they can be grouped into three different classes: BAR and N-BAR domain proteins such as endophilin, amphiphysin and sorting nexin 9, have high intrinsic curvatures and are found to stabilize narrow tubules *in vitro* (89, 91-93). In addition, N-BAR proteins contain amphipathic helices that can insert into the bilayer to facilitate membrane remodeling (89, 91, 92). F-BAR domain proteins such as CIP4 and pacsin/syndapin, have more shallow intrinsic curvatures, and hence are found to generate wider tubules *in vitro* (94, 95). Finally, I-BAR domain proteins such as IRSp53 and MIM, have convex membrane-binding surfaces, and are observed to generate invaginations *in vitro* (96, 97).

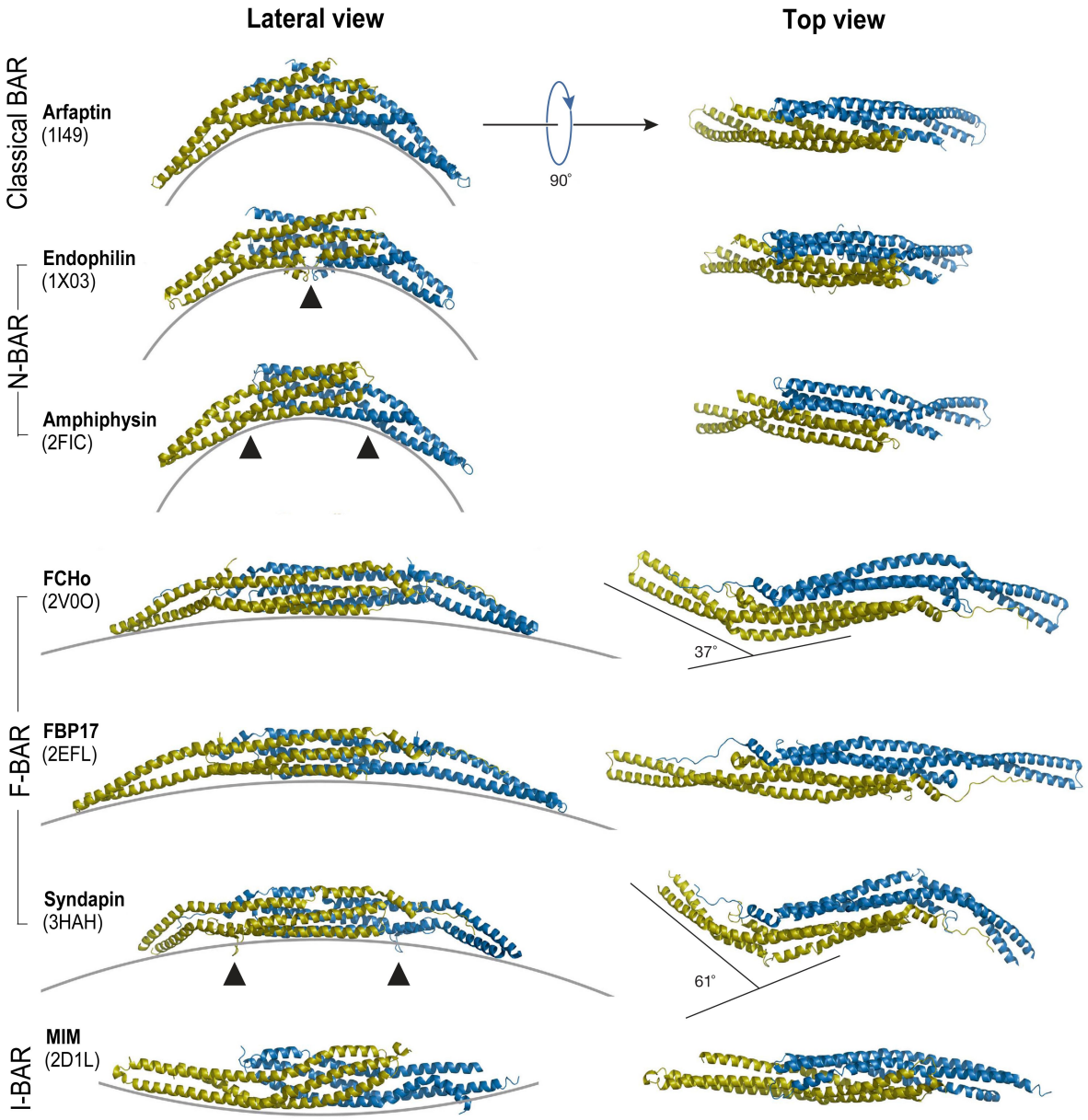

Figure 1.2 BAR domains from different sub-families adopt different degrees of curvature. Each structure depicts a BAR dimer (one monomer colored in yellow, the other in blue), and is viewed from the side (left panel) or from the top (right panel). Triangles indicate the location of amphipathic helices (endophilin and amphiphysin) or hydrophobic loops (syndapin) that are inserted into the bilayer during membrane deformation. Figure taken from (87).

One of the most studied process involving BAR domain proteins is clathrin-mediated endocytosis. Work by several research groups elegantly showed the recruitment of different classes of BAR domains at different times during the generation of an endocytic vesicle (reviewed in (87)). The absolute requirement of BAR domain proteins was called into question due to the redundancy of multiple BAR proteins of the same class that are involved in similar pathways. This could be related to different propensities of the various BAR domain proteins to sense or induce curvature. Moreover, many members of the BAR superfamily also contain additional interacting modules to target phosphoinositides and other proteins, thus making them adaptors in cellular processes. For example, the Src homology 3 (SH3) domain in pacsin, endophilin and amphiphysin allows these BAR domain proteins to interact with dynamin, N-WASP, and synaptojanin, linking endocytosis with the regulation of actin cytoskeleton (90). With the identification of the family's newest member, Pinkbar, which generates planar membrane sheets (98), and reports of several BAR proteins that exhibit divergent membrane sculpting behaviors from members of their respective sub-families (99), we think that certain BAR domain-containing proteins have probably evolved to be more versatile in their abilities to sense curved topology and induce membrane deformation.

1.8.2 Pacsin-1: an F-BAR domain

Pacsin-1 is the brain-specific isoform of the pacsin/syndapin family; it is also one of the most versatile membrane remodeler in its F-BAR domain sub-family. In addition to a shallow concave curvature typical of an F-BAR domain protein, pacsin-1 possesses hydrophobic loops that can be inserted into one leaflet of the bilayer and aid

in its membrane remodeling abilities (95): highly-curved pearling structures and thin tubules were generated *in vitro*, in addition to the more canonical wide tubules expected from an F-BAR domain. This membrane sculpting versatility could be attributed to the unique structure of its F-BAR domain.

The versatile membrane deformation abilities of pacsin-1$^{F\text{-}BAR}$ belie the activity of full-length pacsin-1, which is more inhibited in its membrane remodeling potential as demonstrated *in vitro* (95) and in cells (100). However, potent *in vitro* tubulation activity of the full-length protein can be unleashed when bound to the proline-rich domain (PRD) of dynamin-1 via pacsin-1's SH3 domain (101). The mechanism of pacsin-1's activation has been speculated upon based on the determination of the crystal structure of full-length pacsin-1, but not well described functionally (101). Pacsin-1 is implicated in clathrin-mediated endocytosis at the synapse, where it not only plays a role as membrane topology regulator, it is also responsible for recruiting key proteins required in the pathway, such as dynamin-1. Interestingly, under intense stimulation conditions of neurons, additional clathrin-independent endocytosis pathways are activated, where pacsin-1 has been shown to play an important role alongside dynamin-1 as well (102, 103). The autoinhibition of pacsin-1 could reflect tight regulation of its *in vivo* activity in synaptic vesicle recycling pathways by key accessory proteins.

While there are studies on the specific protein-protein interactions needed to activate pacsin-1, less is known about the interplay between lipid composition and membrane remodeling of pacsin-1 and of BAR domain proteins in general. Separate studies on amphiphysin (104) and endophilin N-BAR (105) demonstrated that the

curvature sensing and curvature inducing functions in both proteins are decoupled, depending on the bound protein density. At dilute concentrations, amphiphysin and endophilin N-BAR merely sense areas of high membrane curvature (i.e. on tubes pulled from GUVs); at high concentrations, both proteins form scaffolds along the tube and can change the tube diameter. While these studies help elucidate the possible *in vivo* versatility of BAR domain proteins, they do not shed light on the active roles played by lipids. Active lipid sorting that is mediated by membrane curvature has been shown using outer leaflet model membrane mixtures, where micropipette aspiration techniques were used to pull narrow tubules from GUVs (86, 106, 107). Based on available ternary phase diagrams of outer leaflet models, several studies reported that Ld + Lo phase separation can be induced when lipid mixtures were close to a phase boundary (86, 106), or when minor lipid components, such as GM1, were crosslinked by CTB (86). It would be helpful for further investigations of the interplay between BAR domain proteins and lipid phase behavior during membrane deformation if model mixtures of the PM inner leaflet were available.

1.8.3 Thesis aim 2: Investigating the mechanism of pacsin-1 mediated membrane deformation *in vitro*

In Chapter 4, we investigated the activation of full-length pacsin-1 by dynamin-1 PRD using mutational studies of the PRD, liposome binding assays and *in vitro* membrane deformation assays. In addition, we also examined various factors such as liposome preparation methods and membrane properties that affect the membrane sculpting ability of pacsin-1, and other BAR domain-containing proteins.

Efforts have also been invested in examining the phase behavior of inner leaflet model systems. Results of various attempts are described in Appendix A.

1.9 Retroviral assembly and budding: HIV-1 Gag and lipid rafts

One of the first steps in HIV-1 assembly involves binding of the polyprotein Gag to the PM inner leaflet of host cells. Multimerization of Gag, followed by incorporation of viral genomic RNA and glycoproteins, eventually result in budding and releasing of viral particles outside the cell (108). Binding of Gag is mediated by its N-terminal matrix (MA) domain, which contains a conserved polybasic patch, a myristate group, and a phosphatidylinositol-4,5-bisphosphate, $PI(4,5)P_2$, binding pocket.

HIV-1 Gag is said to bud from lipid rafts. This statement is supported by several observations: 1) The lipid composition of retroviral envelopes is enriched in glycosphingolipids and cholesterol compared to the host cell PM (109-111); 2) proteins that are usually found in rafts were observed to associate with HIV-1 particles (112); and 3) cholesterol depletion affected the maintenance of intact viral particles and decreased viral infectivity (113). In addition, lipids from influenza and HIV-1 virions were found in DRMs, and their solubilities were dependent on cholesterol (114, 115). The preferential association of HIV-1 Gag with ordered lipids and cholesterol may be true, but how Gag acquires raft-like compositions when there is a lack of direct evidence for the existence of rafts in the inner leaflet of the PM remains a question to be answered. Do Gag proteins selectively bind to cholesterol-enriched raft-like regions, or does Gag-membrane association induce the formation of a raft-

like phase on the outer leaflet of the PM? These questions also relate to the mechanism of leaflet coupling (mentioned above) that is a current active area of research.

1.9.1 Thesis aim 3: Investigating the effects of lipid composition on HIV-1 Gag-membrane association

The preference of HIV-1 Gag for raft-like lipid compositions has not been systematically examined *in vitro*. While it is established that membrane net negative charge strongly governs Gag-membrane interactions, the effects of cholesterol and acyl chain saturation of phospholipids on Gag membrane affinity are not known. In Chapter 5, using ESR to determine the membrane order of various series of model membrane mixtures and *in vitro* liposome flotation assays to assess Gag-membrane association, we examined the dependence of HIV-1 Gag membrane affinity to cholesterol concentrations, acyl chain saturation, and type of PS species.

References

1. Steim, J.M., M.E. Tourtellotte, J.C. Reinert, R.N. McElhaney, and R.L. Rader. 1969. Calorimetric evidence for the liquid-crystalline state of lipids in a biomembrane. Proc. Natl. Acad. Sci. U.S.A. 63: 104–109.

2. Huang, J., and G.W. Feigenson. 1999. A microscopic interaction model of maximum solubility of cholesterol in lipid bilayers. Biophysj. 76: 2142–2157.

3. Singer, S.J., and G.L. Nicolson. 1972. The fluid mosaic model of the structure of cell membranes. Science. 175: 720–731.

4. Simons, K., and G. van Meer. 1988. Lipid sorting in epithelial cells. Biochemistry. 27: 6197–6202.

5. Simons, K., and E. Ikonen. 1997. Functional rafts in cell membranes. Nature. 387: 569–572.

6. Lingwood, D., and K. Simons. 2010. Lipid rafts as a membrane-organizing principle. Science. 327: 46–50.

7. Verkleij, A.J., R.F. Zwaal, B. Roelofsen, P. Comfurius, D. Kastelijn, et al. 1973. The asymmetric distribution of phospholipids in the human red cell membrane. A combined study using phospholipases and freeze-etch electron microscopy. Biochim. Biophys. Acta. 323: 178–193.

8. Devaux, P.F. 1991. Static and dynamic lipid asymmetry in cell membranes. Biochemistry. 30: 1163–1173.

9. Kiessling, V., C. Wan, and L.K. Tamm. 2009. Domain coupling in asymmetric lipid bilayers. BBA - Biomembranes. 1788: 64–71.

10. Murase, K., T. Fujiwara, Y. Umemura, K. Suzuki, R. Iino, et al. 2004. Ultrafine membrane compartments for molecular diffusion as revealed by single molecule techniques. Biophysj. 86: 4075–4093.

11. Kusumi, A., C. Nakada, K. Ritchie, K. Murase, K. Suzuki, et al. 2005. Paradigm shift of the plasma membrane concept from the two-dimensional continuum fluid to the partitioned fluid: high-speed single-molecule tracking of membrane molecules. Annu. Rev. Biophys. Biomol. Struct. 34: 351–378.

12. Samelson, L.E. 2002. Signal transduction mediated by the T cell antigen receptor: the role of adapter proteins. Annu. Rev. Immunol. 20: 371–394.

13. Holowka, D., J.A. Gosse, A.T. Hammond, X. Han, P. Sengupta, et al. 2005. Lipid segregation and IgE receptor signaling: A decade of progress.

Biochimica et Biophysica Acta (BBA) - Molecular Cell Research. 1746: 252–259.

14. Fuller, D.M., and W. Zhang. 2009. Regulation of lymphocyte development and activation by the LAT family of adapter proteins. Immunol. Rev. 232: 72–83.

15. Sheets, E.D., D. Holowka, and B. Baird. 1999. Critical role for cholesterol in Lyn-mediated tyrosine phosphorylation of FcepsilonRI and their association with detergent-resistant membranes. The Journal of Cell Biology. 145: 877–887.

16. Brown, D.A., and J.K. Rose. 1992. Sorting of GPI-anchored proteins to glycolipid-enriched membrane subdomains during transport to the apical cell surface. Cell. 68: 533–544.

17. Brown, D.A., and E. London. 1998. Structure and origin of ordered lipid domains in biological membranes. J Membrane Biol. 164: 103–114.

18. Simons, K., and D. Toomre. 2000. Lipid rafts and signal transduction. Nat Rev Mol Cell Biol. 1: 31–39.

19. Schroeder, R., E. London, and D. Brown. 1994. Interactions between saturated acyl chains confer detergent resistance on lipids and glycosylphosphatidylinositol (GPI)-anchored proteins: GPI-anchored proteins in liposomes and cells show similar behavior. Proceedings of the National Academy of Sciences. 91: 12130–12134.

20. Ge, M., K.A. Field, R. Aneja, D. Holowka, B. Baird, et al. 1999. Electron spin resonance characterization of liquid ordered phase of detergent-resistant membranes from RBL-2H3 cells. Biophysj. 77: 925–933.

21. London, E., and D.A. Brown. 2000. Insolubility of lipids in triton X-100: physical origin and relationship to sphingolipid/cholesterol membrane domains (rafts). Biochim. Biophys. Acta. 1508: 182–195.

22. Mayor, S., K.G. Rothberg, and F.R. Maxfield. 1994. Sequestration of GPI-anchored proteins in caveolae triggered by cross-linking. Science. 264: 1948–1951.

23. Mayor, S., and F.R. Maxfield. 1995. Insolubility and redistribution of GPI-anchored proteins at the cell surface after detergent treatment. Mol. Biol. Cell. 6: 929–944.

24. Heerklotz, H. 2002. Triton promotes domain formation in lipid raft mixtures. Biophysj. 83: 2693–2701.

25. Brown, D.A. 2006. Lipid rafts, detergent-resistant membranes, and raft targeting signals. Physiology (Bethesda). 21: 430–439.

26. Fastenberg, M.E., H. Shogomori, X. Xu, D.A. Brown, and E. London. 2003. Exclusion of a transmembrane-type peptide from ordered-lipid domains (rafts) detected by fluorescence quenching: extension of quenching analysis to account for the effects of domain size and domain boundaries. Biochemistry. 42: 12376–12390.

27. Shogomori, H., A.T. Hammond, A.G. Ostermeyer-Fay, D.J. Barr, G.W. Feigenson, et al. 2005. Palmitoylation and intracellular domain interactions both contribute to raft targeting of linker for activation of T cells. J. Biol. Chem. 280: 18931–18942.

28. Baumgart, T., A.T. Hammond, P. Sengupta, S.T. Hess, D.A. Holowka, et al. 2007. Large-scale fluid/fluid phase separation of proteins and lipids in giant plasma membrane vesicles. Proc. Natl. Acad. Sci. U.S.A. 104: 3165–3170.

29. Lingwood, D., J. Ries, P. Schwille, and K. Simons. 2008. Plasma membranes are poised for activation of raft phase coalescence at physiological temperature. Proceedings of the National Academy of Sciences. 105: 10005–10010.

30. Levental, I., D. Lingwood, M. Grzybek, U. Coskun, and K. Simons. 2010. Palmitoylation regulates raft affinity for the majority of integral raft proteins. Proceedings of the National Academy of Sciences. 107: 22050–22054.

31. Levental, I., M. Grzybek, and K. Simons. 2011. Raft domains of variable properties and compositions in plasma membrane vesicles. Proceedings of the National Academy of Sciences. 108: 11411–11416.

32. Kaiser, H.J., D. Lingwood, I. Levental, J.L. Sampaio, L. Kalvodova, et al. 2009. Order of lipid phases in model and plasma membranes. Proc. Natl. Acad. Sci. U.S.A. 106: 16645–16650.

33. Feigenson, G.W. 2007. Phase boundaries and biological membranes. Annu. Rev. Biophys. Biomol. Struct. 36: 63–77.

34. Feigenson, G.W. 2009. Phase diagrams and lipid domains in multicomponent lipid bilayer mixtures. Biochimica et Biophysica Acta (BBA) - Biomembranes. 1788: 47–52.

35. Buboltz, J.T., C. Bwalya, K. Williams, and M. Schutzer. 2007. High-Resolution Mapping of Phase Behavior in a Ternary Lipid Mixture: Do Lipid−Raft Phase Boundaries Depend on the Sample Preparation Procedure? Langmuir. 23: 11968–11971.

36. Veatch, S.L., and S.L. Keller. 2005. Seeing spots: Complex phase behavior in simple membranes. Biochimica et Biophysica Acta (BBA) - Molecular Cell Research. 1746: 172–185.

37. Veatch, S., and S. Keller. 2005. Miscibility Phase Diagrams of Giant Vesicles Containing Sphingomyelin. Phys. Rev. Lett. 94.

38. Veatch, S.L., K. Gawrisch, and S.L. Keller. 2006. Closed-loop miscibility gap and quantitative tie-lines in ternary membranes containing diphytanoyl PC. Biophysj. 90: 4428–4436.

39. Zhao, J., J. Wu, F.A. Heberle, T.T. Mills, P. Klawitter, et al. 2007. Phase studies of model biomembranes: Complex behavior of DSPC/DOPC/Cholesterol. Biochimica et Biophysica Acta (BBA) - Biomembranes. 1768: 2764–2776.

40. Silvius, J.R., D. del Giudice, and M. Lafleur. 1996. Cholesterol at different bilayer concentrations can promote or antagonize lateral segregation of phospholipids of differing acyl chain length. Biochemistry. 35: 15198–15208.

41. Korlach, J., P. Schwille, W.W. Webb, and G.W. Feigenson. 1999. Characterization of lipid bilayer phases by confocal microscopy and fluorescence correlation spectroscopy. Proc. Natl. Acad. Sci. U.S.A. 96: 8461–8466.

42. Baumgart, T., G. Hunt, E.R. Farkas, W.W. Webb, and G.W. Feigenson. 2007. Fluorescence probe partitioning between Lo/Ld phases in lipid membranes. Biochimica et Biophysica Acta (BBA) - Biomembranes. 1768: 2182–2194.

43. Reeves, J.P., and R.M. Dowben. 1969. Formation and properties of thin-walled phospholipid vesicles. J. Cell. Physiol. 73: 49–60.

44. Akashi, K., H. Miyata, H. Itoh, and K. Kinosita. 1996. Preparation of giant liposomes in physiological conditions and their characterization under an optical microscope. Biophysj. 71: 3242–3250.

45. Angelova, M., S. Soleau, P. Méléard, F. Faucon, and P. Bothorel. 1992. Preparation of giant vesicles by external AC electric fields. Kinetics and applications. Trends in Colloid and Interface Science VI. : 127–131.

46. Méléard, P., C. Gerbeaud, T. Pott, L. Fernandez-Puente, I. Bivas, et al. 1997. Bending elasticities of model membranes: influences of temperature and sterol content. Biophysj. 72: 2616–2629.

47. Montes, L., A. Alonso, F. Goni, and L.A. Bagatolli. 2007. Giant Unilamellar Vesicles Electroformed from Native Membranes and Organic Lipid Mixtures under Physiological Conditions☆. Biophys. J. 93: 3548–3554.

48. Pott, T., H. Bouvrais, and P. Méléard. 2008. Giant unilamellar vesicle formation under physiologically relevant conditions. Chemistry and Physics of Lipids. 154: 115–119.

49. Vequi-Suplicy, C.C., K.A. Riske, R.L. Knorr, and R. Dimova. 2010. Vesicles with charged domains. Biochim. Biophys. Acta. 1798: 1338–1347.

50. Baykal-Caglar, E., E. Hassan-Zadeh, B. Saremi, and J. Huang. 2012. Preparation of giant unilamellar vesicles from damp lipid film for better lipid compositional uniformity. Biochim. Biophys. Acta. 1818: 2598–2604.

51. Cheng, H.-T., Megha, and E. London. 2009. Preparation and properties of asymmetric vesicles that mimic cell membranes: effect upon lipid raft formation and transmembrane helix orientation. J. Biol. Chem. 284: 6079–6092.

52. Chiantia, S., P. Schwille, A.S. Klymchenko, and E. London. 2011. Asymmetric GUVs prepared by MβCD-mediated lipid exchange: an FCS study. Biophys. J. 100: L1–3.

53. Cheng, H.-T., and E. London. 2011. Preparation and properties of asymmetric large unilamellar vesicles: interleaflet coupling in asymmetric vesicles is dependent on temperature but not curvature. Biophys. J. 100: 2671–2678.

54. Zhao, J., J. Wu, H. Shao, F. Kong, N. Jain, et al. 2007. Phase studies of model biomembranes: Macroscopic coexistence of Lα+Lβ, with light-induced coexistence of Lα+Lo Phases. Biochimica et Biophysica Acta (BBA) - Biomembranes. 1768: 2777–2786.

55. Ayuyan, A.G., and F.S. Cohen. 2006. Lipid Peroxides Promote Large Rafts: Effects of Excitation of Probes in Fluorescence Microscopy and Electrochemical Reactions during Vesicle Formation. Biophys. J. 91: 2172–2183.

56. Morales-Penningston, N.F., J. Wu, E.R. Farkas, S.L. Goh, T.M. Konyakhina, et al. 2010. GUV preparation and imaging: minimizing artifacts. Biochim. Biophys. Acta. 1798: 1324–1332.

57. Sharma, P., R. Varma, R.C. Sarasij, Ira, K. Gousset, et al. 2004. Nanoscale organization of multiple GPI-anchored proteins in living cell membranes. Cell. 116: 577–589.

58. Harder, T., P. Scheiffele, P. Verkade, and K. Simons. 1998. Lipid domain structure of the plasma membrane revealed by patching of membrane components. The Journal of Cell Biology. 141: 929–942.

59. Sengupta, P., D. Holowka, and B. Baird. 2007. Fluorescence Resonance

Energy Transfer between Lipid Probes Detects Nanoscopic Heterogeneity in the Plasma Membrane of Live Cells. Biophys. J. 92: 3564–3574.

60. Swamy, M.J., L. Ciani, M. Ge, A.K. Smith, D. Holowka, et al. 2006. Coexisting Domains in the Plasma Membranes of Live Cells Characterized by Spin-Label ESR Spectroscopy. Biophys. J. 90: 4452–4465.

61. Munro, S. 2003. Lipid rafts: elusive or illusive? Cell. 115: 377–388.

62. Simons, K., and M.J. Gerl. 2010. Revitalizing membrane rafts: new tools and insights. Nat Rev Mol Cell Biol. 11: 688–699.

63. Hess, S.T., T.J. Gould, M.V. Gudheti, S.A. Maas, K.D. Mills, et al. 2007. Dynamic clustered distribution of hemagglutinin resolved at 40 nm in living cell membranes discriminates between raft theories. Proceedings of the National Academy of Sciences. 104: 17370–17375.

64. Eggeling, C., C. Ringemann, R. Medda, G. Schwarzmann, K. Sandhoff, et al. 2009. Direct observation of the nanoscale dynamics of membrane lipids in a living cell. Nature. 457: 1159–1162.

65. van Zanten, T.S., A. Cambi, M. Koopman, B. Joosten, C.G. Figdor, et al. 2009. Hotspots of GPI-anchored proteins and integrin nanoclusters function as nucleation sites for cell adhesion. Proceedings of the National Academy of Sciences. 106: 18557–18562.

66. Ehrig, J., E.P. Petrov, and P. Schwille. 2011. Near-critical fluctuations and cytoskeleton-assisted phase separation lead to subdiffusion in cell membranes. Biophys. J. 100: 80–89.

67. Machta, B.B., S. Papanikolaou, J.P. Sethna, and S.L. Veatch. 2011. Minimal model of plasma membrane heterogeneity requires coupling cortical actin to criticality. Biophys. J. 100: 1668–1677.

68. Veatch, S.L., P. Cicuta, P. Sengupta, A. Honerkamp-Smith, D. Holowka, et al. 2008. Critical fluctuations in plasma membrane vesicles. ACS Chem. Biol. 3: 287–293.

69. Honerkamp-Smith, A.R., S.L. Veatch, and S.L. Keller. 2009. An introduction to critical points for biophysicists; observations of compositional heterogeneity in lipid membranes. BBA - Biomembranes. 1788: 53–63.

70. Kusumi, A., and K. Suzuki. 2005. Toward understanding the dynamics of membrane-raft-based molecular interactions. Biochim. Biophys. Acta. 1746: 234–251.

71. Feigenson, G.W., and J. Buboltz. 2001. Ternary phase diagram of

dipalmitoyl-PC/dilauroyl-PC/cholesterol: Nanoscopic domain formation driven by cholesterol. Biophys. J. 80: 2775–2788.

72. Heberle, F.A., J. Wu, S.L. Goh, R.S. Petruzielo, and G.W. Feigenson. 2010. Comparison of three ternary lipid bilayer mixtures: FRET and ESR reveal nanodomains. Biophys. J. 99: 3309–3318.

73. Pathak, P., and E. London. 2011. Measurement of lipid nanodomain (raft) formation and size in sphingomyelin/POPC/cholesterol vesicles shows TX-100 and transmembrane helices increase domain size by coalescing preexisting nanodomains but do not induce domain formation. Biophys. J. 101: 2417–2425.

74. Ionova, I.V., V.A. Livshits, and D. Marsh. 2012. Phase diagram of ternary cholesterol/palmitoylsphingomyelin/palmitoyloleoyl-phosphatidylcholine mixtures: spin-label EPR study of lipid-raft formation. Biophys. J. 102: 1856–1865.

75. Elson, E.L., E. Fried, J.E. Dolbow, and G.M. Genin. 2010. Phase Separation in Biological Membranes: Integration of Theory and Experiment. Annu. Rev. Biophys. 39: 207–226.

76. Liu, J., S. Qi, J.T. Groves, and A.K. Chakraborty. 2005. Phase segregation on different length scales in a model cell membrane system. J. Phys. Chem. B. 109: 19960–19969.

77. Fan, J., M. Sammalkorpi, and M. Haataja. 2010. Formation and regulation of lipid microdomains in cell membranes: theory, modeling, and speculation. FEBS LETTERS. 584: 1678–1684.

78. Konyakhina, T.M., S.L. Goh, J. Amazon, F.A. Heberle, J. Wu, et al. 2011. Control of a Nanoscopic-to-Macroscopic Transition: Modulated Phases in Four-Component DSPC/DOPC/POPC/Chol Giant Unilamellar Vesicles. Biophys. J. 101: L8–L10.

79. Mukherjee, S., and F.R. Maxfield. 2004. Membrane domains. Annu. Rev. Cell Dev. Biol. 20: 839–866.

80. Yeagle, P.L. 1985. Cholesterol and the cell membrane. Biochim. Biophys. Acta. 822: 267–287.

81. Ejsing, C.S., E. Duchoslav, J. Sampaio, K. Simons, R. Bonner, et al. 2006. Automated Identification and Quantification of Glycerophospholipid Molecular Species by Multiple Precursor Ion Scanning. Anal. Chem. 78: 6202–6214.

82. Wang, T.Y., and J.R. Silvius. 2001. Cholesterol does not induce segregation

of liquid-ordered domains in bilayers modeling the inner leaflet of the plasma membrane. Biophysj. 81: 2762–2773.

83. Shimokawa, N., M. Hishida, H. Seto, and K. Yoshikawa. 2010. Phase separation of a mixture of charged and neutral lipids on a giant vesicle induced by small cations. Chemical Physics Letters. 496: 59–63.

84. Devaux, P.F., and R. Morris. 2004. Transmembrane asymmetry and lateral domains in biological membranes. Traffic. 5: 241–246.

85. Wan, C., V. Kiessling, and L.K. Tamm. 2008. Coupling of Cholesterol-Rich Lipid Phases in Asymmetric Bilayers †. Biochemistry. 47: 2190–2198.

86. Sorre, B., A. Callan-Jones, J.-B. Manneville, P. Nassoy, J.-F. Joanny, et al. 2009. Curvature-driven lipid sorting needs proximity to a demixing point and is aided by proteins. Proceedings of the National Academy of Sciences. 106: 5622–5626.

87. Qualmann, B., D. Koch, and M.M. Kessels. 2011. Let's go bananas: revisiting the endocytic BAR code. EMBO J. 30: 3501–3515.

88. McMahon, H.T., and J.L. Gallop. 2005. Membrane curvature and mechanisms of dynamic cell membrane remodelling. Nat Cell Biol. 438: 590–596.

89. Peter, B.J., H.M. Kent, I.G. Mills, Y. Vallis, P.J.G. Butler, et al. 2004. BAR domains as sensors of membrane curvature: the amphiphysin BAR structure. Science. 303: 495–499.

90. Itoh, T., and P. DeCamilli. 2006. BAR, F-BAR (EFC) and ENTH/ANTH domains in the regulation of membrane–cytosol interfaces and membrane curvature. Biochimica et Biophysica Acta (BBA) - Molecular and Cell Biology of Lipids. 1761: 897–912.

91. Gallop, J.L., C.C. Jao, H.M. Kent, P.J.G. Butler, P.R. Evans, et al. 2006. Mechanism of endophilin N-BAR domain-mediated membrane curvature. EMBO J. 25: 2898–2910.

92. Masuda, M., S. Takeda, M. Sone, T. Ohki, H. Mori, et al. 2006. Endophilin BAR domain drives membrane curvature by two newly identified structure-based mechanisms. EMBO J. 25: 2889–2897.

93. Wang, Q., H.Y.K. Kaan, R.N. Hooda, S.L. Goh, and H. Sondermann. 2008. Structure and plasticity of Endophilin and Sorting Nexin 9. Structure. 16: 1574–1587.

94. Shimada, A., H. Niwa, K. Tsujita, S. Suetsugu, K. Nitta, et al. 2007. Curved EFC/F-BAR-Domain Dimers Are Joined End to End into a Filament for

Membrane Invagination in Endocytosis. Cell. 129: 761–772.

95. Wang, Q., M.V.A.S. Navarro, G. Peng, E. Molinelli, S.L. Goh, et al. 2009. Molecular mechanism of membrane constriction and tubulation mediated by the F-BAR protein Pacsin/Syndapin. Proc. Natl. Acad. Sci. U.S.A. 106: 12700–12705.

96. Mattila, P.K., A. Pykäläinen, J. Saarikangas, V.O. Paavilainen, H. Vihinen, et al. 2007. Missing-in-metastasis and IRSp53 deform PI(4,5)P2-rich membranes by an inverse BAR domain-like mechanism. The Journal of Cell Biology. 176: 953–964.

97. Saarikangas, J., H. Zhao, A. Pykäläinen, P. LaurinmAki, P.K. Mattila, et al. 2009. Molecular Mechanisms of Membrane Deformation by I-BAR Domain Proteins. Current Biology. 19: 95–107.

98. Pykäläinen, A., M. Boczkowska, H. Zhao, J. Saarikangas, G. Rebowski, et al. 2011. Pinkbar is an epithelial-specific BAR domain protein that generates planar membrane structures. Nat Struct Mol Biol. 18: 902–907.

99. Guerrier, S., J. Coutinho-Budd, T. Sassa, A. Gresset, N.V. Jordan, et al. 2009. The F-BAR Domain of srGAP2 Induces Membrane Protrusions Required for Neuronal Migration and Morphogenesis. Cell. 138: 990–1004.

100. Kumar, V., R. Fricke, D. Bhar, S. Reddy-Alla, K.S. Krishnan, et al. 2009. Syndapin promotes formation of a postsynaptic membrane system in Drosophila. Mol. Biol. Cell. 20: 2254–2264.

101. Rao, Y., Q. Ma, A. Vahedi-Faridi, A. Sundborger, A. Pechstein, et al. 2010. Molecular basis for SH3 domain regulation of F-BAR-mediated membrane deformation. Proc. Natl. Acad. Sci. U.S.A. 107: 8213–8218.

102. Andersson, F., J. Jakobsson, P. Low, O. Shupliakov, and L. Brodin. 2008. Perturbation of Syndapin/PACSIN Impairs Synaptic Vesicle Recycling Evoked by Intense Stimulation. Journal of Neuroscience. 28: 3925–3933.

103. Clayton, E.L., V. Anggono, K.J. Smillie, N. Chau, P.J. Robinson, et al. 2009. The Phospho-Dependent Dynamin-Syndapin Interaction Triggers Activity-Dependent Bulk Endocytosis of Synaptic Vesicles. Journal of Neuroscience. 29: 7706–7717.

104. Sorre, B., A. Callan-Jones, J. Manzi, B. Goud, J. Prost, et al. 2011. Nature of curvature coupling of amphiphysin with membranes depends on its bound density. Proceedings of the National Academy of Sciences.

105. Zhu, C., S.L. Das, and T. Baumgart. 2012. Nonlinear sorting, curvature generation, and crowding of endophilin N-BAR on tubular membranes.

Biophys. J. 102: 1837–1845.

106. Roux, A., D. Cuvelier, P. Nassoy, J. Prost, P. Bassereau, et al. 2005. Role of curvature and phase transition in lipid sorting and fission of membrane tubules. EMBO J. 24: 1537–1545.

107. Heinrich, M., A. Tian, C. Esposito, and T. Baumgart. 2010. Dynamic sorting of lipids and proteins in membrane tubes with a moving phase boundary. Proc. Natl. Acad. Sci. U.S.A. 107: 7208–7213.

108. Ono, A. 2010. HIV-1 assembly at the plasma membrane. Vaccine. 28: B55–B59.

109. Chan, R., P.D. Uchil, J. Jin, G. Shui, D.E. Ott, et al. 2008. Retroviruses human immunodeficiency virus and murine leukemia virus are enriched in phosphoinositides. Journal of Virology. 82: 11228–11238.

110. Aloia, R.C., H. Tian, and F.C. Jensen. 1993. Lipid composition and fluidity of the human immunodeficiency virus envelope and host cell plasma membranes. Proc. Natl. Acad. Sci. U.S.A. 90: 5181–5185.

111. Brügger, B., B. Glass, P. Haberkant, I. Leibrecht, F.T. Wieland, et al. 2006. The HIV lipidome: a raft with an unusual composition. Proc. Natl. Acad. Sci. U.S.A. 103: 2641–2646.

112. Ott, D.E. 2008. Cellular proteins detected in HIV-1. Rev. Med. Virol. 18: 159–175.

113. Ono, A., A.A. Waheed, and E.O. Freed. 2007. Depletion of cellular cholesterol inhibits membrane binding and higher-order multimerization of human immunodeficiency virus type 1 Gag. Virology. 360: 27–35.

114. Scheiffele, P., A. Rietveld, T. Wilk, and K. Simons. 1999. Influenza Viruses Select Ordered Lipid Domains during Budding from the Plasma Membrane. Journal of Biological Chemistry. 274: 2038–2044.

115. Holm, K., K. Weclewicz, R. Hewson, and M. Suomalainen. 2003. Human immunodeficiency virus type 1 assembly and lipid rafts: Pr55(gag) associates with membrane domains that are largely resistant to Brij98 but sensitive to Triton X-100. Journal of Virology. 77: 4805–4817.

CHAPTER 2

Towards a better raft model: Modulated phases in the 4-component bilayer, DSPC/DOPC/POPC/CHOL[‡]

2.1 Abstract

The Ld + Lo coexistence region within the DSPC/DOPC/POPC/CHOL mixture displays a nanoscopic-to-macroscopic transition of phase domains as POPC is replaced by DOPC. Previously, we have shown that the transition goes through a modulated phase regime during this replacement, where patterned liquid phase morphologies were observed on GUVs. Here, we describe a more detailed investigation of the modulated phase regime along two different thermodynamic tielines within the Ld + Lo region of this four-component mixture. Using fluorescence microscopy of GUVs, we found the modulated phase regime to occur at relatively narrow DOPC/(DOPC+POPC) ratios. This "modulated phase window" shifts to higher values of DOPC/(DOPC+POPC) when cholesterol concentration is increased, and coexisting phases become closer in properties. Monte Carlo simulations reproduced the patterns observed on GUVs, using a competing interactions model of line tension and curvature energies. Sufficiently low line tension and high bending moduli are required to generate stable modulated phases. Altogether, our studies indicate that by tuning lipid composition, both domain size and morphology can be altered drastically within a narrow composition space. This lends insight to a possible mechanism for

[‡] The following sections are reproduced from: Goh, S.L., Amazon, J.J., and Feigenson, G.W. 2013. Towards a better raft model: Modulated phases in the 4-component bilayer, DSPC/DOPC/POPC/CHOL. Biophys. J. 104 (4): 853-862, with modifications to conform to the required format. S.L.G. prepared GUVs, executed fluorescence microscopy experiments, analyzed and processed all experimental images. J.J.A. performed theoretical calculations and simulations.

cells to reorganize plasma membrane compartmentalization simply by tuning local membrane composition or line tension.

2.2 Introduction

The lipid raft model postulated that functional domains exist in the plasma membrane (PM), arising from nonrandom mixing of lipids and proteins (1). This lateral heterogeneity would serve to compartmentalize the bilayer and facilitate cellular processes such as immune signaling and endocytosis that occur at the membrane. Evidence of heterogeneities in cell PM is found in many studies (2-4), with size scales of domains ranging from nanoscopic to microscopic depending on the experimental conditions and detection methods used. If these heterogeneities are related to coexisting Ld and Lo phases, then they can be studied in chemically simplified, lipid-only model membrane systems.

Micron-sized domains have been detected in cell membranes after crosslinking (5, 6). Soon after the lipid raft hypothesis was proposed, Harder *et al.* (4) demonstrated that raft elements at the PM can be crosslinked using antibodies or toxins. Their studies suggested that the PM could be phase-separated, where segregation of raft and non-raft compartments was due to different lipid environments. In IgE receptor signaling, receptors are crosslinked by antigens, resulting in clustering of protein components in raft-like domains (7, 8). In other studies, domains characteristic of Ld and Lo phases were observed in biomembrane preparations such as giant plasma membrane vesicles (9) and plasma membrane spheres (10) when cholera toxin-B was added. These studies collectively imply that macroscopic phase

separation can be found in the cell PM, but only when components are crosslinked with antigens, antibodies, toxins or chemicals.

In unperturbed cells, micron-sized Ld + Lo domains are not observed. Instead, nanoscopic domains are detected using methods more sensitive to small length-scales, such as FRET (3, 11), ESR (12) and stimulated emission depletion (STED) far-field fluorescence nanoscopy (13). In particular, FRET (11) and ESR (12) detected nanodomains that have Ld and Lo characteristics, indicating that liquid-liquid phase separation could occur at the nanoscopic scale in resting cells. A current view pictures lipid rafts as nanoassemblies enriched in long-chain saturated sphingolipids and cholesterol, possibly of short lifetime, that can be induced when needed to form more stable platforms to promote enzymatic reactions at the membrane (2).

The physical-chemical basis for membrane rafts being small has remained unclear. Chemically defined model membrane mixtures are useful for studying underlying physical interactions that govern nonrandom mixing in the more complex cell PM (14). The first clear and direct observation of macroscopic phase-separated domain size and shape was reported using fluorescence imaging of GUVs (15); this method has proven to be an invaluable tool for studying model membranes. Many three-component mixtures consisting of a high-melting lipid, low-melting lipid and cholesterol readily display Ld + Lo phase coexistence (16-20). These include mixtures that contain only phosphatidylcholines and cholesterol, or mixtures that contain sphingomyelin (SM). Usually, biologically rare lipids such as distearoyl-phosphatidylcholine (DSPC), dioleoyl-phosphatidylcholine (DOPC) and diphytanoyl-phosphatidylcholine (DiPhyPC) are used to drive the phase separation, because these

lipids are not only immiscible, but also the phase domains are macroscopic, clearly displaying interesting phase behavior that allows for the construction of thermodynamic phase diagrams that are so useful for predicting mixing behavior of other similar systems.

While most three-component phase diagrams describe macroscopic phase behavior, there have been a few mixtures reported where nanoscopic Ld + Lo regions have been detected. In fact, perhaps the first lipid mixtures displaying nanodomains was reported more than a decade ago (21) in dipalmitoyl-phosphatidylcholine/dilauroyl-phosphatidylcholine/cholesterol (DPPC/DLPC/CHOL) mixtures using FRET and dipyrene-PC excimer/monomer ratio to detect phase separation that did not show up in GUV imaging. Later, when a more biologically common lipid such as palmitoyl-oleoyl-phosphatidylcholine (POPC) replaced the low-melting lipid DOPC, nanoscopic Ld + Lo domains were detected in DSPC- and SM-containing mixtures (22-24). These three-component mixtures that display nanodomains might be superior models for studying physical properties of raft nanoassemblies in cellular PM. However, aside from crosslinking events that drastically change domain size in cells and model membranes (9, 10, 25), the nature of this nanoscopic to macroscopic size change is not well understood. A better model is needed to study the nano-to-macro transition of domain size (and shape) without extreme perturbations, and preferably under steady-state conditions: Equilibrium thermodynamics can provide a good starting point to make predictions about the behaviors of such systems.

Previously, we have shown that equilibrium, constant temperature variation of lipid composition is all that is required to change phase domain size and morphology (26). As POPC is replaced gradually with DOPC, patterned phase domains (modulated phases) form in the DSPC/DOPC/POPC/CHOL system over a defined range of compositions. This was the first report of liquid modulated phases in free-floating bilayer systems, although modulated phases have been previously observed, e.g. in magnetic fluids and in lipid monolayers (27). Modulated phase morphology occurs for two coexisting liquid phases when line tension drives the minimization of domain perimeter, while an opposing long-range interaction competes with line tension to break up the domain, typically into periodic patterns.

A long-range repulsive interaction can arise from various sources. For example, long-range dipole-dipole repulsion acts to stabilize superstructures in monolayers (28). Theoretical studies show that dipole repulsion might occur in cells between transmembrane proteins and lipids to maintain nanodomains (29). However, dipole repulsion in bilayers is only effective over distances of a few nanometers, so is not likely to be responsible for the observed micron-scale periodic patterns (26, 30). Lateral tension is another long-range and effectively repulsive force, which could arise, for example, from adsorption of membranes onto a solid surface, thereby modulating line energy and inducing formation of striped patterns. This was observed on bilayer vesicles adsorbed on the surface of supported bilayers (31) and for Pb deposited onto Cu surfaces (32). In addition, osmotic swelling might also apply enough tension to GUVs to cause macroscopic phase separation (33). Moreover, patterned phase morphologies can also arise from critical fluctuations in bilayers, a

dynamic process that occurs when line tension is low close to the critical point (34, 35). In all of these examples, *competing* interactions are required to stabilize periodic structures.

Recently, we modeled the formation of modulated phases on the surface of GUVs by use of Monte Carlo simulations of a competing interactions model of line tension and curvature energies (36). Curvature energies have been shown in many studies to be a long-range repulsive force that can modulate coexisting liquid phases into periodic domains (30, 35, 37). Differences in phase properties, in particular, bending moduli, could impose constraints on a phase to preferentially assume areas of particular curvature (38). Using interferometry coupled with fluorescence imaging, Kaizuka and Groves (30) distinguished different areas of curvature on modulated phase domains on quasi-planar lipid bilayers. At the macroscopic scale, competing interactions between curvature energies and line tension provide a plausible explanation for the stabilization of modulated phase patterns on unsupported bilayers.

In this study, we employed widefield fluorescence microscopy of GUVs, systematically changing mixture composition, to observe that modulated phases are observed within the Ld + Lo volume of the four-component mixture, DSPC/DOPC/POPC/CHOL. The compositional range of this modulated phase regime varies depending on the location within the two-phase region; in particular, a greater fraction of DOPC is required for patterns to appear, the shorter the tieline that connects the coexisting phases, hence the more alike the phases are. We concluded that in the presence of the competing interaction from curvature energies, line tension exerts the main control over the occurrence of patterned domains at different

compositions within the Ld + Lo region. Together, these observations are consistent with phase thickness mismatch controlling the line tension, with the thickness of the Ld phase in particular being under strong control via its composition.

2.3 Materials And Methods

2.3.1 Materials

Phospholipids were purchased from Avanti Polar Lipids (Alabaster, AL). Cholesterol was from Nu Chek Prep (Elysian, MN). Fluorescent dye C12:0-DiI (1,1′-didodecyl-3,3,3′,3′-tetramethylindocarbocyanine perchlorate) was from Invitrogen (Carlsbad, CA). Concentrations of phospholipid stocks were determined to <1% error with inorganic phosphate assay (39, 40), and purity of >99% was checked with thin layer chromatography of 30 μg samples. Briefly, lipids were spotted onto pre-washed and activated silica gel GHL Uniplates (Analtech, Newark, DE). Plates were developed with chloroform/methanol/water, 65/25/4. Cholesterol stock solution was prepared by standard gravimetric procedures to ~0.2%. Fluorescent dye concentrations were determined using absorption spectroscopy on an HP 8452A spectrophotometer (Hewlett-Packard, Palo Alto, CA).

2.3.2 Sample preparation

GUVs were prepared using the electroformation method (41) according to procedures in (17, 26), with the following modifications: Lipid films were swelled at 55° C in either 100 mM sucrose or 100 mM glucose in an AC field of 5Hz for two hours to form GUVs, then cooled to room temperature (23° C) over 12 hours. Samples were harvested into microcentrifuge tubes (Fisher Scientific) using large orifice pipet

tips (Fisher Scientific), and let settle for at least two hours before observation. Since samples were not harvested into a solution of lower density as done previously, this longer settling time was required before microscopy observations. Only identical glucose (or sucrose) solutions were used on both sides of the GUV in order to minimize perturbations from any osmotic gradient across the membranes, because changes in the osmotic pressure of the GUVs can influence modulated phase morphologies. Glucose may be superior to sucrose for this purpose as it can equilibrate in a time of hours across membranes to relieve any osmotic gradients that may occur during sample annealing (42). Neither of the sugar solutions strongly affected the modulated phase window of the compositions examined nor the yield of the samples.

2.3.3 Fluorescence microscopy and image analyses

Widefield microscopy was performed on a Nikon Diaphot-TMD inverted microscope at 23°C using a 60X 1.4NA oil immersion objective. To minimize light-induced artifacts, neutral density filters (ND = 1.0) were used, and GUVs were first located in bright field mode before illumination for fluorescence. Samples contained 0.02 mol% C12:0 DiI, imaged with 535-550 nm excitation and 565-610 nm emission. Images were collected with a Photometrics charge-coupled device camera CoolSNAP$_{HQ2}$ (Tucson, Arizona). All images were contrast-enhanced and analyzed using NIS Elements Basic Research Software (MVI, Inc.).

To determine the compositional range of modulated phases, the number of GUVs with various phase morphologies (uniform, patterned, or macroscopic-round domains) at each composition examined was counted (see Table 2.2). The fraction of

GUVs displaying modulated phases at each composition was plotted, and the standard error of the mean was determined (see Fig. 2.3).

The area fractions of the two phases on GUV images in Fig. 2.8 were determined using Image J (43). The images were first converted into true binary images. Then representative areas on the vesicles were selected for area fraction calculation. Calculated phase mole fractions were then adjusted for the Lo phase occupying 30% less area than the Ld phase (44, 45). These Lo area fractions were compared to the expected area fractions of the compositions, calculated using the lever arm rule and the phase boundaries determined at ρ = 30% (unpublished, TM Konyakhina, J Wu, JD Mastroianni, FA Heberle, and GW Feigenson; from here onwards referred to as "unpublished, TM Konyakhina *et al*.").

2.3.4 Simulation model

To model the experimental observations we used a Monte Carlo simulation of the competition between line tension and curvature (36). The model uses the Helfrich Energy Functional to describe the energetics of a two-phase membrane:

$$\mathrm{H}\left[\phi, H, G\right] = \gamma L + \iint_S \kappa\left(\phi\right)\left[H\right]^2 dA + \iint_S \bar{\kappa}\left(\phi\right) G dA$$

The three fields defined on the surface are the local phase (ϕ), defined to be 0 in Ld and 1 in Lo, the mean curvature (H), and the Gaussian curvature (G). The first term is the line tension contribution, the energy per unit length (γ) multiplied by the total length of the phase boundary (L), which favors the formation of macroscopic round domains to minimize the perimeter/area ratio.

The second term is the mean curvature (H) contribution, which couples to the energy through the bending modulus (κ), which varies depending on the local phase. This is integrated over the membrane surface (S). Similarly the third term is the Gaussian curvature (G) contribution, which couples through the saddle-splay modulus ($\bar{\kappa}$) that also depends on the local phase.

We represented the GUV in our simulation as a triangulated surface with spherical topology (36). Energy is minimized by a two-stage metropolis algorithm:

1) The phases on two randomly chosen vertices were exchanged and this move was accepted or rejected based on the change in energy (with probability $e^{-\Delta E/kT}$);
2) A randomly chosen vertex was moved a small amount in a random direction and this move was accepted or rejected based on the change in energy (with probability $e^{-\Delta E/kT}$).

After iterating this process, the lattice eventually relaxed to a minimal energy state (to within thermal fluctuations.) We found that for certain values of the energetic parameters, the minimal energy configuration takes on morphologies consistent with the modulated phases observed in the DSPC/DOPC/POPC/CHOL system.

2.4 Results

We previously reported observations at a limited number of compositions of a modulated phase regime in DSPC/DOPC/POPC/CHOL (26). Here, we have systematically examined modulated phases within the Ld + Lo coexistence region in the four-component system. Starting from the three-component DSPC/POPC/CHOL

mixture at fixed DSPC/CHOL ratio, POPC was replaced with DOPC as described by the replacement ratio, ρ,

$$\rho \equiv \frac{\chi_{DOPC}}{\chi_{DOPC} + \chi_{POPC}} (\%)$$

where χ_{DOPC} and χ_{POPC} are mole fractions of DOPC and POPC. Experimental design is illustrated in Fig. 2.1. At a chosen DSPC/CHOL ratio starting from the POPC face of the tetrahedron, a series of samples was prepared traveling in composition space from one face to another of the tetrahedral phase diagram ("ρ-trajectory"). Using well-determined phase boundaries and thermodynamic tielines from previous studies (22) and unpublished results in the four-component mixture (unpublished, TM Konyakhina *et al.*), we found modulated phases occurring at a range of ρ values along two different approximated tielines close to the previously measured tielines in the liquid-liquid coexistence region.

2.4.1 Modulated phases occur at similar ρ values along a given tieline

The first tieline examined (tieline 1) is located slightly above the bottom phase boundary of the Ld + Lo region (Fig. 2.2). Six starting compositions with defined DSPC/CHOL ratios were chosen along tieline 1 for the investigation of the modulated phase compositional window (compositions T1A-F, Table 2.1). At all chosen

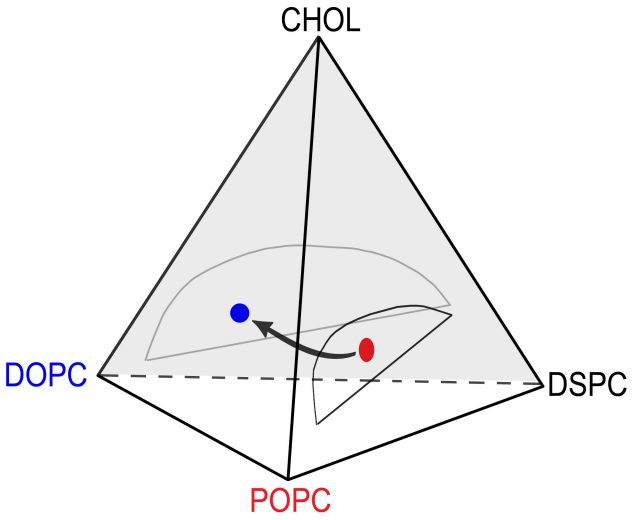

Figure 2.1 The compositional path for investigation of modulated phases is shown within the Ld + Lo volume of DSPC/DOPC/POPC/CHOL. Schematic shows the progression along a "ρ-trajectory" through the tetrahedral phase diagram as POPC is replaced by DOPC.

Table 2.1 Compositions examined in modulated phase window studies

Composition	X_{DSPC}	$X_{DOPC + POPC}$	X_{CHOL}
T1A	0.487	0.25	0.263
T1B	0.45	0.30	0.25
T1C	0.413	0.35	0.237
T1D	0.375	0.40	0.225
T1E	0.30	0.50	0.20
T1F	0.225	0.60	0.175
T2A	0.395	0.30	0.305
T2B	0.283	0.45	0.267
T2C	0.17	0.60	0.23

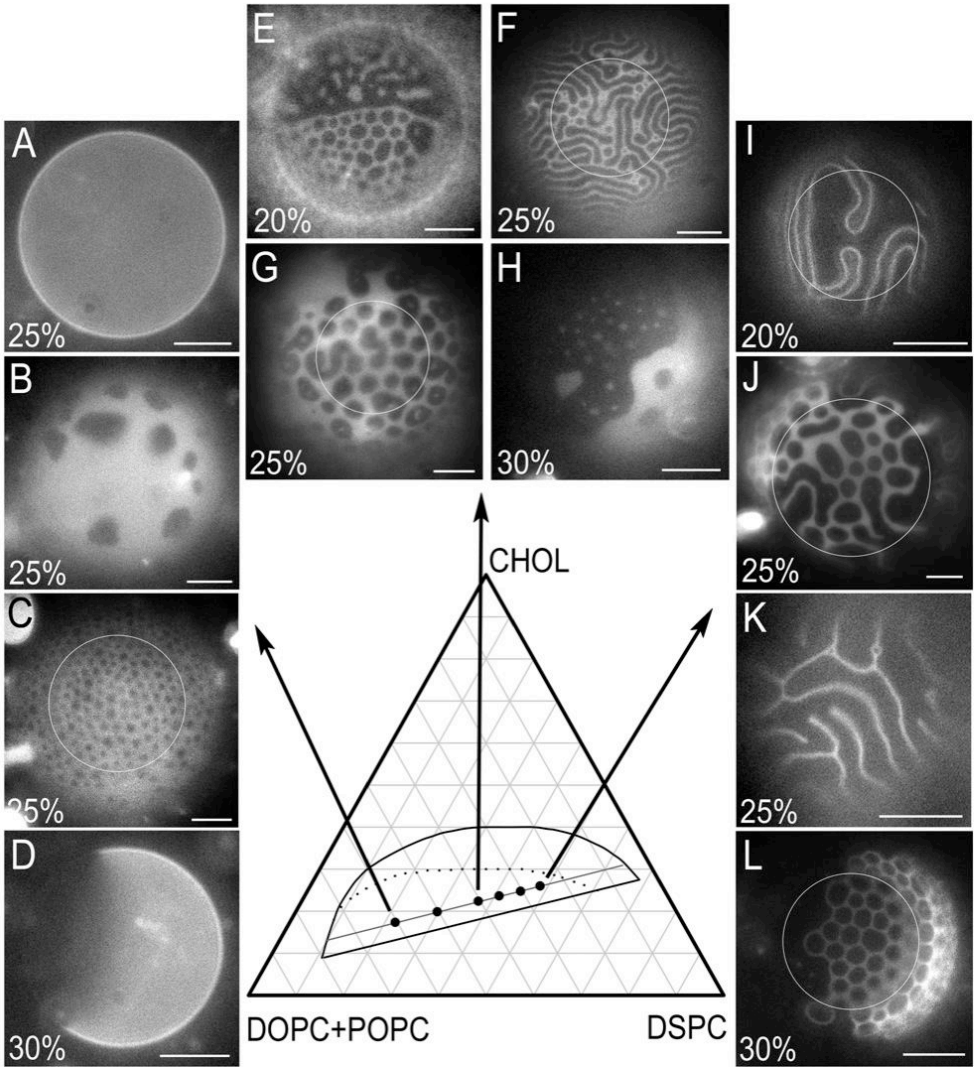

Figure 2.2 Modulated phase patterns are observed along tieline 1 at 20% ≤ ρ ≤ 30%. The ρ value for each GUV is noted in each image. Images were contrast enhanced and cropped. Composite images of two focused slices contain a white ring marking the boundary of the composite image. For reference, the upper Ld + Lo boundary is shown for ρ = 0% (dotted) and ρ = 100% (solid); both ρ-slices share a common lower boundary (solid) (unpublished, TM Konyakhina *et al*.). GUV compositions DSPC/(DOPC + POPC)/CHOL are (A-D) 0.225/0.60/0.175 (T1F), (E-H) 0.375/0.40/0.225 (T1D), (I-L) 0.487/0.25/0.263 (T1A). The dye C12:0-DiI (0.02 mol%) partitions into Ld. Scale bars, 10 μm; temperature, 23°C.

compositions, the majority of GUVs appeared uniform at ρ < 15%, where domains are nanoscopic (22).

Modulated phase patterns started to occur at ρ = 15% for composition T1A, located on the far right on tieline 1 (Fig. 2.3 *A*). At ρ = 20%, patterned domains were observed in compositions T1A-D (Fig. 2.2 and 2.3 *A*). For compositions T1E and T1F, this modulated phase "window" begins at ρ = ~ 25%. The fraction of patterned GUVs in compositions T1E-F, where the predominant phase has changed to Ld-rich, was less than that found for compositions T1A-D (Fig. 2.3 *A*), where the predominant phase is Lo-rich. In T1F, only ~ 25% of the GUVs analyzed displayed modulated morphologies, the other GUVs either being uniform or displaying large round domains (Fig. 2.3 *A*, Table 2.2). For all the compositions examined on tieline 1, the modulated phase window ends at ρ = ~ 30-35% (Fig. 2.3 *A*), with higher ρ values showing rounded macroscopic domains. A typical progression of GUV morphologies from the onset to the end of a modulated phase window is shown for composition T1B in Fig. 2.4.

We observe the occurrence and behavior of modulated phases to follow rules that govern phase separation along thermodynamic tielines. On the far right of tieline 1, Ld is the minor phase, forming thin stripes, honeycomb, or stripe-like patterns that resembled 2D-bubbles on a predominant Lo phase on the surface of GUVs (Fig. 2.2, *I-L*). As the Ld phase fraction increases, either by moving towards the left side of the tieline or by increasing ρ, thin stripes start to coarsen (Fig. 2.2, *C* and *G*), typically giving rise at higher ρ values to larger dispersed Lo domains with irregular edges (Fig

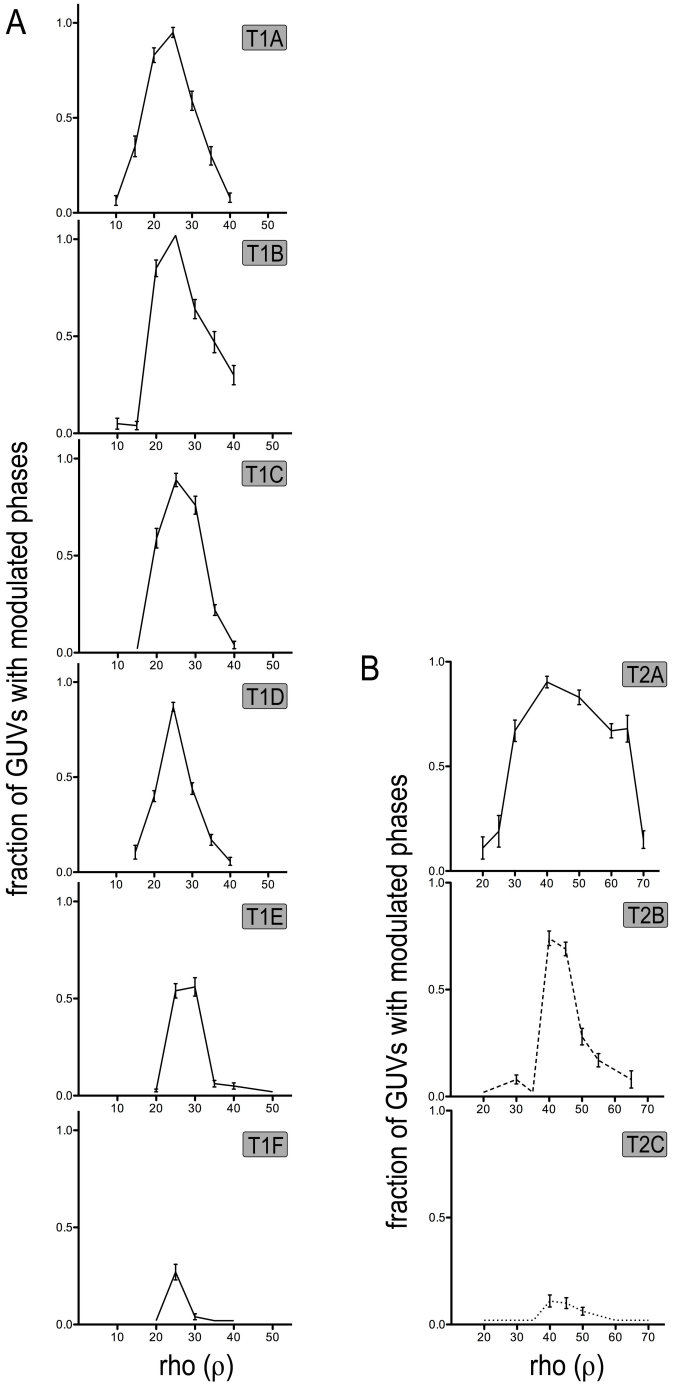

Figure 2.3. The width of the modulated phase window varies along two tielines. Fractions of GUVs that displayed modulated phase patterns at various ρ values are plotted for (A) compositions T1A-F along tieline 1, and (B) compositions T2A-C along tieline 2. Error bars, mean ± SE.

Table 2.2 Percentage of GUVs having the observed morphologies along tieline 1

Composition	ρ	Uniform (%)	Modulated (%)	Macroscopic (%)	N
T1A	10	95	5	-	87
	15	64	36	-	69
	20	10	90	-	93
	25	1	93	6	94
	30	-	57	43	96
	35	-	28	72	87
	40	-	6	94	95
T1B	10	97	3	-	37
	15	98	2	-	42
	20	16	84	-	76
	25	-	100	-	52
	30	-	62	38	97
	35	-	45	55	84
	40	-	28	72	82
T1C	15	100	-	-	45
	20	40	58	2	95
	25	-	87	13	97
	30	-	74	26	91
	35	-	20	80	212
	40	-	2	98	53
T1D	15	91	9	-	56
	20	58	42	-	261
	25	4	86	10	222
	30	4	42	54	259
	35	1	15	85	157
	40	1	4	95	82
T1E	20	99	0.5	0.5	145
	25	44	53	3	179
	30	1	55	44	108
	35	5	4	91	142
	40	-	3	97	116
	50	-	-	100	55
T1F	20	100	-	-	90
	25	43	25	30	116
	30	9	2	89	86
	35	-	-	100	21
	40	10	-	90	41

Table 2.2 shows the count distribution of three main GUV morphologies (uniform, modulated domains; macroscopic round domains) observed at various ρ values at six compositions (fixed DSPC/CHOL ratios) along tieline 1.

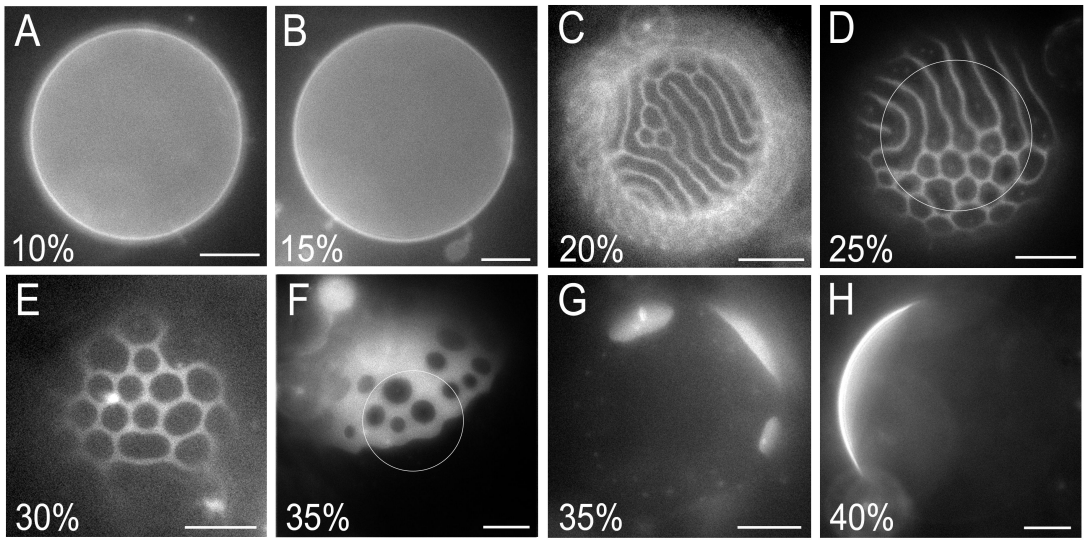

Figure 2.4. Typical progression of GUV morphologies through a ρ-trajectory at composition T1B. The ρ value for each GUV is noted in each image. All images were contrast enhanced and cropped. Composite images of two focused slices contain a white ring marking the boundary of the composite image. GUVs appeared uniform before the onset of the modulated phase window ($\rho < 20\%$), and displayed macroscopic round domains after the modulated phase window ($\rho > 30\%$). GUVs have the composition DSPC/(DOPC+POPC)/CHOL = 0.45/0.30/0.25. C12:0-DiI (0.02 mol%) partitions into Ld. Scale bars 10 μm; temperature, 23°C.

2.2, *E* and *H*; Fig. 2.4 *F*). The mole fractions of Ld and Lo on patterned GUVs follow the lever arm rule (see Fig. 2.8).

In summary, modulated phases occurred at ~ 20% ≤ ρ ≤ ~ 30% for all compositions examined along tieline 1. However, this window narrowed to 25% ≤ ρ ≤ 30% for T1E, and a well-defined modulated composition range was not observed for T1F.

2.4.2 Increasing cholesterol concentration moves modulated phase windows to higher ρ values

Along tieline 1, the width of the modulated phase windows has a composition range of ~ 10-15% in ρ. We investigated the compositional values and width of the modulated phase window on a different tieline at higher cholesterol concentration within the Ld + Lo region. We note that at higher cholesterol concentrations, the compositions of the coexisting phases become more similar, as described by shorter tielines.

We examined three compositions along tieline 2 (Table 2.1, Fig. 2.5). At composition T2A, the modulated phase window began at ρ = ~ 30%, persisting up to ρ = ~ 65% (Fig. 2.3 *B*). This compositional window is much broader than those found for compositions on tieline 1. The types of patterns observed for T2A (Fig. 2.5, *I-L*) are similar to patterns we find for T1 Lo-rich compositions. Towards the left of T2A at composition T2B, the modulated phase window narrows significantly, occurring at 40% ≤ ρ ≤ 50% (Fig. 2.3 *B*). In addition to stripes and honeycomb-like patterns, larger domains with uneven edges were also observed at T2B (Fig. 2.5 *H*). Finally, on the left side of tieline 2 at composition T2C, a smaller fraction (<10%) of the GUVs

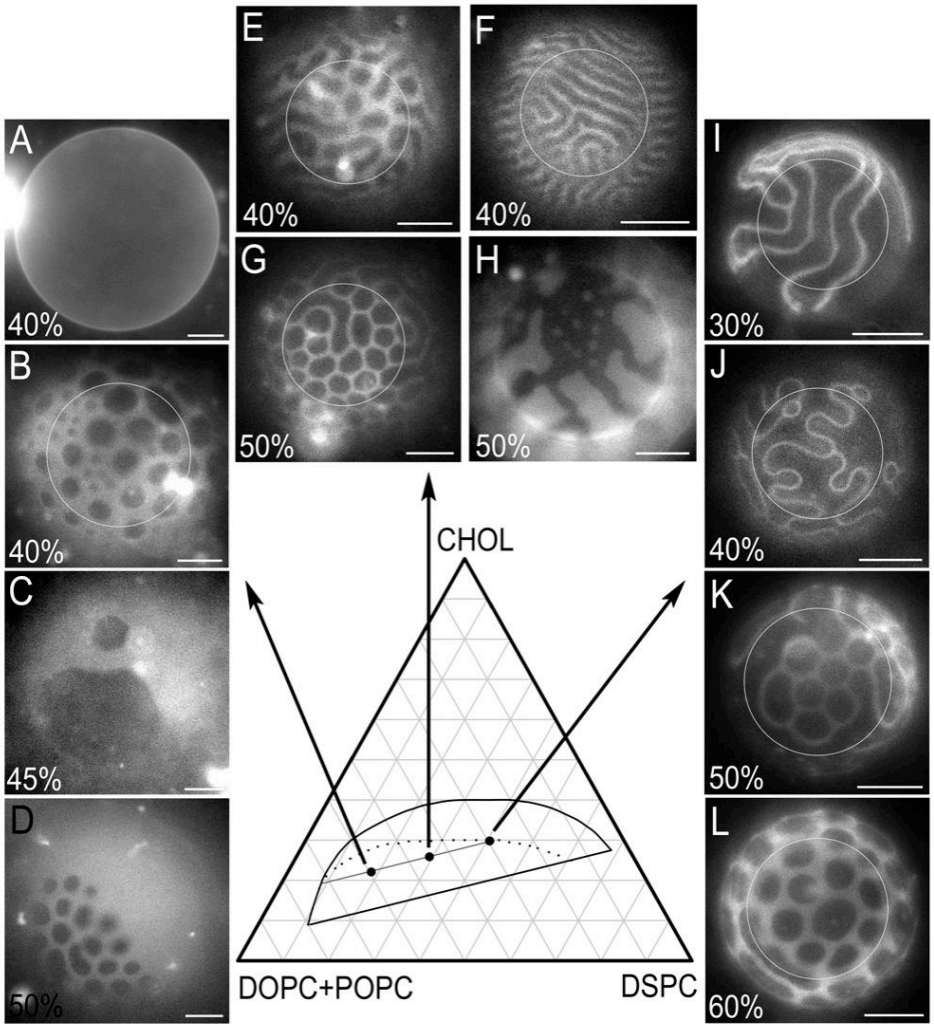

Figure 2.5 Modulated phase patterns are observed along tieline 2 at different compositional windows. The ρ value for each GUV is noted in each image. Images were processed and shown as in Fig. 2.2. For reference, the upper Ld + Lo boundary is shown for ρ = 0% (*dotted)* and ρ = 100% (*solid*); GUV compositions DSPC/(DOPC + POPC)/CHOL are *(A-D)* 0.17/0.60/0.23 (T2C), *(E-H)* 0.283/0.45/0.267 (T2B), *(I-L)* 0.395/0.30/0.305 (T2A). Scale bars, 10 μm; temperature, 23°C.

Table 2.3 Percentage of GUV having the observed morphologies along tieline 2

Composition	ρ	Uniform (%)	Modulated (%)	Macroscopic (%)	N
T2A	20	89	11	-	35
	25	81	19	-	27
	30	32	68	-	84
	40	4	90	6	113
	50	1	83	16	117
	60	-	67	33	193
	65	-	68	32	53
	70	1	15	84	73
T2B	20	100	-	-	54
	30	94	6	-	126
	35	100	-	-	64
	40	18	72	10	175
	50	6	69	25	217
	55	-	26	74	129
	60	-	15	85	131
	70	-	6	94	35
T2C	20	100	-	-	12
	25	100	-	-	52
	30	100	-	-	78
	35	100	-	-	74
	40	44	9	47	101
	45	57	8	35	115
	50	8	4	88	117
	60	17	-	83	124
	70	12	-	88	51

Table 2.3 shows the count distribution of three main GUV morphologies (uniform, modulated domains; macroscopic round domains) observed at various ρ values at three compositions (fixed DSPC/CHOL ratios) along tieline 2.

examined appeared patterned when 40% ≤ ρ < 50% (Fig. 2.3 *B,* Table 2.3). Similar to T1F, we were not able to determine a well-defined modulated phase window for T2C.

2.4.3 Area fractions of phases influence the modulated phase compositional range

We observed a narrowing of the modulated phase windows and a decrease in the fraction of patterned GUVs at compositions having Ld fractions > ~ 50% along tielines 1 and 2. In other words, even with the same composition of Ld and the same composition of Lo phases in equilibrium, a switch from the predominant phase being Lo to its being Ld changes the modulated phase morphology. This is not a change in percolation, which describes the connectivity of phases, because we observed that the Ld phase is the continuous phase when modulated phase morphology is present. Thus, we observed that the appearance/disappearance of modulated phases and the types of patterns found depend on which phase area fraction is greater.

The location of this changeover in area predominance could aid in our understanding of how modulated phase patterns evolve along a tieline. However, when modulated phase patterns are examined, it can be difficult to determine which phase area fraction is greater. Therefore, in order to find the changeover compositions, we left the modulated phase regime, and used just slightly higher ρ values where domains are round. In this macroscopic regime, changeover in phase area dominance is related to a change in phase percolation, which is the criterion that was examined in the following experiments.

For tieline 1, samples were prepared at ρ = 40%. This ρ value lies just outside the modulated phase window for the compositions examined in Fig. 2.2. A series of 10 samples were prepared (Fig. 2.6). GUVs from compositions A-D displayed Ld phase

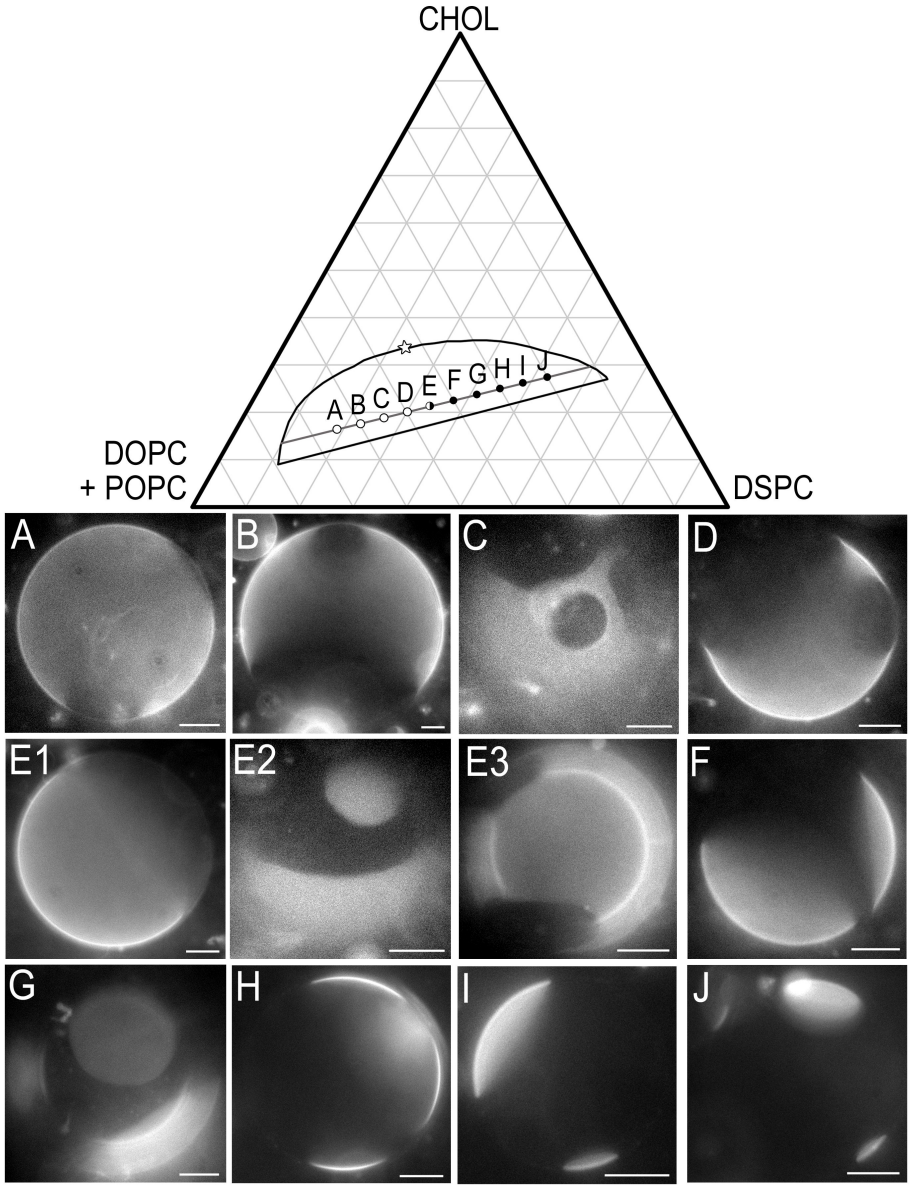

Figure 2.6 Percolation threshold along tieline 1 at ρ = 40%. Domain morphologies of GUVs change along compositions A-J as shown in Fig. 5 A-J. GUVs displayed Ld percolation at A-D (open circles), Lo percolation at F-J (solid circles), and mixed percolation at E1-3 (half open circles). The Ld + Lo boundaries at ρ = 40% is shown, with the approximate position of the critical point (star) (unpublished, TM Konyakhina et al.). GUV compositions DSPC/DOPC/POPC/CHOL are: (A) 0.187/0.26/0.39/0.163, (B) 0.225/0.24/0.36/0.175, (C) 0.263/0.22/0.33/0.187, (D) 0.30/0.20/0.30/0.20, (E) 0.338/0.18/0.27/0.212, (F) 0.375/0.16/0.24/0.225, (G) 0.413/0.14/0.21/0.237, (H) 0.45/0.12/0.18/0.25, (I) 0.487/0.10/0.15/0.263, (J) 0.525/0.08/0.12/0.275. Scale bars, 10 μm; temperature, 23°C.

connectivity (Fig. 2.6, *A-D*). At composition E in Fig. 2.6, both types of phase connectivity were observed (Fig. 2.6, *E1-E3*), indicating that this composition is very close to the changeover composition. Based on the estimated Ld + Lo boundaries at ρ = 40% (unpublished, TM Konyakhina *et al*.), composition E is located at ~ 52 mole% Ld phase, which occupies an area fraction of ~ 61%. The predominant phase switches to Lo at compositions located to the right of the changeover point (Fig. 2.6, *F-J*). It should be noted that for compositions in the middle region of the tieline, where the area fractions of Lo and Ld phases are close to equal, the majority of GUVs displayed a single round Ld (or Lo) domain. This is an indication that the samples were well equilibrated, without multiple small kinetically trapped domains. The changeover point occurred when the mole fraction of Ld is roughly equal to that of Lo. But because the Lo occupies ~ 30% less area than Ld (43, 44), Ld area fraction predominated at the changeover point.

Similar area changeover experiments were conducted along tieline 2, but at ρ = 70%, where large round domains were found for the compositions examined (Fig. 2.7). The changeover composition for this tieline was determined to be near composition E, shown in Fig. 2.7, where both types of phase connectivity were observed. The mole fraction of Ld at composition E is ~ 46% according to phase boundaries at ρ = 70% (unpublished, TM Konyakhina *et al*.), whereas its area fraction is ~ 55%. At compositions located to the left of the changeover, most of the GUVs displayed Ld phase connectivity (Fig. 2.7, *A-D*), whereas Lo is the predominant phase at compositions located to the right of the changeover (Fig. 2.7, *F-G*). Similar to the ρ = 40% studies above, the changeover point occurred at a composition where the mole

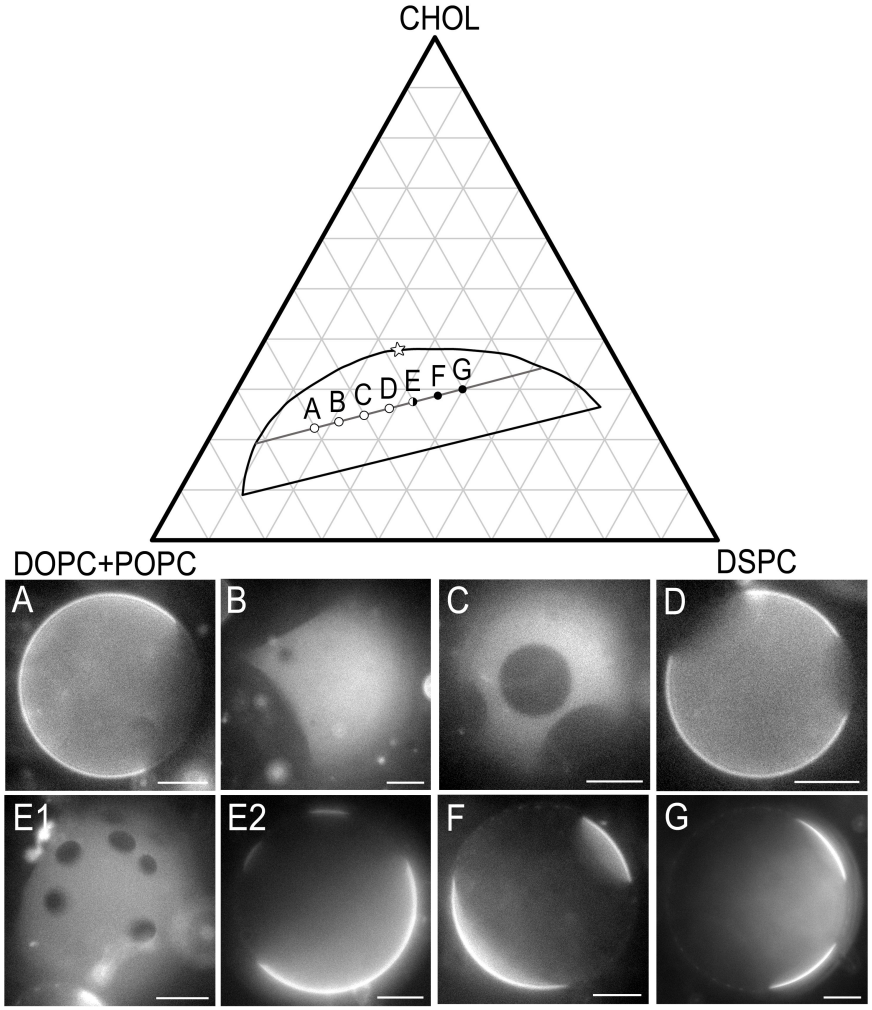

Figure 2.7 Percolation threshold along tieline 2 at ρ = 70%. Domain morphologies of GUVs change for compositions *A*-*G*. GUVs displayed Ld percolation at *A*-*D* (*open circles*), Lo percolation at *F* and *G* (*solid circles)*, and mixed percolation at *E1* and *2* (*half open circles*). The Ld + Lo boundary at ρ = 70% is shown, with the position of the critical point (*star*) (unpublished, TM Konyakhina *et al.*). GUV compositions DSPC/DOPC/POPC/CHOL are: *(A)* 0.17/0.42/0.18/0.23, *(B)* 0.21/0.385/0.165/0.24, *(C)* 0.247/0.35/0.15/0.253, *(D)* 0.283/0.315/0.135/0.267, *(E)* 0.32/0.28/0.12/0.28, *(F)* 0.358/0.245/0.105/0.292, *(G)* 0.395/0.21/0.09/0.305. Scale bars, 10 μm; temperature, 23°C.

fractions of both phases are roughly equal, but where Ld area fraction predominates over Lo.

The locations of the area fraction changeover points at ρ = 40% and ρ = 70% offer guides for estimating the phase area predominance for the compositions examined in the modulated phase regime. Compositions to the left of the changeover points on both tielines, such as T1E-T1F on tieline 1, and T2B-T2C on tieline 2, have narrower modulated phase windows compared to the Lo-predominant compositions on the right of the changeover points. Thus, we find a consistent influence of phase area predominance on the modulated phase behavior along a tieline.

2.5 Discussion

2.5.1 Three regimes of domain size and morphology

We observe three separate regimes within the Ld + Lo region, which differ in domain size and morphology: nanoscopic, modulated, and macroscopic. Simply by tuning the ratio of DOPC/(DOPC+POPC), i.e. increasing ρ, we obtain GUVs that are uniform by fluorescence microscopy but that contain nanodomains, then modulated phases, and finally, macroscopic, round liquid domains. These transitions occur at compositions that vary only slightly for ρ trajectories that start along the same tieline, but which change significantly as cholesterol concentration is increased, i.e. along a different tieline. For example, nanodomains occur up to ρ = ~ 15% along tieline 1, but can persist up to ρ = 40% at higher cholesterol concentration (Fig. 2.3).

In almost all of the compositions examined, the transition from nanoscopic to macroscopic round domains goes through a regime where domains appear patterned.

The range of this modulated phase window hardly varied along tieline 1, but did change with cholesterol concentration between tielines 1 and 2 within the Ld + Lo region. We observed a broader modulated phase window at composition T2A along tieline 2 (higher cholesterol) than for composition T1A along tieline 1.

The transition of domain size from nanoscopic to macroscopic along a ρ-trajectory is relatively well defined, even abrupt compared to the gradual change in all of the phase boundaries of this four-component system as the low-melting lipid changes from POPC to DOPC. The upper boundary of the Ld + Lo region shifts smoothly from 30% to 40% CHOL between ρ = 0-100% (22). In contrast, GUVs change from uniform to patterned within a ~ 5% change in ρ. In addition, at many compositions within the two-phase region, the range of ρ values where modulated phases occur is only about 10% in composition space. This could have implications for biological membranes, providing a means for cells to abruptly change the sizes and connectivities of membrane compartments simply by tuning local membrane composition.

2.5.2 Experimental observations are consistent with a competing interactions model of line tension and curvature energies

In a system where liquid phases coexist, line tension drives the minimization of domain boundary between the two phases, resulting in the formation of a single round domain, unless an additional term competes with line tension to maintain high domain perimeters. Previously, using Monte Carlo simulations, we have shown that a competing interactions model of line tension and curvature energies can result in the formation of modulated phases in a liquid-liquid coexistence region (36). Low line

tension values (0.01 pN) and high bending moduli ratios ([10-100] x 10^{-19} J) of the two phases are required to generate stripe-like and honeycomb patterns on the surface of simulated GUVs.

Experimental results in this study are consistent with this competing interactions model: At fixed line tension and bending moduli values, domain morphologies on simulated GUVs change with the area fraction of each phase (Fig 2.8, *E-H*). Experimentally, we observed similar changes in modulated phase patterns on actual GUVs as we move along tieline 1 at a fixed ρ = 30% (Fig. 2.8, *A-D*). A comparison of experimental and simulated GUV morphologies is shown in Figure 2.8. When Lo is the dominant phase, thin stripes, honeycomb, and 2D-bubble-like patterns formed by the Ld phase are observed. The linewidths of these patterns coarsen as the area fraction of Ld increases, until eventually, dispersed, uneven Lo domains on an overall Ld-rich GUV are found. Whereas phase patterns on simulated GUVs do not always exactly match the patterns observed on experimental GUVs, the types of patterns (i.e. stripe-like, 2D-bubble-like) are alike. Furthermore, Lo area fractions used in the simulations in Fig. 2.8, *E-H* are remarkably similar to the area fractions measured from the GUV images in Fig. 2.8, *A-D,* which in turn correspond approximately to the area fractions estimated from the location of these compositions along tieline 1 at ρ = 30% (see Materials and Methods for details). Thus, modulated phases appear to follow the lever arm rule.

Based on the changeover compositions obtained for both tielines, and the compositional range of modulated phases, we find that a change in which phase area

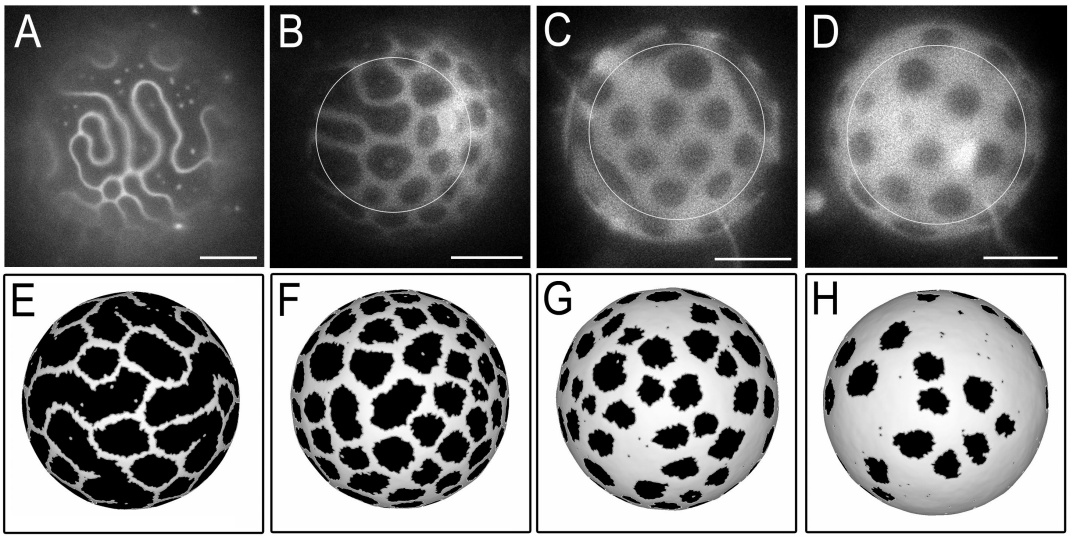

Figure 2.8 Phase fractions of modulated phase patterns along a tieline at ρ= 30% follow the lever arm rule. A comparison of experimental (*A-D*) and simulated (*E-H*) GUVs along tieline 1 at ρ= 30%, with only the phase fractions of Ld and Lo varied. The Lo area fraction of GUVs *A-D* was measured to be 0.75, 0.56, 0.45, and 0.25, respectively. Images were processed and shown as described in Fig. 2.2 GUV compositions DSPC/DOPC/POPC/CHOL at 23°C are: *(A)* 0.487/0.075/0.175/0.263, *(B)* 0.413/0.105/0.245/0.237, *(C)* 0.30/0.15/0.35/0.20, *(D)* 0.225/0.18/0.42/0.175; C12:0-DiI (0.02 mol%) partitions into Ld. Scale bars 10 μm; temperature, 23°C. Simulation parameters for GUVs *E-H:* $\gamma = 0.015 pN$, $\kappa_d = 10 \times 10^{-19} J$, $\kappa_o = 150 \times 10^{-19} J$, $\bar{\kappa}_d = -10 \times 10^{-19} J$, $\bar{\kappa}_o = -150 \times 10^{-19} J$, GUV radius = 25 μm. Lo area fractions used: *(E)* 0.80, *(F)* 0.60, *(G)* 0.40, *(H)* 0.20. Simulations performed by J.J.A.

fraction is predominant has a strong influence on the appearance of modulated phases. For example, at a fixed value of ρ = 25% along tieline 1, thin stripe-like and honeycomb-like patterns were found in Lo-rich compositions (Fig. 2.2, *F*, *G*, *J* and *K*), whereas thicker linewidths of honeycomb patterns (Fig. 2.2 *C*) and dispersed Lo domains with uneven edges (Fig. 2.2 *B*) occur in Ld-rich compositions. In addition to different patterns, the relative phase area fractions could also influence the decrease (or absence) of modulated phases: a significantly smaller fraction of GUVs was patterned at Ld-dominant compositions T1E and T1F at ρ = 25% compared to Lo-dominant compositions on the right end of tieline 1 (Fig. 2.3 *A*). Similarly, no patterned GUVs were observed for T2C at ρ = 30% compared to T2A, and the fraction of patterned GUVs at ρ = 40% for T2C is also lower than that obtained for T2A and T2B (Fig. 2.3 *B*). One possible reason for a lower fraction of patterned GUVs having Ld-rich compositions is simply that the appearance of a distinct pattern is less obvious when the Lo domains are fewer and more sparsely distributed on the GUV. Where Lo predominates, stripe-like and honeycomb-like phase patterns form favorably. When Ld predominates, Ld stripes coarsen and Lo domains become sparse but with the morphology of individual Lo domains remaining relatively unchanged. A change in phase predominance to Ld relatively abruptly changes phase morphology, resulting in narrower modulated phase windows at compositions located on the Ld-rich side of a tieline. Although fluorescence microscopy has proven to be useful in detecting modulated phases on GUVs, its resolution is diffraction-limited, and could be a reason why patterned morphologies were not as readily detectable at compositions on the Ld-rich end of tielines for example, if Lo domains are isolated and near or below the

diffraction limit in an Ld matrix. Hence, we are currently exploring spectroscopic methods such as FRET and ESR as alternative ways to detect the modulated phase regime.

2.5.3 Line tension determines the compositional range of modulated phases

While both line tension and curvature energies are important, simulations show that the line tension is the controlling factor for the formation of modulated phases (36). Assuming that modulated phases occur within a fixed range of line tension values, during the transition from nanoscopic to modulated to macroscopic round domains along a ρ-trajectory at fixed DSPC/CHOL ratios, perhaps the system is going through three separate regimes of line tension values (Fig. 2.9). These distinct line tension regimes could occur at different ρ values for compositions located on different tielines due to changes in properties of the coexisting phases. For example, on a tieline closer to the critical point, Ld and Lo phase properties are more similar, hence the line tension would be smaller. In such cases, more DOPC would be required to increase the line tension to the value that yields modulated phases. Indeed, experimentally we observed a broader modulated phase regime for T2A on tieline 2 compared to the equivalent composition T1A on tieline 1, with the modulated phase window occurring at higher ρ values along tieline 2. Even a very simple model can illustrate this effect, i.e. a linear variation of line tension with ρ as shown in Fig. 2.9. An alternative model is perhaps more likely in light of recent small-angle neutron scattering measurements where domain size was found to vary linearly with bilayer thickness (46), implying a squared dependence of line tension on ρ. Consistent with low line tension values in the proximity of a modulated phase regime, we observed GUVs with uneven domain

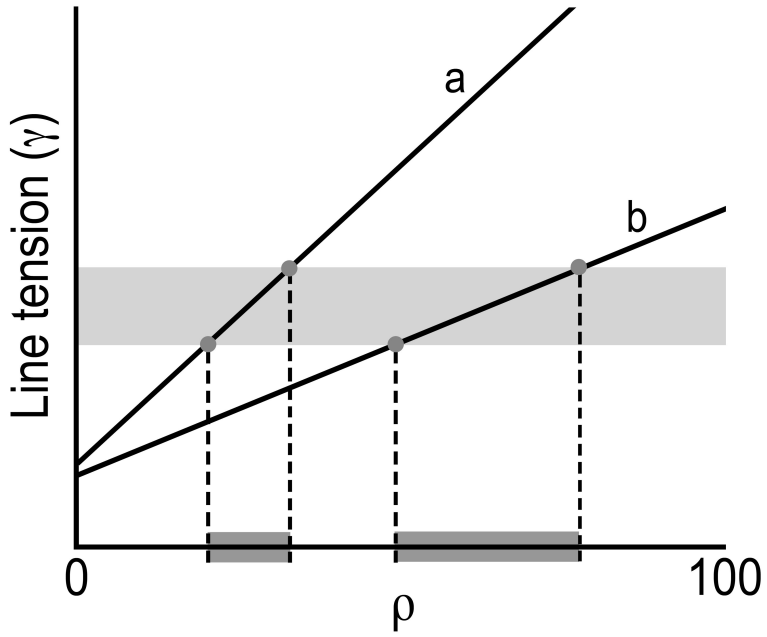

Figure 2.9 The modulated phase window broadens and shifts to higher ρ as the critical point is approached. A schematic diagram comparing line tension vs. ρ plots for a composition located on one tieline (line *a*), and a composition on a shorter tieline, located closer to the critical point (line *b*). Modulated phases only occur when line tension lies within a specific range of values (0.015 to 0.030 pN), based on simulations (36).

edges that sometimes move during our observations, at compositions near the modulated-to-macroscopic round transition (Fig. 2.2 *H,* 2.4 *F* and 2.5 *H*).

The competing interactions model shows that modulated phases are thermodynamically stable, and that kinetic trapping only occurs when the line tension is high (36). Consistently, we observed that at compositions just outside the modulated phase regime (eg. ρ = 40%), where macroscopic round domains were observed but line tension values are still relatively low, the majority of GUVs displayed a single Ld (or Lo) domain in the matrix of the opposite phase. If extensive kinetic trapping were present, GUVs would display multiple round domains. This further indicates that our experimental procedures produced equilibrium domain morphologies, consistent with the model of competing interactions.

Using the competing interactions model, as line tension is increased, domains coarsen, coalesce, and eventually round up (Fig. 2.10, *E-H*). Increasing line tension in a simulation is equivalent to increasing ρ values in GUV experiments. A similar evolution of domain morphologies was also observed on actual GUVs during the nano-to-macro transition along a ρ-trajectory (Fig. 2.10, *A-B* and Fig. 2.4). Simply by modeling our system as two coexisting liquids where the modulated phase behavior is driven by line tension, we obtained remarkable correlation between model and experimental observations in the modulated and macroscopic regime when curvature energies are applied as the force opposing line tension. This model might be applicable to the nanoscopic regime, if different or additional competing forces such as dipole repulsion could be operating to stabilize nanodomains. Understanding these interactions would be valuable for describing nanoheterogeneities that exist in cell

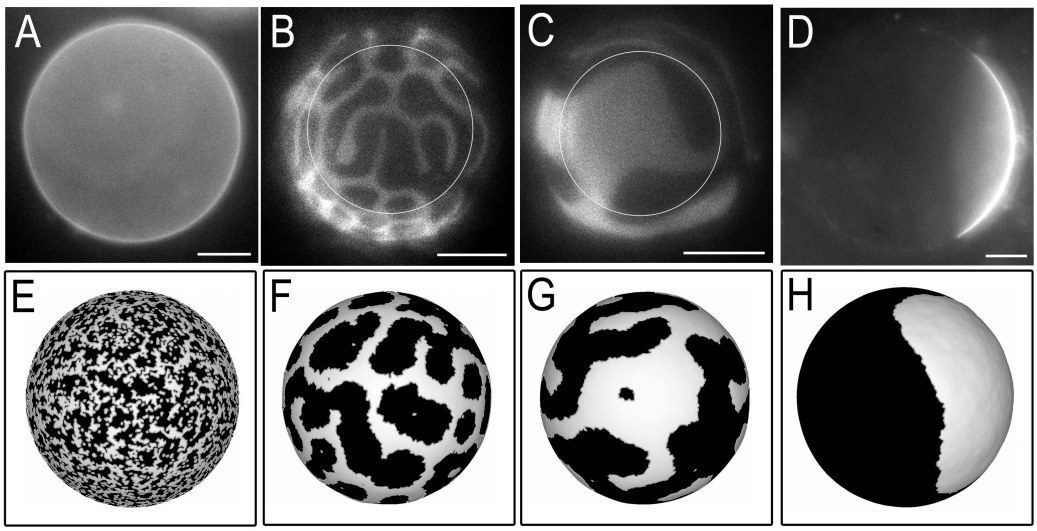

Figure 2.10 Changing only the line tension term in simulations is sufficient to produce modulated phase patterns through a ρ-trajectory. A comparison of experimental (*A-D*) and simulated (*E-H*) GUVs at composition T2A through a ρ-trajectory. GUVs appear uniform before the onset of the modulated phase window (*A*, *E*), and displayed macroscopic round domains at the end of the window (*D, H*). Images were processed and shown as described in Fig. 2.2. GUVs (*A-D*) have the composition DSPC/(DOPC+POPC)/CHOL = 0.395/0.30/0.305, with the ρ-values: *(A)* 20%, *(B)* 40%, *(C)* 65%, *(D)* 70%; C12:0-DiI (0.02 mol%) partitions into Ld. Scale bars 10 μm; temperature, 23°C. Simulation parameters for GUVs *E-H:* $P = 0.65$, $\kappa_d = 20 \times 10^{-19} J$, $\kappa_o = 150 \times 10^{-19} J$, $\bar{\kappa}_d = -20 \times 10^{-19} J$, $\bar{\kappa}_o = -150 \times 10^{-19} J$, GUV radius = 25 μm. Line tension (pN) values are: *(E)* 0.005, *(F)* 0.02, *(G)* 0.03, *(H)* 0.50. Simulations performed by J.J.A.

plasma membranes.

2.6 Conclusion

In this study, we have shown that there are three regimes that vary in domain size and shape within the Ld + Lo liquid-liquid immiscibility volume of DSPC/DOPC/POPC/CHOL. By tuning the fraction of low melting lipid that is DOPC, we observe a transition from nanodomains to modulated phases, and finally to macroscopic round domains on GUVs. The modulated phase patterns can be modeled using competing interactions between line tension and curvature energies. We found that line tension is the main factor controlling the location of the modulated phase regime: the lower the line tension at $\rho = 0$, the more DOPC is required.

This view that Ld + Lo phase morphology can be controlled by competition of line tension with an opposing interaction that favors small domains might extend to the nanodomain regime, if there exist interaction(s) at that distance scale, such as lipid-lipid dipolar repulsion, that favor small domains. In that case, the plasma membranes of cells might exhibit patterned phase morphology, rather than the simple picture of small Lo rafts floating in a large Ld sea. Furthermore, as we observe for the mixture studied here, it might be that lower line tension leads to smaller phase domains, as well as to a higher ρ window. If so, then the convenient use of fluorescence microscopy for determining the ρ window for a given mixture might be a substitute for less convenient direct measurement of domain size at the nanoscale.

References

1. Simons, K., and E. Ikonen. 1997. Functional rafts in cell membranes. Nature. 387: 569–572.

2. Lingwood, D., and K. Simons. 2010. Lipid rafts as a membrane-organizing principle. Science. 327: 46–50.

3. Sharma, P., R. Varma, R.C. Sarasij, Ira, K. Gousset, et al. 2004. Nanoscale organization of multiple GPI-anchored proteins in living cell membranes. Cell. 116: 577–589.

4. Harder, T., P. Scheiffele, P. Verkade, and K. Simons. 1998. Lipid domain structure of the plasma membrane revealed by patching of membrane components. The Journal of Cell Biology. 141: 929–942.

5. Holowka, D., J.A. Gosse, A.T. Hammond, X. Han, P. Sengupta, et al. 2005. Lipid segregation and IgE receptor signaling: A decade of progress. Biochimica et Biophysica Acta (BBA) - Molecular Cell Research. 1746: 252–259.

6. Sengupta, P., B. Baird, and D. Holowka. 2007. Lipid rafts, fluid/fluid phase separation, and their relevance to plasma membrane structure and function. Seminars in Cell & Developmental Biology. 18: 583–590.

7. Field, K.A., D. Holowka, and B. Baird. 1997. Compartmentalized activation of the high affinity immunoglobulin E receptor within membrane domains. J. Biol. Chem. 272: 4276–4280.

8. Holowka, D., E.D. Sheets, and B. Baird. 2000. Interactions between Fc (epsilon) RI and lipid raft components are regulated by the actin cytoskeleton. Journal of Cell Science. 113: 1009–1019.

9. Baumgart, T., A.T. Hammond, P. Sengupta, S.T. Hess, D.A. Holowka, et al. 2007. Large-scale fluid/fluid phase separation of proteins and lipids in giant plasma membrane vesicles. Proc. Natl. Acad. Sci. U.S.A. 104: 3165–3170.

10. Lingwood, D., J. Ries, P. Schwille, and K. Simons. 2008. Plasma membranes are poised for activation of raft phase coalescence at physiological temperature. Proceedings of the National Academy of Sciences. 105: 10005–10010.

11. Sengupta, P., D. Holowka, and B. Baird. 2007. Fluorescence Resonance Energy Transfer between Lipid Probes Detects Nanoscopic Heterogeneity in the Plasma Membrane of Live Cells. Biophys. J. 92: 3564–3574.

12. Swamy, M.J., L. Ciani, M. Ge, A.K. Smith, D. Holowka, et al. 2006. Coexisting Domains in the Plasma Membranes of Live Cells Characterized by Spin-Label ESR Spectroscopy. Biophys. J. 90: 4452–4465.

13. Eggeling, C., C. Ringemann, R. Medda, G. Schwarzmann, K. Sandhoff, et al. 2009. Direct observation of the nanoscale dynamics of membrane lipids in a living cell. Nature. 457: 1159–1162.

14. van Meer, G., D.R. Voelker, and G.W. Feigenson. 2008. Membrane lipids: where they are and how they behave. Nat Rev Mol Cell Biol. 9: 112–124.

15. Korlach, J., P. Schwille, W.W. Webb, and G.W. Feigenson. 1999. Characterization of lipid bilayer phases by confocal microscopy and fluorescence correlation spectroscopy. Proc. Natl. Acad. Sci. U.S.A. 96: 8461–8466.

16. Feigenson, G.W. 2009. Phase diagrams and lipid domains in multicomponent lipid bilayer mixtures. Biochimica et Biophysica Acta (BBA) - Biomembranes. 1788: 47–52.

17. Zhao, J., J. Wu, F.A. Heberle, T.T. Mills, P. Klawitter, et al. 2007. Phase studies of model biomembranes: Complex behavior of DSPC/DOPC/Cholesterol. Biochimica et Biophysica Acta (BBA) - Biomembranes. 1768: 2764–2776.

18. Veatch, S.L., and S.L. Keller. 2003. Separation of liquid phases in giant vesicles of ternary mixtures of phospholipids and cholesterol. Biophysj. 85: 3074–3083.

19. Veatch, S., and S. Keller. 2005. Miscibility Phase Diagrams of Giant Vesicles Containing Sphingomyelin. Phys. Rev. Lett. 94.

20. Veatch, S.L., K. Gawrisch, and S.L. Keller. 2006. Closed-loop miscibility gap and quantitative tie-lines in ternary membranes containing diphytanoyl PC. Biophysj. 90: 4428–4436.

21. Feigenson, G.W., and J. Buboltz. 2001. Ternary phase diagram of dipalmitoyl-PC/dilauroyl-PC/cholesterol: Nanoscopic domain formation driven by cholesterol. Biophys. J. 80: 2775–2788.

22. Heberle, F.A., J. Wu, S.L. Goh, R.S. Petruzielo, and G.W. Feigenson. 2010. Comparison of three ternary lipid bilayer mixtures: FRET and ESR reveal nanodomains. Biophys. J. 99: 3309–3318.

23. Pathak, P., and E. London. 2011. Measurement of lipid nanodomain (raft) formation and size in sphingomyelin/POPC/cholesterol vesicles shows TX-100 and transmembrane helices increase domain size by coalescing preexisting nanodomains but do not induce domain formation. Biophys. J. 101: 2417–2425.

24. Ionova, I.V., V.A. Livshits, and D. Marsh. 2012. Phase diagram of ternary cholesterol/palmitoylsphingomyelin/palmitoyloleoyl-phosphatidylcholine

mixtures: spin-label EPR study of lipid-raft formation. Biophys. J. 102: 1856–1865.

25. Hammond, A.T., F.A. Heberle, T. Baumgart, D. Holowka, B. Baird, et al. 2005. Crosslinking a lipid raft component triggers liquid ordered-liquid disordered phase separation in model plasma membranes. Proc. Natl. Acad. Sci. U.S.A. 102: 6320–6325.

26. Konyakhina, T.M., S.L. Goh, J. Amazon, F.A. Heberle, J. Wu, et al. 2011. Control of a Nanoscopic-to-Macroscopic Transition: Modulated Phases in Four-Component DSPC/DOPC/POPC/Chol Giant Unilamellar Vesicles. Biophys. J. 101: L8–L10.

27. Seul, M., and D. Andelman. 1995. Domain shapes and patterns: the phenomenology of modulated phases. Science. 267: 476–483.

28. McConnell, H.M. 1991. Structures and Transitions in Lipid Monolayers at the Air-Water Interface. Annu. Rev. Phys. Chem. 42: 171–195.

29. Liu, J., S. Qi, J.T. Groves, and A.K. Chakraborty. 2005. Phase segregation on different length scales in a model cell membrane system. J. Phys. Chem. B. 109: 19960–19969.

30. Kaizuka, Y., and J.T. Groves. 2010. Bending-mediated superstructural organizations in phase-separated lipid membranes. New J. Phys. 12: 095001.

31. Rozovsky, S., Y. Kaizuka, and J.T. Groves. 2005. Formation and Spatio-Temporal Evolution of Periodic Structures in Lipid Bilayers. J. Am. Chem. Soc. 127: 36–37.

32. Plass, R., N.C. Bartelt, and G.L. Kellogg. 2002. Dynamic observations of nanoscale self-assembly on solid surfaces. Journal of Physics: Condensed Matter. 14: 4227.

33. Hamada, T., Y. Kishimoto, T. Nagasaki, and M. Takagi. 2011. Lateral phase separation in tense membranes. Soft Matter. 7: 9061–9068.

34. Honerkamp-Smith, A.R., S.L. Veatch, and S.L. Keller. 2009. An introduction to critical points for biophysicists; observations of compositional heterogeneity in lipid membranes. BBA - Biomembranes. 1788: 53–63.

35. Baumgart, T., S.T. Hess, and W.W. Webb. 2003. Imaging coexisting fluid domains in biomembrane models coupling curvature and line tension. Nature. 425: 821–824.

36. Amazon, J.J., S.L. Goh, and G.W. Feigenson. 2013. Competition between line tension and curvature stabilizes modulated phase patterns on the surface of

giant unilamellar vesicles. A simulation study. Phys. Rev. E Stat. Nonlin. Soft Matter Phys. In press.

37. Hu, J., T. Weikl, and R. Lipowsky. 2011. Vesicles with multiple membrane domains. Soft Matter. 7: 6092.

38. Parthasarathy, R., C.-H. Yu, and J.T. Groves. 2006. Curvature-Modulated Phase Separation in Lipid Bilayer Membranes. Langmuir. 22: 5095–5099.

39. Frost, A., R. Perera, A. Roux, K. Spasov, O. Destaing, et al. 2008. Structural Basis of Membrane Invagination by F-BAR Domains. Cell. 132: 807–817.

40. Kingsley, P.B., and G.W. Feigenson. 1979. Synthesis of a Perdeuterated Phospholipid - 1,2-Dimyristoyl-Sn-Glycero-3-Phosphocholine-D72. Chemistry and Physics of Lipids. 24: 135–147.

41. Angelova, M., S. Soleau, P. Méléard, F. Faucon, and P. Bothorel. 1992. Preparation of giant vesicles by external AC electric fields. Kinetics and applications. Trends in Colloid and Interface Science VI. : 127–131.

42. Bresseleers, G.J., H.L. Goderis, and P.P. Tobback. 1984. Measurement of the glucose permeation rate across phospholipid bilayers using small unilamellar vesicles. Effect of membrane composition and temperature. Biochim. Biophys. Acta. 772: 374–382.

43. Schneider, C.A., W.S. Rasband, and K.W. Eliceiri. 2012. NIH Image to ImageJ: 25 years of image analysis. Nat Meth. 9: 671–675.

44. Mills, T.T., G.E.S. Toombes, S. Tristram-Nagle, D.-M. Smilgies, G.W. Feigenson, et al. 2008. Order parameters and areas in fluid-phase oriented lipid membranes using wide angle X-ray scattering. Biophys. J. 95: 669–681.

45. Alwarawrah, M., J. Dai, and J. Huang. 2010. A molecular view of the cholesterol condensing effect in DOPC lipid bilayers. J. Phys. Chem. B. 114: 7516–7523.

46. Heberle, F.A., R.S. Petruzielo, J. Pan, P. Drazba, N. Kucerka, R.F. Standaert, G.W. Feigenson, and J. Katsaras. 2013. Bilayer thickness mismatch controls domain size in model membranes. J. Am.Chem. Soc. doi:10.1021/ja3113615

CHAPTER 3
Temperature-dependent studies on modulated phases in DSPC/DOPC/POPC/CHOL mixtures

3.1 Abstract

We have determined that a modulated phase regime occurs between the nanoscopic-to-macroscopic domain size transition in Ld + Lo regions of DSPC/DOPC/POPC/CHOL mixtures. While theoretical studies have demonstrated the thermodynamic stability of modulated phases in this system (Chapter 2, ref. 36), the thermal stability of these patterned fluid domains have not been examined experimentally. In this chapter, we applied FRET and fluorescence imaging of GUVs to study temperature effects on modulated phases in bilayers. We found that probe partitioning behavior along a tieline in the modulated phase regime is similar to that in mixtures exhibiting canonical macroscopic phase separation. Using FRET, we determined the miscibility transition temperature, and the Ld + Lo phase boundaries as a function of temperature at $\rho = 20\%$ along a tieline within the two-phase region. FRET and GUV results reveal a domain size transition from patterned to nanoscopic fluid domains above 35°C. We also observed that modulated phase patterns are reversible after brief temperature cycles, offering evidence for the thermodynamic stability of this interesting state of matter.

3.2 Introduction

Modulated phases are found in diverse physical and chemical systems, including ferrofluids, superconducting films, and lipid monolayers and bilayers (1-4).

Periodic domains manifested as stripes and two-dimensional "bubbles" that are usually arranged in a hexagonal pattern have been commonly observed. The maintenance and stabilization of modulated morphologies are governed by the interplay between local attractive forces (i.e. line tension), and long-range repulsive forces.

In lipid bilayer systems, micron-sized modulated phase patterns can be stabilized by membrane curvature energies that compete with low line tension. Coexisting domains with different bending moduli result in curvature mismatch at the domain perimeters, with the less "rigid" domains being more curved (5, 6). Theoretical studies have shown that this repulsive curvature energy can stabilize dispersed domains in bilayers (5, 7, 8). On the other hand, a few experimental studies conducted on mixtures that contained charged lipids have also found patterned domains. There, electrostatic repulsion between domains with like-charges is probably responsible for stabilizing a dispersed domain organization (9, 10).

Modulated phases seem to behave like stable macroscopic coexisting phases and we are certain that they are not artifacts from photo-oxidation. Indeed, light-induced patterned domains have been reported in some model membrane mixtures (11, 12). Previously, we have shown that modulated morphologies in DSPC/DOPC/POPC/CHOL mixtures can be obtained via different types of imaging methods including wide-field, confocal, two-photon, and differential interference contrast (DIC) microscopies (4). This indicated that the patterns are not dependent upon the intensity, duration of illumination, and the wavelength of light impinged onto samples. Most importantly, we observed patterned domains even in the absence of a

fluorescent probe via DIC (Fig. 3.1); high concentrations of fluorophores have been shown to worsen light-induced artifacts (12, 13). In addition, modulated phase patterns in our systems are stable for at least 24 hours after formation.

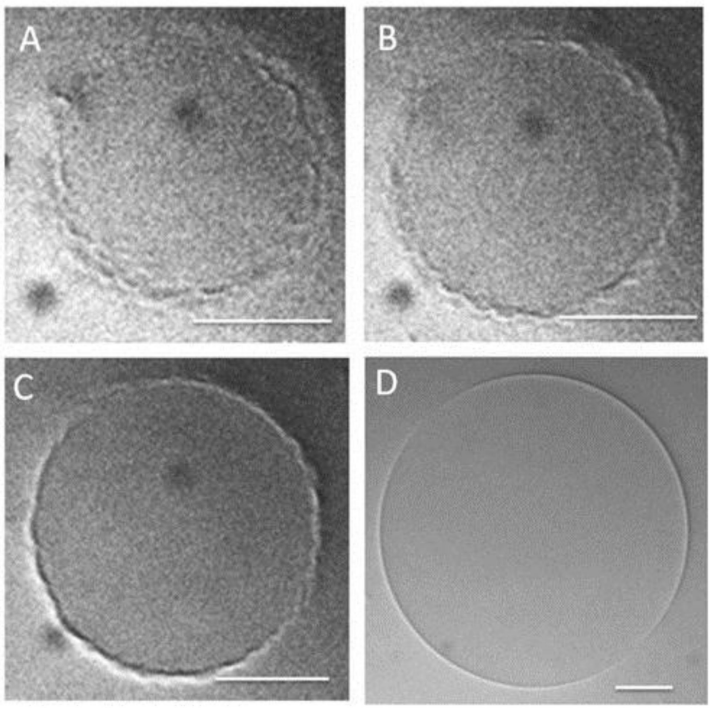

FIGURE 3.1 DIC images of a probe-free GUV displaying modulated phases. Scalloped edges on a patterned GUV with no fluorescent probe (A-C) compared to a uniform GUV (D). The same GUV imaged at different z-planes is shown in (A-C). Compositions DSPC/DOPC/POPC/CHOL: (A-C) 0.45/0.06/0.24/0.25; (D) 0.45/0.03/0.27/0.25. Scale bars 10 μm; temperature, 23°C. Figure taken from (4).

The effects of temperature on phase behavior can connect to the thermodynamic nature of membrane mixtures. Temperature-dependent studies on miscibility boundaries in a few ternary model membrane mixtures have been reported. The direct observations of domain disappearance and reappearance upon heating and cooling GUVs on the microscope stage have led to the construction of several miscibility transition maps of the Ld + Lo regions in DPPC/ DOPC/ CHOL (14, 15), PSM/DOPC/CHOL (16), stearoyl-SM (SSM)/DOPC/CHOL (17), and DPPC/DiPhyPC/CHOL (18). Furthermore, the kinetics of domain formation could also be captured upon cooling GUVs at selected compositions: striped and polka dotted morphologies were observed as domain grew via ripening, spinodal decomposition, and viscous fingering (14). Stable and reversible critical fluctuations have been observed in DPPC/DiPhyPC/CHOL mixtures upon temperature cycling (18). While microscopy studies (mentioned above) are exceptionally useful for obtaining temperature-dependent phase behavior of membrane mixtures, care must be taken to avoid light-induced artifacts that could skew the results.

Using fluorescence microscopy of GUVs, we revealed a nanoscopic to macroscopic transition of domain size that goes through a modulated phase regime in the Ld + Lo volume of DSPC/DOPC/POPC/CHOL mixtures (Chapter 2). We reported that modulated phases follow the lever arm rule along a tieline and can be modeled using a competing interactions model of line tension and curvature energy (19). While the composition-dependent evolution of modulated phases was examined, the thermodynamic nature of these fluid patterned phases has not been investigated experimentally. Monte Carlo simulations revealed that modulated phases were

energetically more stable than macroscopic round domains (19). Patterned phase morphologies were obtained on simulated GUVs for different initial states and different pathways of phase separation and domain formation, indicating that the patterns are thermodynamically stable. Experimentally, we are interested in examining the effects of temperature on the phase behavior of Ld + Lo patterned domains. How does temperature affect the transition of domain size and shape changes? Are modulated phases thermodynamically stable? Do modulated phases behave like genuine phases that can be studied using spectroscopy methods? These are questions that we would like to investigate.

The thermal stability of modulated phases in bilayers was examined in this study. Using GUVs, we found that patterns could be reversible upon heating and cooling vesicles. In addition, we also employed FRET to obtain the temperature-dependent phase behavior along a tieline within a modulated phase regime, and observed a miscibility transition at higher temperatures. Coupled with GUV observations, we discovered a switch from modulated to nanoscopic phases at elevated temperatures.

3.3 Materials and Methods

3.3.1 Materials

All phospholipids were purchased from Avanti Polar Lipids (Alabaster, AL). The cholesterol was from Nu Chek Prep (Elysian, MN). Fluorescent dyes Bodipy-PC (2-(4,4-difluoro-5,7-dimethyl-4-bora-3a,4a-diaza-s-indacene-3-pentanoyl)-1-hexadecanoyl-sn-glycero-3-phosphocholine) and C12:0-DiI (1,1′-didodecyl-3,3,3′,3′-

tetramethylindocarbocyanine perchlorate) were purchased from Invitrogen (Carlsbad, CA); DHE (ergosta-5,7,9(11),22-tetraen- 3b-ol) was purchased from Sigma-Aldrich (St. Louis, MO). Inorganic phosphate assay (20) was used to determine the concentrations of phospholipid stocks to <1% error, and purity of >99% was checked with thin layer chromatography. Briefly, lipids were spotted onto pre-washed and activated silica gel GHL UNIPLATES (Analtech, Newark, DE). The plates were then developed with chloroform/methanol/water = 65/25/4. Cholesterol stock solution was prepared by standard gravimetric procedures to ~0.2%. All fluorescent dye concentrations were determined using absorption spectroscopy on an HP 8452A spectrophotometer (Hewlett-Packard, Palo Alto, CA).

3.3.2 GUV sample preparation

GUVs were prepared using the electroformation procedure according to (4). Briefly, dried lipid film on indium tin oxide-coated slides (Delta Technologies, Stillwater, MN) were swelled in 100mM sucrose at 55°C for 2 hours. Samples were then cooled to room temperature (23°C) over 10-12 hours before harvesting into eppendorf tubes (Fisher Scientific). Vesicles were left to settle for ~2 hours before microscope observations. For studying shorter annealing times, samples were cooled from 55°C to 23°C in two, four or eight hours before harvesting into eppendorf tubes.

3.3.3 Fluorescence microscopy

For imaging, a few microliters of sample were placed in a chamber, made from a 0.25 mm-thick silicone “cage” (Grace Bio-Labs, Bend, Oregon) that was sandwiched between a glass cover slip and a glass microscope slide. Wide-field imaging was performed on an inverted Nikon Diaphot-TMD using a 60X 1.4NA oil

immersion objective. To minimize light exposure, vesicles were first located in bright field mode before fluorescence illumination. GUVs contained 0.02 mol% C12:0-DiI, which partitions into the Ld phase. Images were taken with a Photometrics charge-coupled device camera CoolSNAP$_{HQ2}$ (Tucson, Arizona), using 535-550 nm excitation and 565-610 nm emission. For temperature studies on the Nikon Diaphot-TMD, an objective heater (ALA Scientific Instruments, Farmingdale, NY) controlled by an MTC-20/2S temperature control system (npi electronic GmbH, Tamm, Germany), and a stage heater (Biostage 600, 20/20 Technology Inc., Wilmington, NC) were used to heat and cool GUV samples. Typically, samples were heated to ~35°C in 5 min, and then cooled back to 25-26°C in ~7 min. Images were taken before heating, right after heating (at the higher temperature), and immediately after cooling for comparison of morphologies on the same GUV. For bulk determination of patterned domains in a sample, the harvested samples (in eppendorf tubes) were heated to the desired temperature in 2-5 min using a heating block, and cooled back to room temperature in 7-15 min. Observation chambers were prepared to image samples either after the heat/cool cycle or immediately after heating the samples to high temperature. All images were analyzed using NIS Elements Basic Research Software (MVI, Inc., Avon, MA).

Confocal imaging was performed on an inverted Zeiss LSM 710 confocal microscope using a 63X 1.4NA oil immersion objective. C12:0-DiI was excited at 561 nm (1.5% laser power) with pinhole 99 μm, and emission collected at 568 – 674 nm. Special attention was taken to minimize exposure to fluorescence illumination: GUVs were first located using low power (~1.0%) laser excitation at 633 nm, and bright field

collection mode (all wavelengths). Only a few z-stacks (6-8 μm) were taken right at the surface of GUVs to enable determination of patterned phase domains before heating the samples for temperature studies. Temperature studies on the Zeiss 710 were conducted as described above, but using an objective heater, stage-top incubation chamber, and a circulating water bath (Julabo Labortechnik GmbH, Seelbach, Germany), all controlled by TempModule S1 (Carl Zeiss Microscopy, LLC, Thornwood, NY). Confocal images were analyzed with Zeiss ZEN software.

3.3.4 FRET sample preparation and data collection

FRET samples were prepared according to procedures described in (21) with the following modifications: A series of samples (trajectory) were prepared at 1% compositional resolution along a tieline within the Ld + Lo region of DSPC/DOPC/POPC/CHOL. Compositions at the endpoints of this trajectory were DOPC/POPC/CHOL = 0.18/0.72/0.10 and DSPC/CHOL = 0.675/0.325. Each sample received the following probe:lipid ratio of fluorescent dyes: DHE (1:100), Bodipy-PC (1:1500), and C12:0-DiI (1:2000). Single dye controls were prepared at ~10% compositional resolution along the trajectory, each with the same probe:lipid ratio as dispensed in the samples. For samples or controls that contained 1% DHE, the concentrations of cholesterol in those samples were lowered by 1% to account for the non-negligible amount of additional cholesterol analog. Furthermore, samples and controls were randomized during preparation in order to minimize systematic errors.

Multilamellar vesicles in an aqueous suspension were formed using the rapid solvent exchange (RSE) method (22). This allowed the removal of chloroform from each sample rapidly, replacing it with RSE buffer (5mM PIPES, 200 mM KCl, 1mM

EDTA, pH7.0) to form hydrated bilayers without going through a dried lipid film state. Samples were ramped from 50°C to 23°C at 2°C/hour in a water bath, and held at 23°C for at least 24 hours before data collection.

Fluorescence data was collected on a F7000 spectrofluorimeter (Hitachi High Technologies America, Schaumburg, IL) that was equipped with a temperature-controlled cuvette holder (Quantum Northwest, Inc.). For measurement, each sample was diluted to 25 μM with RSE buffer in a cuvette while applying gentle stirring. The fluorescence intensities from six excitation/emission channels (λ, nm) were measured, using 5 nm bandpass for excitation and emission slits, and 2s integration time:

DHE fluorescence (327/393),
Bodipy-PC stimulated emission (327/517),
Bodipy-PC fluorescence (505/517),
C12:0-DiI stimulated emission (505/565),
C12:0-DiI fluorescence (549/565),
Vesicle scattering (430/420).

Data were collected for all samples and controls in the trajectory, starting at 23°C. The temperature of the water bath was then raised to the next higher temperature (30°C), and all samples were equilibrated for at least 4 hours before fluorescence data were collected. This was done subsequently for data collection at 35°C, 40°C, 45°C and 50°C. After data collection was performed at 50°C, all samples were cooled down to

23°C again at 2°C/hour, and an additional set of data was collected at 23°C to confirm whether Ld + Lo immiscibility was still detectable.

3.3.5 SP-FRET data analysis

The profiles of steady-state probe-partitioning FRET (SP-FRET) have been used in phase-separated multicomponent membrane mixtures to determine regions of phase coexistence along a series of samples in composition space (15, 21, 23). Abrupt changes in the steady-state partitioning of fluorescent probes at phase boundaries can cause changes in the energy transfer efficiencies of probe pairs, resulting in:

1. *r*egion of *e*nhanced FRET *e*fficiency (REE) when two probes partition favorably into the same phase, causing an increase in energy transfer;
2. *r*egion of *r*educed FRET *e*fficiency (RRE) when two probes segregate into two coexisting phases, causing a decrease in energy transfer.

We are most interested in utilizing the two stimulated acceptor emission (SAE) channels for the comparison of SP-FRET at the various temperatures along the tieline. However, since the SAE channels contained non-FRET contribution from lipid vesicle scattering, donor bleedthrough and acceptor emission resulting from their direct excitation pathways, controls were used to correct for these contributions according to (21). In addition, to minimize noise that could arise from sample-to-sample variation, the corrected SAE signal (F_{SAE}) was further normalized according to

$$F = \frac{F_{SAE}}{\sqrt{F_D \cdot F_A}}$$

where F_D and F_A are scattering-corrected intensities from the donor and acceptor channels. The final FRET signal, F, for each probe pair was plotted in all figures shown in this study.

To determine the location of the Ld + Lo phase boundary along the trajectory, we used the SP-FRET profile from the DHE and Bodipy-PC FRET pair, which displayed an RRE. The phase boundaries at the left and right end of the trajectory were determined using the segmental linear regression function in Prism (v5.0d, GraphPad Software, Inc., San Diego, CA). Briefly, the intersection point of two straight-line regions at the vicinity of a phase boundary was determined for the data collected at each temperature (see Fig. 3.6 and 3.7).

The Bodipy-PC and C12:0-DiI FRET pair displayed a profile characteristic of an REE, where a peak was observed near the phase boundary located towards the Lo-rich (right) end of the trajectory. The attenuation of this REE peak at higher temperatures can be quantified by calculating the first derivative of the SP-FRET curve. Absence of a peak maximum indicates the disappearance of the phase boundary (see Fig. 3.9).

3.4 Results

Modulated phases in bilayers have been examined using mainly fluorescence microscopy of GUVs that are prepared via electroswelling ((4) and Chapter 2). Usually, GUVs are formed at high temperature (55°C), and allowed to anneal for 10-12 hours. Stripe-like and 2D-bubble-like patterns seemed stable up to at least 24 hours after the formation of GUVs, but the thermodynamic nature of modulated phases on

GUVs have not been studied extensively. In particular, we are interested in the effects of temperature on the stability of modulated phase patterns. For simplicity, all the GUVs examined in this study have the composition DSPC/DOPC/POPC/CHOL = 0.45/0.06/0.24/0.25, which has been previously shown to lie within a modulated phase regime ((4), Chapter 2). This composition is also located within the coexisting liquid-disordered and liquid-ordered (Ld + Lo) region at ρ = 20% of the four-component system, with ρ defined as,

$$\rho \equiv \frac{\chi_{DOPC}}{\chi_{DOPC} + \chi_{POPC}}(\%)$$

where χ_{DOPC} and χ_{POPC} are mole fractions of DOPC and POPC respectively.

3.4.1 Modulated phases formed in shorter GUV annealing durations

As an initial study, we investigated whether modulated phases on GUVs can be obtained with shorter annealing times. Instead of the usual 10-12 hour annealing period, we performed experiments where samples were cooled down to room temperature (from 55°C) in two, four, and eight hours. We observed patterned morphologies in samples that were annealed in as short as two hours. However, the sample yields were poor because we harvested the GUVs at high temperature, when they could have been more fragile, and we might have ruptured or distorted many intact vesicles. In an attempt to mitigate this problem, we allowed the samples to anneal more rapidly (four and eight hours) before harvesting them into eppendorf

tubes. For both four- and eight-hour annealing times, we still saw modulated phase patterns on GUVs.

While modulated phase patterns are observed on GUVs with shorter annealing times, a true test of the reversibility (and stability) of these patterns should involve *in situ* heating and cooling of the same GUVs on the microscope stage. It would be especially interesting if there were a strong correlation between the phase patterns before and after a heat/cool cycle.

3.4.2 Modulated phases are reversible upon heating and cooling

Upon heating the patterned GUVs to 33-35°C on the microscope stage, we observed a disappearance of modulated phase patterns: GUVs appeared uniform at the higher temperature. When the same GUVs were cooled rapidly to 25-27°C, a variety of morphologies were observed. Examples of GUV morphologies before heating, at 35°C, and upon cooling to ~25°C are shown in Fig. 3.2. While similar stripe-like, honeycomb, or bubble-like patterns could reappear (Fig. 3.2, *A3, B3, C3* and Fig. 3.3 *A*), we did not detect any strong correlation between the phase patterns before and after a temperature cycle. In addition, uniform (Fig. 3.2 *E3* and Fig. 3.3 *B*) and dispersed round domains (polka-dots) have also been observed (Fig. 3.2, *D3* and 2, *C* and *D*). These experiments were performed using both wide-field and confocal fluorescence microscopies, with similar results.

To allow for the examination of a larger number of GUVs, we performed the same heat (35°C)/ cool experiments on bulk GUVs, freely suspended in eppendorf tubes. Different populations of GUVs were examined before and after the 35°C temperature cycle. We observed that 100% of the GUVs observed appeared uniform at

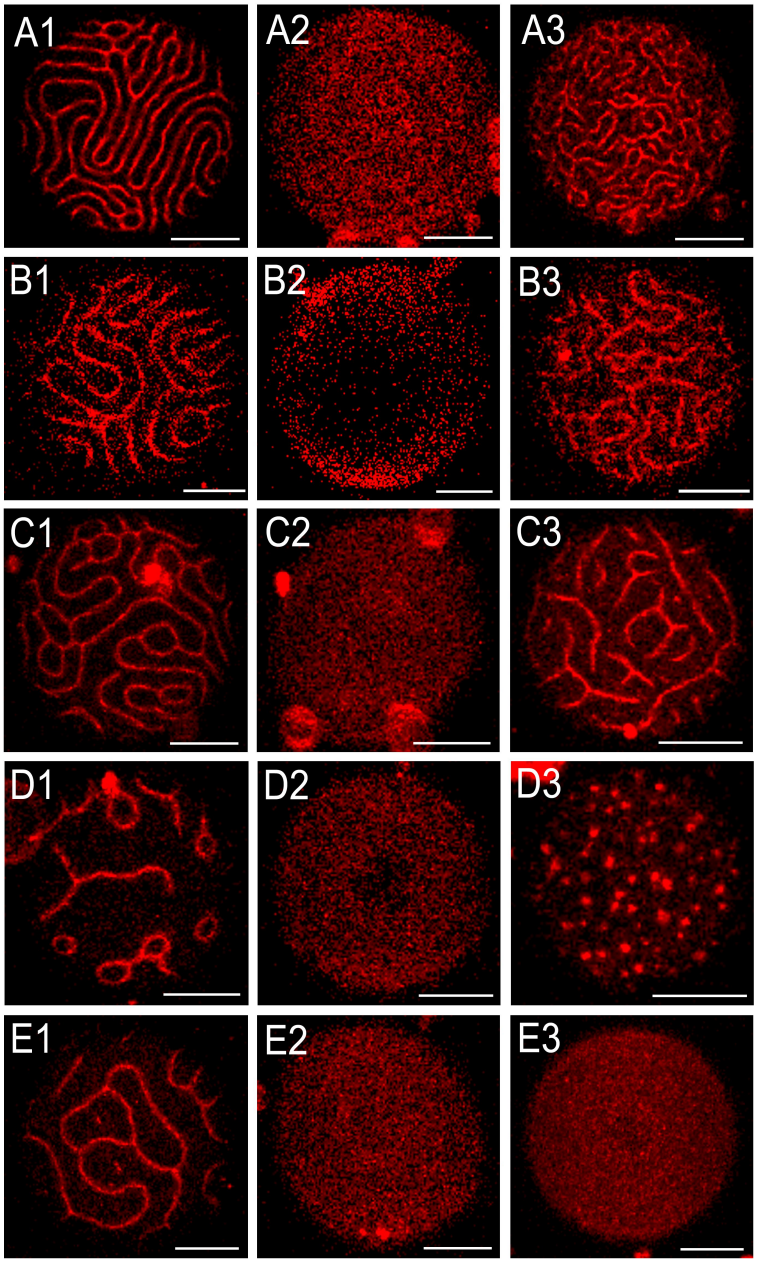

Figure 3.2 GUVs display various morphologies after a brief heating and cooling cycle. Maximum z-projections of GUV surfaces imaged with confocal microscopy are shown. The same GUVs are shown in each row, imaged at different times throughout the temperature cycle, as described in Materials and Methods. GUVs in the left column (A1-E1) showed patterned domains before the temperature cycle (23°C). At 35°C, the same GUVs looked uniform (center column, A2-E2). After brief cooling back to ~25°C, GUVs displayed a mixture of uniform and patterned morphologies (right column, A3-E3). All GUV compositions are DSPC/DOPC/POPC/CHOL = 0.45/0.06/0.24/0.25. Dye C12:0-DiI (0.02 mol%) partitions into Ld phase. Scale bars, 10 μm.

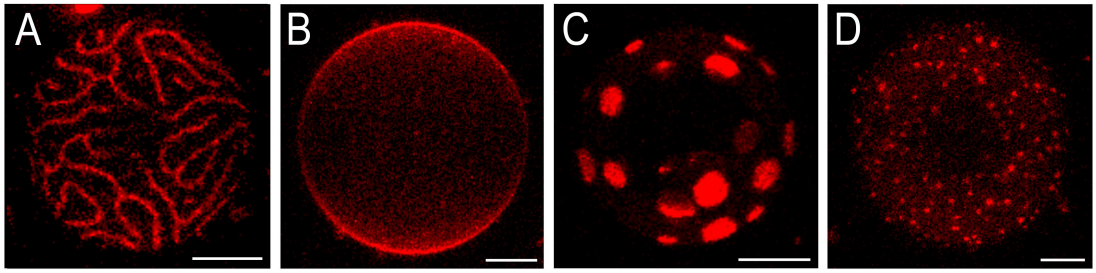

Figure 3.3 Common types of morphologies observed on GUVs after a 35°C temperature cycle. Maximum z-projections of confocal images of GUV surfaces are shown after a heat (35°C)/ cool cycle, performed as described in Fig. 1. The majority of GUV surfaces displayed stripe-like patterned domains (A), while uniform (B), macroscopic round domains (C) and dispersed uneven Ld dots (D) were also observed. GUVs contained the composition DSPC/DOPC/POPC/CHOL = 0.45/0.06/0.24/0.25. Dye C12:0-DiI (0.02 mol%) partitions into Ld phase. Temperature, ~25°C ; scale bars, 10 μm.

Table 3.1 Percentage of GUVs displaying the observed morphologies before and after heat/cool cycles

Experimental condition	% uniform	% modulated	% macroscopic-round	% unknown	N
Before heat (23°C)	17	83	-	-	128
After heat (35°C)/cool	22	61	15	2	177
After heat (50°C)/cool	21	67	12	-	66

Count distribution of GUVs that displayed uniform, modulated or macroscopic-round domain morphologies at DSPC/(DOPC+POPC)/CHOL = 0.45/0.30/0.25 (ρ = 20%) before and after heat/cool cycles, examined for two different higher temperatures.

Table 3.2 Percentage of modulated GUVs with various patterned morphologies before and after a heat/cool cycle.

Experimental condition	% 2D-bubbles and stripes	% honeycomb	% dispersed Ld, uneven edges	% dispersed Ld dots	% patch-like	% combination of >1 morphologies	N
Before (23°C)	92.5	1.9	-	-	-	5.7	106
After heat (35°C)/cool	69.4	0.9	17.6	1.9	3.7	6.5	108

Count distribution of the variety of patterns observed in GUVs with modulated phases at DSPC/(DOPC+POPC)/CHOL = 0.45/0.30/0.25 (ρ = 20%) before and after a heat/cool cycle, examined for 35°C.

35°C. Before the heat/cool cycle, 17% of the GUVs observed appeared uniform, while 83% displayed modulated phase patterns (Table 3.1). Of the GUVs that were patterned, ~ 93% were stripes or 2D-bubble-like (Table 3.2). After the heat/cool cycle, only 61% of the GUVs were patterned; the remaining were uniform (22%), undetermined (2%), or displayed macroscopic round domains (15%) (Table 3.1). The types of patterns observed on GUVs, after a heat/cool cycle, are as follow: stripes and bubble-like morphologies consisted ~ 69% of the total observed GUVs with modulated phases, whereas ~ 18% of the GUVs displayed dispersed Ld domains with uneven or fluctuating edges. The remaining morphology types consisted of dispersed spots, honeycomb, patches, or combination of two or more different patterns (Table 3.2). Overall, the majority of GUVs still displayed modulated phases upon quick heating to 35°C, followed by immediate cooling to room temperature.

The disappearance of modulated phase patterns at ~ 35°C and reappearance of patterns upon cooling led us to a question about the nature of modulated phases at higher temperature: Is the composition a one-phase mixture? Or do nanoscopic coexisting phases persist at 35°C? One significant weakness of fluorescence microscopy is that it is diffraction limited, and hence, cannot be used to investigate the evolution of domain size (if any) with increasing temperatures. We turn to a second, more sensitive method for this investigation: FRET.

3.4.3 FRET detects coexisting phases at higher temperatures in the modulated phase regime

FRET has been used successfully to detect coexisting phases in multicomponent bilayer mixtures (24-26). Due to its sensitivity to small length scales,

it is especially useful for the detection of nanoscopic domains in both model membranes and cell plasma membranes (21, 23, 27, 28). To investigate the coexistence of Lo + Ld phases at different temperatures in the modulated phase regime, we employed the SP-FRET method (15, 21). A trajectory was prepared along a tieline that is located slightly above the lower boundary of the Ld + Lo region in DSPC/DOPC/POPC/CHOL at ρ= 20% (Fig. 3.4 *A*); the GUV composition that was studied above also lies on this trajectory. Three fluorescent probes consisting of two FRET pairs were used: DHE and Bodipy-PC segregate into Lo and Ld phases, respectively; Bodipy-PC and C12:0-DiI partition into the same phase (Ld). SP-FRET profiles of the two FRET pairs were used to determine the location of phase boundaries as a function of temperature. Measurements were performed sequentially at a total of six different temperatures: 23°C, 30°C, 35°C, 40°C, 45°C, and 50°C.

At 23°C, the DHE-Bodipy-PC FRET profile displayed an RRE, characterized by a dip in FRET signal in the two-phase region compared to that in the one-phase regions (Fig. 3.4 *B*). In contrast, the Bodipy-PC-DiI FRET profile presented an REE lineshape, characterized by a peak near the phase boundary within the two-phase region (Fig. 3.4 *C*). Both profiles confirmed that the modulated phase regime displays lineshapes that are similar to those found in a canonical macroscopic phase coexistence region (15, 20). In addition, when samples were re-measured at 23°C after being cooled down slowly from 50°C, the same lineshapes of the FRET profiles from both probe pairs were obtained again, indicating that the coexisting phases were indeed stable and at equilibrium (Fig. 3.5). Using segmental linear regression on the DHE-Bodipy-PC FRET profile, the phase boundaries of the Ld + Lo region along the

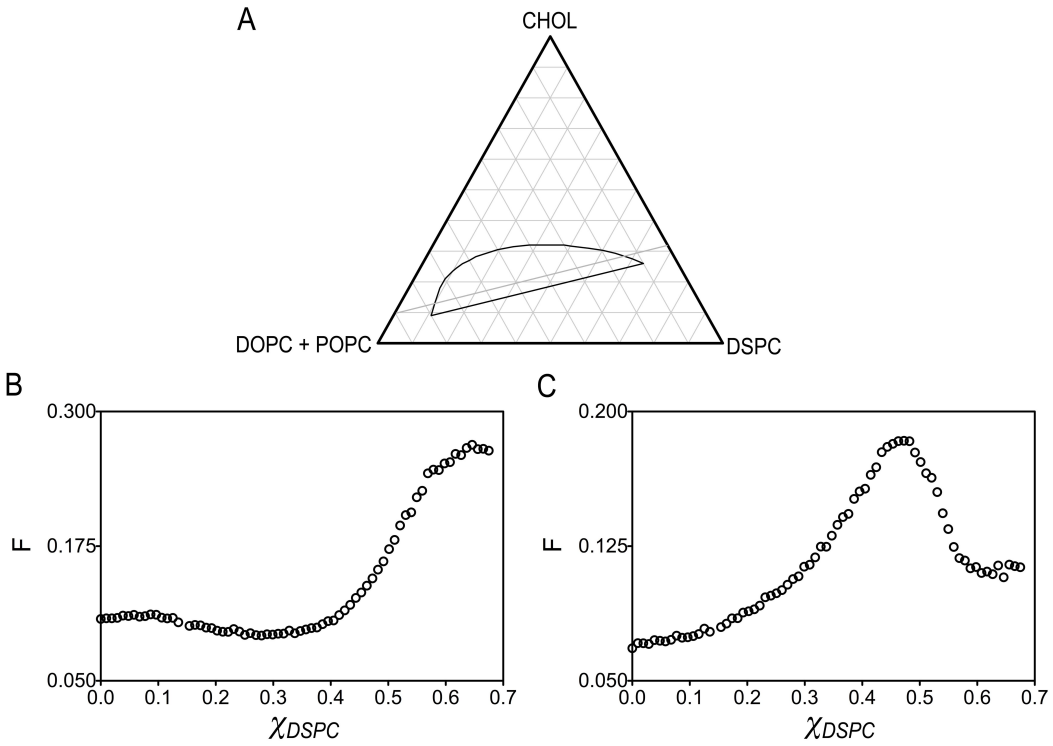

Figure 3.4 SP-FRET profiles along a tieline at ρ= 20% display regions of reduced and enhanced efficiencies. (A) A trajectory of samples traversing the Ld + Lo region were prepared and SP-FRET of two FRET pairs were analyzed as described in Materials and Methods. Phase diagram situates the Ld + Lo region at ρ= 20% of DSPC/DOPC/POPC/CHOL. (B) FRET between DHE and Bodipy-PC shows a region of reduced efficiency at 23°C. (C) FRET between Bodipy-PC and C12:0-DiI shows a region of enhanced efficiency at 23°C. Concentrations of dyes in each sample (mol %): DHE, 1%; Bodipy-PC, 0.067%; C12:0-DiI, 0.05%.

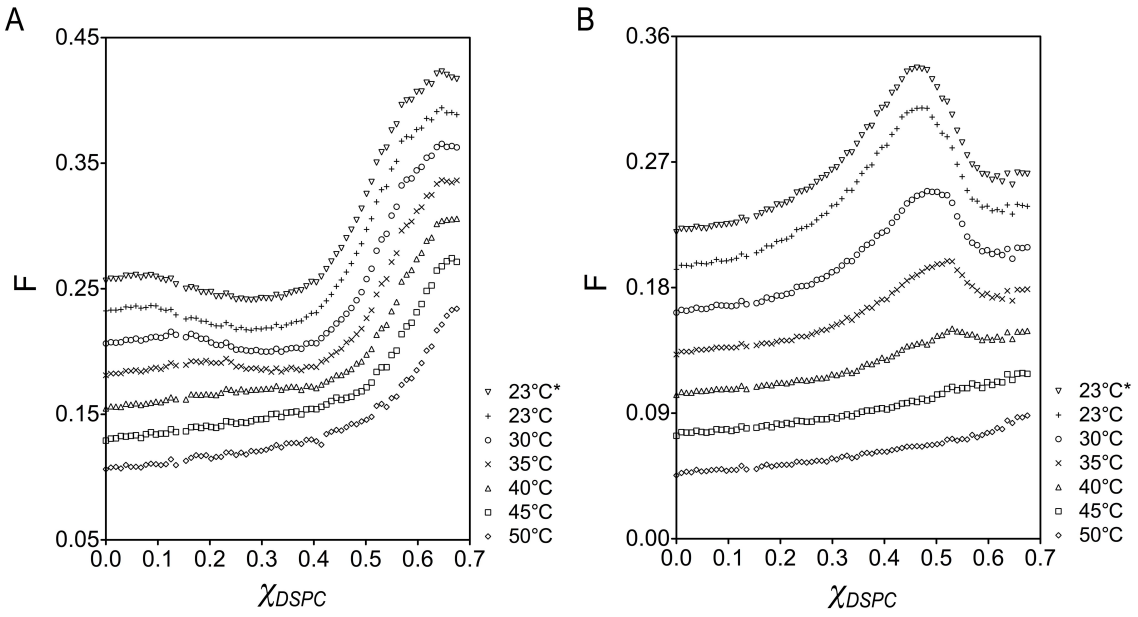

Figure 3.5 Attenuation of FRET at higher temperatures indicates disappearance of phase boundaries. SP-FRET was analyzed for the same FRET pairs along the trajectory described in Fig. 3A, at 23°C, 30°C, 35°C, 40°C, 45°C, and 50°C. (A) The region of reduced efficiency in DHE-Bodipy-PC FRET became more shallow and eventually disappeared at increasingly high temperatures, but reappeared upon cooling back to room temperature (*inverted triangles*), as described in Materials and Methods. (B) The peak of enhanced efficiency between Bodipy-PC and C12:0-DiI attenuated at higher temperatures, until it was not visibly obvious at 50°C. Reappearance of the peak was achieved upon controlled cooling to room temperature (*inverted triangles*). Dye concentrations in each sample were as described in Fig. 3. 4

trajectory were determined to be between $\chi_{DSPC} \approx 0.09$ and $\chi_{DSPC} \approx 0.58$ (see Fig. 3.6 *A* and 3.7 *A*), consistent with the Ld + Lo phase boundaries at ρ = 20% that was previously determined (unpublished, TM Konyakhina, J Wu, JD Mastroianni, FA Heberle, and GW Feigenson).

As temperature was increased gradually from 23°C to 50°C, the reduced (or enhanced) FRET efficiency regions for both FRET pairs became less defined due to increased miscibility of the lipid mixtures at higher temperatures (Fig. 3.5). In addition, the overall amplitudes of the FRET signals at higher temperatures were also attenuated, probably due to collisional quenching of probes at elevated temperatures. Despite that, the reduced FRET efficiency region in the DHE-Bodipy-PC profiles still revealed evidence of phase boundaries at temperature T ≤ 40°C (Fig. 3.6 and 3.7). The onset of coexisting Ld + Lo phases at the low χ_{DSPC} compositions along the trajectory is detectable up to 40°C based on segmental linear regression (Fig. 3.6 and 3.8). However, this boundary was observed to shift towards higher χ_{DSPC} from 30°C to 40°C: phase boundaries were detected at χ_{DSPC} values of 0.14, 0.20, and 0.24 at 30°C, 35°C and 40°C respectively, shrinking the Ld + Lo region towards the right half of the phase diagram (Fig. 3.6 *A-D* and Fig. 3.8). On the other hand, the location of the phase boundary on the Lo-rich end of the trajectory (high χ_{DSPC}) remained unchanged at $\chi_{DSPC} \sim 0.575$ up to 40°C (Fig. 3.7 *A-D*). At T ≥ 45°C, clear RRE regions were not detected; DHE-Bodipy-PC FRET increased monotonically from low to high χ_{DSPC}

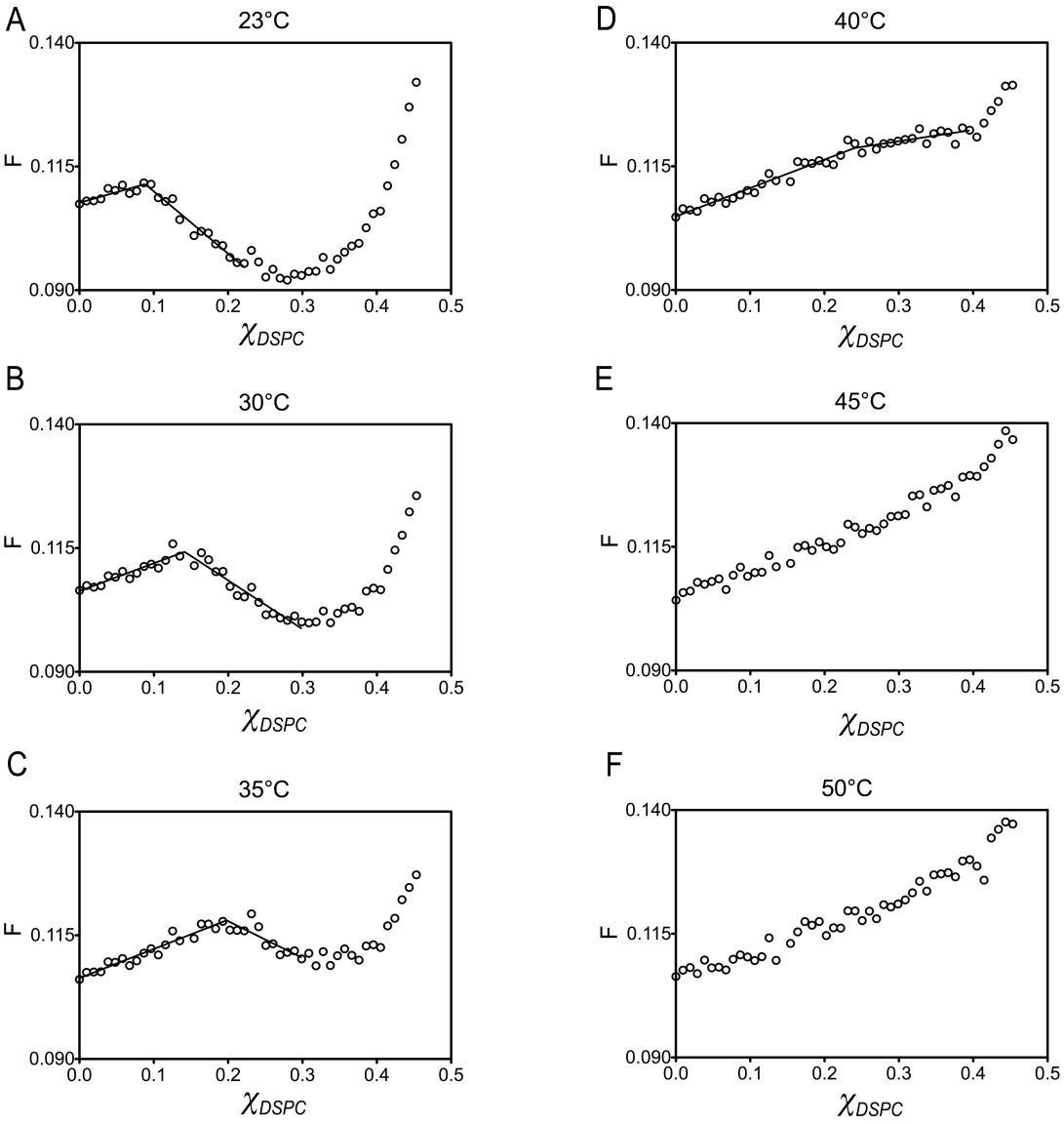

Figure 3.6 The left region of the DHE-Bodipy FRET profile shows boundary shifts at higher temperatures. A zoom-in of the FRET profiles in Fig. 3.5 *A* are shown for $\chi_{DSPC} = 0$ to $\chi_{DSPC} = \sim 0.45$ at various temperatures. The phase boundaries representing the onset of the two-phase (Ld + Lo) region were obtained by performing segmental linear regression. Boundaries shifted towards higher χ_{DSPC} until 40°C (A-D). Phase boundaries were not detected at 45°C (E) and 50°C (F).

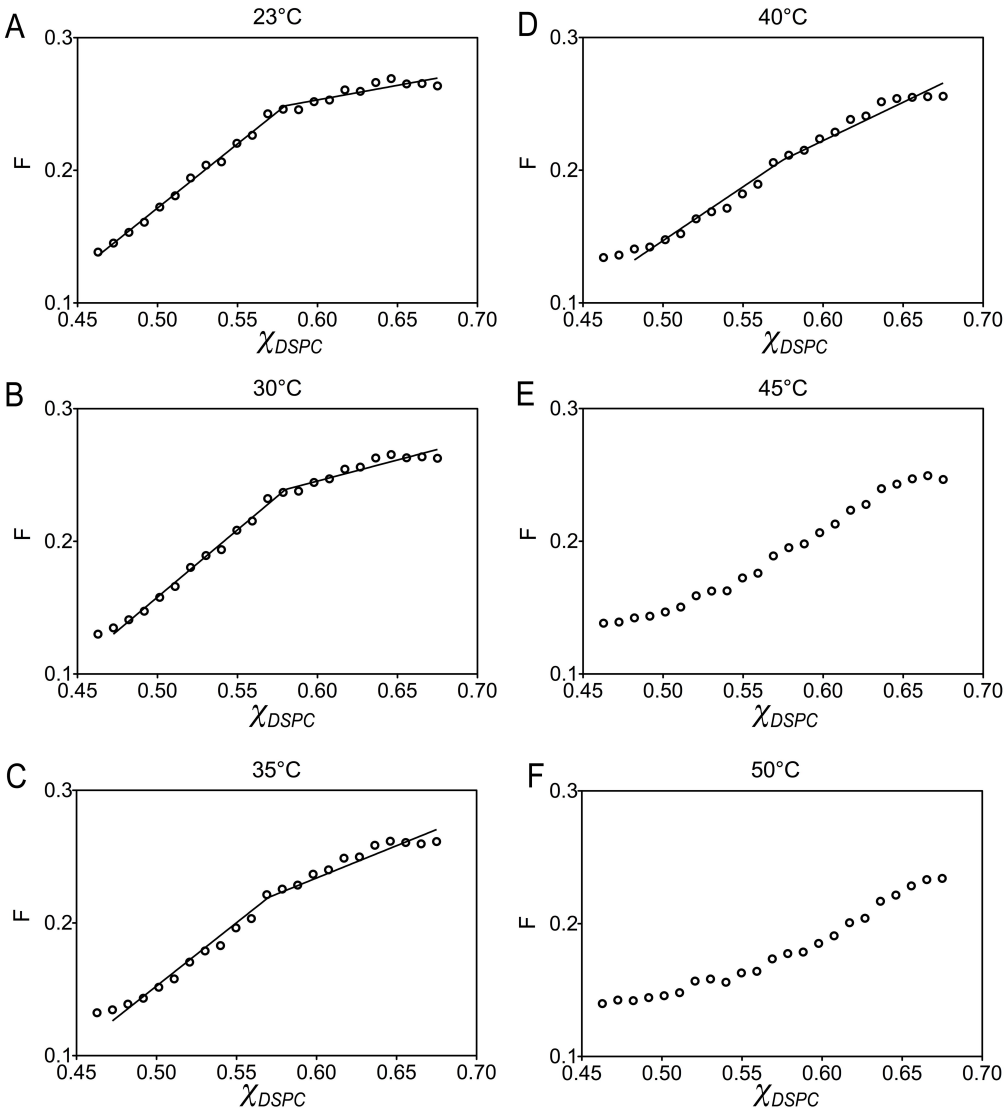

Figure 3.7 Phase boundaries can be determined from the right region of the DHE-Bodipy FRET profile. A zoom-in of the FRET profiles in Fig. 3.5 *A* are shown for $\chi_{DSPC} =\sim 0.46$ to $\chi_{DSPC} = 0.675$ at various temperatures. Boundaries were obtained as described in Fig. 5, and were found to be unchanged ($\chi_{DSPC} =\sim 0.575$) up to 40°C (A-D). Phase boundaries were not detected at 45°C (E) and 50°C (F).

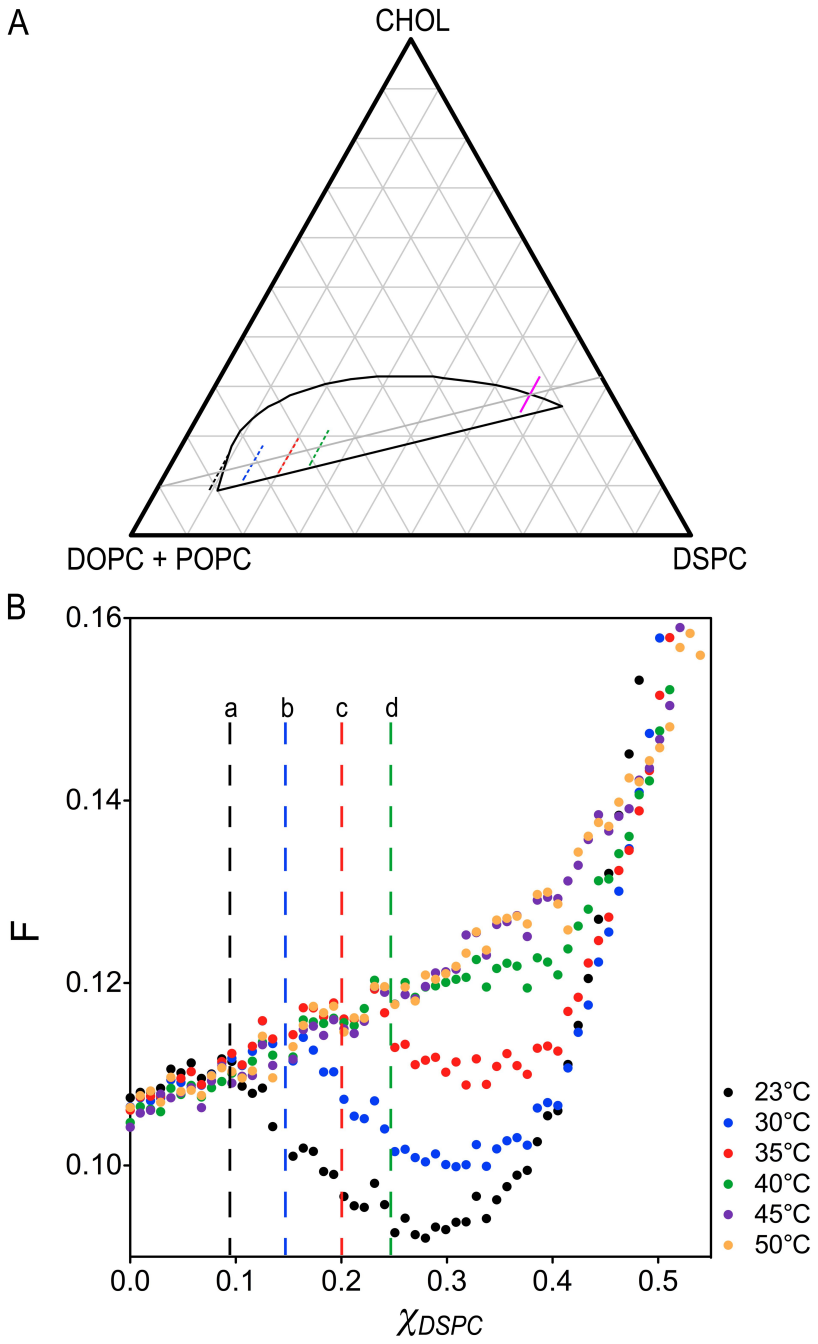

Figure 3.8 A summary of Ld + Lo phase boundaries as a function of temperature at ρ= 20%. (A) The phase boundaries determined in Fig. 3.6 and 3.7 at each temperature are situated on the phase diagram of DSPC/DOPC/POPC/CHOL at ρ= 20%. (B) Stacked plots of DHE-Bodipy FRET profiles analyzed in Fig. 5 are shown. Phase boundaries (χ_{DSPC}) obtained from 23°C to 40°C are: (*a*) 0.09, (*b*) 0.14, (*c*) 0.20, and (*d*) 0.24.

(Fig. 3.6 *E-F* and Fig. 3.7 *E-F*). A summary of the shift in phase boundaries at elevated temperatures is shown in Fig. 3.8.

For the second FRET pair, Bodipy-PC and C12:0-DiI, the position of the REE "peak" remained relatively unchanged as temperature was increased (Fig. 3.5 *B*). Nonetheless, attenuation of the peak height was noticeable at higher temperatures. To more accurately detect the disappearance of the peak, which is an indication that the mixtures are completely miscible, we calculated the first derivative trace of the Bodipy-DiI FRET profile at each temperature (Fig. 3.9). The slope of the FRET profile would change drastically around the peak region; absence of a drastic slope change indicates lack of a REE peak. We found that an enhanced FRET peak was detectable up to 40°C (Fig. 3.9 *A-D*). At 45°C, a shadow of a peak was observed (Fig. 3.9 *E*), but not at 50°C (Fig. 3.9 *F*). These results indicated that the phase boundary on the right of the Ld + Lo region is unchanged up to 40°C, corroborating results from DHE-Bodipy FRET profiles.

SP-FRET from two distinct FRET pairs detected coexisting Ld and Lo domains at elevated temperatures, up to ~ 45°C. As temperature is gradually increased from 23°C to 40°C, the Ld + Lo region was observed to shrink, and the phase boundary shifted towards compositions with higher DSPC content. The compositions along the trajectory were ideally mixed at 50°C.

3.4.4 Modulated phases on GUVs are reversible upon heating to 50°C

Temperature-dependent FRET studies revealed that the miscibility transition temperature of the Ld + Lo coexistence region at $\rho = 20\%$ is between 45°C and 50°C.

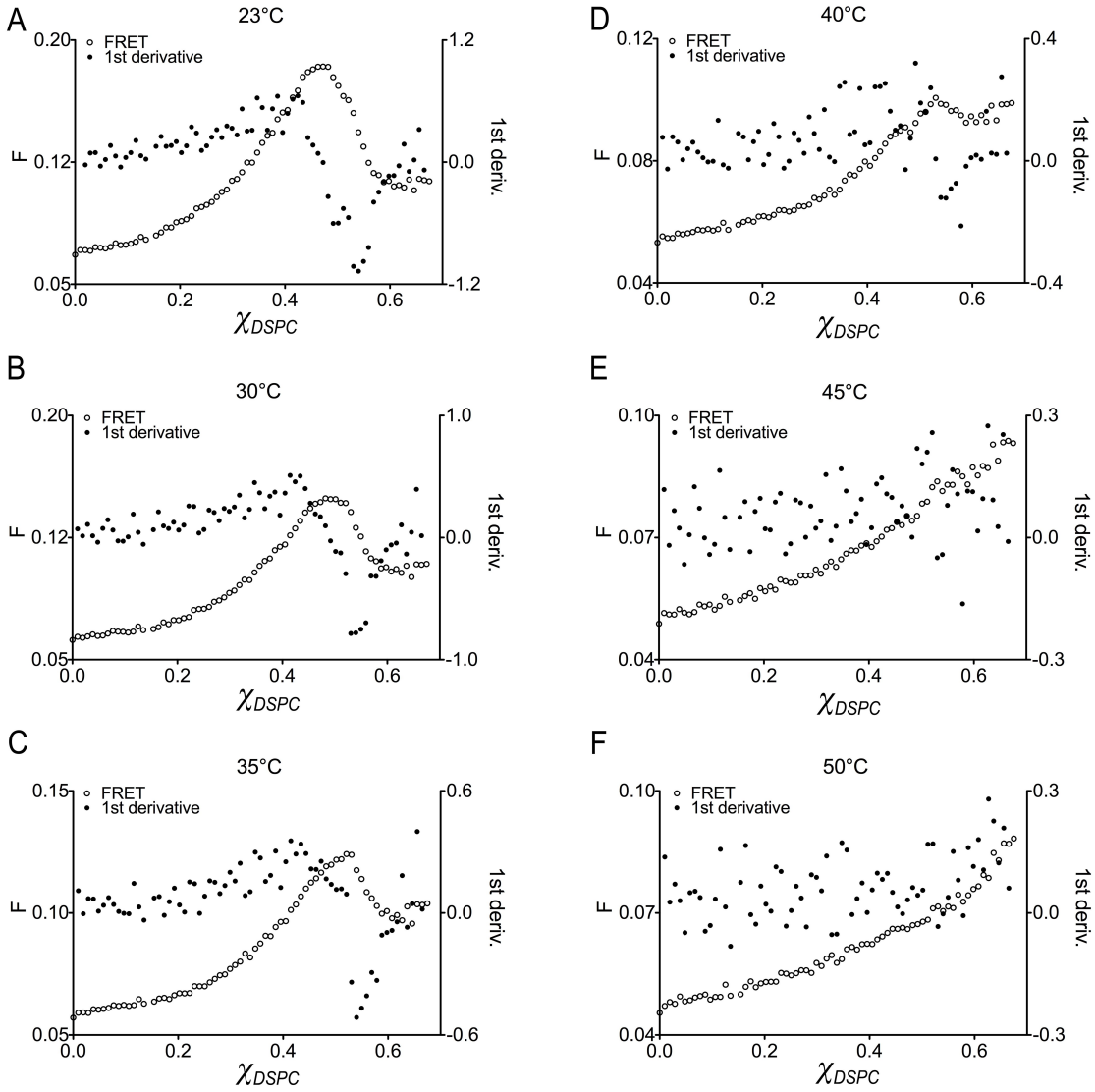

Figure 3.9 Disappearance of the enhanced FRET peak in Bodipy-C12:0-DiI at higher temperatures indicates miscibility. SP-FRET between Bodipy-PC and C12:0-DiI (open circles) and the first derivative of the FRET profile (solid circles) are plotted for temperatures 23°C to 50°C. The REE peak was detected from 23°C to 404 (A-D), barely detectable at 45°C (E), and not observed at 50°C (F).

To further our investigation on the thermal stability of modulated phase patterns on GUVs, we wanted to examine whether modulated phases are still reversible upon heating GUVs to complete miscibility, followed by immediate cooling to room temperature. When we heated individual GUVs on the microscope stage to ~50°C, we observed that the patterns disappeared (via wide-field fluorescence microscopy). Upon cooling the samples back to ~25°C in 15-20 min, we saw many GUVs displayed dispersed macroscopic round domains that looked like polka dots. This morphology is typical of macroscopic phase separation of liquid phases that are kinetically trapped.

To compare our *in situ* studies with bulk measurements on a larger population of GUVs, we heated freely suspended GUVs in eppendorf tubes to 50°C using a heating block, and cooled the samples close to room temperature before microscopy observations. Modulated phase patterns reappeared on 67% of the GUVs observed, while 21% looked uniform, and 12% displayed macroscopic round "polka-dotted" domains (Table 3.1). These observations are similar to the morphologies observed when GUVs were only heated to 35°C and cooled, suggesting that modulated phase patterns are reversible even when samples were heated to complete miscibility. The discrepancies between our *in situ* and bulk studies are discussed below.

3.5 Discussion

3.5.1 Temperature-dependent FRET reveals miscibility transition in the modulated phase regime

Using FRET, we have systematically investigated the effects of temperature on the phase behavior of mixtures that display modulated phase patterns on GUVs. Data

collection was performed at six different temperatures over a period of ~ five days on samples that were prepared on the same day; this indicates that modulated phases are stable for up to at least five days. Along a trajectory that goes through the Ld + Lo region at $\rho = 20\%$, both probe pairs reported FRET profiles that were characteristic of Ld and Lo phase coexistence up to $T < 45°C$. While phase boundaries cannot be determined from the DHE-Bodipy-PC FRET profiles at $T \geq 45°C$, an extremely shallow peak can still be deciphered from the Bodipy-PC-DiI profile at $T = 45°C$ (Fig. 3.5), which led us to deduce that the liquid immiscibility region ends at $45°C < T \leq 50°C$.

The robust behavior of the FRET pairs used in this study indicates that modulated phases behave just like genuine phases that are thermodynamically stable. Narrowing of the liquid immiscibility region at higher temperatures has been reported in many studies of ternary mixtures that consist of lipids with high Tm, low Tm, and cholesterol (14, 15, 17). In almost all of those studies, the miscibility transition temperature of the entire Ld + Lo region depends on the Tm of the high Tm lipid, probably due to the Lo phase being enriched with the saturated high Tm lipid. For example, the liquid miscibility transition temperature in SSM/DOPC/CHOL mixtures was found to be 46°C (17), where the Tm of SSM is 57°C (29). In a separate study, Veatch and Keller (30) revealed the miscibility transition of the Ld + Lo region in DPPC/DOPC/CHOL mixtures to be ~ 40°C, where the Tm of high-melting DPPC is 41°C . Our current study at $\rho = 20\%$ revealed that the liquid miscibility transition probably lies at $45°C < T \leq 50°C$, consistent with DSPC having a Tm of 55°C. In addition, a separate temperature-dependent FRET study conducted by Robin S.

Petruzielo along a tieline traversing the Ld + Lo region of DSPC/DOPC/CHOL also showed the miscibility transition occurring at ~50°C (personal communication). Altogether, this shows that modulated phases in DSPC/DOPC/POPC/CHOL possess coexisting Ld + Lo phases with properties that are akin to canonical macroscopic phase separation in ternary model membrane mixtures, where liquid miscibility transition is dependent on the melting temperature of the Lo phase.

3.5.2 FRET and GUV studies reveal nanoscopic domains at higher temperatures

We observed that GUVs that displayed modulated phase patterns looked uniform upon heating to ~ 35°C. The two possible explanations for this observation are: 1) the mixture is a single phase at 35°C, or 2) the mixture is still phase-separated but the domains are smaller than the diffraction limit. Using a FRET pair (DHE and Bodipy-PC) that segregates into different phases at the onset of the two-phase coexistence region, we were able to determine the phase boundaries along the trajectory at the various temperatures investigated. We observed narrowing of the Ld + Lo region towards higher DSPC content from 30°C to 40°C; compositions that are enriched in low T_m lipids become miscible at lower temperatures compared to compositions that are DSPC-rich. The composition of the GUVs that was examined in this study is Lo-rich, located on the far right of the trajectory, within the Ld + Lo region. At 35°C, this particular composition would still be phase-separated, according to our FRET results. Hence, this indicates that the GUVs examined contained nanoscopic domains at 35°C that were just not detected using conventional microscopy methods.

3.5.3 Reversibility of modulated phase patterns on GUVs

Upon quick heating to 35°C followed by immediate cooling (< 10 min) to room temperature, we observed that a mixed variety of morphologies would reappear on the surface of GUVs. This was true when the same individual GUVs were examined through the heat and cool cycle at the microscope stage, or when larger populations of GUVs were observed after they were heated and cooled separately in bulk. The reappearance of modulated phase patterns on the majority (~ 60%) of GUVs observed after a heat (35°C)/ cool cycle indicates thermodynamic stability of modulated phases, and suggests the possibility that nanoscopic domains could already be patterned. In addition, we observed a larger variety of patterns on GUVs that have been cycled through heating (35°C) and cooling, compared to the patterns before the temperature cycle, where stripes and bubble-like morphologies dominate in this particular composition (Table 3.2). This could be due to energetic degeneracy of the different types of patterns at a given composition. The ~22% of GUVs that looked uniform after heating (35°C) and cooling is probably the result of this particular composition (at $\rho = 20\%$), which is located at the beginning of a modulated phase window (Chapter 2). However, there is still ~ 15% of the GUVs observed that displayed dispersed macroscopic round (polka-dotted) domains. Two immediate explanations come to mind: 1) the brief temperature cycles caused the coexisting patterned domains to be kinetically trapped into polka-dotted macroscopic domains; 2) the domains on a small percentage of patterned GUVs were originally kinetically trapped, and then energetically released upon a brief heat/cool cycle to form dispersed round domains. The low line tension in mixtures that display modulated phases

requires an opposing long-range repulsion, probably originating from curvature energies-, to stabilize the domains. Due to the sensitivity of modulated phases to mechanical properties of the bilayer, the formation of patterned phases could be more strongly affected by kinetic processes compared to phase-separated mixtures in a high line tension regime. However, it is also entirely possible that the quick cooling (in <15 min) caused domains to be kinetically trapped, forming polka dots. For a more complete study on the thermodynamic stability of modulated phase patterns, the GUVs should be allowed to anneal at a slower rate after brief heating (and after initial observations on the microscope). If patterned domains reappear, then we can confirm that modulated phases are stable, and the polka dotted domains observed are indeed trapped states.

One additional factor that could also affect GUV domain morphology during the temperature cycles performed *in situ* on the microscope stage is adhesion effects on GUVs that were touching the glass cover slip. Indeed, contractile tension exerted onto GUVs adsorbed onto solid surfaces has been shown to affect both vesicle size and domain morphologies (31). This could explain the discrepancy between our *in situ* and bulk studies of heating GUVs to 50°C and subsequent cooling to room temperature. We observed that many GUVs displayed polka-dotted domains upon cooling on the microscope stage when they are in contact with a glass surface. However, when this experiment was performed on freely suspended GUVs (in an eppendorf tube), more GUVs with modulated phase patterns were observed upon fast cooling from ~ 50°C (Table 3.1). These observations suggest that when starting from one-phase lipid mixtures at elevated temperatures, the formation of modulated phases

upon rapid cooling could be strongly affected by external effects, such as glass adhesion, which could result in kinetic trapping of domains. Trapped coarsening of domains could occur due to coupling between membrane mechanical properties (such as elasticity and bending moduli), vesicle shape, and phase separation (32). Surface adhesion could very well perturb vesicle shape, which could directly influence the morphologies of phase-separated domains. Furthermore, Amazon *et al.* (19) demonstrated previously that the bending energy arising from the difference in bending moduli between coexisting liquid phases could compete with line tension to stabilize modulated phase patterns. Hence, any perturbations that could affect curvature energies of GUVs could influence domain morphology. For example, changes in the osmotic gradient across bilayers could affect the formation of patterned domains; this effect could be amplified in GUVs at elevated temperatures that are rapidly cooled while some areas of the vesicles are in contact with a glass surface. More sophisticated studies using some form of tethering method could be conducted to examine the true effects of temperature on modulated phase patterns *in situ*.

3.6 Conclusion

Modulated phases within the Ld + Lo volume of the four-component DSPC/DOPC/POPC/CHOL system can be obtained by tuning the concentrations of the low T_m lipids, DOPC and POPC (Chapter 2). In this study, we investigated the effects of temperature on the stability of modulated phase patterns on GUVs. We find a switch in phase morphologies on GUVs upon heating to ~35°C, where patterns disappeared. Systematic FRET studies along a tieline at $\rho = 20\%$ revealed that

coexisting Ld + Lo domains persist up to ~45°C, and that the miscibility transition of the Ld + Lo region (at ρ= 20%) lies at 45°C < T ≤ 50°C. This shows that modulated phases are stable states of matter that can be examined using SP-FRET at elevated temperatures. Coupled with GUV observations, we conclude that a transition into the nanoscopic regime occurs at ~35°C at the GUV composition that was examined in this study.

The thermodynamic nature of modulated phase patterns was also examined by performing brief temperature cycles on GUVs. We found that the phase patterns were somewhat reversible upon taking GUVs through temperature cycles up to 35°C or 50°C, although a small percentage of GUVs that displayed macroscopic polka dots morphologies upon cooling led us to believe that kinetics could be more strongly involved in the formation of modulated phase patterns. In addition, we also do not discount the possibility of osmotic gradient changes that might have occurred during the temperature cycles, which could have affect the formation of modulated phase patterns by affecting membrane elasticity and shape. The discrepancies in the results of our *in situ* and bulk studies for the 50°C temperature cycle also imply that adhesion effects of the glass surface (from the cover slip) onto GUVs could strongly affect formation of modulated phase patterns.

3.7 Future Directions

This study provides the basis for further temperature-dependent studies on the modulated phase regime using FRET and fluorescence microscopy of GUVs. A more complete map of the miscibility transition region in the entire Ld + Lo volume of

DSPC/DOPC/POPC/CHOL can be obtained using SP-FRET, utilizing the same probes (DHE, Bodipy-PC, C12:0-DiI). Specifically, temperature-dependent FRET data can be collected for the same tieline used in this study, but at each 10% ρ−increment. In addition, a different (shorter) tieline at higher cholesterol concentrations within the Ld + Lo region at various ρ values should also be explored.

A miscibility transition map obtained from FRET studies can be useful for guiding GUV studies. So far, we have only explored the temperature effects on the reversibility of modulated phase patterns on an Lo-rich composition, where complete miscibility of mixtures occur at high temperature (close to 50°C). It would be interesting to compare temperature cycling effects on Ld-rich compositions along the same tieline, and also on compositions on a higher cholesterol-tieline that have a broader modulated phase window (Chapter 2). For all temperature cycling studies, where GUVs are heated to an elevated temperature and cooled subsequently in a short time period, bulk studies on large population of GUVs can be done. However, a more elegant study would involve *in situ* examination of the same tethered GUVs through a temperature cycle.

To prevent possible strong adhesion effects on the formation of modulated phases, the vesicles would have to be tethered in some way so that direct contact with the glass surface is minimized. Biotin-avidin linkages are strong bonds that have been used successfully to tether small unilamellar vesicles to a glass surface in single molecule studies (32). Various types of biotinylated molecules such as biotin-BSA, biotin-PEG, and biotinylated-PE are commercially available. While the tools are available for tethering studies, it is actually a non-trivial task to successfully tether a

GUV without affecting its lipid mixing properties. We have done preliminary studies using GUVs doped with very small amounts of biotinylated-PE, and tethering molecules such as biotin-BSA, biotin-PEG, neutravidin, and streptavidin. Mixed results were obtained, mainly due to the inconsistency in coating glass cover slips with biotinylated molecules, which can lead to over- or under-pinning of GUVs to the treated surface, distortion of vesicle shape, and ultimately, perturbation to modulated phase patterns. In fact, biotin-avidin tethering of GUVs has been shown recently to influence macroscopic phase behavior of ternary model membrane mixtures (33). In addition to tethering, another possible method of immobilizing GUVs while preventing direct glass contact could involve entrapping the vesicles in a matrix. One could imagine the choice of matrix being crucial, for both temperature studies and for preserving the phase behavior on the GUVs. A recent study reported successful entrapment of GUVs in a porous matrix consisted of silica glasses (34). However the entrapment did cause perturbations to membrane properties, such as phase behavior, vesicle shape, and bilayer hydration. While *in situ* examination of temperature effects on modulated phase patterns is more superior to bulk studies, extreme care must be taken to develop tethering or entrapment methods that would not perturb the sensitive modulated phase patterns on GUVs.

We have shown that tuning DOPC/POPC ratios (ρ) allows the control of domain size and morphology from the nanoscopic to the macroscopic regime within the Ld + Lo region of DSPC/DOPC/POPC/CHOL mixtures. A detailed description of how temperature governs the nano-to-macro transition and the evolution of domain morphologies would complement the known composition-dependence studies.

References

1. Seul, M., and D. Andelman. 1995. Domain shapes and patterns: the phenomenology of modulated phases. Science. 267: 476–483.

2. Keller, S.L., and H. McConnell. 1999. Stripe Phases in Lipid Monolayers near a Miscibility Critical Point. Phys. Rev. Lett. 82: 1602–1605.

3. Kaizuka, Y., and J.T. Groves. 2010. Bending-mediated superstructural organizations in phase-separated lipid membranes. New J. Phys. 12: 095001.

4. Konyakhina, T.M., S.L. Goh, J. Amazon, F.A. Heberle, J. Wu, et al. 2011. Control of a Nanoscopic-to-Macroscopic Transition: Modulated Phases in Four-Component DSPC/DOPC/POPC/Chol Giant Unilamellar Vesicles. Biophys. J. 101: L8–L10.

5. Semrau, S., T. Idema, T. Schmidt, and C. Storm. 2009. Membrane-mediated interactions measured using membrane domains. Biophys. J. 96: 4906–4915.

6. Baumgart, T., S.T. Hess, and W.W. Webb. 2003. Imaging coexisting fluid domains in biomembrane models coupling curvature and line tension. Nature. 425: 821–824.

7. Hu, J., T. Weikl, and R. Lipowsky. 2011. Vesicles with multiple membrane domains. Soft Matter. 7: 6092.

8. Funkhouser, C.M., F.J. Solis, and K. Thornton. 2010. Dynamics of two-phase lipid vesicles: effects of mechanical properties on morphology evolution. Soft Matter.

9. Spurlin, T.A., and A.A. Gewirth. 2007. Charge dependence of a nanoscale supercrystal phase in a supported lipid bilayer. J. Am. Chem. Soc. 129: 11906–11907.

10. Negishi, M., H. Kitahata, and K. Yoshikawa. 2009. Emergence of superstructures from a homogeneous lipid sphere. J. Phys. Chem. B. 113: 3264–3268.

11. Ayuyan, A.G., and F.S. Cohen. 2006. Lipid Peroxides Promote Large Rafts: Effects of Excitation of Probes in Fluorescence Microscopy and Electrochemical Reactions during Vesicle Formation. Biophys. J. 91: 2172–2183.

12. Zhao, J., J. Wu, H. Shao, F. Kong, N. Jain, et al. 2007. Phase studies of model biomembranes: Macroscopic coexistence of Lα+Lβ, with light-induced coexistence of Lα+Lo Phases. Biochimica et Biophysica Acta (BBA) - Biomembranes. 1768: 2777–2786.

13. Morales-Penningston, N.F., J. Wu, E.R. Farkas, S.L. Goh, T.M. Konyakhina, et al. 2010. GUV preparation and imaging: minimizing artifacts. Biochim. Biophys. Acta. 1798: 1324–1332.

14. Veatch, S.L., and S.L. Keller. 2003. Separation of liquid phases in giant vesicles of ternary mixtures of phospholipids and cholesterol. Biophysj. 85: 3074–3083.

15. Buboltz, J.T., C. Bwalya, K. Williams, and M. Schutzer. 2007. High-Resolution Mapping of Phase Behavior in a Ternary Lipid Mixture: Do Lipid−Raft Phase Boundaries Depend on the Sample Preparation Procedure? Langmuir. 23: 11968–11971.

16. Veatch, S., and S. Keller. 2005. Miscibility Phase Diagrams of Giant Vesicles Containing Sphingomyelin. Phys. Rev. Lett. 94.

17. Farkas, E.R., and W.W. Webb. 2010. Precise and millidegree stable temperature control for fluorescence imaging: application to phase transitions in lipid membranes. Rev. Sci. Instrum. 81: 093704.

18. Veatch, S.L., K. Gawrisch, and S.L. Keller. 2006. Closed-loop miscibility gap and quantitative tie-lines in ternary membranes containing diphytanoyl PC. Biophysj. 90: 4428–4436.

19. Amazon, J.J., S.L. Goh, and G.W. Feigenson. 2013. Competition between line tension and curvature stabilizes modulated phase patterns on the surface of giant unilamellar vesicles. A simulation study. Phys. Rev. E Stat. Nonlin. Soft Matter Phys. In press.

20. Kingsley, P.B., and G.W. Feigenson. 1979. Synthesis of a Perdeuterated Phospholipid - 1,2-Dimyristoyl-Sn-Glycero-3-Phosphocholine-D72. Chemistry and Physics of Lipids. 24: 135–147.

21. Heberle, F.A., J. Wu, S.L. Goh, R.S. Petruzielo, and G.W. Feigenson. 2010. Comparison of three ternary lipid bilayer mixtures: FRET and ESR reveal nanodomains. Biophys. J. 99: 3309–3318.

22. Buboltz, J.T., and G.W. Feigenson. 1999. A novel strategy for the preparation of liposomes: rapid solvent exchange. Biochim. Biophys. Acta. 1417: 232–245.

23. Feigenson, G.W., and J. Buboltz. 2001. Ternary phase diagram of dipalmitoyl-PC/dilauroyl-PC/cholesterol: Nanoscopic domain formation driven by cholesterol. Biophys. J. 80: 2775–2788.

24. Brown, A.C., K.B. Towles, and S.P. Wrenn. 2007. Measuring Raft Size as a Function of Membrane Composition in PC-Based Systems: Part II Ternary Systems. Langmuir. 23: 11188–11196.

25. Silvius, J.R. 2003. Fluorescence energy transfer reveals microdomain formation at physiological temperatures in lipid mixtures modeling the outer leaflet of the plasma membrane. Biophysj. 85: 1034–1045.

26. Silvius, J.R., and I.R. Nabi. 2006. Fluorescence-quenching and resonance energy transfer studies of lipid microdomains in model and biological membranes. Mol. Membr. Biol. 23: 5–16.

27. Sengupta, P., D. Holowka, and B. Baird. 2007. Fluorescence Resonance Energy Transfer between Lipid Probes Detects Nanoscopic Heterogeneity in the Plasma Membrane of Live Cells. Biophys. J. 92: 3564–3574.

28. Sharma, P., R. Varma, R.C. Sarasij, Ira, K. Gousset, et al. 2004. Nanoscale organization of multiple GPI-anchored proteins in living cell membranes. Cell. 116: 577–589.

29. Estep, T.N., W.I. Calhoun, Y. Barenholz, R.L. Biltonen, G.G. Shipley, et al. 1980. Evidence for metastability in stearoylphingomyelin bilayers. Biochemistry. 19: 20–24.

30. Veatch, S.L., O. Soubias, S.L. Keller, and K. Gawrisch. 2007. Critical fluctuations in domain-forming lipid mixtures. Proc. Natl. Acad. Sci. U.S.A. 104: 17650–17655.

31. Rozovsky, S., Y. Kaizuka, and J.T. Groves. 2005. Formation and Spatio-Temporal Evolution of Periodic Structures in Lipid Bilayers. J. Am. Chem. Soc. 127: 36–37.

32. Yanagisawa, M., M. Imai, T. Masui, S. Komura, and T. Ohta. 2007. Growth dynamics of domains in ternary fluid vesicles. Biophysj. 92: 115–125.

33. Benítez, J.J., A.M. Keller, and P. Chen. 2010. Nanovesicle trapping for studying weak protein interactions by single-molecule FRET. Meth. Enzymol. 472: 41–60.

34. Sarmento, M.J., M. Prieto, and F. Fernandes. 2012. Reorganization of lipid domain distribution in giant unilamellar vesicles upon immobilization with different membrane tethers. Biochim. Biophys. Acta. 1818: 2605–2615.

35. Esquembre, R., S.N. Pinto, J.A. Poveda, M. Prieto, and C.R. Mateo. 2012. Immobilization and characterization of giant unilamellar vesicles (GUVs) within porous silica glasses. Soft Matter. 8: 408–417.

CHAPTER 4

Versatile membrane deformation potential of activated pacsin[§]

4.1 Abstract

Endocytosis is a fundamental process in signaling and membrane trafficking. The formation of vesicles at the plasma membrane is mediated by the G protein dynamin that catalyzes the final fission step, the actin cytoskeleton, and proteins that sense or induce membrane curvature. One such protein, the F-BAR domain-containing protein pacsin, contributes to this process and has been shown to induce a spectrum of membrane morphologies, including tubules and tube constrictions in vitro. Full-length pacsin isoform 1 (pacsin-1) has reduced activity compared to its isolated F-BAR domain, implicating an inhibitory role for its C-terminal SH3 domain. Here we show that the autoinhibitory, intramolecular interactions in pacsin-1 can be released upon binding to the entire proline-rich domain (PRD) of dynamin-1, resulting in potent membrane deformation activity that is distinct from the isolated F-BAR domain. Most strikingly, we observe the generation of small, homogenous vesicles with the activated protein complex under certain experimental conditions. In addition, liposomes prepared with different methods yield distinct membrane deformation morphologies of BAR domain proteins and apparent activation barriers to pacsin-1's activity.

[§] The following sections are reproduced from: Goh, S.L.,[1] Wang, Q.,[1] Byrnes, L.J., and Sondermann, H. 2012. Versatile membrane deformation potential of activated pacsin. PLoS ONE 7(12): e51628. doi:10.1371/ journal.pone.0051628 ([1]co-first authors), with modifications to conform to the required format. S.L.G., Q.W., and L.J.B. performed initial preliminary experiments. Q.W. performed SAXS and pacsin isoform experiments, analyzed SAXS data, and performed theoretical calculations. S.L.G. performed all remaining experiments. S.L.G., Q.W., and L.J.B. analyzed data.

Theoretical free energy calculations suggest bimodality of the protein-membrane system as a possible source for the different outcomes, which could account for the coexistence of energetically equivalent membrane structures induced by BAR domain-containing proteins in vitro. Taken together, our results suggest a versatile role for pacsin-1 in sculpting cellular membranes that is likely dependent both on protein structure and membrane properties.

4.2 Introduction

Local differences and dynamic changes in curvature are hallmarks of cellular membranes, contributing to the identity of organelles and to mechanisms in membrane trafficking and signaling (1). Peripheral and integral membrane proteins have been identified that either promote or stabilize membrane curvature at different locations in the cell. For example, endocytosis relies on the coordinated interplay of coat and adaptor proteins to initiate the formation and stabilization of a bud-neck structure, followed by the recruitment of the large G protein dynamin and subsequent fission (2-6). In addition, reorganization of the actin cytoskeleton via the recruitment and activation of Wiskott-Alrich Syndrome proteins (WASP) provides another driving force in this process (7, 8).

Proteins containing a BAR domain have emerged as facilitators of membrane trafficking and fission by directly stabilizing tubular membrane structures *in vitro* and in cells (9-11). They can be divided into three distinct structural classes based on their deformation activity and structures: BAR and N-BAR domain-containing proteins (e.g. endophilin, amphiphysin, sorting nexin 9, and APPL1) prefer highly curved

membranes; F-BAR domain-containing proteins (e.g. CIP4, FCHo2, pacsin/syndapin) are often associated with wider tubules; and inverse or I-BAR domain-containing proteins (e.g. IRSp53; MIM) induce membrane invaginations (10, 12-16). The BAR domain fold consists of three helices that form a six-helix bundle in a dimeric assembly, the predominant quaternary structure in solution (13). The preference for distinct membrane curvatures is partially encoded in the particular folds of the different subfamilies. The dimeric BAR domains resemble an overall crescent shape. N-BAR and F-BAR domains have a concave surface lined with positively charged residues and other motifs involved in membrane interactions (13, 17-20). The intrinsic curvature of N-BAR domains is higher than that of F-BAR domains characterized to date, and the lower degree of curvature of the latter often matches their preference for wider membrane tubules (21-23). In contrast, the convex surface in I-BAR proteins mediates membrane interactions and promotes filopodia formation (24). The most recent member of the I-BAR family, Pinkbar, is a unique case of a rather flat dimer that prefers flat membrane supports (25).

Recently, some exceptions to these correlations have been reported for F-BAR domain-containing proteins. In addition to its canonical function of stabilizing wide tubules, the F-BAR domain of FCHo2 also facilitates the formation of tubules with high curvature (2, 22). srGAP2, a protein involved in neuronal migration and morphogenesis, contains an F-BAR domain based on its primary sequence, yet induces I-BAR-like membrane protrusions (26). Another example is pacsin, also known as syndapin, which has been shown to induce a wide range of membrane deformations, including membrane tubules of various diameters, pearling structures

and invaginations (27-29). Structural and functional analyses revealed multiple features that may contribute to pacsin's unique morphogenetic potential (27-31), especially the finding that its F-BAR domain adopts a distinct lateral curvature in addition to its concave surface (Fig. 4.1 *A*). These geometric constraints may contribute to the variability in pacsin-induced membrane morphologies and its potential to form different types of higher-order lattices on lipid bilayers (27). Another striking feature is a short loop within helix 2 that forms an amphipathic wedge, proposed to dip into the acyl chain layer of one bilayer leaflet (Fig. 4.1 *A*) (27-31). Indeed, insertion of amphipathic helices or loops has been identified as one of the main forces in the generation of membrane curvature (17, 32, 33). Other factors that may contribute to this activity include protein oligomerization and electrostatic interactions of the curved protein scaffold with the membrane (21, 23, 27, 34, 35).

Three isoforms of pacsin are found in mammals, with expression levels being tissue-specific: pacsin-1 is enriched in neurons, pacsin-2 is ubiquitously expressed, and pacsin-3 is found mainly in muscle (36). All three isoforms contain a conserved C-terminal SH3 domain that interacts with the PRD of several proteins, including those of dynamin and WASP, providing a link between endocytosis and the cytoskeleton (8, 36-39). SH3 domain-mediated activation of neural WASP (N-WASP) is required for regulating actin polymerization, which is essential for proper neuromorphogenesis and cellular motility (30, 39). On a cellular level, pacsin contributes to clathrin-dependent endocytosis and the recycling of synaptic vesicles via its SH3 domain engagement with dynamin's PRD. The pacsin-dynamin interaction is especially important during high neuronal activity, where the complex has been

implicated in clathrin-independent pathways of synaptic vesicle retrieval (40-42). In addition to the SH3 domain, a recent study revealed two phosphorylation sites within the F-BAR domain of pacsin-1 that can regulate its membrane sculpting potential, providing another means of pacsin-1 regulation in cells (43).

The PRD is a non-catalytic domain of dynamin located at the C-terminus of the G protein. In addition to interacting with SH3 domain-containing proteins, which targets dynamin to endocytotic sites (44-46), the PRD is also important for the self-assembly and self-activation of dynamin (47). Being the most divergent region among the three dynamin isoforms, the PRD confers isoform-specific functions. Recent studies have shown that the PRD is responsible for differential self-assembly propensities and coated pit localization in an isoform-specific manner, providing tissue-specific regulation (48-51). On a molecular level, the PRD binds to SH3 domain proteins via core PxxP motifs that are usually flanked by basic residues on one or both sides (46, 52).

Recently, we reported that pacsin-1 is autoinhibited *in vitro* (27), which is consistent with the suppressed activity of its fruit fly paralog *in vivo* (38). Both studies identified the SH3 domain as an autoinhibitory feature. Based on small-angle X-ray scattering (SAXS) experiments, we proposed a compact structure for pacsin-1, in which the SH3 domains fold back onto the F-BAR dimer (Fig. 4.1 *B*) (27). Confirmation of such a model came from the crystal structure of full-length pacsin-1, validated by mutagenesis and peptide competition studies that revealed increased tubulation activity upon dislodging pacsin's SH3 domain from the F-BAR domain dimer (28).

Here, we report pacsin-1's membrane deformation ability in the presence of the full-length PRD of dynamin-1 *in vitro*, and demonstrate a role for the polybasic PRD in modulating the sculpting potential of pacsin-1. While we observed membrane tubules under certain experimental conditions, consistent with previous results, we also noted vesicle formation as a dominant feature using standard liposome preparation methods. A similar observation was made with full-length endophilin bound to the entire PRD, suggesting a more general mechanism by which membrane scaffolding and insertion mechanism could directly facilitate fission. We also reveal that membrane properties of the liposomes play an influential role in the curvature generating activities of pacsin-1. Such a notion is supported by pacsin-1's variable membrane deformation potential with liposomes prepared following different protocols, which further highlights bimodality in the protein-membrane system, and pacsin-1's potential versatility in generating or reacting to membrane curvature during membrane trafficking.

4.3 Materials and Methods

4.3.1 Protein expression and purification

Human, full-length pacsin isoforms 1-3, pacsin-1$^{F\text{-}BAR}$ (residues 1-325), pacsin-2$^{F\text{-}BAR}$ (residues 1-324), pacsin-3$^{F\text{-}BAR}$ (residues 1-322), pacsin-1^{P437L} and mouse full-length endophilin-A1 and endophilin$^{N\text{-}BAR}$ (residues 1-256) were produced following standard molecular biology and liquid chromatography techniques. The coding regions of the pacsin and endophilin constructs described above were amplified

by standard PCR and cloned into a modified pET28a expression plasmid (Novagen) yielding N-terminally hexahistidine-tagged SUMO fusion proteins. The hexahistidine-tagged SUMO-moiety was cleavable by addition of the protease Ulp-1 from *S. cerevisiae*. Proteins were expressed and purified as described previously (27, 35).

Mouse dynamin-1 PRD (residues 747-842) in the expression vector pGEX-6P-1 was kindly provided by the De Camilli laboratory (Yale University). Truncation mutants (GST-PRD^{trunc1} and GST-PRD^{trunc2}) were generated by amplifying the corresponding regions by standard PCR. Point mutants were produced using site-directed mutagenesis (Stratagene Quikchange). All PRD constructs were expressed and purified as GST fusion proteins (resin: GSTrap, GE Healthcare), following the manufacturer's instructions. GST fusion proteins were subjected to size exclusion chromatography on a Superdex 200 column (GE Healthcare) equilibrated in gel filtration buffer (25 mM Tris- HCl, pH 7.5, 150 mM NaCl). Proteins were concentrated in a Centricon ultrafiltration device (10 kDa cutoff; Millipore) to a final concentration of ~0.5-1 mM (~25-50 mg/ml). Protein aliquots were frozen in liquid nitrogen and stored at -80°C.

4.3.2 Liposome preparation via the freeze/thaw method (FT)

Folch fraction I lipids (Sigma) were dissolved in chloroform and stored at -20°C. Appropriate amounts of lipids were dispensed into glass tubes, followed by evaporation of chloroform under a stream of nitrogen gas until a film was formed. Samples were subjected to high vacuum to remove residual organic solvent (final gauge reading ~35 mTorr). The dry lipid film was resuspended in buffer (25 mM Tris-HCl, pH 7.5, 50 mM NaCl) to a concentration of 2-10 mg/ml by alternate vortexing

and short incubations in a 45°C water bath. Finally, the hydrated liposomes were subjected to five freeze-thaw cycles using liquid nitrogen.

4.3.3 Liposome preparation via the sonication/freeze-thaw method (SFT).

Hydrated liposomes resuspended from dried film (as described above) were sonicated to clarity in a bath sonicator (Laboratory Supplies Co., Inc), followed by 8-10 freeze-thaw cycles using liquid nitrogen. Liposomes were incubated at 30°C for 1 hour before use in negative stain EM or liposome co-pelleting experiments.

4.3.4 Liposome preparation via the rapid solvent exchange method (RSE)

Liposomes were prepared according to procedures described in Buboltz and Feigenson (53), and modified as previously described (54). Briefly, lipids in chloroform solution were dispensed into glass tubes. After the addition of buffer (25 mM Tris-HCl, pH 7.5, 50 mM NaCl), the mixture was vortexed under vacuum for one minute and then sealed under argon gas, yielding 2-10 mg/mL hydrated liposomes for negative-stain EM or liposome co-pelleting experiments.

4.3.5 Liposome extrusion

Hydrated liposomes prepared from either the FT or RSE method were extruded 21-41 times through polycarbonate filters of pore sizes ranging from 100 nm to 1000 nm (Avestin, Inc). Extruded liposomes were used on the day of extrusion.

4.3.6 Dynamic Light Scattering (DLS)

Size distributions of various liposome preparations (0.5 mg/ml) were measured using dynamic light scattering on a Malvern Zetasizer Nano-ZS. A minimum of three measurements were made per sample. The mean liposome size for each extrusion preparation was calculated from the frequency distribution curve as:

$$Mean = \int xP(x)dx \equiv \bar{x}$$

The skewness of the each distribution was analyzed as:

$$Skew = \int \left(\frac{x - \bar{x}}{\sigma} \right)^3 P(x)dx$$

where σ is the standard deviation of the distribution. The skew value becomes increasingly positive for filter pore sizes ≥400 nm, indicating a broader size distribution containing larger liposomes. Based on the average skewness calculated for each extrusion preparation, representative distribution curves are shown (see Fig. 4.15).

4.3.7 Liposome co-pelleting assay

Equal volumes of liposomes (0.5 mg/ml) and proteins (5-10 μM) were incubated in 40 μl low salt buffer for 20 min at room temperature. Samples were centrifuged in an Optima MAX-E ultracentrifuge (Beckman) equipped with a TLA-100 rotor at 87,000 rpm at 4°C for 1 hour. After carefully removing supernatant, pellets were resuspended in 40 μl low salt buffer, and both fractions were analyzed by SDS-PAGE. Gels were stained with SYPRO Ruby (Sigma) and quantified using Image J.

4.3.8 Liposome flotation assay

100 nm-extruded liposomes (8 mg/ml) and proteins (8-15 μM) were incubated in 25 μl low salt buffer (25 mM Tris-Cl, pH7.5, 50 mM NaCl) for 20 min at room temperature. 75 μl of 70% (w/v) sucrose that was prepared in the same buffer was added to each reaction. After mixing, 80 μl of the mixture was placed at the bottom of a 250 μl ultracentrifuge tube. This was then overlaid with 90 μl of 40% (w/v) sucrose,

and 40 µl of 4% (w/v) sucrose. Samples were centrifuged in an Optima MAX-E ultracentrifuge (Beckman) equipped with a TLA-100 rotor at 87,000 rpm at 4°C for 1 hour. After centrifugation, 7 x 30 µl fractions were then carefully removed from the top to the bottom of each tube and analyzed by SDS-PAGE. Gels were stained with SYPRO Ruby (Sigma) and quantified in Image J. Proteins or protein complexes found in the top three fractions were indicated as membrane bound.

4.3.9 Negative Staining Electron Microscopy (EM)

Liposomes (1 mg/ml) made from Folch fraction I (bovine) brain lipids (Sigma) or synthetic lipids (27.5/27.5/45 = POPC/POPE/POPS, Avanti Polar Lipids, Inc.) were incubated in the presence or absence of proteins (5-10 µM, unless indicated otherwise) in low salt buffer for 5 min at room temperature. The sample was applied to a carbon-formvar-coated copper grid (Electron Microscopy Sciences) and incubated for two minutes. Excess liquid was carefully removed by blotting with a wet Kimwipe (Kimberly-Clark). The grids were stained three times with 6 µl of 2% filtered uranyl acetate solution, blotted immediately after each stain application. Samples were air-dried before imaging. Membrane morphologies were examined on a FEI Morgagni Transmission Electron Microscope with the electron energy set to 80 kV. Representative images were taken on an AMT camera with a direct magnification of 18kx-44kx. Liposome size measurements and quantitation of vesicle size distributions were performed using ImageJ.

4.3.10 GST pull-down experiments

50 µl pre-packed GST resin (GST SpinTrap, GE Healthcare) was washed with binding buffer (25 mM Tris-Cl, pH7.5, 100 mM NaCl). Various purified GST-PRD

recombinant proteins were incubated with the resin for 1 hour at 4°C with gentle rocking. Excess unbound proteins were removed by centrifuging for 30 s at 100 *g*. The resin was then washed 5 times with binding buffer. Various purified pacsin-1 "prey" proteins were then incubated with the resin for 2h at 4°C with gentle rocking. Unbound proteins were removed via centrifugation and the resin was washed 5 times. Finally, all proteins were eluted from the resin with elution buffer (10mM glutathione, 25 mM Tris-Cl, pH 7.5, 100 mM NaCl) after 10 min incubation.

4.4 Results

4.4.1 Pacsin isoforms have different levels of membrane sculpting activity

Previously, we and others reported an SH3-dependent autoinhibition mechanism for the brain-specific pacsin-1 (27, 28, 38). We have now extended the analysis to the other two human isoforms, pacsin-2 and 3. The purified, isolated F-BAR domains or full-length proteins were incubated with liposomes made from Folch (I) brain lipids following a standard sonication/freeze-thaw protocol, followed by visualization via negative-stain transmission electron microscopy (EM). As previously observed, the F-BAR domain of pacsin-1 (pacsin-$1^{F\text{-}BAR}$) produced three distinct membrane morphologies under these conditions (Fig. 4.1 *C*): wide tubules (open triangle), narrow tubules (dashed arrow) and pearling or beads-on-a-string structures (solid arrows). Similar narrow tubules, but with slightly larger diameter, have been noted in reactions with another F-BAR domain protein FCHo2, and have been attributed to residues predicted to mediate membrane interactions not lining up perfectly with the concave surface of the F-BAR domain (2, 22). Such a mismatch is also the case for pacsin's F-

BAR domain, and the pearling structures may represent an extreme case also driven by insertion of the wedge loop. In contrast, full-length pacsin-1 showed markedly reduced membrane deformation activity (Fig. 4.1 *C*) (27).

A reduction of the membrane deformation potential of pacsin-1 can be achieved when the isolated SH3 domain was added to the F-BAR domain in trans (unpublished data), supporting the proposed model in which the SH3 domain binds to the F-BAR domain and reduces its activity (27, 28). In fact, the molecular dimensions (R_g, D_{max}) computed based on a full-length pacsin-1 crystal structure (28) closely resemble those based on small-angle X-ray scattering (27), demonstrating that the compact, autoinhibited conformation of pacsin-1 observed in the crystalline state also dominates in solution (Fig. 4.1 *B*). While the SAXS-based, low-resolution structural model of autoinhibited pacsin-1 was consistent with a compact conformation seen in the crystal structure, the SAXS-based model suggests an alternative binding site of the SH3 domain on the F-BAR domain dimer (*circles* in Fig. 4.1 *B*) (27). This observation could indicate multiple docking positions for the SH3 domain on the F-BAR domain, consistent with the variability observed in the crystal structures (28).

While the F-BAR domain of pacsin-2 and 3 produced similar membrane morphologies under these conditions, the autoinhibition of the full-length proteins appeared to be different from that of pacsin-1 (Fig. 4.1 *C*). Full-length pacsin-2 was still able to generate wide tubules, but its vesiculation ability was observed to be impaired. On the other hand, the autoinhibition of full-length pacsin-3 appeared to be less pronounced or absent, even. A minor but noticeable difference in these

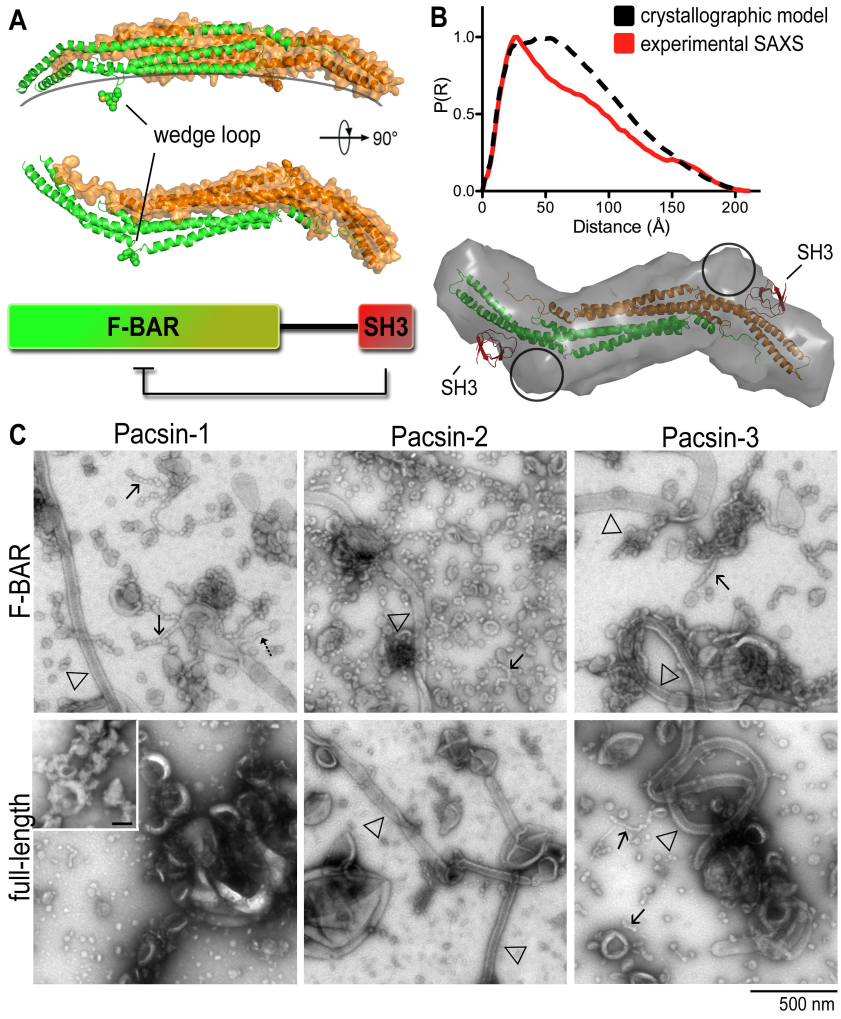

Figure 4.1 Membrane deformation by human pacsin isoforms. (A) Domain organization and structure of pacsin-1. The structure shows a F-BAR domain dimer with the protomers shown in green and orange, respectively. (B) SAXS-based comparison of full-length pacsin-1 in solution and in crystals. Distant distribution functions, Rg and Dmax values were determined based on the full-length crystal structure (28) and the solution scattering data (27). R_g/D_{max} (crystal)=212/60 Å; R_g/D_{max} (SAXS)=215/58 Å. Discrepancies between the respective distance distribution functions can be explained by the flexible linkers that connect the F-BAR and SH3 domains and were not modeled in the crystal structures. (C) Negative-stain electron micrographs. The membrane deformation potential of human pacsin isoforms and their isolated F-BAR domains was monitored by EM. Folch fraction I liposomes were incubated with purified proteins (5-10 μM), and processed as described in Materials and Methods. Arrows indicate specific membrane morphologies (solid arrows, pearling structures; dashed arrows, narrow tubules; open triangles, wide tubules). Inset shows liposome-only control; scale bar, 100 nm. Experiments in this figure performed by Q.W.

micrographs is the absence of the narrow tubules that were observed with the F-BAR domain of pacsin-1 and FCHo2. A potential explanation may involve variations in the degree of lateral curvature and/or flexibility of the distal tips within the F-BAR domain of pacsin-1 and 2, as suggested by a recent crystallographic analysis of different pacsin isoforms (31). Considering the high sequence divergence in the linker regions and the high degree of conservation of the F-BAR and SH3 domains, the nature of the linker segment may also contribute to the different morphogenic potential and degree of autoregulation among the isoforms.

4.4.2 Activation of full-length pacsin-1 by dynamin-1 PRD

The SH3 domain of pacsin binds to the PRD of proteins involved in endocytosis such as dynamin, synaptojanin and WASP/N-WASP (55, 56). Incubation of pacsin-1 with a minimal PRD peptide from dynamin increases its tubulation activity *in vitro* (28), indicating that PRD-SH3 domain interactions relieve the intra-molecular, autoinhibited conformation in full-length pacsin-1, likely by releasing the SH3 domains from the F-BAR dimer. The previous studies were conducted with a minimal peptide of the PRD that has reduced affinity for pacsin compared to the entire PRD (28). Here, we used the full-length PRD of dynamin-1 that includes the full binding sequence (Fig. 4.2 *A*) (52). In addition, liposomes were prepared either with Folch (I) lipids or with a synthetic lipid mixture that have properties resembling the lipid composition in the inner leaflet of the plasma membrane (57, 58). Liposomes were incubated with full-length pacsin-1 in the presence or absence of dynamin-1 PRD fused to GST (GST-PRD). As a control, the isolated GST moiety was co-incubated with pacsin-1 and liposomes.

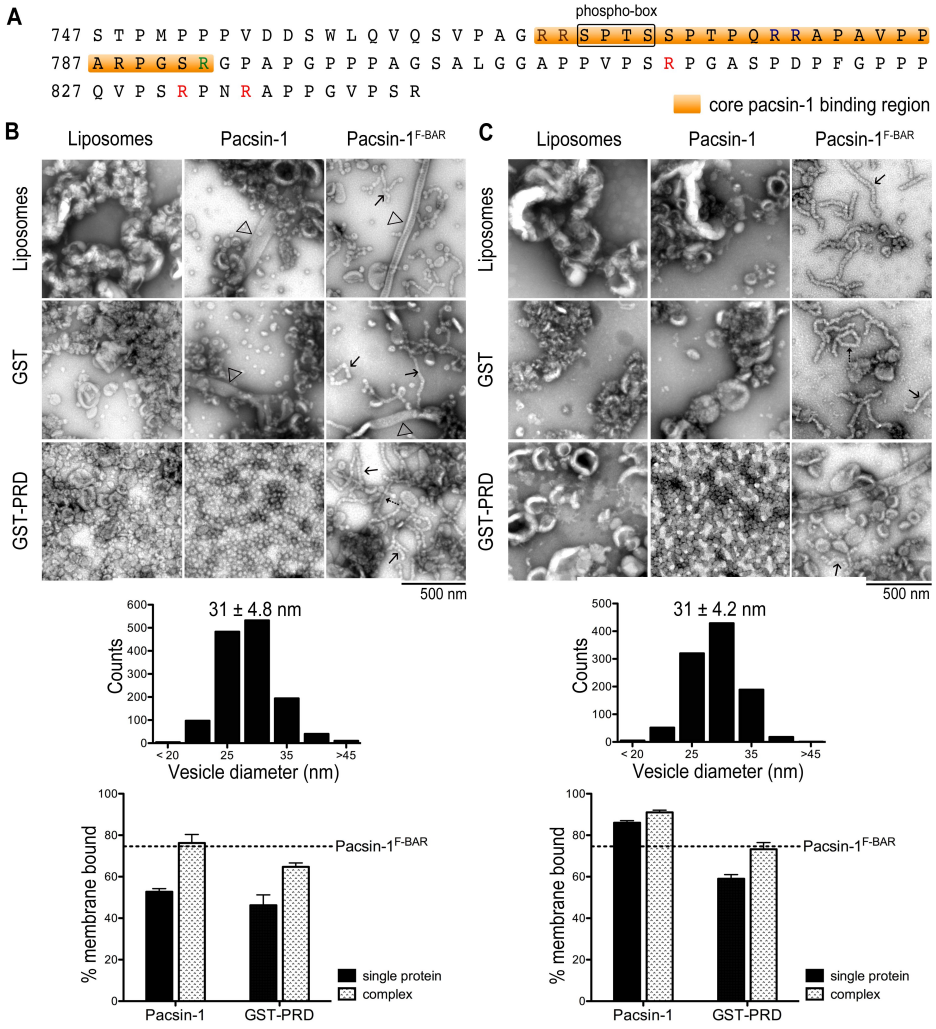

Figure 4.2 Activation of pacsin-1 by the PRD of dynamin-1. (A) Sequence of the mouse dynamin-1 PRD. A regulatory sequence (phospho-box), the core pacsin-1 binding region (orange) and arginine residues are highlighted. The sequence is 100% identical to the human dynamin-1 PRD. The mouse PRD was expressed as GST-fusion protein. (B) Negative-stain EM with Folch liposomes. Liposomes were imaged as described before following incubations with the indicated proteins and protein complexes (top panel). The histogram (middle panel) shows the size distribution of the vesicles produced by pacsin-1 in the presence of GST-PRD. Vesicle diameters were quantified from electron micrographs taken from three independent experiments. Liposome-protein co-pelleting assays (bottom panel) were used to assess the amount of protein bound to lipid vesicles. The horizontal, dashed line indicates the lipid-bound fraction of the isolated pacsin-1 F-BAR domain under similar conditions. Two-tailed unpaired t-tests for both pacsin-1 and GST-PRD were $p < 0.05$, $N = 4$. (C) Negative-stain EM with synthetic lipid mixtures. Experiments were carried out as described in (B), but using liposomes with the composition POPC/ POPE/ POPS= 27.5/ 27.5/ 45. Error bars represent standard deviations of a minimum of 3 independent experiments.

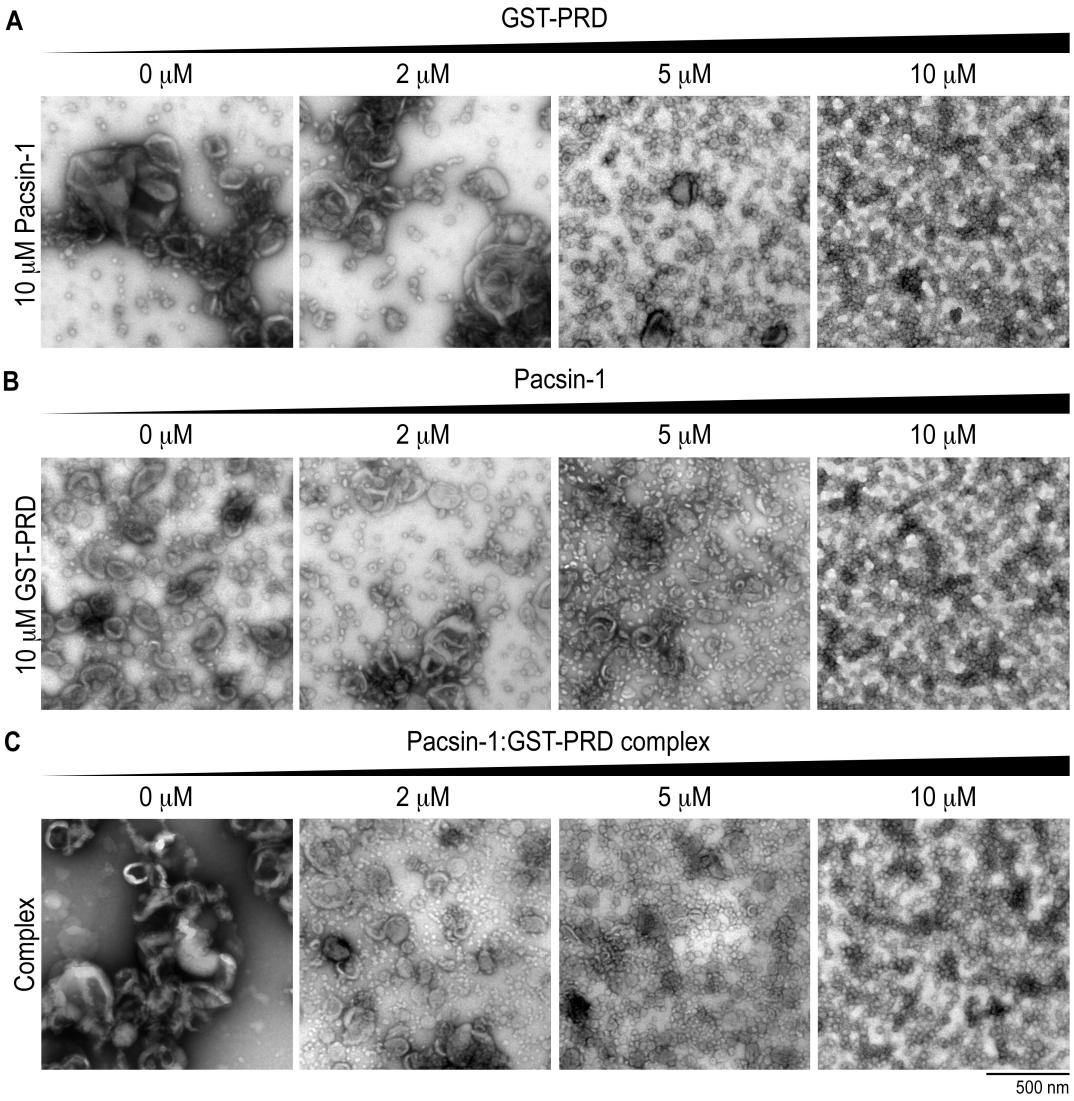

Figure 4.3 Vesiculation activity of pacsin-1 in the presence of GST-PRD is found over a wide range of protein concentrations. Negative-stain electron micrographs were taken on Folch liposomes incubated with increasing concentrations of GST-PRD (constant full-length pacsin-1), (A), of full-length pacsin-1 (constant GST-PRD), (B), or of pacsin-1/GST-PRD complexes, (C). Experiments performed by Q.W.

Full-length pacsin-1 maintained minimal tubulation activity in the presence of GST, similar to findings with pacsin-1 alone (Fig. 4.2 *B*). Also, the isolated F-BAR domain was insensitive to the presence of GST or GST-PRD. In stark contrast, addition of GST-PRD to full-length pacsin-1 resulted in the appearance of vesicular structures in the micrographs. The morphology of the vesicles was homogeneous, with an average diameter of 31 ± 4.8 nm (Fig. 4.2 *B*), and distinct from the tubules reported for mouse pacsin-1-PRD peptide complexes in cells or with phosphatidylserine liposomes (28). The abundance of vesicles is dependent on relative pacsin-1 and GST-PRD concentrations in the reaction, with no tubular structures being observed at any protein concentration under these conditions (Fig. 4.3). Similar results were obtained when a SUMO moiety was used as the fusion partner for the dynamin-1 PRD (Fig. 4.4 *A*). While GST has the propensity to form dimers, the SUMO moiety is believed to present the PRD as a monomeric ligand, indicating that a simple binding mode between the SH3 domain and the PRD is responsible for modulating pacsin-1's membrane deformation activity. Furthermore, GST-PRD and pacsin-1 co-migrate in size-exclusion chromatography (SEC), indicating the formation of a stable complex (Fig. 4.5 *A*). Only a minor fraction, as indicated by the shoulder preceding the main peak appears to form higher-order complexes, most likely corresponding to a complex formed between the PRD and pacsin-1 in a tetrameric form. On the other hand, mutation of the central proline residue in the ligand-binding site of pacsin's SH3 domain (pacsin-1^{P437L}) (55) prevented PRD binding, resulting in absence of stable complex formation (Fig. 4.5 *B*). Consequently, small homogeneous vesicles were not observed in liposome incubations in the presence of both pacsin-1^{P437L} and GST-PRD

(see Fig. 4.9 *A*), confirming the importance of direct SH3-PRD interactions in stimulating pacsin-1's vesiculation activity. In addition, we also observed that mutation of a critical methionine residue on the pacsin-1 wedge loop to lysine (pacsin-1^{M126K}, [27]) suppressed vesiculation activity in the presence of GST-PRD (Fig. 4.6), corroborating our previous conclusions about the role of the wedge loop in pacsin's membrane sculpting potential [27].

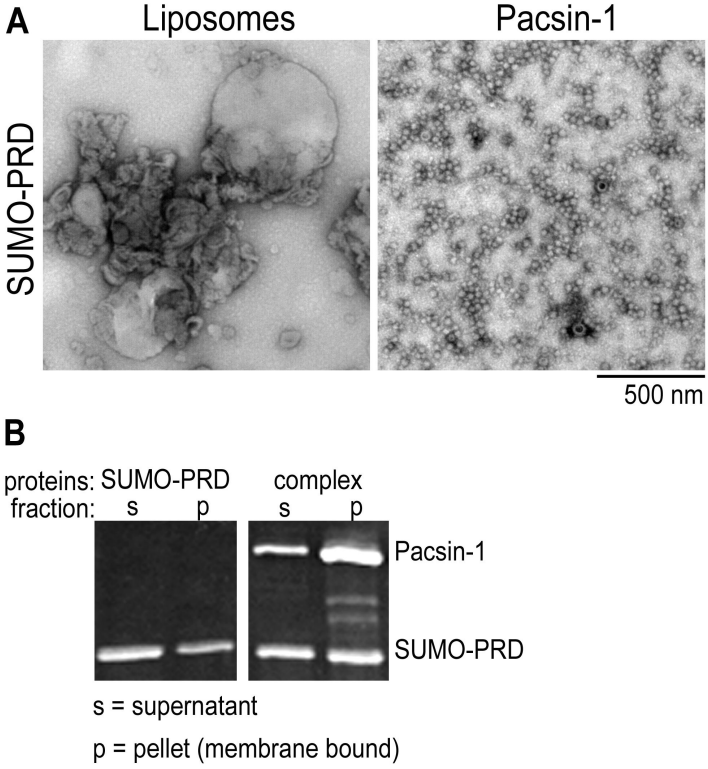

Figure 4.4 Activation of pacsin-1 occurs in the presence of SUMO-PRD. (A) Negative-stain EM images of Folch liposomes following incubation with the indicated proteins or protein complexes as described previously. (B) Representative images of SDS-PAGE gels from liposome co-pelleting assays. Proteins or protein complexes were co-incubated with Folch liposomes, and the amounts of proteins in the supernatant and pellet (membrane bound) fractions were analyzed, as described in Materials and Methods.

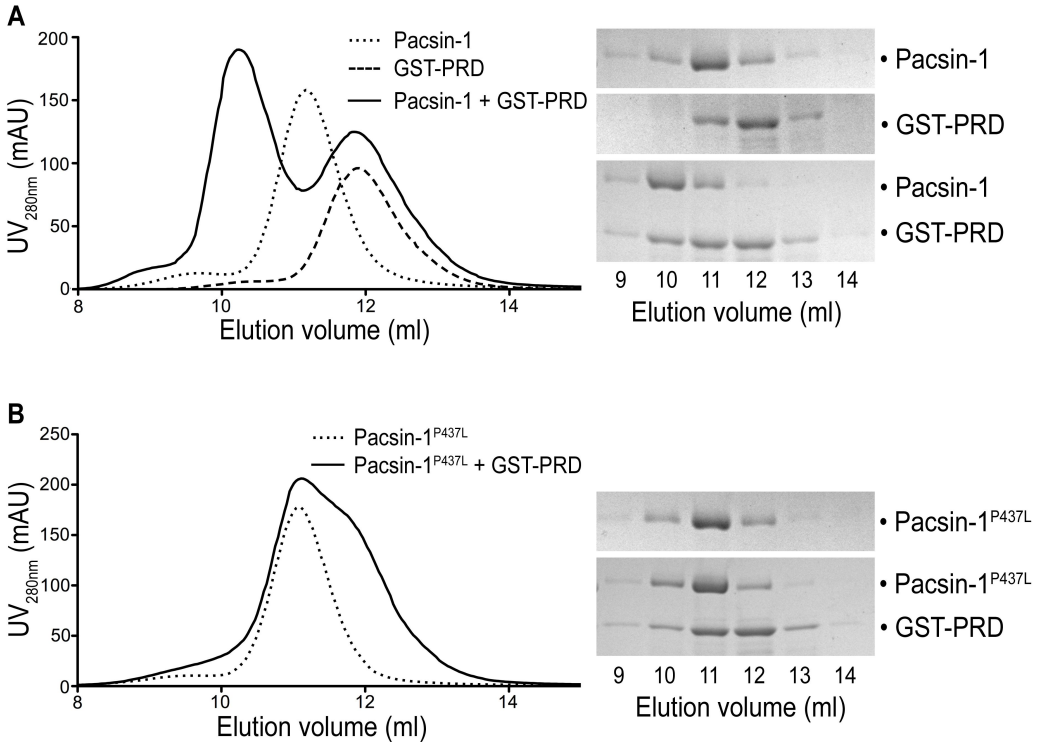

Figure 4.5 Co-migration of pacsin-1 and GST-PRD in size exclusion chromatography (SEC) indicates formation of a stable complex. (A) Wild-type pacsin-1. Human wild-type pacsin-1 (40 μM) and GST-PRD (80 μM) were incubated for 15 min, and subjected to size-exclusion chromatography. Protein-containing fractions were analyzed by using SDS-PAGE and Coomassie staining. (B) Pacsin-1^{P437L}. A similar analysis was carried out with a single-point mutant of pacsin-1, in which the peptide binding site is disrupted.

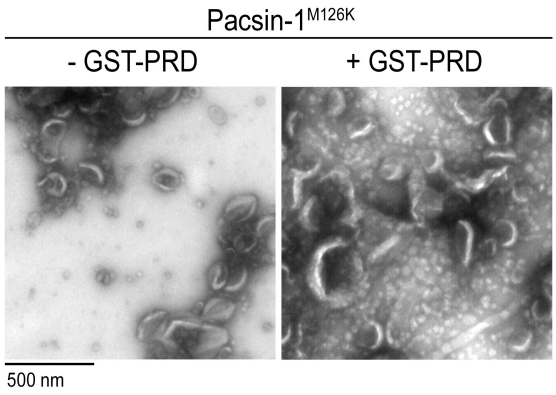

Figure 4.6 Mutation of the wedge loop affects the vesiculation of pacsin-1 in the presence of GST-PRD. Negative-stain EM images of Folch liposomes incubated with the wedge loop mutant, pacsin-1^{M126K} alone or in the presence of GST-PRD. Experiments performed by Q.W.

Although Folch (I) lipids represent a natural and widely used lipid mixture, its uncertainty in composition and potential batch-to-batch variability pose concerns. We repeated the membrane deformation assays described above with a synthetic lipid mixture (POPC/POPE/POPS = 27.5/27.5/45). We found that the lipid deformation activities of pacsin-1 and pacsin-1$^{F\text{-}BAR}$ were rather similar to those observed with Folch (I) liposomes. Pacsin-1$^{F\text{-}BAR}$ almost exclusively produced pearling structures, which at times resembled less sharply defined narrow tubules, whereas full-length pacsin-1 remained relatively inactive (Fig. 4.2 *C*). The addition of GST-PRD resulted in the appearance of homogenous vesicles with a mean diameter of 31 ± 4.2 nm (Fig. 4.2 *C*). Student's t-test revealed that they were no different from the ones generated in Folch (I) lipids ($p= 0.89$, two-tailed unpaired, $1000< N< 1400$). Analogous to experiments conducted in Folch lipids, no vesiculation was observed when GST-PRD was added to the SH3-binding mutant pacsin-1^{P437L} (unpublished data).

Previous studies converged on a model by which the binding of the PRD to pacsin-1 sequesters the SH3 domains from the F-BAR domains, leading to an increased membrane sculpting potential of pacsin-1 (27, 28). To investigate whether this activation step also resulted in increased membrane affinity of pacsin-1, we performed liposome co-pelleting assays using Folch (I) liposomes. The fractions (%) of proteins found in the pellet (membrane bound) and in the supernatant were detected using SYPRO Ruby gel stain and quantified in ImageJ (see Fig.4.7 *A* for representative of gels). Our analyses revealed that only 53% of full-length pacsin-1 was membrane bound, compared to 75% of the isolated F-BAR (Fig. 4.2 *B*). GST-PRD alone also possesses appreciable membrane binding affinity, with 46% found in the membrane fraction. When GST-PRD is co-incubated with full-length pacsin-1 and liposomes, the membrane-bound fractions of both pacsin-1 and GST-PRD increased significantly to 76% and 65%, respectively (Fig. 4.2 *B*; student's t-test, $p< 0.05$). On the other hand, the membrane bound fraction of pacsin-1^{P437L} was 46%, and remained relatively unchanged (51%) when GST-PRD is added. Similarly, the presence of GST-PRD had no effect on the membrane affinity of pacsin-$1^{F\text{-}BAR}$ (unpublished data). While this assay may not distinguish between enhanced direct protein-membrane interactions and increased protein tethering associations at the membrane (between pacsin-1 and GST-PRD), it still represented enhanced recruitment of both proteins only in the presence of each other. These results were recapitulated in liposome flotation assays using a sucrose gradient (Fig. 4.8 *A* and *B*), further corroborating the increased membrane affinities of full-length pacsin-1 and GST-PRD upon co-

incubation with Folch liposomes. A comparable trend was also observed using synthetic lipid mixtures (Fig. 4.2 *C*).

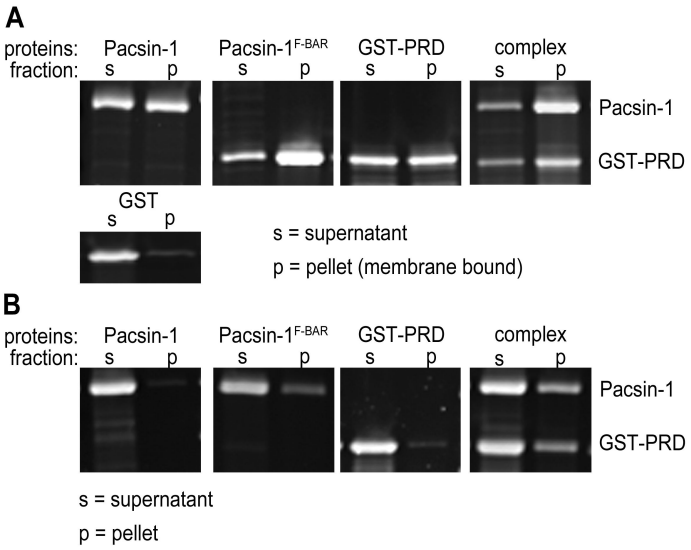

Figure 4.7 Representative images of SDS-PAGE gels from liposome co-pelleting assays.The amounts of proteins in the supernatant and pellet fractions were analyzed in the presence of Folch liposomes (0.5 mg/ml), (A), and in the absence of liposomes, (B). Gels were stained with SYPRO Ruby and experiments were conducted as described in Materials and Methods.

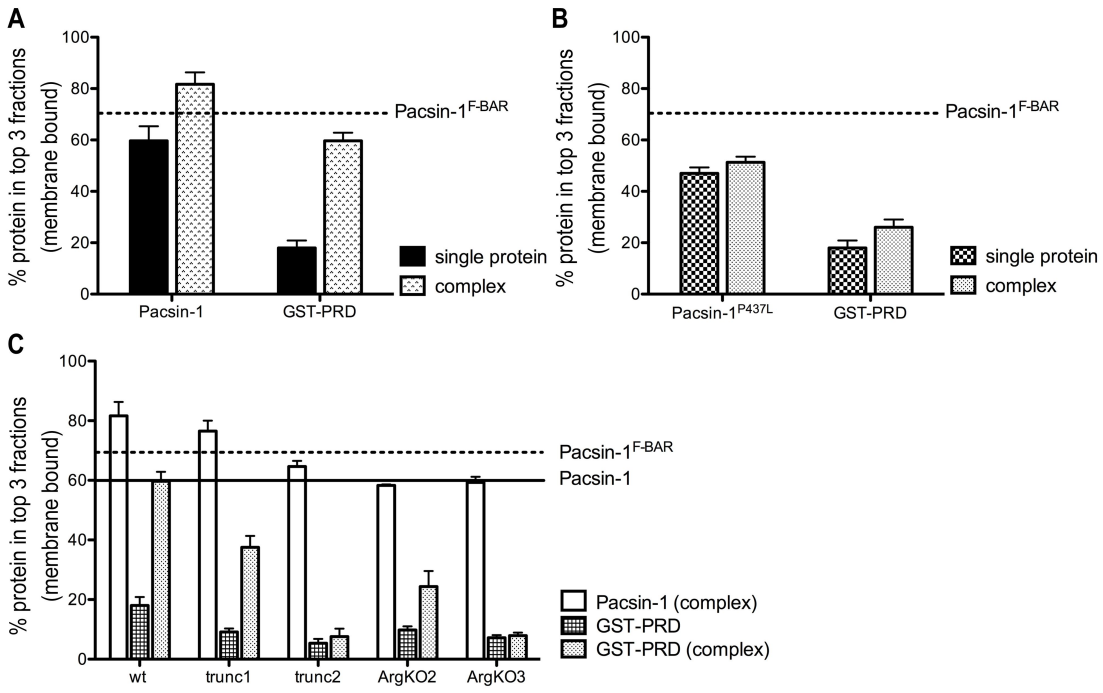

Figure 4.8 Analysis of the membrane binding affinity of pacsin-1 constructs and pacsin-PRD complexes. Liposome flotation assays were employed to assess the amount of membrane bound proteins. The horizontal, dashed lines indicate the lipid-bound fraction of the isolated pacsin-1 F-BAR domain under similar conditions. (A) Membrane bound fractions of wild-type pacsin-1 and GST-PRD in isolation and in complex. (B) Membrane bound fractions of pacsin-1^{P437L} and GST-PRD in isolation and in complex. (C) Similar experiments and analysis as in (A) and (B), examining the membrane bound fractions of pacsin-1 in the presence of GST-PRD mutants. The horizontal solid line indicates the lipid-bound fraction of the isolated full-length pacsin-1 under similar conditions as shown in (A). Error bars represent standard deviations of a minimum of 3 independent experiments.

4.4.3 Basic residues within the dynamin-1 PRD are required for full activation of pacsin-1

Activation of pacsin-1 upon addition of a shorter dynamin-1-derived PRD peptide (residue 769-790) has been previously reported, where the activated pacsin-1 generated tubules *in vitro* (28). Under the conditions used here, where the entire PRD of dynamin-1 was employed, vesicles appeared to be the dominant morphology observed in electron micrographs. This apparent discrepancy of membrane morphologies could originate from the differences in the PRD construct used and/or in experimental conditions, such as protein concentrations, liposome compositions and liposome physical properties. The PRD of dynamin-1 contains several PxxP motifs and has a polybasic nature, among which residues 768-792 have been shown to be important for high-affinity pacsin-dynamin interactions (52). To determine whether specific segments of the PRD are responsible for full activation of pacsin-1, we created two truncation mutants of GST-PRD (Fig. 4.9 *A*) and performed *in vitro* membrane deformation assays.

Incubation of pacsin-1 with a truncated PRD construct that removes part of the core binding segment (GST-PRD^{trunc2}; aa747-780) completely abolished pacsin-1's ability to generate vesicles. Instead, only tubules were observed on the micrographs (Fig. 4.9 *A*). In contrast, when GST-PRD was shortened at its C-terminus by only 30 amino acids (GST-PRD^{trunc1}; aa747-810), pacsin-1 still maintained its ability to generate homogeneous vesicles that are indistinguishable from the ones generated in the presence of the entire GST-PRD (Fig. 4.9 *A*, and Fig. 4.10 *A*). Furthermore, co-pelleting assays of Folch liposomes revealed an increase in the fraction of membrane

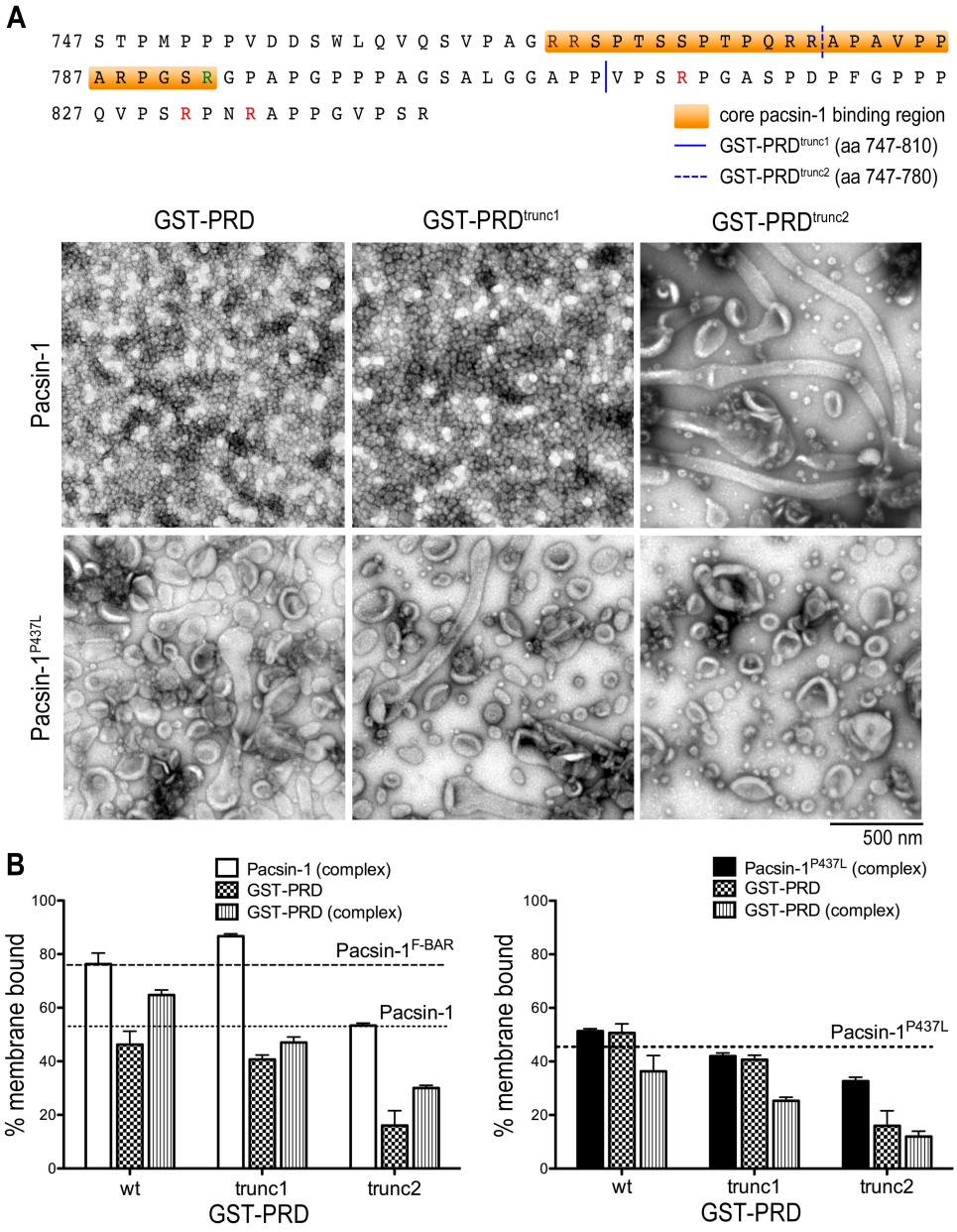

Figure 4.9 Effect of GST-PRD truncation mutants on the membrane deformation activity of pacsin-1. (A) Membrane deformation of Folch liposomes. The sequences of mouse dynamin-1 PRD truncation mutants GST-PRD^{trunc1} and GST-PRD^{trunc2} are shown (top panel). Negative-stain EM images are shown after incubation of liposomes with the indicated protein complexes. Either wild-type human pacsin-1 or a corresponding protein with a single-point mutation in the SH3 domain (pacsin-1^{P437L}) was used. (B) Liposome co-pelleting assay. Liposome binding assays were carried out with the complexes used in (A). The horizontal, dashed lines indicate the lipid-bound fraction of the isolated pacsin-1 F-BAR domain and isolated full-length pacsin-1 under similar conditions. Error bars represent standard deviations of a minimum of 3 independent experiments.

bound pacsin-1 in the presence of GST-PRD^{trunc1}, but not in the presence of the shorter PRD construct, GST-PRD^{trunc2} (Fig. 4.9 *B*). Liposome flotation assays corroborated these results (Fig. 4.8 *C*). Our results are consistent with earlier reports, which identified residues 768-792 in the PRD as being responsible for pacsin-1's interaction with dynamin-1, and also indicate that arginines and PxxP motifs that lie within the last 30 residues of GST-PRD were dispensable for pacsin-1's vesiculation activity.

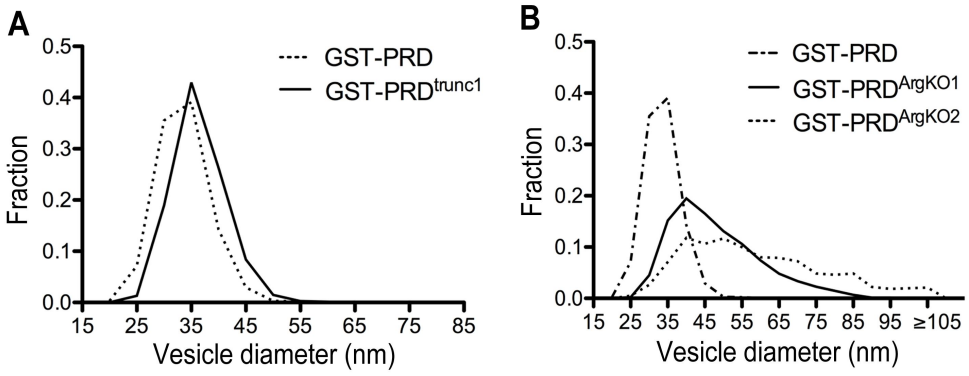

Figure 4.10 Size distribution of vesicles generated by pacsin-1 in the presence of wild-type and various GST-PRD mutants. (A) Vesicles produced by pacsin-1 with wild-type or GST-PRD^{trunc1}. The mean diameters are not significantly different based on a two-tailed unpaired t-test ($p< 0.1$, $750< N< 1400$). (B) Vesicles produced by pacsin-1 in the presence of GST-PRD^{ArgKO1} and GST-PRD^{ArgKO2}. Vesicle diameters produced by the mutant GST-PRD variants are significantly different from the wild-type case based on a two-tailed unpaired t-test ($p< 0.0001$ for GST-PRD^{ArgKO1}; $p< 0.005$ for GST-PRD^{ArgKO2}; $750< N< 1300$).

As an alternative strategy to determine whether the polybasic nature of the PRD is important for pacsin's vesiculation activity, we generated various GST-PRD mutants that contain arginine-to-alanine point mutations (Fig. 4.11 *A*). Using full-length GST-PRD with neutralizing mutations within the last 30 residues, we first mutated the two arginines immediately upstream of the regulatory phospho-box (GST-PRD^{ArgKO1}, Fig. 4.11 *A*). Upon incubation with pacsin-1, we observed that pacsin-1 lost its ability to generate 31 nm-vesicles (Fig. 4.11 *A*). The average vesicle size was 46 ± 12 nm, and the overall size distribution was broader compared to experiments carried out with wild-type GST-PRD (Fig. 4.10 *B*). Further mutations of arginine residues that reside within the proposed core binding sequence of GST-PRD (GST-PRD^{ArgKO2}) resulted in increased heterogeneity of vesicle sizes produced by pacsin-1, whereby the mean diameters were significantly different from those induced by wild-type GST-PRD (Fig. 4.11 *A,* and Fig. 4.10 *B*). Only occasional tubules were observed when pacsin-1 was incubated with the most neutralized mutant, GST-PRD^{ArgKO3}. In addition, pelleting assays revealed a gradual decrease in the fraction of membrane-bound pacsin-1 (and GST-PRD) as arginine residues were sequentially neutralized in the mutants GST-PRD^{ArgKO1}, GST-PRD^{ArgKO2} and GST-PRD^{ArgKO3} (Fig. 4.11 *B*).

To examine the effect of various GST-PRD mutants on SH3-PRD affinity, we conducted GST pull-down experiments. For the truncation mutants, we observed weaker binding between pacsin-1 and GST-PRD^{trunc1} compared to the entire GST-PRD, and essentially no interaction between pacsin-1 and GST-PRD^{trunc2} (Fig. 4.12). Since the truncation in GST-PRD^{trunc2} removed some of the validated core binding sequences, the lack of strong interaction between pacsin-1 and GST-PRD^{trunc2} was

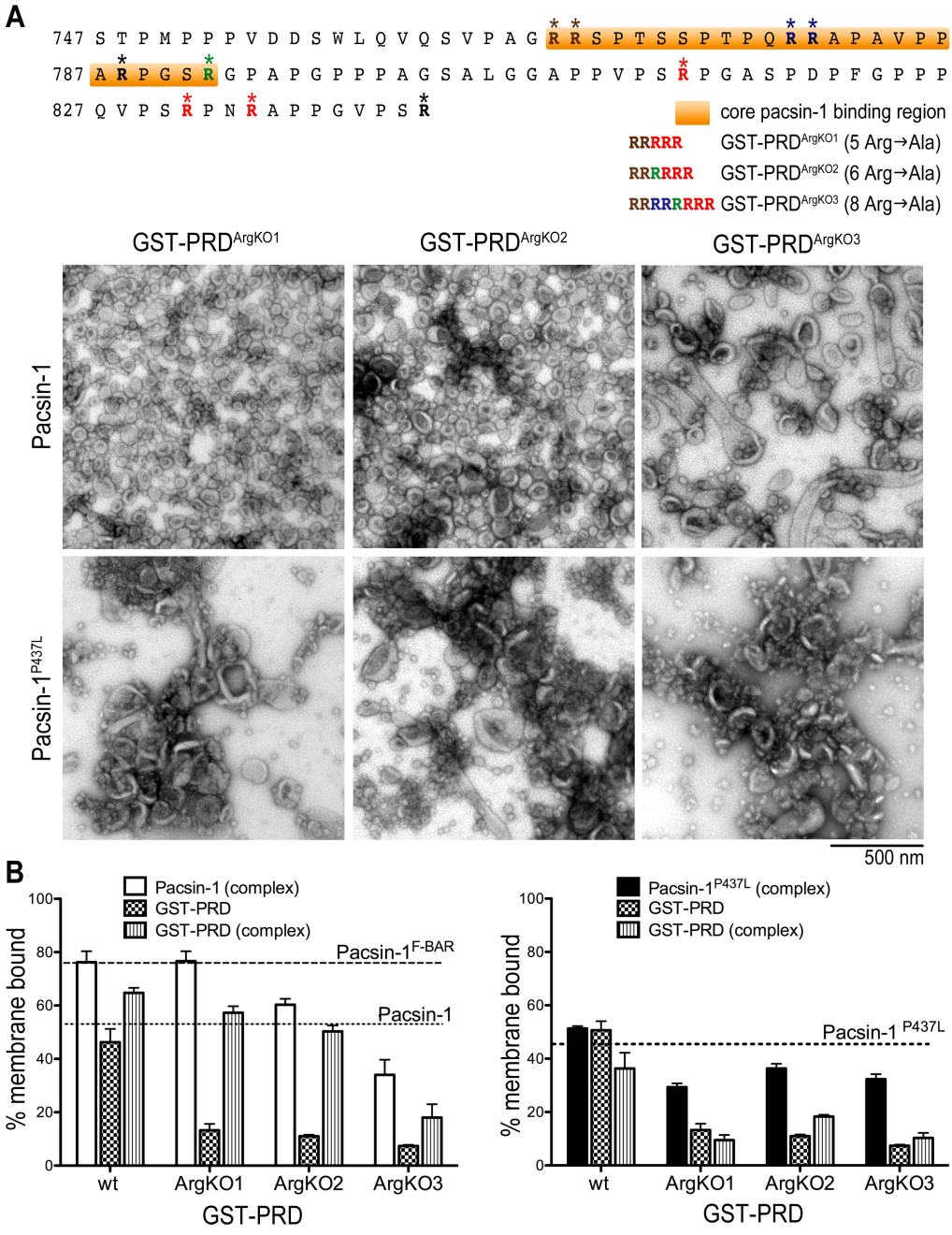

Figure 4.11 The role of arginine residues within the dynamin-1 PRD in pacsin-1's membrane deformation potential. (A) Membrane deformation of Folch liposomes. The positions of Arg-to-Ala mutations (GST-PRD^{ArgKO1}, GST-PRD^{ArgKO2} and GST-PRD^{ArgKO3}) in the mouse dynamin-1 PRD protein sequence are shown (top panel). Negative-stain EM images are shown after incubation of liposomes with the indicated protein complexes. (B) Liposome co-pelleting assay. Liposome binding assays were carried out as described in Fig. 4.9 Error bars represent standard deviations of a minimum of 3 independent experiments.

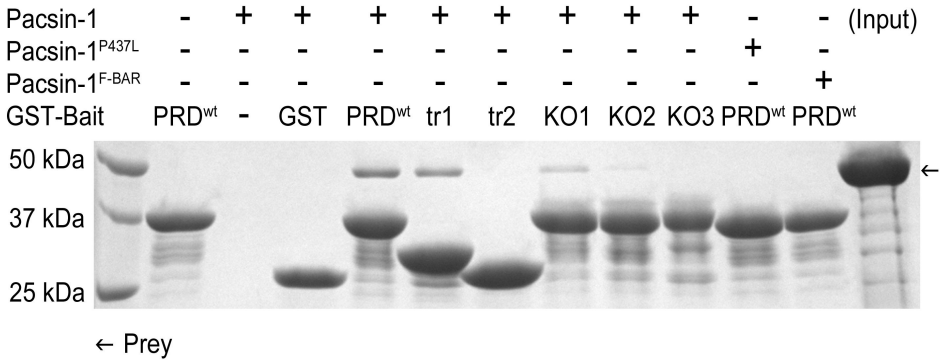

Figure 4.12 Pacsin-PRD complex formation. GST pull-down experiments were carried out by using wild-type and mutant forms of GST-PRD to examine their interactions with pacsin-1. Complexes were eluted and analyzed by SDS-PAGE and Coomassie-staining. Bait proteins: wild-type GST-PRD (PRD^{wt}), GST-PRD^{trunc1} (tr1), GST-PRD^{trunc2} (tr2), GST-PRD^{ArgKO1} (KO1), GST-PRD^{ArgKO2} (KO2), GST-PRD^{ArgKO3} (KO3) and GST (negative control).

expected. Pull-down data for the arginine-to-alanine point mutants corroborated pelleting assay results, whereby sequential neutralization of arginine residues in the PRD mutants resulted in their decreased affinities for pacsin-1 (Fig. 4.12). Altogether, we confirmed that within the entire GST-PRD, neutralizing mutations on arginine residues residing within the core binding motif (aa768-792) disrupted pacsin-PRD interactions, which correlated with the gradual loss of pacsin-1's ability to generate vesicles as the number of mutations increased. Based on our mutagenesis study, the polybasic nature of the entire PRD contributes mainly towards interaction of the PRD with pacsin-1. High-affinity binding of the SH3 of pacsin-1 to intact core binding sequences in the PRD, and the resulting higher efficiency in membrane recruitment of the complex establishes its enhanced membrane sculpting activity.

4.4.4 GST-PRD also modulates membrane deformation activity of endophilin-A1

The PRD of dynamin has been implicated in many studies to interact with SH3 domains of various proteins, one of which is another BAR domain protein, endophilin-A1 (59).Endophilin-A1 is enriched in neurons and functions in the recycling of synaptic vesicles (12, 17, 60, 61), where it has been shown recently to couple fission with clathrin uncoating events via its SH3 domain-mediated interactions with synaptojanin and dynamin (62). Similar to pacsin-1, endophilin has an N-terminal membrane binding and curvature-inducing module, an N-BAR domain that is connected to the C-terminal SH3 domain via a linker peptide (60). Consistent with previous reports (12, 17, 19), both endophilin full-length and its isolated N-BAR domain (endophilin$^{N\text{-}BAR}$) are able to generate tubules from Folch liposomes *in vitro* (Fig. 4.13 *A*). The tubules produced by full-length endophilin were on average narrower than tubules produced by endophilin$^{N\text{-}BAR}$ (30 nm vs. 45 nm).

When endophilin-A1 was incubated with GST-PRD, we observed a switch from tubulation to vesiculation activity (Fig. 4.13 *A*). The vesicles were homogeneous, with a mean diameter of 24 ± 2.7 nm, which was smaller than vesicles generated by pacsin-1 (Fig. 4.13 *B*). This could reflect the intrinsic structural differences of the two proteins, with the endophilin N-BAR domain adopting a higher degree of curvature than the F-BAR domain of pacsin. Unlike the small vesicles that were generated by endophilin$^{N\text{-}BAR}$ at high protein concentrations (13), vesiculation here appeared not to be caused by use of excess protein since vesicles were the main morphology observed over a wide range of protein concentrations under similar experimental conditions (unpublished data). Vesiculation required the presence of the SH3 domain, as

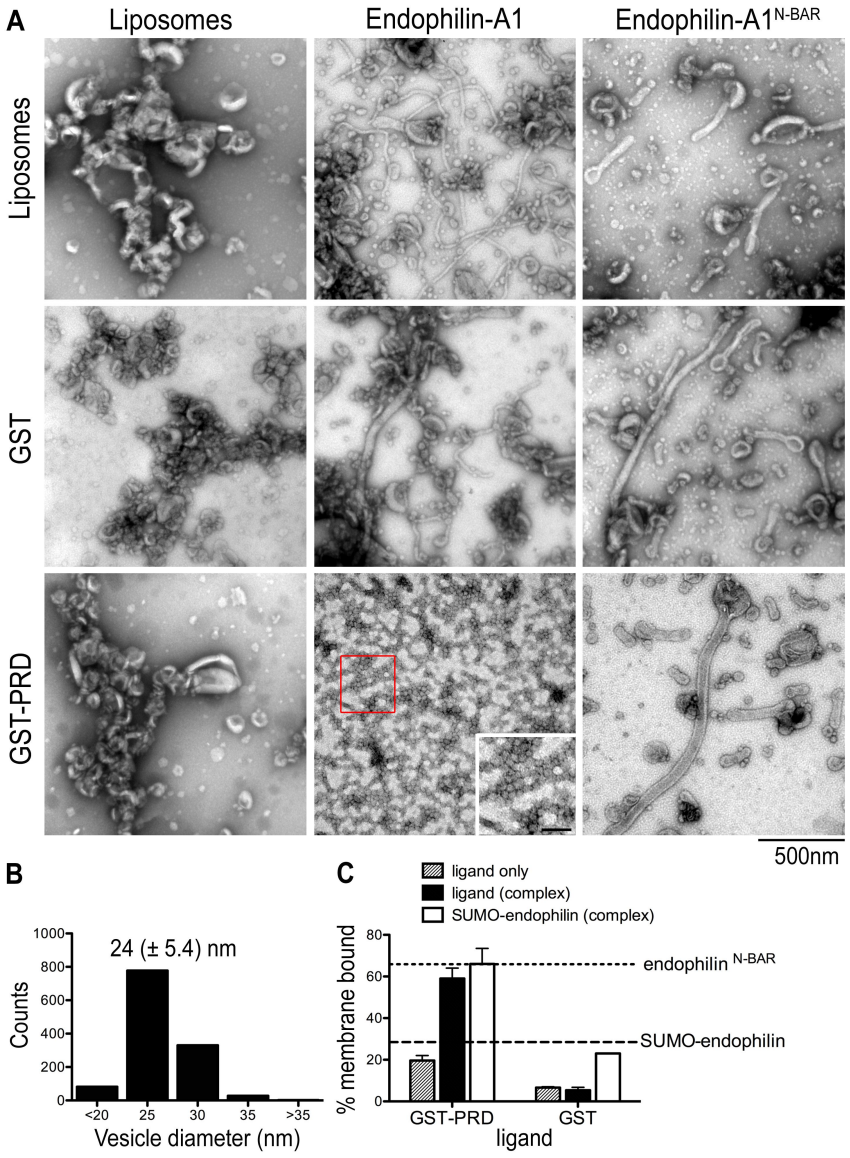

Figure 4.13 Activation of full-length endophilin-A1 by GST-PRD. (A) Negative-stain EM with Folch liposomes. Assays with endophilin-A1 (full-length or N-BAR domain; 10 μM) were carried out as described before. The inset shows a zoomed-in view of the red box area of the image, with scale bar = 100 nm. (B) Statistical analysis of vesicle size distribution. Diameters of vesicles produced by endophilin in the presence of GST-PRD were quantified from electron micrographs taken from three independent experiments. (C) Liposome co-pelleting assay with Folch liposomes. Liposome binding assays were carried out as described in Fig. 4.9. The horizontal, dashed lines indicate the lipid-bound fraction of the isolated endophilin-A1 N-BAR (expressed as His_6-SUMO-fusion protein) domain and isolated full-length endophilin-A1 under similar conditions. Error bars represent standard deviations of a minimum of 3 independent experiments.

incubations of endophilin$^{N\text{-}BAR}$ with GST-PRD did not result in vesicle generation (Fig. 4.13 *A*).

The effect of endophilin-PRD complex formation on the membrane affinity of endophilin was examined using co-pelleting assays. Since full-length endophilin has a molecular weight close to GST-PRD, we expressed and purified endophilin fused to an N-terminal SUMO moiety (SUMO-endophilin) to enable analysis in pelleting assays. SUMO-endophilin still retained tubulation activity and co-migrated with GST-PRD as a stable complex in SEC experiments (unpublished data). Similar to experiments with pacsin-1, pelleting assays revealed increased

membrane binding of endophilin and GST-PRD as a complex compared to their membrane affinities as separate entities (Fig. 4.13 *C*). This was not observed when GST was used as the ligand (Fig. 4.13 *C*). Taken together, the functional and binding assays impart similar influences of GST-PRD on the membrane sculpting potential of endophilin and pacsin-1, suggesting a more general effect of dynamin-1's PRD on its BAR-SH3 domain-containing binding partners.

4.4.5 Liposome properties impact membrane deformation abilities of BAR domain proteins

Cellular membranes are subject to constant dynamic changes and alterations in response to cellular events. Heterogeneity in lipid composition and curvature could give rise to a wide range of membrane physical properties that may influence the sculpting potential of BAR/F-BAR domain proteins. Pacsin-1 has been reported to produce a large spectrum of membrane morphologies *in vitro*, ranging from vesicular structures to tubules of varying diameter (27-29), which could be influenced by the

properties of the membrane support. Here, we asked whether the physical properties of the liposomes could account for the generation of different morphologies. Factors such as preparation methods, buffer ionic strength, multivalent cations, and lipid composition have been known to affect membrane curvature (liposome size) and lamellarity (63, 64), which could in turn affect membrane bending elasticity (32), binding affinities of proteins, and thus, membrane sculpting abilities of BAR domain proteins. Here, we concentrated on the effects of different liposome preparation methods on membrane deformation activities of BAR domain proteins.

We employed three distinct methods for comparison. The protocol used thus far to generate liposomes involved the rehydration of a dried lipid film in aqueous buffer, followed by brief sonication and freeze-thaw cycles ("SFT method") (23). Sonication produces small unilamellar liposomes (with an average diameter of 20-30 nm), whereas freeze-thaw cycles equilibrate ions across membranes, which leads to fusion of bilayers to form larger liposomes (63). The SFT method likely produces liposomes with a range of sizes and lamellarity; electron micrographs revealed that a large percentage of the liposomes were unilamellar and less than one micron in diameter, consistent with dynamic light scattering (DLS) data (Fig. 4.14 *A*; unpublished data). Another method generally used to prepare hydrated bilayers from a dry film deposition involves no sonication, but only freezing and thawing of a hydrated suspension of lipids ("FT method") (65). This second method produces multi-lamellar liposomes of a wide range of sizes, from <100 nm to few microns, as determined by DLS (Fig. 4.14 *A*; see Fig. 4.15 *A*). The third method, rapid solvent exchange ("RSE method"), allows a fast exchange of organic solvent with aqueous

buffer, avoiding the dry film state that can cause artifactual de-mixing of lipids (53). The size range of RSE liposomes is similar to that of liposomes prepared by the FT method (Fig. 4.14 *A*; see Fig. 4.15 *B*), but with a lower average lamellarity of ~1.5 (53).

In vitro membrane deformation experiments were performed with Folch lipids using liposomes prepared from the three methods described above, where we compared the membrane deformation activities of pacsin-1$^{F\text{-}BAR}$, full-length pacsin-1, and pacsin-1 in the presence of GST-PRD. In addition, we included a canonical F-BAR domain, that of CIP4 (CIP4$^{F\text{-}BAR}$), which has been reported to stabilize relatively wide membrane tubules (21). Consistent with previous observations, CIP4$^{F\text{-}BAR}$ more efficiently generated tubules from larger liposomes (in RSE and FT preparations) than from SFT liposomes (Fig. 4.14 *B*). Pacsin-1$^{F\text{-}BAR}$ produced both tubules and pearling structures in all three liposome preparations, but wide tubules (and shorter pearlings) dominated in RSE and FT liposomes (Fig. 4.14 *B*). Unexpectedly, despite its previously reported autoinhibited membrane deformation activity, full-length pacsin-1 displayed noticeable tubulation activities in RSE and FT liposomes even in the absence of GST-PRD (Fig. 4.14 *B*). The variable extent of membrane sculpting activity of pacsin-1 in the three types of liposome preparations could indicate an initial preference for shallower membrane curvature of the full-length protein, which is more abundant in RSE and FT liposome preparations.

The membrane deformation activity of pacsin-1 in the presence of GST-PRD was also examined in the three different liposome preparations. Both tubules and vesicles were observed in RSE and FT liposomes, compared to SFT liposomes that

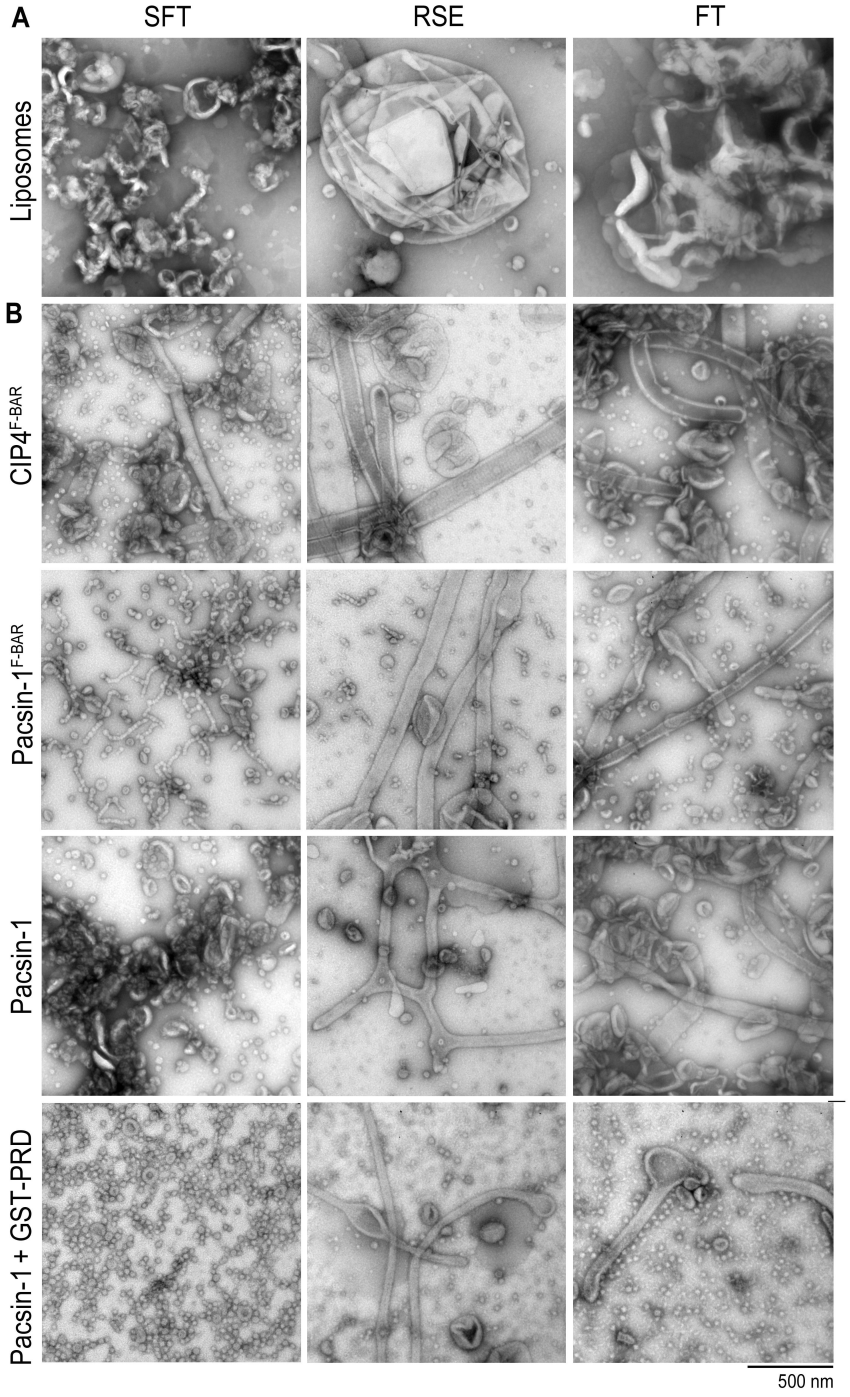

Figure 4.14 Effect of liposome preparation method on protein-induced membrane deformation. (A) Negative-stain EM of liposomes prepared via sonication/ freeze-thaw (SFT), rapid solvent exchange (RSE), and freeze-thaw (FT) methods. (B) Membrane deformation activities of various pacsin-1 constructs (5-10 μM) and $CIP4^{F\text{-}BAR}$ (10 μM) in Folch liposomes prepared following three different methods. Incubations and imaging were carried out as described previously.

yielded only small vesicles (Fig. 4.14 *B*). However, the morphology of the vesicles was different from that generated from SFT liposomes: the former have less-defined perimeters, especially those generated from RSE liposomes. RSE and FT preparations also yielded vesicles at higher pacsin-PRD concentrations (≥10 μM) whereas tubules were found at all protein concentrations (unpublished data), which may indicate a concentration-dependent phenomenon similar to that reported for N-BAR domain-containing proteins (13).

Using the three preparation methods described above, we have explored the effects of liposomes with broad size distributions and distinct lamellar properties on the membrane sculpting abilities of F-BAR domain proteins. Even though RSE liposomes have much lower average lamellarity than FT liposomes, the membrane morphologies generated by F-BAR proteins were similar in both liposome preparations under our experimental conditions. To further investigate how membrane curvature may govern membrane deformation activities of pacsin-1, pacsin-1$^{F\text{-}BAR}$ and pacsin-1-PRD complex, we prepared liposomes of different size distributions by extruding FT or RSE liposomes through polycarbonate membranes with defined pore sizes. Extrusion produces unilamellar liposomes with well-defined sizes if the pore size used is ≤ 100 nm; with pore sizes ≥ 200 nm, the resulting liposomes contain mixed lamellarity and broader size distribution (66). Extrusion is also another popular method for preparing liposomes, and hence provides a valuable comparison to the approaches described above.

Starting with FT or RSE liposomes, we used five membrane pore sizes for extrusion: 1000 nm, 800 nm, 400 nm, 200 nm, and 100 nm. DLS revealed narrow size

distributions for 100 nm and 200 nm extruded liposomes, but broader distributions as the filter pore size increased (Fig. 4.15 *A* and *B*). The size distributions and mean hydrodynamic sizes were comparable in extrusion preparations from FT or RSE liposomes, with narrower distributions at 100 nm and 200 nm, and slightly lower mean values when extruding from RSE liposomes (Fig. 4.15 *B*). The mean liposome diameters obtained from 100 nm and 200 nm filter pores were ~120 nm and ~160 nm respectively, but increased only gradually when larger pore sizes were employed (Fig. 4.15 *C*). This is consistent with the trends reported previously (67). For the largest pore size (1000 nm), the mean liposome size obtained was only ~360 nm, indicating the lack of direct correlation between extrusion filter pore size and actual liposome sizes obtained, when the filter pores ≥ 200 nm were used (Fig. 4.15 *C*).

We examined the *in vitro* membrane deformation activity of pacsin-1, pacsin-$1^{F\text{-}BAR}$ and pacsin-1 in the presence of GST-PRD in all extruded liposome preparations. In general, the membrane sculpting abilities of the proteins were not markedly different in liposomes that were extruded from FT or RSE liposomes. Pacsin-$1^{F\text{-}BAR}$ generated wide tubules and short pearlings in all sizes of extruded liposomes (Fig. 4.16 and Fig. 4.17). On the other hand, pacsin-1 displayed low tubulation activity in liposomes that were extruded through 1000 nm, 800 nm and 400 nm filter pores (Fig. 4.16 and Fig. 4.17). Almost no tubules were observed in the 200 nm and 100 nm liposome preparations, indicating a strong dependence of pacsin-1's tubulation activity on membrane curvature. The membrane deformation activity of pacsin-1 in the presence of GST- PRD was comparable in all sizes of extruded liposomes, whereby tubular structures were produced in a background of small

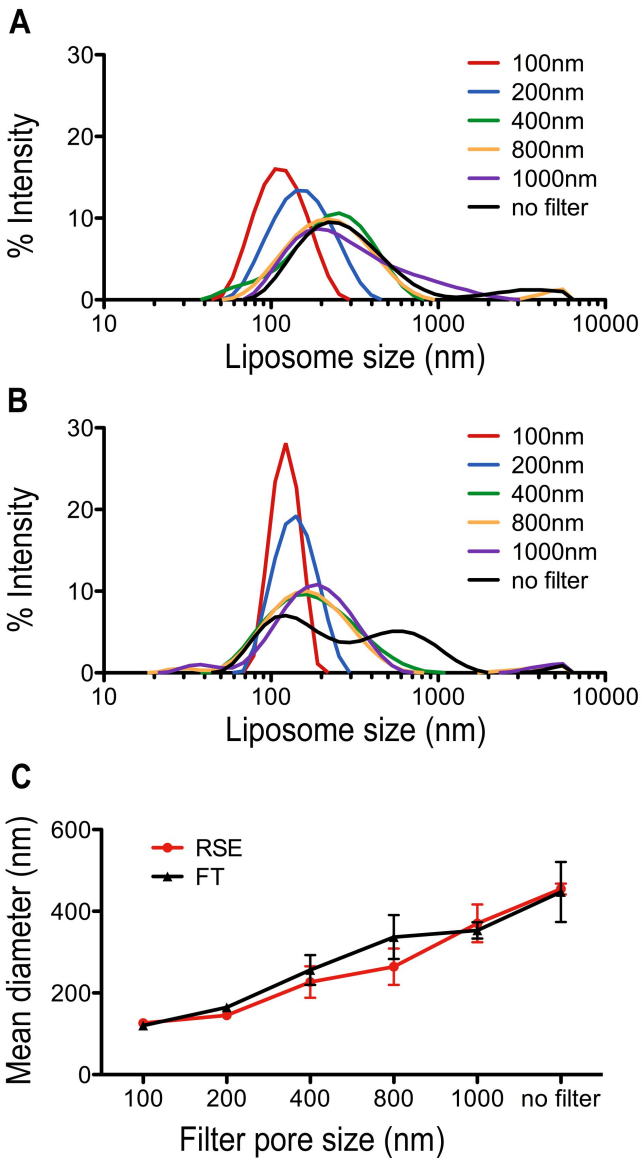

Figure 4.15 Dynamic light scattering analysis on the size distribution of liposomes produced by extrusion. (A) Representative frequency distributions of FT liposomes that were extruded through various filter pore sizes. Narrower distributions were observed with 100 nm and 200 nm pore size. (B) Representative frequency distributions of RSE liposomes that were extruded through various filter pore sizes. Similar to (A), narrower distributions were found using 100 nm and 200 nm pore sizes compared to larger pore sizes. (C) Mean liposome diameters calculated from the intensity distributions of extruded RSE and FT liposomes are similar for each pore size. Standard deviations are shown for $N \geq 3$ measurements at each filter pore size. With the exception of 100 nm and 200 nm pore sizes, the mean diameter obtained is always smaller than the actual pore size used. The mean for non-extruded RSE and FT liposomes was ~450 nm.

vesicles. The morphology of the vesicles generated were similar to those produced from FT and RSE liposomes (Fig. 4.14 *B*), and the overall activity was not strongly dependent on the curvature of starting liposomes.

These comparative studies demonstrate that properties of the starting materials can influence the membrane remodeling potential of BAR domain proteins *in vitro*. While there is no ultimate superior method of preparing liposomes for *in vitro* membrane deformation assays, the observation that different preparation methods can give rise to various liposome properties can aid in the investigation of protein-induced membrane deformations. Multi-lamellarity not only reduces the effective liposome surface area that is exposed for protein binding, but also results in stiffer membranes (higher membrane bending modulus) that require more energy for remodeling.

In addition, certain BAR domain-containing proteins are also sensitive to size (curvature) of the liposomes (21, 27); for example, full-length pacsin-1 is more active with larger liposomes as starting material. Under our experimental conditions, pacsin-1 displayed increased ability to generate more vesicular structures in the presence of GST-PRD, even when given a wide range of liposome sizes. We also observed that the canonical F-BAR protein CIP4$^{F\text{-}BAR}$ preferentially tubulates large liposomes, consistent with previous studies (21). Contrastingly, pacsin-1$^{F\text{-}BAR}$ appeared to have a broader curvature preference, generating variable membrane structures depending on the type of liposomes available. This versatility could be important in determining the role of pacsin-1 in membrane trafficking at the synapse.

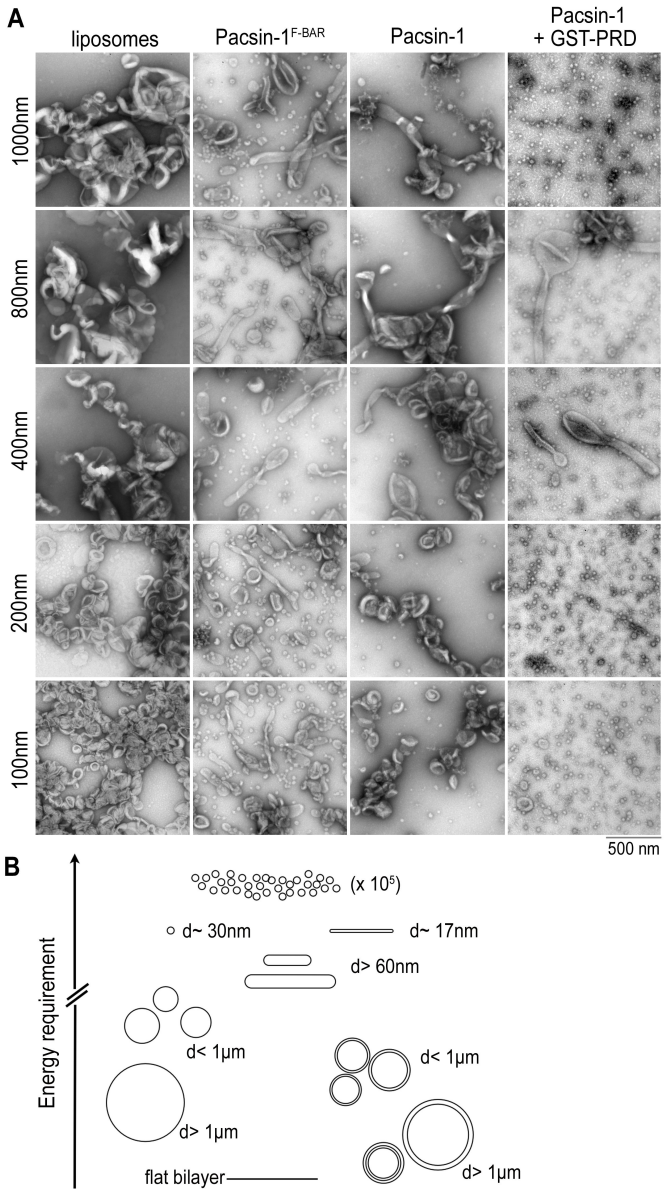

Figure 4.16 Effect of liposome diameter on protein-induced membrane deformation. (A) Negative-stain EM of extruded liposomes. Folch liposomes were prepared using the freeze-thaw (FT) method, followed by extrusion using pore sizes ranging from 100-1000 nm. Protein incubations and imaging was carried out as described above. (B) Model of modulated, protein-induced membrane deformation potential. The schematic diagram illustrates the energies required to generate various membrane morphologies, which is likely dependent on the system's initial energy state. Considering only membrane properties and a constant number of lipid molecules in each system, more energy is needed to generate a defined number of smaller vesicles from larger, multi-lamellar liposomes, compared to smaller, uni-lamellar liposomes as the starting material. The system may also be subject to bimodality, where distinct structures (vesicle vs. tubule) could coexist as energetically equivalent structures.

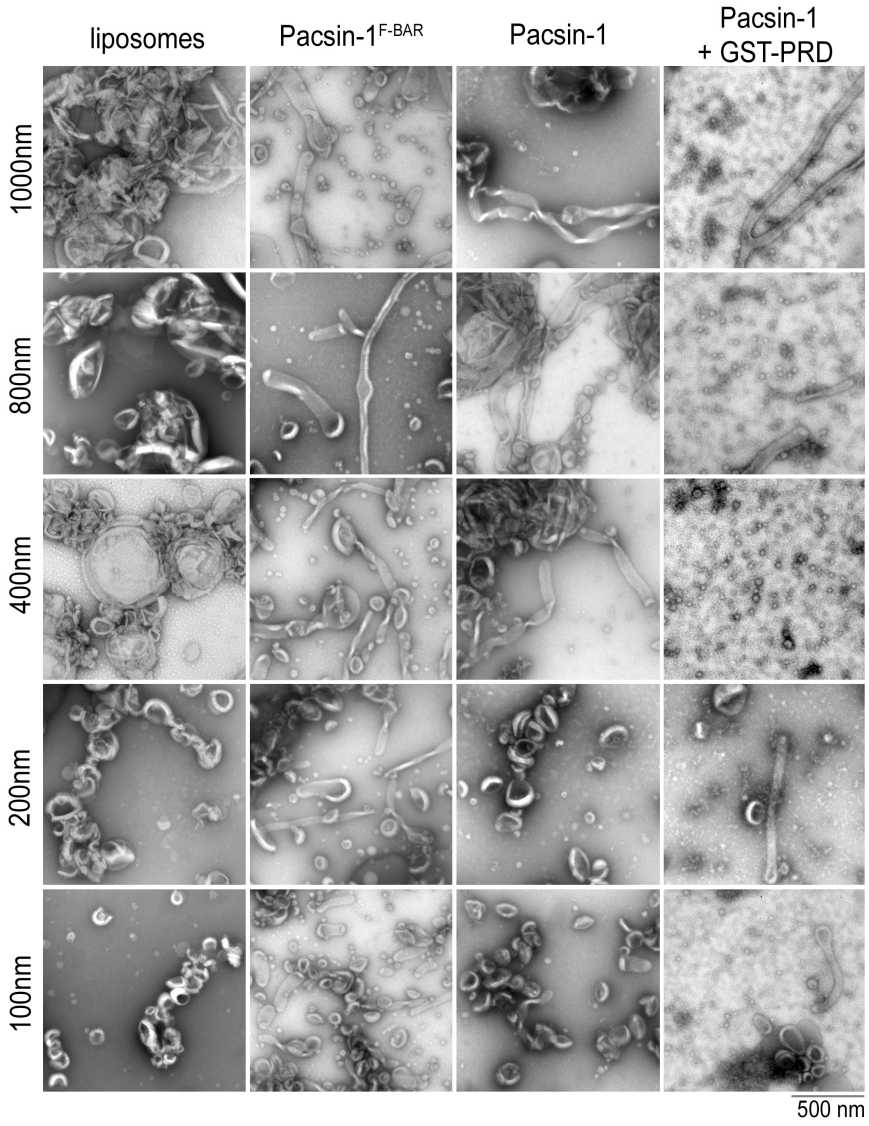

Figure 4.17 Effect of (RSE) liposome diameter on protein-induced membrane deformation. Negative-stain EM of extruded liposomes. Folch liposomes were prepared using the rapid solvent exchange (RSE) method, followed by extrusion using different pore sizes ranging from 100-1000 nm. Protein incubations and imaging was carried out as described before.

4.4.6 Energetic considerations for pacsin-mediated membrane tubulation and vesiculation (calculations performed by Q.W.)

N-BAR-mediated tubulation is predominantly driven by the insertion of amphipathic helices into the head group-acyl chain interface of one membrane leaflet (17-19). Based on theoretical estimations, protein shape and protein-membrane electrostatic interactions provide only a minor component to curvature generation (33, 68). Consistently, similar calculations applied to pacsin-$1^{F\text{-}BAR}$ showed that while charge and shape complementarity between pacsin-1 and the membrane may contribute sufficient energy to stabilize wide and even narrow tubules, they may not account for the generation of vesicular structures (27).

Experimentally, the membrane deformation potential of pacsin-$1^{F\text{-}BAR}$ is sensitive to mutations in the amphipathic wedge loop and ionic strength of the buffer, indicating a mechanism involving the insertion of its wedge loop into one leaflet of the bilayer (27). In order to assess the contribution of hydrophobic insertions on pacsin-mediated membrane sculpting, we estimated the wedge loop bending potential, taking into account the coupling of the two membrane leaflets (details are described in Appendix B) (33). The quantity ε describes the ratio between the surface of the outer and inner leaflet upon membrane bending. Insertion of motifs such as amphipathic helices or loops will counteract the initial surface mismatch. A comparison of ε and the surface area of these inserted motifs to the total membrane interaction surface of the protein scaffold provide an estimate of the energetic contribution from the wedge loop insertion to the bending process.

The N-BAR domains of endophilin and amphiphysin can effectively convert flat lipid bilayers into tubules with a radius R~20-25 nm *in vitro*. Based on the crystal structures of the two proteins, their insertion motifs of the N-BAR domains account for approximately 50% and 25% (0.5 and 0.25, expressed as fractions) of the total membrane interaction interface, respectively (13, 17, 20, 33). Both values are higher than the estimated excess surface ratio (ε~0.17-0.22) that would initially be generated by the bending of a flat membrane to a tube with a radius, R=20-25 nm (Appendix B). This implies that the hydrophobic units in N-BAR domains are sufficient to counteract the surface area mismatch in a bent bilayer, which is consistent with the conclusions that have been drawn from the elastic model of laterally coupled monolayers (33).

Unlike the amphipathic helices in amphiphysin that span a total area of 12 nm^2, the two wedge loops in the dimeric F-BAR domain of pacsin span only an area of 1.5 nm^2. Assuming the extreme case of 100% membrane coverage with the F-BAR domain, the highest surface occupancy of these insertion units is only 5%-7% of the total membrane interaction interface. This number is far below the required ε~0.31-0.5 for a tube with radius, R=10-15 nm (Appendix B). Similar conclusions can be made based on the elastic model of membrane monolayers. On an uncoupled monolayer, 10-12% of the membrane surface must be occupied by the insertion motif in order to generate a curvature with R=10 nm. Based on these estimations, it is unlikely that pacsin's potential of generating highly curved membrane morphologies is solely driven by the insertion mechanism.

4.5 Discussion

Bending membranes requires energy because bilayers tend to resist shape changes. Proteins contribute to this energy requirement via electrostatic interactions, scaffolding mechanisms, and the insertion of amphipathic helices or hydrophobic loops. Based on energetic considerations described above, it appears likely that the F-BAR domain of pacsin-1 relies on both scaffolding and hydrophobic insertions to deform membranes, with neither mechanism alone having the capacity to effectively shape membranes into the structures that were observed in our *in vitro* experiments. Both mechanisms may contribute additively to the deformation of membranes by counteracting the area mismatch between the two leaflets that would arise upon curvature generation, and by stabilizing a preferred membrane topology that is compatible with the shape imposed by the protein structure (27). A mismatch in geometry between proteins and the membrane would destabilize their interaction, leading to potential disruption of protein lattices and changes in membrane remodeling propensities.

During membrane remodeling, the system's total free energy is a summation of the protein-membrane interaction energy and the internal energies of the protein and bilayer:

$$E_{total} = I_{protein} + I_{bilayer} + E_{protein\text{-}bilayer}$$

We assume that within the scope of elastic Gaussian theory, both internal energy terms are constant. Consequently, the membrane-protein interaction represents the major variable energy term in the system. From plotting the radii of tubes and vesicles against the energy density (energy per area) required for protein-induced membrane

deformations, it is obvious that there are energetically equivalent structures that could potentially coexist (Appendix B; illustrated in Fig. 4.16 *B*). According to this simple approximation, a cylindrical structure (tubule) with a radius R and a spherical structure (vesicle) with a radius 2R represent systems with theoretically identical surface free energy density (Appendix B). These estimations suggest that the system can be subject to bimodality, producing either narrow membrane tubules or vesicular structures, consistent with our experimental observations. Bimodality, in contrast to bistability, does not assume an identical origin. Indeed, we observed markedly different membrane morphologies induced by full-length pacsin-1, pacsin-$1^{F\text{-}BAR}$ or PRD-bound pacsin-1 depending on the method that was used to prepare the initial liposomes. Differences in the frequency by which tubules and vesicles occur may be caused by differences of the initial liposome properties from which these structures arise.

Varying properties of the starting materials may elicit different apparent energetic barriers in the BAR protein-induced membrane deformation process. Variation in liposome properties such as lamellarity and size (curvature) could present different initial energy states that may dictate the likelihood of proteins to generate particular membrane morphologies in the system (Fig. 4.16 *B*). For example, more energy is required to generate the same final number of 30 nm-vesicles from a system that initially contains larger liposomes than one that contains smaller liposomes (Appendix B). Consistently, we observed that when given larger liposomes as the starting material (i.e. in FT and RSE liposomes, Fig. 4.14 *B*), pacsin-1-PRD produced higher numbers of tubules and fewer vesicular structures, the latter being the dominant

morphology when smaller liposomes (SFT liposomes) were provided as starting material.

Even though properties of the liposomes used in the *in vitro* assays could determine the outcome of the membrane sculpting process, the intrinsic structural characteristics of BAR domain proteins appear to be a main determinant of the range of morphologies that are generated. Under our experimental conditions, bimodality was observed in pacsin-1 and pacsin-$1^{F\text{-}BAR}$ induced membrane morphologies, but not in the typical F-BAR protein, $CIP4^{F\text{-}BAR}$. The versatile ability of pacsin-$1^{F\text{-}BAR}$ to stabilize tubules of different sizes and invaginations is attributed to its S-shaped conformation (encoding two principal curvatures) and wedge loop insertion (27). In contrast, $CIP4^{F\text{-}BAR}$ only produced wide tubules regardless of the liposome properties, coinciding with a single principle curvature of the domain that prefers membranes of more shallow curvature (21, 23).

The autoinhibition of full-length pacsin-1 and the role of its SH3 domains in regulating its membrane deformation activity have been demonstrated both *in vivo* (38) and *in vitro* (27, 28). Our liposome binding data showed that full-length pacsin-1 still interacts with membranes, albeit with decreased affinity, and prefers less-curved membranes compared to the isolated F-BAR domain. This may imply that other mechanisms, such as prevention of wedge loop insertion and/or protein oligomerization impair pacsin-1's membrane sculpting potential. In contrast, studies on endophilin-1 and its isolated N-BAR domain produced different results from comparable experiments with pacsin-1. Despite differences in membrane affinity, both full-length endophilin-1 and endophilin-$1^{N\text{-}BAR}$ still retained potent tubulation

activities. The presence of four amphipathic helices presented by the N-BAR domain suggests that the insertion mechanism dominates in endophilin-dependent membrane tubulation (17, 19). Differences in the average tubule diameters produced by full-length endophilin-1 and endophilin-1$^{N\text{-}BAR}$ could be due to different lateral protein-protein interactions, resulting in protein scaffolds with differing membrane curvature preferences.

While it is difficult to separate and quantify the relative contributions that affect protein-mediated membrane deformation, we demonstrate that high-affinity binding of the entire PRD to the SH3 domains of pacsin-1 results in a more efficient recruitment of the complex to membranes compared to that observed for the individual proteins. The high SH3-PRD affinity is dependent on intact core binding motifs in the PRD (aa768-792) (46, 52), as demonstrated by our pull-down and mutagenesis studies, and is required for the increased membrane deformation activities observed in pacsin-1 and endophilin-1. In short, binding of the PRD sequesters the SH3 domains away from the F-BAR or BAR domains, and appears to be the main mechanism of activation.

It is not immediately obvious why sequestration of SH3 domains away from the F-BAR or BAR domains would alter the membrane deformation capacity of the proteins. Yet, we identified several experimental conditions under which we observed tubulation with the isolated F-BAR and N-BAR domains, but vesiculation in the context of complexes containing full-length pacsin or endophilin and the PRD of dynamin-1. Binding of pacsin-1 to full-length GST-PRD (or SUMO-PRD) may have induced some formation of higher-order oligomers in the absence of membranes. We

observed a small shoulder to the left of the pacsin-PRD main elution peak in the gel filtration profile (Fig. 4.5 *A*), and also small amounts of the pacsin-PRD complex co-pelleting in the absence of liposomes (Fig. 4.7 *B*). Pacsin-1's altered membrane sculpting propensity could be a result of the PRD-SH3 interactions further enabling the arrangement of pacsin-1 into higher-order oligomers on the membrane to facilitate deformation. The formation of oligomers on membranes has been reported in several independent studies conducted on other BAR domain proteins (23, 34, 69).

Another possible explanation for the increased membrane deformation activity of the complex is more efficient targeting of pacsin-1 and endophilin-1 to membranes, as facilitated by their interaction with dynamin's PRD, imposes local steric confinement that can drive membrane deformation. Indeed, steric confinement of membrane-bound green fluorescent proteins and the ENTH domain of epsin have been shown to induce tubulation from targeted domains on giant unilamellar vesicles (70, 71), a process that is also likely dependent on membrane properties (70, 72). Electrostatic binding of positively charged surfaces from both pacsin-1 and PRD may locally attract acidic lipids, altering local membrane mechanical properties that may favor deformation. Furthermore, this enhanced complex-membrane interaction could stress the bilayer to an extent that it becomes unstable. This instability could lead to or promote vesiculation under additional perturbations, like those found in the negative staining procedure. In contrast, tubular structures such as those stabilized by endophilin's N-BAR domain, have a high degree of curvature yet remain stable under the experimental conditions used here, suggesting a PRD-complex specific phenomenon. Recently, Boucrot *et. al.* (73) showed that shallow insertions of

amphipathic helices by epsin's ENTH domains are sufficient for vesiculation, whereas the presence of BAR domain scaffolds could limit the full potential of hydrophobic insertions, such as in endophilin and amphiphysin. It is possible that the limiting effect of the BAR scaffold could be diminished upon complex formation between the full-length proteins and the PRD, thus unleashing the vesiculation potential of the proteins driven by shallow hydrophobic insertions under certain conditions.

Even under the simple, minimalist conditions of *in vitro* experiments, we have identified multiple factors that could affect the thermodynamics and kinetics of membrane remodeling. In cells, the plasma membrane is constantly changing due to various cellular processes. As an adaptable and efficient membrane sculptor, regulated by its SH3 module, pacsin-1 could function at various stages during membrane trafficking. The importance of pacsin-1 is evident in synaptic vesicle recycling, where it recruits dynamin to fission sites (74). Furthermore, multiple studies have revealed a principle role for pacsin-1 at the synapse during high neuronal activity (40, 42, 75). In that scenario, dephosphorylation of dynamin-1 on its PRD leads to complex formation with pacsin-1 and an increase in bulk endocytosis (40). One hypothesis is that pacsin may contribute in a more regulated and direct fashion to the endocytotic capacity of a cell under certain conditions, likely facilitated by the actin cytoskeleton, a model that will need further corroboration. In addition, cellular membranes may differentially attract a distinct subset of BAR domain-containing proteins in a curvature-dependent manner. Alternatively, a difference in local curvatures may determine the outcome of BAR domain-mediated membrane interactions.

4.6 Conclusion

Our *in vitro* experiments provide simple models that suggest a synergistic relationship between pacsin (or endophilin) and dynamin in membrane remodeling, which is an energetically expensive process that is dependent on both protein structural characteristics and membrane properties. We observed that details in the starting liposome materials, which differ depending on the preparation protocols-, could affect the resulting *in vitro* membrane deformation activities of pacsin-1 constructs. Functional versatility of pacsin-1 observed in this study is mainly attributed to protein structure, with a dependence on membrane properties, but the significance of this versatility to cellular functions is still unclear. The detailed molecular mechanism of protein-membrane interplay in facilitating membrane fission is only beginning to be unraveled.

References

1. Shibata, Y., J. Hu, M.M. Kozlov, and T.A. Rapoport. 2009. Mechanisms shaping the membranes of cellular organelles. Annu. Rev. Cell Dev. Biol. 25: 329–354.

2. Henne, W.M., E. Boucrot, M. Meinecke, E. Evergren, Y. Vallis, et al. 2010. FCHo Proteins Are Nucleators of Clathrin-Mediated Endocytosis. Science. 328: 1281–1284.

3. Pucadyil, T.J., and S.L. Schmid. 2009. Conserved Functions of Membrane Active GTPases in Coated Vesicle Formation. Science. 325: 1217–1220.

4. Ferguson, S.M., S. Ferguson, A. Raimondi, S. Paradise, H. Shen, et al. 2009. Coordinated actions of actin and BAR proteins upstream of dynamin at endocytic clathrin-coated pits. Developmental Cell. 17: 811–822.

5. Wu, M., B. Huang, M. Graham, A. Raimondi, J.E. Heuser, et al. 2010. Coupling between clathrin-dependent endocytic budding and F-BAR-dependent tubulation in a cell-free system. Nat Cell Biol. 12: 902–908.

6. Doherty, G.J., and H.T. McMahon. 2009. Mechanisms of endocytosis. Annu. Rev. Biochem. 78: 857–902.

7. Merrifield, C.J., B. Qualmann, M.M. Kessels, and W. Almers. 2004. Neural Wiskott Aldrich Syndrome Protein (N-WASP) and the Arp2/3 complex are recruited to sites of clathrin-mediated endocytosis in cultured fibroblasts. Eur. J. Cell Biol. 83: 13–18.

8. Kessels, M.M., and B. Qualmann. 2002. Syndapins integrate N-WASP in receptor-mediated endocytosis. EMBO J. 21: 6083–6094.

9. Qualmann, B., D. Koch, and M.M. Kessels. 2011. Let's go bananas: revisiting the endocytic BAR code. EMBO J. 30: 3501–3515.

10. Itoh, T., and P. DeCamilli. 2006. BAR, F-BAR (EFC) and ENTH/ANTH domains in the regulation of membrane–cytosol interfaces and membrane curvature. Biochimica et Biophysica Acta (BBA) - Molecular and Cell Biology of Lipids. 1761: 897–912.

11. McMahon, H.T., and J.L. Gallop. 2005. Membrane curvature and mechanisms of dynamic cell membrane remodelling. Nat Cell Biol. 438: 590–596.

12. Farsad, K., N. Ringstad, K. Takei, S.R. Floyd, K. Rose, et al. 2001. Generation of high curvature membranes mediated by direct endophilin bilayer interactions. The Journal of Cell Biology. 155: 193–200.

13. Peter, B.J., H.M. Kent, I.G. Mills, Y. Vallis, P.J.G. Butler, et al. 2004. BAR domains as sensors of membrane curvature: the amphiphysin BAR structure. Science. 303: 495–499.

14. Takei, K., V.I. Slepnev, V. Haucke, and P. De Camilli. 1999. Functional partnership between amphiphysin and dynamin in clathrin-mediated endocytosis. Nat Cell Biol. 1: 33–39.

15. Tsujita, K., S. Suetsugu, N. Sasaki, M. Furutani, T. Oikawa, et al. 2006. Coordination between the actin cytoskeleton and membrane deformation by a novel membrane tubulation domain of PCH proteins is involved in endocytosis. The Journal of Cell Biology. 172: 269–279.

16. Mattila, P.K., A. PykAlAinen, J. Saarikangas, V.O. Paavilainen, H. Vihinen, et al. 2007. Missing-in-metastasis and IRSp53 deform PI(4,5)P2-rich membranes by an inverse BAR domain-like mechanism. The Journal of Cell Biology. 176: 953–964.

17. Gallop, J.L., C.C. Jao, H.M. Kent, P.J.G. Butler, P.R. Evans, et al. 2006. Mechanism of endophilin N-BAR domain-mediated membrane curvature. EMBO J. 25: 2898–2910.

18. Jao, C.C., B.G. Hegde, J.L. Gallop, P.B. Hegde, H.T. McMahon, et al. 2010. Roles of Amphipathic Helices and the Bin/Amphiphysin/Rvs (BAR) Domain of Endophilin in Membrane Curvature Generation. Journal of Biological Chemistry. 285: 20164–20170.

19. Masuda, M., S. Takeda, M. Sone, T. Ohki, H. Mori, et al. 2006. Endophilin BAR domain drives membrane curvature by two newly identified structure-based mechanisms. EMBO J. 25: 2889–2897.

20. Weissenhorn, W. 2005. Crystal Structure of the Endophilin-A1 BAR Domain. Journal of Molecular Biology. 351: 653–661.

21. Shimada, A., H. Niwa, K. Tsujita, S. Suetsugu, K. Nitta, et al. 2007. Curved EFC/F-BAR-Domain Dimers Are Joined End to End into a Filament for Membrane Invagination in Endocytosis. Cell. 129: 761–772.

22. Henne, W.M., H.M. Kent, M.G.J. Ford, B.G. Hegde, O. Daumke, et al. 2007. Structure and Analysis of FCHo2 F-BAR Domain: A Dimerizing and Membrane Recruitment Module that Effects Membrane Curvature. Structure. 15: 839–852.

23. Frost, A., R. Perera, A. Roux, K. Spasov, O. Destaing, et al. 2008. Structural Basis of Membrane Invagination by F-BAR Domains. Cell. 132: 807–817.

24. Saarikangas, J., H. Zhao, A. PykAlAinen, P. LaurinmAki, P.K. Mattila, et al.

2009. Molecular Mechanisms of Membrane Deformation by I-BAR Domain Proteins. Current Biology. 19: 95–107.

25. PykAlAinen, A., M. Boczkowska, H. Zhao, J. Saarikangas, G. Rebowski, et al. 2011. Pinkbar is an epithelial-specific BAR domain protein that generates planar membrane structures. Nat Struct Mol Biol. 18: 902–907.

26. Guerrier, S., J. Coutinho-Budd, T. Sassa, A. Gresset, N.V. Jordan, et al. 2009. The F-BAR Domain of srGAP2 Induces Membrane Protrusions Required for Neuronal Migration and Morphogenesis. Cell. 138: 990–1004.

27. Wang, Q., M.V.A.S. Navarro, G. Peng, E. Molinelli, S.L. Goh, et al. 2009. Molecular mechanism of membrane constriction and tubulation mediated by the F-BAR protein Pacsin/Syndapin. Proc. Natl. Acad. Sci. U.S.A. 106: 12700–12705.

28. Rao, Y., Q. Ma, A. Vahedi-Faridi, A. Sundborger, A. Pechstein, et al. 2010. Molecular basis for SH3 domain regulation of F-BAR-mediated membrane deformation. Proc. Natl. Acad. Sci. U.S.A. 107: 8213–8218.

29. Shimada, A., K. Takano, M. Shirouzu, K. Hanawa-Suetsugu, T. Terada, et al. 2010. Mapping of the basic amino-acid residues responsible for tubulation and cellular protrusion by the EFC/F-BAR domain of pacsin2/Syndapin II. FEBS LETTERS. 584: 1111–1118.

30. Edeling, M.A., S. Sanker, T. Shima, P.K. Umasankar, S. Höning, et al. 2009. Structural requirements for PACSIN/Syndapin operation during zebrafish embryonic notochord development. PLoS ONE. 4: e8150.

31. Plomann, M., J.G. Wittmann, and M.G. Rudolph. 2010. A Hinge in the Distal End of the PACSIN 2 F-BAR Domain May Contribute to Membrane-Curvature Sensing. Journal of Molecular Biology. 400: 129–136.

32. Zimmerberg, J., and M.M. Kozlov. 2005. How proteins produce cellular membrane curvature. Nat Rev Mol Cell Biol. 7: 9–19.

33. Campelo, F., H.T. McMahon, and M.M. Kozlov. 2008. The Hydrophobic Insertion Mechanism of Membrane Curvature Generation by Proteins⋆. Biophys. J. 95: 2325–2339.

34. Yarar, D., C.M. Waterman-Storer, and S.L. Schmid. 2007. SNX9 Couples Actin Assembly to Phosphoinositide Signals and Is Required for Membrane Remodeling during Endocytosis. Developmental Cell. 13: 43–56.

35. Wang, Q., H.Y.K. Kaan, R.N. Hooda, S.L. Goh, and H. Sondermann. 2008. Structure and plasticity of Endophilin and Sorting Nexin 9. Structure. 16: 1574–1587.

36. Modregger, J., B. Ritter, B. Witter, M. Paulsson, and M. Plomann. 2000. All three PACSIN isoforms bind to endocytic proteins and inhibit endocytosis. Journal of Cell Science. 113: 4511–4521.

37. Qualmann, B., and R.B. Kelly. 2000. Syndapin isoforms participate in receptor-mediated endocytosis and actin organization. The Journal of Cell Biology. 148: 1047–1062.

38. Kumar, V., R. Fricke, D. Bhar, S. Reddy-Alla, K.S. Krishnan, et al. 2009. Syndapin promotes formation of a postsynaptic membrane system in Drosophila. Mol. Biol. Cell. 20: 2254–2264.

39. Dharmalingam, E., A. Haeckel, R. Pinyol, L. Schwintzer, D. Koch, et al. 2009. F-BAR Proteins of the Syndapin Family Shape the Plasma Membrane and Are Crucial for Neuromorphogenesis. Journal of Neuroscience. 29: 13315–13327.

40. Clayton, E.L., V. Anggono, K.J. Smillie, N. Chau, P.J. Robinson, et al. 2009. The Phospho-Dependent Dynamin-Syndapin Interaction Triggers Activity-Dependent Bulk Endocytosis of Synaptic Vesicles. Journal of Neuroscience. 29: 7706–7717.

41. Ferguson, S.M., G. Brasnjo, M. Hayashi, M. Wölfel, C. Collesi, et al. 2007. A selective activity-dependent requirement for dynamin 1 in synaptic vesicle endocytosis. Science. 316: 570–574.

42. Andersson, F., J. Jakobsson, P. Low, O. Shupliakov, and L. Brodin. 2008. Perturbation of Syndapin/PACSIN Impairs Synaptic Vesicle Recycling Evoked by Intense Stimulation. Journal of Neuroscience. 28: 3925–3933.

43. Quan, A., J. Xue, J. Wielens, K.J. Smillie, V. Anggono, et al. 2012. Phosphorylation of syndapin I F-BAR domain at two helix-capping motifs regulates membrane tubulation. Proc. Natl. Acad. Sci. U.S.A. 109: 3760–3765.

44. Shpetner, H.S., J.S. Herskovits, and R.B. Vallee. 1996. A Binding Site for SH3 Domains Targets Dynamin to Coated Pits. Journal of Biological Chemistry. 271: 13–16.

45. Okamoto, P.M., J.S. Herskovits, and R.B. Vallee. 1997. Role of the Basic, Proline-rich Region of Dynamin in Src Homology 3 Domain Binding and Endocytosis. Journal of Biological Chemistry. 272: 11629–11635.

46. Grabs, D., V.I. Slepnev, Z. Songyang, C. David, M. Lynch, et al. 1997. The SH3 Domain of Amphiphysin Binds the Proline-rich Domain of Dynamin at a Single Site That Defines a New SH3 Binding Consensus Sequence. Journal of Biological Chemistry. 272: 13419–13425.

47. Muhlberg, A.B., D.E. Warnock, and S.L. Schmid. 1997. Domain structure and

intramolecular regulation of dynamin GTPase. EMBO J. 16: 6676–6683.

48. Liu, Y.-W., M.C. Surka, T. Schroeter, V. Lukiyanchuk, and S.L. Schmid. 2008. Isoform and Splice-Variant Specific Functions of Dynamin-2 Revealed by Analysis of Conditional Knock-Out Cells. Mol. Biol. Cell. 19: 5347–5359.

49. Barylko, B., L. Wang, D.D. Binns, J.A. Ross, T.C. Tassin, et al. 2010. The Proline/Arginine-Rich Domain Is a Major Determinant of Dynamin Self-Activation. Biochemistry. 49: 10592–10594.

50. Liu, Y.W., S. Neumann, R. Ramachandran, S.M. Ferguson, T.J. Pucadyil, et al. 2011. PNAS Plus: Differential curvature sensing and generating activities of dynamin isoforms provide opportunities for tissue-specific regulation. Proc. Natl. Acad. Sci. U.S.A. 108: E234–E242.

51. Raimondi, A., S.M. Ferguson, X. Lou, M. Armbruster, S. Paradise, et al. 2011. Overlapping Role of Dynamin Isoforms in Synaptic Vesicle Endocytosis. Neuron. 70: 1100–1114.

52. Anggono, V., and P.J. Robinson. 2007. Syndapin I and endophilin I bind overlapping proline-rich regions of dynamin I: role in synaptic vesicle endocytosis. Journal of Neurochemistry. 102: 931–943.

53. Buboltz, J.T., and G.W. Feigenson. 1999. A novel strategy for the preparation of liposomes: rapid solvent exchange. Biochim. Biophys. Acta. 1417: 232–245.

54. Zhao, J., J. Wu, F.A. Heberle, T.T. Mills, P. Klawitter, et al. 2007. Phase studies of model biomembranes: Complex behavior of DSPC/DOPC/Cholesterol. Biochimica et Biophysica Acta (BBA) - Biomembranes. 1768: 2764–2776.

55. Qualmann, B., J. Roos, P.J. DiGregorio, and R.B. Kelly. 1999. Syndapin I, a synaptic dynamin-binding protein that associates with the neural Wiskott-Aldrich syndrome protein. Mol. Biol. Cell. 10: 501–513.

56. McPherson, P.S., F. Simpson, N.K. Hussain, B. Qualmann, R.B. Kelly, et al. 1999. SH3-domain-containing proteins function at distinct steps in clathrin-coated vesicle formation. Nat Cell Biol. 1: 119–124.

57. Kiessling, V., C. Wan, and L.K. Tamm. 2009. Domain coupling in asymmetric lipid bilayers. BBA - Biomembranes. 1788: 64–71.

58. Devaux, P.F. 1991. Static and dynamic lipid asymmetry in cell membranes. Biochemistry. 30: 1163–1173.

59. Ringstad, N., Y. Nemoto, and P. De Camilli. 1997. The SH3p4/Sh3p8/SH3p13 protein family: Binding partners for synaptojanin and dynamin via a Grb2-like

Src homology 3 domain. Proceedings of the National Academy of Sciences. 94: 8569–8574.

60. Ringstad, N., H. Gad, P. Low, G. Di Paolo, L. Brodin, et al. 1999. Endophilin/SH3p4 is required for the transition from early to late stages in clathrin-mediated synaptic vesicle endocytosis. Neuron. 24: 143–154.

61. Llobet, A., J.L. Gallop, J.J.E. Burden, G. Camdere, P. Chandra, et al. 2011. Endophilin Drives the Fast Mode of Vesicle Retrieval in a Ribbon Synapse. Journal of Neuroscience. 31: 8512–8519.

62. Milosevic, I., S. Giovedi, X. Lou, A. Raimondi, C. Collesi, et al. 2011. Recruitment of Endophilin to Clathrin-Coated Pit Necks Is Required for Efficient Vesicle Uncoating after Fission. Neuron. 72: 587–601.

63. Pick, U. 1981. Liposomes with a large trapping capacity prepared by freezing and thawing of sonicated phospholipid mixtures. Arch. Biochem. Biophys. 212: 186–194.

64. Higashi, K., S. Suzuki, H. Fujii, and Y. Kirino. 1987. Preparation and some properties of giant liposomes and proteoliposomes. Journal of Biochemistry. 101: 433–440.

65. Mayer, L.D., M.J. Hope, P.R. Cullis, and A.S. Janoff. 1985. Solute distributions and trapping efficiencies observed in freeze-thawed multilamellar vesicles. Biochim. Biophys. Acta. 817: 193–196.

66. Mayer, L.D., M.J. Hope, and P.R. Cullis. 1986. Vesicles of variable sizes produced by a rapid extrusion procedure. Biochim. Biophys. Acta. 858: 161–168.

67. Manneville, J.-B., C. Leduc, B. Sorre, and G. Drin. 2012. Studying in vitro membrane curvature recognition by proteins and its role in vesicular trafficking. Methods Cell Biol. 108: 47–71.

68. Campelo, F., G. Fabrikant, H.T. McMahon, and M.M. Kozlov. 2010. Modeling membrane shaping by proteins: Focus on EHD2 and N-BAR domains. FEBS Lett. 584: 1830–1839.

69. Mim, C., H. Cui, J. Gawronski-Salerno, A. Frost, E. Lyman, et al. 2012. Structural Basis of Membrane Bending by the N-BAR Protein Endophilin. Cell. 149: 137–145.

70. Stachowiak, J.C., C.C. Hayden, and D.Y. Sasaki. 2010. Steric confinement of proteins on lipid membranes can drive curvature and tubulation. Proc. Natl. Acad. Sci. U.S.A. 107: 7781–7786.

71. Stachowiak, J.C., E.M. Schmid, C.J. Ryan, H.S. Ann, D.Y. Sasaki, et al. 2012. Membrane bending by protein–protein crowding. Nat Cell Biol. 14: 944–949.

72. Liu, A.P., D.L. Richmond, L. Maibaum, S. Pronk, P.L. Geissler, et al. 2008. Membrane-induced bundling of actin filaments. Nat Phys. 4: 789–793.

73. Boucrot, E., A. Pick, G. Çamdere, N. Liska, E. Evergren, et al. 2012. Membrane Fission Is Promoted by Insertion of Amphipathic Helices and Is Restricted by Crescent BAR Domains. Cell. 149: 124–136.

74. Koch, D., I. Spiwoks-Becker, V. Sabanov, A. Sinning, T. Dugladze, et al. 2011. Proper synaptic vesicle formation and neuronal network activity critically rely on syndapin I. EMBO J. 30: 4955–4969.

75. Anggono, V., K.J. Smillie, M.E. Graham, V.A. Valova, M.A. Cousin, et al. 2006. Syndapin I is the phosphorylation-regulated dynamin I partner in synaptic vesicle endocytosis. Nat Neurosci. 9: 752–760.

CHAPTER 5

HIV-1 Gag can sense the cholesterol and acyl chain environment in model membranes[**]

5.1 Abstract

Negatively charged lipid bilayer mixtures were previously found to favor binding of HIV-1 Gag to membranes. While there are cellular evidence proposing that HIV-1 proteins bud from lipid rafts, it had been unclear whether HIV-1 Gag has an increased affinity for ordered, raft-like lipid compositions. Using *in vitro* flotation assays and ESR measurements, we found that HIV-1 Gag is sensitive to cholesterol concentrations and acyl chain saturations of the bilayer, in a way that is not directly correlated with the membrane order.

5.2 Introduction

The assembly and budding of retroviruses from host cells are important processes to ensure the viability of retroviruses in their replication lifecycle. The retroviral structural Gag plays a vital role in these processes at the PM via its N-terminal MA domain (1). The MA domain of HIV-1 Gag mediates interaction with negatively charged phospholipids at the membrane via three structural features: a conserved polybasic patch, an N-terminal myristate group, and a binding pocket for

[**] The following sections are rewritten using main results from: Dick, R.A., Goh, S.L., Feigenson, G.W., and Vogt, V.M. 2012. HIV-1 Gag can sense the cholesterol and acyl chain environment in model membranes. Proc. Natl. Acad. Sci. U.S.A. 109 (46): 18761-18766. S.L.G. prepared liposome mixtures for extrusion, performed ESR experiments and analyzed ESR data. R.A.D. prepared all constructs, performed and analyzed all liposome flotation assays.

$PI(4,5)P_2$ (2, 3). Indeed, the presence of Gag alone is sufficient for assembly and budding, generating virus-like particles (4). However, much is still unknown about the mechanism of viral assembly and budding, especially regarding the role played by lipids in the PM of host cells.

All retroviral particles have a lipid envelope that is derived from the PM of their host cells. Interestingly, many studies have shown that the lipid compositions of viral envelopes are not identical to that of the PM of the host cell (4-7). A recent mass spectrometry study comparing lipid compositions of virus envelopes and host cell PM revealed that viral envelopes from HIV-1 and murine leukemia virus are significantly enriched in several lipid species, including phosphoinositides, glycosphongolipids, ceramide and cholesterol (4). Moreover, they identified the enrichment of $PI(4,5)P_2$, and demonstrated that the depletion of $PI(4,5)P_2$ reduced HIV budding, confirming previous implications on the importance of $PI(4,5)P_2$ in facilitating HIV-Gag-membrane association (2, 3, 8).

The disparity in the lipid compositions of viral envelope and host cell PM invites questions of how retrovirus obtains its lipids, and more importantly, questions regarding the interplay between viral proteins and lipids in the plasma membrane in facilitating assembly and budding. One hypothesis is that viral particles bud out of selected regions in the plasma membrane that are enriched in specific lipids, resulting in viral lipid envelopes with compositions that are not representative of the average plasma membrane lipid composition. This hypothesis became more attractive when Simons and Ikonen introduced the concept of "lipid rafts" as functional domains in the plasma membrane that facilitate various cellular processes (9). The lipid components

of rafts include sphingolipids, glycosphingolipids and cholesterol; all of which are enriched in viral envelopes (4-7). On the other hand, raft-like domains could be induced by Gag upon membrane binding and formation of a Gag lattice.

One consistent commonly observed enrichment in viral envelopes is that of cholesterol. The depletion of cholesterol from virion envelopes using methyl-β-cyclodextrin affected the maintenance of intact HIV-1 and simian immunodeficiency virus structures, and decreased viral infectivity (10-12). Not only is cholesterol important for efficient viral assembly and budding, it is also required for the formation of lipid rafts, based on live cells and model membrane studies (13). Chemically well-defined mixtures that contain a high-melting saturated lipid such as DSPC or sphingomyelin, a low-melting unsaturated phospholipid such as DOPC, and cholesterol produce macroscopic Ld and Lo phase separation that can be used to describe micron-sized rafts in cells (14). Recent studies have also shown that the coexisting Lo and Ld domains can even be nanoscopic (14, 15). Since cholesterol seems to be the common denominator in the formation of lipid rafts and the maintenance of virulence in retroviruses, it seems very plausible that viral assembly and budding is closely connected to, and even dependent on lipid rafts. Despite that, it is yet to be determined whether retroviruses target pre-existing lipid rafts in the PM for assembly and budding, mainly because stable lipid rafts have not been directly observed in resting cells.

Another major challenge to understanding how viral particles acquire raft-like lipid composition is the lack of evidence for the presence of rafts in the PM inner leaflet. Unlike outer leaflet models, mixtures prepared from lipids representing the

inner leaflet of the PM such as PE and PS do not display liquid-liquid phase separation (16). However, coupling of the two leaflets has been demonstrated on freely suspended GUVs (17) and supported bilayers (18, 19), where phase separation on one leaflet can influence the phase behavior of lipids in the opposite leaflet. While leaflet coupling provides an alternative mechanism for the inner leaflet to acquire raft-like heterogeneity, the detailed conditions under which domains can be induced should be closely examined in freely suspended bilayers.

In this work, we examined the influence of cholesterol and acyl chain compositions on HIV-1 Gag membrane affinity using liposome flotation assays. Simple model membrane mixtures of PC, PS and cholesterol were chosen for our systematic studies. Even though they are not good representations of lipids typically found in the inner leaflet of the PM, their phase behavior is better understood, and known phase boundaries can be used to guide appropriate mixture selections (15, 20). We found behavior that had not previously been reported, that Gag membrane affinity is sensitive to acyl chain saturation, as well as to previously recognized net negative charge and cholesterol content in the mixtures examined.

5.3 Experimental Methods

5.3.1 Materials

All phospholipids were purchased from Avanti Polar Lipids (Alabaster, AL). Cholesterol was purchased from Nu Chek Prep (Elysian, MN) and spin-labeled fatty acid, 16-DOXYL-stearic acid (16-DSA) was from Sigma-Aldrich (St. Loius, MO). Concentration of phospholipid stocks were determined to < 1% via inorganic

phosphate assay (21). Cholesterol stock was prepared by standard gravimetric methods to ~0.2%. Purity of all phospholipids were determined to be > 99% via TLC. Briefly, lipids were spotted onto washed and activated silica gel GHL UNIPLATES (Analtech, Newark, DE) and developed with 65/25/4 = chloroform/methanol/water for phosphatidylcholines, and 60/30/6 = chloroform/methanol/ammonia for phosphatidylserines. For TLC of PI(4,5)P2 lipids, the plates were washed with 5% potassium oxalate solution, activated, and developed with 40/13/15/12/7 = chloroform/ methanol/ acetone/ acetic acid/ water.

5.3.2 Liposome preparation (for binding and flotation assays)

Multi-lamellar liposomes were prepared according to the RSE method described in (22), modified as previously described (20). After dispensing lipids into glass tubes, buffer (20 mM HEPES, pH 7.0) was added to each sample. The mixture was vortexed under vacuum for 90 s and sealed under argon gas, yielding 10 mg/mL hydrated liposomes. Liposome samples were stored at 4°C up to one week before extrusion.

To prepare large unilamellar vesicles (LUVs), the Avanti Mini-Extruder block was heated to 45°C. Liposomes were extruded 41 times through 100 nm polycarbonate filters (Avanti Polar Lipids, Inc.). Extruded liposomes were used within one week. (Robert A. Dick, R.A.D, performed the extrusions).

5.3.3 Liposome binding and flotation assay

All liposome binding and flotation assays were performed by R.A.D., as described in (23). Briefly, radioactively labeled HIV-Gag was translated in the TNT coupled T7 rabbit reticulocyte reaction (Promega) with [35S]methionine/cysteine

added to the mix (Perkin-Elmer; ExPRE35S35 protein labeling mix). Liposome binding assays in large-format was performed for experiments in Fig. 5.1 and 5.2, as described in (24); small-format assays was performed with modifications for Fig. 5.3, described previously in (25). 5 μL of the reticulocyte transcription reaction was diluted three-fold in buffer (20 mM HEPES, pH 7.0), followed by addition of 50 μg of extruded LUVs (final LUV concentration was 8.5 mg/mL). The mix was incubated at ~22°C for 10 min, before layering it onto a sucrose gradient. Samples were centrifuged at 90,000 rpm in a TLA-100 rotor (Beckman) for 1 hour. Four fractions from each reaction were collected, and analyzed using SDS-PAGE.

5.3.4 ESR sample preparation

Multi-lamellar liposomes were prepared according to the RSE method described above. Each sample contained ~1800 nmoles of lipids and 0.2 mol% of the spin label 16-DSA. After the addition of buffer (20mM HEPES, pH 7.0, 30mM NaCl, 0.4mM $MgCl_2$), the mixture was vortexed under vacuum for 90 s and sealed under argon gas, yielding ~ 1 mg/mL hydrated liposomes. Samples were then placed into a 50°C water bath and cooled to ambient temperature at 2°C/hour. Liposomes were pelleted and transferred to 1.5-1.8 x 100 mm glass capillaries before measurement. ESR spectra of all samples were collected on a 9.4 GHz Bruker cw-ESR EMS spectrometer at ambient temperature. Typical instrument settings were: center field = 3320 G, sweep width = 100 G, modulation frequency = 100 kHz, modulation amplitude = 1 G, time constant = conversion time = 81.92 s, resolution = 2000 points. Nine scans were averaged for each sample.

5.3.5 ESR data analysis

The first derivative of the spectra for each sample was baseline-corrected and normalized using the peak maximum. A_{max} and A_{min} were determined directly from the spectra, as shown in Fig. 5.1. The order parameter of each sample was calculated according to Schorn and Marsh (26) using the hyperfine tensor (A_{xx}, A_{yy}, A_{zz}) = (5.9, 5.4, 32.9 G), using the following equation:

$$S = \frac{A_{max} - A_{min}}{2A_{zz} - (A_{xx} + A_{yy})}$$

where S is the order parameter.

5.4 Results

To investigate the effects of cholesterol, acyl chains and net negative charge on HIV-Gag-membrane interactions, we used liposome flotation assays. Radiolabeled Gag was synthesized in an *in vitro* reticulocyte translation system, and binding to LUVs was measured by flotation through a sucrose gradient (24, 27). ESR was used to probe membrane order in model membrane mixtures. The spin-label probe, 16-DSA, is a 16-carbon fatty acid, with a nitroxide labeled at the end of its acyl chain (Fig. 5.2). It is presumed to have relatively equal partitioning into Ld and Lo phase. Hence, the nitroxide is able to report on the order of its local environment in both Ld and Lo phases, if they coexist in a mixture.

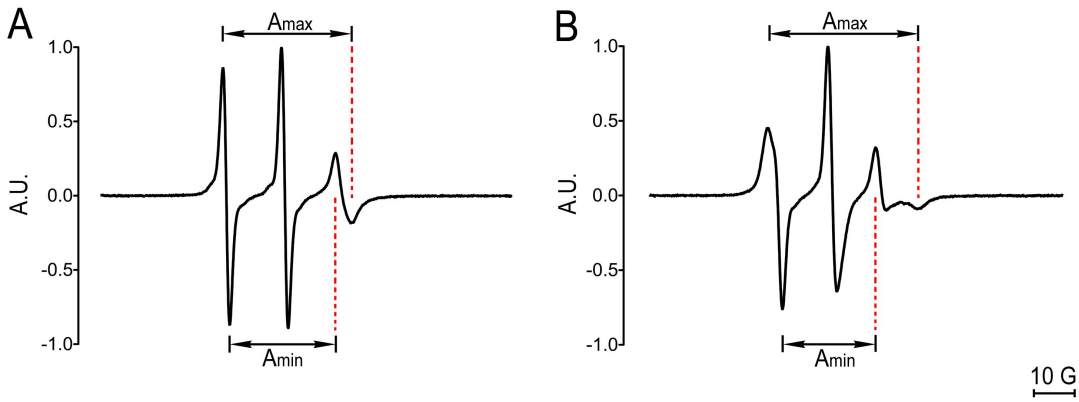

Figure 5.1. Typical 9.4 GHz ESR spectra for 16-DSA in Ld and Lo phases. Spectra were normalized, A_{max} and A_{min} that were used for order parameter calculations are indicated. (A) 16-DSA in an Ld phase with composition: DOPC/DOPS = 0.70/0.30. (B) 16-DSA in an Lo phase with composition: DOPC/DOPS/CHOL = 0.07/0.30/0.63. Data was collected as described in Materials and Methods.

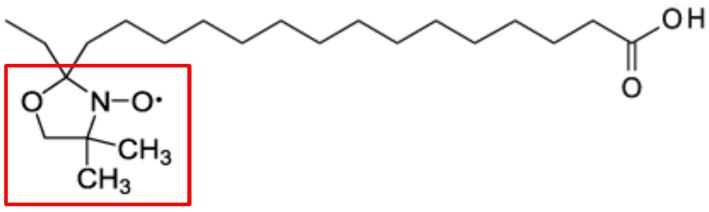

Figure 5.2. Structure of 16-DSA. The nitroxide spin-label (*red box*) is located at the end of the 16:0 fatty acyl chain.

5.4.1 Acyl chain saturation affects the membrane affinity of HIV-1 Gag

Increasing the fraction of negatively charged lipids such as phosphatidylserine (PS) has been found previously to enhance membrane binding of HIV-1 Gag (24, 27, 28). Here, we systematically examined the effects of PS concentrations on Gag-liposome interactions in three different binary PC/PS mixtures. The binary mixtures differ mainly in their acyl chain compositions: DOPC/DOPS, where each phospholipid has two 18:1 (oleoyl) chains; POPC/POPS, where each lipid has one 16:0 (palmitoyl) and one 18:1 (oleoyl) chain; and a natural mixture of egg-PC/brain-PS, where the major types of acyl chains in the PC are 33% 16:0, 32% 18:1, 17% 18:2, and 12% 18:0, whereas brain-PS consisted of mainly 18:0, 18:1 chains. The natural mixture is commonly used in the field for protein-membrane studies and was chosen specifically for comparison with the other two synthetic lipid mixtures. For each binary mixture, a series of samples containing 20% to 90% PS were prepared and tested for Gag membrane affinity.

As expected, the general trend revealed an increase in Gag binding as %PS increased (Fig. 5.3 *A*). However, we also observed that each binary mixture displayed distinct trends. While Gag binding remained low for 20-30% PS in all three binary mixtures, we observed a steep rise in binding for DOPC/DOPS at 40% PS, where Gag had at least five times more membrane affinity compared to the other two mixtures at the same PS concentration. Indeed, Gag appeared to reach its maximum binding to DOPC/DOPS mixtures at 50% PS, whereas the increase in membrane binding in POPC/POPS was gradual and only reached a lower maximum at 80-90% PS. On the

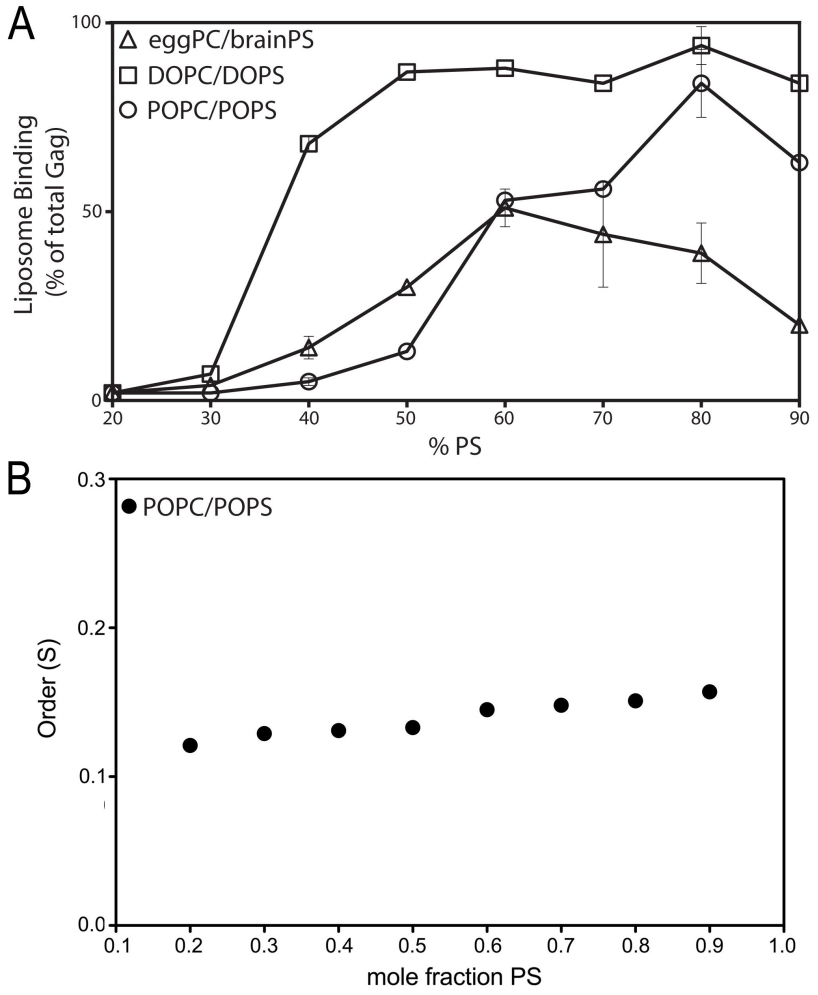

Figure 5.3. Acyl chain saturation affects the membrane affinity of HIV-1 Gag in binary mixtures. (A) [^{35}S]methionine-labeled HIV-1 Gag synthesized in reticulocyte extracts was incubated with extruded 100 nm-liposomes. Binding to three types of binary mixtures with increasing PS mole fractions were determined in flotation assays, via SDS-PAGE and fluorography, as described in Materials and Methods. The percentage of Gag floated was plotted as a function of increasing % PS. Error bars indicate SD (N = 3) for replicas performed at 40% and 80% PS for all three mixtures, and at 60% and 70% for egg-PC/brain-PS. (B) Membrane order, S, in POPC/POPS mixtures were determined via ESR, and plotted as a function of increasing mole fraction PS. (Figure 3 *A* obtained from (23); flotation assays analyzed by R.A.D.).

other hand, Gag binding to egg-PC/brain-PS mixtures increased up to 60% PS, but then decreased slightly at high PS concentrations.

To see if increasing PS concentration affects the packing of lipids in the bilayer, we measured the membrane order of mixtures in the POPC/POPS series using ESR. We found that the order only increased very slightly towards high %PS (Fig. 5.3 *B*). This was expected due to the tendency of PS to become protonated at high concentrations in the bilayer to overcome the electrostatic repulsion of PS-PS head groups. Protonation neutralizes the negative charges on PS molecules, resulting in a lowering of surface charge potential and allowing the molecules to pack more closely in the bilayer. In fact, in bilayers alone, the surface charge potential (or zeta potential) does not continue to increase significantly with the concentration of charged lipids in the bilayer beyond ~30% of charged lipids, regardless of the types of acyl chains (29). This means that the overall negative charge of each lipid mixture examined in Fig.5.3 at a particular PS concentration is equal.

The effect of increasing PS concentration on membrane order seems negligible compared to the huge changes in the Gag binding curves. Despite the surface potential being equal at each %PS examined for each binary mixture, the higher preference of Gag for DOPC/DOPS mixtures suggests that the proteins experienced a higher effective PS concentration in lipids with 18:1, 18:1 chains.

5.4.2 Cholesterol enhances membrane binding of Gag

Many cellular studies provide evidence for the hypothesis that "HIV-1 buds from rafts" (30). Yet, no systematic studies have been performed to study the effects of cholesterol on Gag membrane binding. We employed four series of phospholipid

mixtures with increasing cholesterol concentrations to investigate Gag membrane binding: DSPC (18:0,18:0-PC)/DOPC/DOPS/CHOL, DOPC/DOPS/CHOL, POPC/POPS/CHOL, and egg-PC/brain-PS/CHOL. For each series, the PS concentration was fixed at 30% to ensure sufficient binding of Gag. Cholesterol was increased linearly from 0% to 63%, the maximum solubility of cholesterol in PC bilayers (31). Each series should have samples that vary continuously from Ld to Lo characteristics, which would also allow the evaluation of Gag's preference towards raft-like mixtures. In addition, the range of cholesterol concentrations examined here covers the estimated cholesterol concentrations for cell plasma membranes, which could be as high as 50% (32).

In all four types of mixtures examined, Gag-liposome association increased with increasing cholesterol concentrations, albeit at different rates depending on the mixture (Fig. 5.4 *B*). In the two DOPC-containing mixtures, Gag binding to liposomes displayed a rather steep initial climb that achieved a maximum at ~ 36% CHOL (Fig. 5.4 *B*). On the other hand, Gag displayed a lower membrane affinity in egg-PC/brain-PS/CHOL mixtures (Fig. 5.4 *B*, *triangles*), where binding started to increase only at ~18% CHOL, before gradually increasing and reaching a maximum similar to that observed in DOPC-containing mixtures at the highest cholesterol concentration examined (63%). Finally, in POPC/POPS/CHOL mixtures, binding to liposomes was detected only beginning at ~36% CHOL, where it rose slowly towards a slightly lower maximum, compared to the other three mixtures (Fig. 5.4 *B*, *open circles*).

Increasing cholesterol concentration is known to have a condensing effect on the bilayer, where cholesterol forces the acyl chains of phospholipids to straighten out and

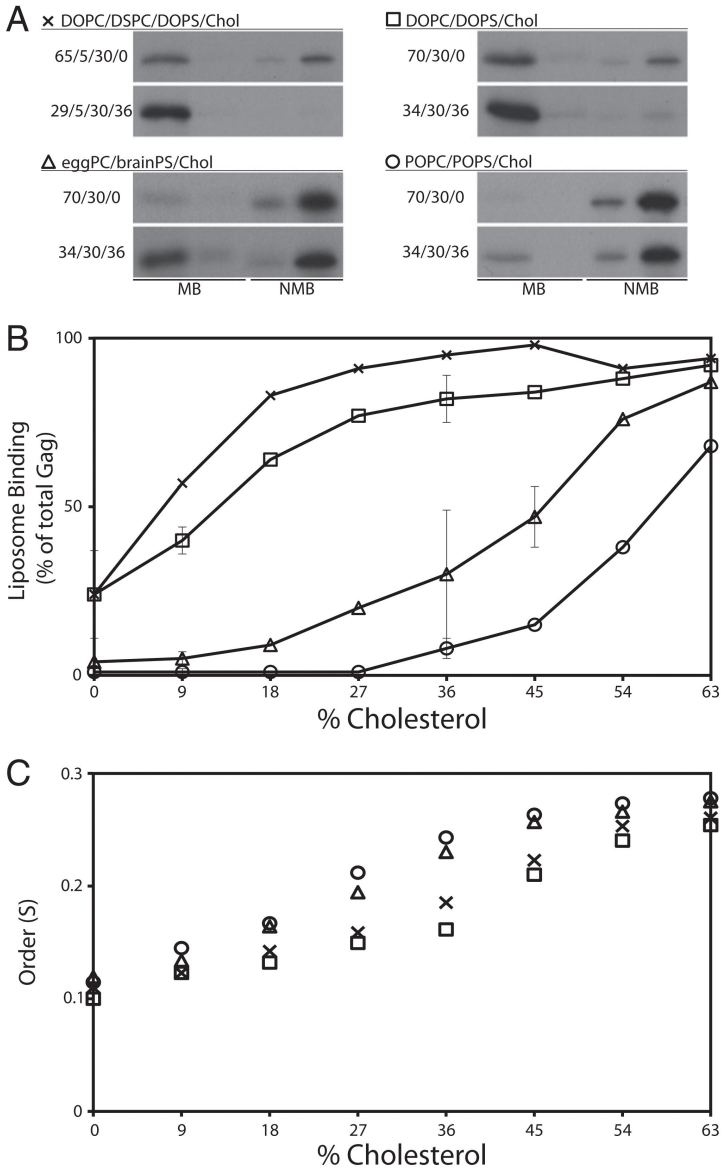

Figure 5.4. Cholesterol concentration influences HIV-1 Gag binding to liposomes. Mixtures contained a fixed 30% PS (and in one case, also contained a fixed 5% DSPC), while ratios of cholesterol to DOPC or POPC were varied. HIV-1 Gag synthesis and flotation analyses were as described in Fig. 3. (A) Examples fluorograms showing fractions of membrane bound, MB (floated liposomes), and non-membrane bound, NMB (one-fourth of the sample loaded compared with MB), in two lipid ratios for each of the four lipid compositions used. (B) Quantification of Gag flotation reactions plotted as a function of increasing % CHOL. Error bars indicate SD (N= 3) for replicas done at 9% and 36% CHOL in the three-component mixtures, for 0% CHOL in DOPC/DOPS/CHOL, and for 45% CHOL in egg-PC/brain-PS/CHOL. (C) Order parameter, *S*, for each composition in the four mixture series in (B), as determined using ESR. (Figure taken from(23); flotation assays analyzed by R.A.D.).

pack more closely, so that the non-polar cholesterol molecules can be shielded by the lipid head groups from the hydrophilic environment right outside the bilayer (33). The explanation for this condensation of lipid area was described as the "umbrella model" (33). As a result, increasing cholesterol concentration results in higher packing density of lipids in the bilayer, causing the membrane to become more ordered.

The effect of cholesterol concentrations on the membrane order in the four types of mixtures studied above was investigated via ESR. As expected, membrane order increased with increasing cholesterol concentrations in all the mixtures series (Fig. 5.4 *C*). The lineshapes of the spectra at low cholesterol concentrations resembled that of typical Ld mixtures, whereas the spectra of high cholesterol concentrations were characteristic of Lo mixtures (Fig. 5.1). The two DOPC-containing mixtures maintained an overall lower order than the natural mixture and the POPC-containing mixture. However, the trend of membrane order varying with cholesterol concentration does not follow the trend of Gag-binding as a function of cholesterol. In particular, Gag was more responsive to DOPC-containing mixtures even at lower cholesterol content (≤ 18%), where the membrane order was very similar for all four types of mixtures examined. This indicated that while Gag membrane affinity is enhanced by cholesterol, it is not driven by the overall membrane order of the mixtures.

5.4.3 Membrane order differentially affects Gag membrane binding

Another way to vary membrane order is to vary the concentration of saturated (or unsaturated) acyl chains in the lipid mixtures. Even though Gag's response to cholesterol seemed decoupled from the increased membrane order induced by

cholesterol, we were interested in examining whether increasing membrane order by altering acyl chain saturation content could elicit a similar response from Gag. In order to conduct this study, a minimum of four components were required in the lipid mixtures used: cholesterol and a PS that were held constant, and two PC lipids, one fully saturated and the other with some degree of unsaturation. Since no known four-component, PS-containing phase diagram has been reported, we used the published liquid-liquid phase boundaries of DSPC/DOPC/CHOL and DSPC/POPC/CHOL systems to guide our choice in lipid mixtures (Fig. 5.5 *A*-*B*; compositions of lipid mixtures listed in Tables 5.1-5.4).

Two sets each of DOPC-containing and POPC-containing mixtures were chosen, where the ratio of the high-melting DSPC and a low-melting lipid (DOPC or POPC) was varied linearly (Fig. 5.5 *A* and *B*). For the DOPC-containing mixtures, constant cholesterol = 40% and PS = 20% were chosen, mainly to ensure that the mixtures stay within a one-phase region to avoidcomplications of data interpretation in two-phase coexisting regions (Fig. 5.5 *A*-*B*). Since Gag binding to DOPC-containing mixtures was already high at 40% CHOL when 30% PS was present (Fig. 5.4 *B*), we chose to reduce the % PS here to maximize the dynamic range for observing Gag binding in this series of mixtures. A series of eight samples beginning on the DOPC/CHOL binary axis were prepared, each containing 20% DOPS; a second series of eight samples beginning on the DSPC/CHOL axis were also examined, each containing 20% DPPS (16:0, 16:0-PS) (Fig. 5.5 *B*). The two series allowed access to the full range of DSPC: DOPC ratios along constant 40% CHOL, and also provided a comparison of employing different PS species on the overall membrane order and Gag

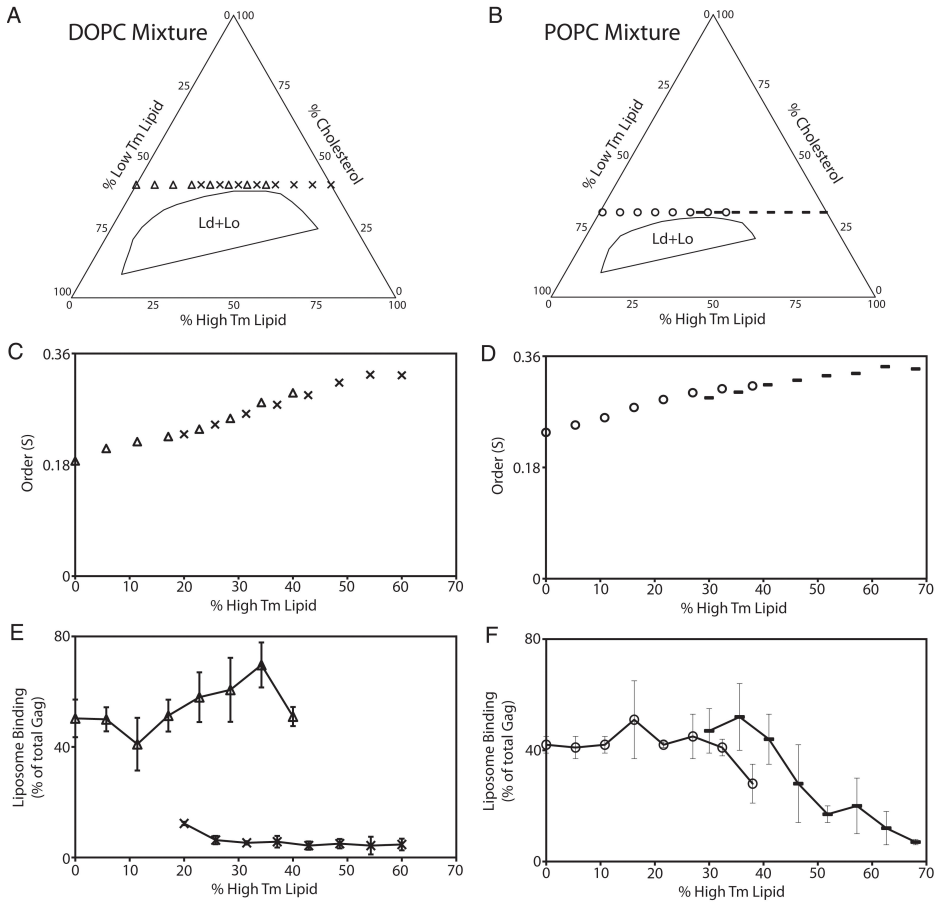

Figure 5.5. Membrane order has complex influence on HIV-1 Gag–membrane binding. HIV-1 Gag and flotation analyses were as described in Fig. 1. (A and B) The mixtures examined are plotted onto phase diagrams that show only the Ld + Lo coexistence regions. While the phase boundaries of four-component mixtures containing PS have not been determined, known boundaries of three-component systems (REF) are presented as a guide for the expected mixing behavior of the four-component mixtures examined. (A) (*triangles*) The ratios of DSPC: DOPC were increased from left to right (5.7% DOPC was replaced with DSPC) in mixtures containing 20% DOPS and 40% CHOL. (*X symbols*) The ratios of DSPC:DOPC were increased from left to right (5.8% DOPC was replaced by DSPC) in mixtures containing 20% DPPS and 40% CHOL. (B) Replacements as performed in (A), except with POPC lipids. POPC was replaced by 5.4% DSPC to increase the DSPC:POPC ratios from left to right, in mixtures containing 30% POPS and 32% CHOL (*open circles*), and in mixtures containing 30% DPPS, 32% CHOL (*dashes*). All compositions should yield a single phase. (C and D) Membrane order in DOPC mixtures (C) and POPC mixtures (D) were determined using ESR. (E and F) Percentage of floated Gag in DOPC-containing liposomes (E) and POPC-containing liposomes (F). Error bars indicate SD ($N \geq 3$) for each data point. (Figure obtained from(23); flotation assays analyzed by R.A.D.).

TABLE 5.1 Ld-like compositions (*triangles)* containing 20% DOPS and 40% CHOL in DSPC/DOPC/DOPS/CHOL mixtures

DOPC mixture	X_{DSPC}	X_{DOPC}	X_{DOPS}	X_{CHOL}
Ld-1	0	0.40	0.20	0.40
Ld-2	0.057	0.343	0.20	0.40
Ld-3	0.114	0.286	0.20	0.40
Ld-4	0.171	0.229	0.20	0.40
Ld-5	0.228	0.172	0.20	0.40
Ld-6	0.285	0.115	0.20	0.40
Ld-7	0.342	0.058	0.20	0.40
Ld-8	0.40	**0**	0.20	0.40

TABLE 5.2 Lo-like compositions (*X symbols)* containing 20% DPPS and 40% CHOL in DSPC/DOPC/DPPS/CHOL mixtures

DOPC mixture	X_{DSPC}	X_{DOPC}	X_{DPPS}	X_{CHOL}
Lo-1	0	0.40	0.20	0.40
Lo-2	0.058	0.342	0.20	0.40
Lo-3	0.115	0.285	0.20	0.40
Lo-4	0.172	0.228	0.20	0.40
Lo-5	0.229	0.171	0.20	0.40
Lo-6	0.286	0.114	0.20	0.40
Lo-7	0.343	0.057	0.20	0.40
Lo-8	0.40	0	0.20	0.40

TABLE 5.3 Ld-like compositions (*open circles)* containing 30% POPS and 32% CHOL in DSPC/POPC/POPS/CHOL mixtures

POPC mixture	X_{DSPC}	X_{POPC}	X_{POPS}	X_{CHOL}
Ld-1	0	0.38	0.30	0.32
Ld-2	0.054	0.326	0.30	0.32
Ld-3	0.108	0.272	0.30	0.32
Ld-4	0.162	0.218	0.30	0.32
Ld-5	0.216	0.164	0.30	0.32
Ld-6	0.27	0.11	0.30	0.32
Ld-7	0.324	0.056	0.30	0.32
Ld-8	0.38	0	0.30	0.32

TABLE 5.4 Lo-like compositions (*dashed lines)* containing 30% DPPS and 32% CHOL in DSPC/POPC/DPPS/CHOL mixtures

POPC mixture	X_{DSPC}	X_{POPC}	X_{DPPS}	X_{CHOL}
Lo-1	0	0.38	0.30	0.32
Lo-2	0.056	0.324	0.30	0.32
Lo-3	0.11	0.27	0.30	0.32
Lo-4	0.164	0.216	0.30	0.32
Lo-5	0.218	0.162	0.30	0.32
Lo-6	0.272	0.108	0.30	0.32
Lo-7	0.326	0.054	0.30	0.32
Lo-8	0.38	0	0.30	0.32

binding. A comparable set of two series was also examined in POPC-containing mixtures, where all samples contained constant cholesterol = 32% and PS = 30%; POPS was used instead of DOPS in these series (Fig. 5.5 *B*).

To investigate how membrane order varies with acyl chain saturation, we measured the membrane order in all the mixtures described above using ESR. We observed that order rose linearly with increasing DSPC concentrations, regardless of the PS species in the mixtures (Fig. 5.5 *C* and *D*). In addition, the lineshapes of the spectra displayed characteristic features of Ld mixtures where the DSPC:low-melting lipid ratio was low, while features typical of Lo mixtures were observed in mixtures containing high DSPC:low-melting lipid ratios instead (Fig. 5.6). Membrane order in DOPC-containing mixtures was lower than that in POPC-containing mixtures at DSPC concentrations up to ~ 50%, indicating that the more saturated chains in POPC afford more order than DOPC even at lower cholesterol concentration (32% vs. 40%). Both types of mixtures still achieved similar maximum order towards high DSPC concentrations (Fig. 5.5 *C* and *D*).

The membrane affinity of Gag to these mixtures, however, did not correlate strongly with membrane order. In mixtures containing 20% DOPS, Gag binding to liposomes remained relatively steady when DSPC:DOPC ratios were gradually increased (Fig. 5.5 *E*, *triangles*). Contrastingly, in mixtures containing 20% DPPS, Gag membrane binding was barely detectable in all the samples examined in the series (Fig.5. 5 *E, x symbols*). When POPC was replaced with DOPC, we observed very different trends in Gag binding. In POPS-containing mixtures, Gag binding was unchanged as DSPC:POPC ratios were increased up to 38% DSPC, at which point

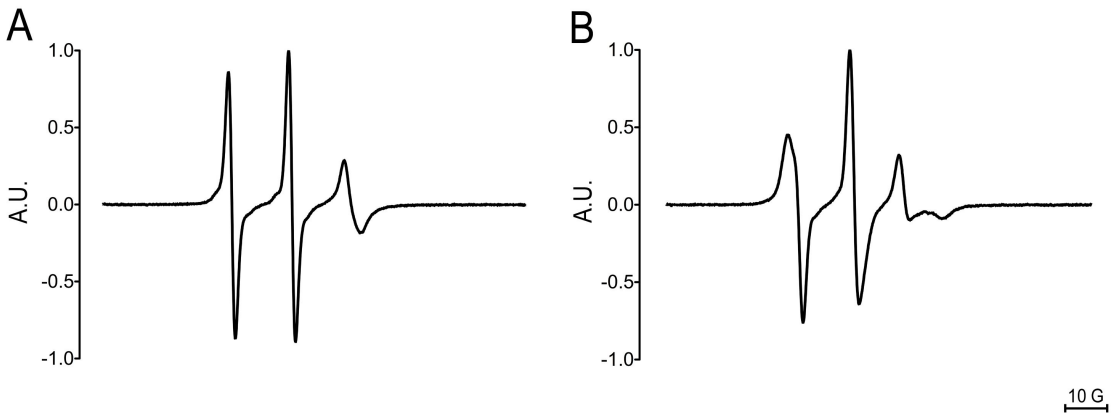

Figure 5.6. ESR spectra of 16-DSA in a typical disordered and ordered environment for the mixture series examined in Fig.5.5. (A) 16-DSA in a disordered environment with composition DOPC/DOPS/CHOL = 0.40/0.20/0.40. (B) 16-DSA in an ordered environment with composition DSPC/DPPS/CHOL = 0.40/0.20/0.40.

binding decreased slightly (Fig. 5.5 *F, open circles*). When 30% DPPS was present in POPC-containing mixtures, Gag displayed appreciable binding to liposomes beginning at 30% DSPC, which then started to decrease at ~46% DSPC, until it finally dropped to almost no binding at the highest DSPC:POPC ratio (Fig. 5.5 *F, dashes*). It is worth noting that Gag bound to DPPS-containing mixtures more strongly in the POPC mixtures, when it did not respond at all to DPPS-containing DOPC mixtures. Even though 10% more DPPS was present in POPC-containing mixtures, the stark contrast in Gag responses suggest that the DPPS appeared to be more "available" for Gag binding in POPC mixtures.

5.5 Discussion

The response of HIV-1 Gag to cholesterol and acyl chain composition in bilayers was examined using liposome flotation assays. Detailed studies that employed chemically well-defined model membrane mixtures led to three main observations of Gag-membrane association: 1) Gag detects the overall acyl chain compositions in bilayers, in addition to PS concentrations; 2) Gag responds to cholesterol concentrations; and 3) Gag is sensitive to the nature of the acyl chains of the PS lipid it interacts with. ESR measurements confirmed that Gag's response to the different mixtures is not correlated solely to membrane order.

While membrane order does not govern membrane affinity of HIV-1 Gag, our results did show that there is a preference for mixtures that contained cholesterol. This preference is shared with the Gag protein of another retrovirus, the murine leukemia virus (MLV), but not with Rous sarcoma virus (RSV) (23). Interestingly, both HIV-1

and MLV Gag proteins are myristoylated on their N-termini, whereas RSV Gag is not lipidated, suggesting that a lipid anchor may enhance sensing of cholesterol content in bilayers. In addition to cholesterol concentrations, membrane binding of all three retroviral Gag proteins was also examined using two mixtures that were distinct in membrane order and contained characteristics of an Ld and Lo mixture, respectively (23). Surprisingly, all three retroviral Gag proteins bound more strongly to the Lo-like mixture, lending support to the hypothesis that viruses could bud from rafts.

The observation that Gag prefers Lo-like mixtures cannot be solely explained by membrane order or cholesterol content due to our results that also showed a dependence of HIV-1 Gag membrane affinity on the acyl chain composition of the mixtures examined (in Fig. 5.3-5.5). The "availability" of the negatively charged PS lipids for Gag binding seemed to differ in different mixtures. For example, Gag seemed to detect a higher effective PS concentration in an environment that contained lipids with unsaturated 18:1, 18:1 chains (Fig. 5.3 *A,* and 5.4 B). In contrast, the saturated DPPS was more available for Gag-binding in POPC-containing mixtures (Fig. 5.5 *F*). If Gag-membrane interactions were solely driven by electrostatics, the disparate binding preferences observed in our studies suggest that the details of lipid-lipid interactions within the bilayer, which could vary in different mixtures, could affect Gag membrane affinity. Specifically, non-random mixing of PS lipids among all the species present in the bilayer could affect the thermodynamic activity of PS in a particular mixture. Indeed, the thermodynamic activity of PS was found to be different from its actual mole fraction in simple binary mixtures (34, 35). Hence, the variability

in PS thermodynamic activities in the mixtures examined here could be an important additional factor towards determining the membrane affinity of Gag.

The lipid mixtures employed in this study contained PC, PS and cholesterol, and were chosen mainly based on known phase behavior of mixtures that are models for the outer leaflet of the PM. Viral particles assemble on the inner leaflet of the PM before budding out of the cell. While these simple mixtures have been useful in our investigation, a better model would include lipids such as PE and $PI(4,5)P_2$, which are found in the inner leaflet. In particular, $PI(4,5)P_2$ has been shown to greatly enhance HIV-1 Gag-membrane binding, both in the absence and presence of cholesterol (23, 27). Compared with outer leaflet mixtures, the phase behavior of true inner leaflet mixtures has not been studied extensively. Macroscopic Lo + Ld phase separation has not been found, leading to the hypothesis that there could be no "rafts" in true inner leaflet model mixtures (16). However, one cannot rule out the possibilities of *inducing* rafts to form in the inner leaflet upon protein binding or from coupling interactions with outer leaflet lipids or phase domains.

Binding of proteins or insertion of transmembrane peptides into the bilayer can affect membrane properties and phase behavior (36, 37). Thus, electrostatic binding of Gag and insertion of its myristoyl anchor into the membrane could induce changes to local membrane properties, such as membrane order, charge distribution, and lipid mixing. These effects may not be obvious when only examining isolated lipid mixtures, and should be done in the presence of proteins. Previous theoretical and experimental studies using short, unstructured basic stretches modeled after proteins such as Src tyrosine kinase and MARCKS protein offer evidence for adsorption of

polybasic motifs affecting local membrane electrostatics, lipid mixing, and even lateral domain formation (36, 38, 39). In cells, formation of a Gag lattice during assembly on the membrane could very well have a substantial effect on local membrane organization. Hence, *in vitro* studies of viral assembly and budding on membranes should consider both proteins and membranes as one entity, which are not mutually exclusive.

5.6 Conclusion

The question of how viral particles might bud from rafts in plasma membranes was pursued *in vitro* using chemically well-defined lipid mixtures. HIV-1 Gag not only responds to net negative charge, as has been previously shown, it also displays sensitivity to the hydrophobic environment within the bilayer. While a higher membrane affinity for cholesterol-containing mixtures was observed, Gag-membrane interactions do not depend on membrane order per se, as determined from ESR. Details of the acyl chains and the PS species in the overall mixture also exert an effect on Gag binding, alluding to the complexity of this process. This study showed that HIV-1 Gag does have a preference to bind to raft-like mixtures that are enriched in cholesterol; but how viral membranes acquire a raft-like composition from inner leaflet lipids that are probably devoid of rafts is still unclear. A better understanding of the effects of Gag binding on membrane properties and lipid mixing can aid future studies on Gag-membrane association.

References

1. Ono, A. 2010. HIV-1 assembly at the plasma membrane. Vaccine. 28: B55–B59.

2. Saad, J.S., J. Miller, J. Tai, A. Kim, R.H. Ghanam, et al. 2006. Structural basis for targeting HIV-1 Gag proteins to the plasma membrane for virus assembly. Proc. Natl. Acad. Sci. U.S.A. 103: 11364–11369.

3. Ono, A., S.D. Ablan, S.J. Lockett, K. Nagashima, and E.O. Freed. 2004. Phosphatidylinositol (4,5) bisphosphate regulates HIV-1 Gag targeting to the plasma membrane. Proc. Natl. Acad. Sci. U.S.A. 101: 14889–14894.

4. Chan, R., P.D. Uchil, J. Jin, G. Shui, D.E. Ott, et al. 2008. Retroviruses human immunodeficiency virus and murine leukemia virus are enriched in phosphoinositides. Journal of Virology. 82: 11228–11238.

5. Aloia, R.C., H. Tian, and F.C. Jensen. 1993. Lipid composition and fluidity of the human immunodeficiency virus envelope and host cell plasma membranes. Proc. Natl. Acad. Sci. U.S.A. 90: 5181–5185.

6. Brügger, B., B. Glass, P. Haberkant, I. Leibrecht, F.T. Wieland, et al. 2006. The HIV lipidome: a raft with an unusual composition. Proc. Natl. Acad. Sci. U.S.A. 103: 2641–2646.

7. Pessin, J.E., and M. Glaser. 1980. Budding of Rous sarcoma virus and vesicular stomatitis virus from localized lipid regions in the plasma membrane of chicken embryo fibroblasts. J. Biol. Chem. 255: 9044–9050.

8. Hamard-Peron, E., F. Juillard, J.S. Saad, C. Roy, P. Roingeard, et al. 2010. Targeting of murine leukemia virus gag to the plasma membrane is mediated by PI(4,5)P2/PS and a polybasic region in the matrix. Journal of Virology. 84: 503–515.

9. Simons, K., and E. Ikonen. 1997. Functional rafts in cell membranes. Nature. 387: 569–572.

10. Campbell, S.M., S.M. Crowe, and J. Mak. 2002. Virion-associated cholesterol is critical for the maintenance of HIV-1 structure and infectivity. AIDS. 16: 2253–2261.

11. Graham, D.R.M., E. Chertova, J.M. Hilburn, L.O. Arthur, and J.E.K. Hildreth. 2003. Cholesterol depletion of human immunodeficiency virus type 1 and simian immunodeficiency virus with beta-cyclodextrin inactivates and permeabilizes the virions: evidence for virion-associated lipid rafts. Journal of Virology. 77: 8237–8248.

12. Ono, A., A.A. Waheed, and E.O. Freed. 2007. Depletion of cellular cholesterol inhibits membrane binding and higher-order multimerization of human immunodeficiency virus type 1 Gag. Virology. 360: 27–35.

13. Lingwood, D., and K. Simons. 2010. Lipid rafts as a membrane-organizing principle. Science. 327: 46–50.

14. Feigenson, G.W. 2009. Phase diagrams and lipid domains in multicomponent lipid bilayer mixtures. Biochimica et Biophysica Acta (BBA) - Biomembranes. 1788: 47–52.

15. Heberle, F.A., J. Wu, S.L. Goh, R.S. Petruzielo, and G.W. Feigenson. 2010. Comparison of three ternary lipid bilayer mixtures: FRET and ESR reveal nanodomains. Biophys. J. 99: 3309–3318.

16. Wang, T.Y., and J.R. Silvius. 2001. Cholesterol does not induce segregation of liquid-ordered domains in bilayers modeling the inner leaflet of the plasma membrane. Biophysj. 81: 2762–2773.

17. Korlach, J., P. Schwille, W.W. Webb, and G.W. Feigenson. 1999. Characterization of lipid bilayer phases by confocal microscopy and fluorescence correlation spectroscopy. Proc. Natl. Acad. Sci. U.S.A. 96: 8461–8466.

18. Wan, C., V. Kiessling, and L.K. Tamm. 2008. Coupling of Cholesterol-Rich Lipid Phases in Asymmetric Bilayers †. Biochemistry. 47: 2190–2198.

19. Kiessling, V., C. Wan, and L.K. Tamm. 2009. Domain coupling in asymmetric lipid bilayers. BBA - Biomembranes. 1788: 64–71.

20. Zhao, J., J. Wu, F.A. Heberle, T.T. Mills, P. Klawitter, et al. 2007. Phase studies of model biomembranes: Complex behavior of DSPC/DOPC/Cholesterol. Biochimica et Biophysica Acta (BBA) - Biomembranes. 1768: 2764–2776.

21. Kingsley, P.B., and G.W. Feigenson. 1979. Synthesis of a Perdeuterated Phospholipid - 1,2-Dimyristoyl-Sn-Glycero-3-Phosphocholine-D72. Chemistry and Physics of Lipids. 24: 135–147.

22. Buboltz, J.T., and G.W. Feigenson. 1999. A novel strategy for the preparation of liposomes: rapid solvent exchange. Biochim. Biophys. Acta. 1417: 232–245.

23. Dick, R.A., S.L. Goh, G.W. Feigenson, and V.M. Vogt. 2012. HIV-1 Gag protein can sense the cholesterol and acyl chain environment in model membranes. Proceedings of the National Academy of Sciences.

24. Chan, J., R.A. Dick, and V.M. Vogt. 2011. Rous sarcoma virus gag has no

specific requirement for phosphatidylinositol-(4,5)-bisphosphate for plasma membrane association in vivo or for liposome interaction in vitro. Journal of Virology. 85: 10851–10860.

25. Dalton, A.K., P.S. Murray, D. Murray, and V.M. Vogt. 2005. Biochemical characterization of rous sarcoma virus MA protein interaction with membranes. Journal of Virology. 79: 6227–6238.

26. Schorn, K., and D. Marsh. 1997. Extracting order parameters from powder EPR lineshapes for spin-labelled lipids in membranes. Spectrochim Acta A. 53: 2235–2240.

27. Chukkapalli, V., I.B. Hogue, V. Boyko, W.S. Hu, and A. Ono. 2008. Interaction between the Human Immunodeficiency Virus Type 1 Gag Matrix Domain and Phosphatidylinositol-(4,5)-Bisphosphate Is Essential for Efficient Gag Membrane Binding. Journal of Virology. 82: 2405–2417.

28. Dalton, A.K., D. Ako-Adjei, P.S. Murray, D. Murray, and V.M. Vogt. 2007. Electrostatic interactions drive membrane association of the human immunodeficiency virus type 1 Gag MA domain. Journal of Virology. 81: 6434–6445.

29. Winiski, A.P., A.C. McLaughlin, R.V. McDaniel, M. Eisenberg, and S. McLaughlin. 1986. An experimental test of the discreteness-of-charge effect in positive and negative lipid bilayers. Biochemistry. 25: 8206–8214.

30. Ono, A. 2010. Relationships between plasma membrane microdomains and HIV-1 assembly. Biol. Cell. 102: 335–350.

31. Huang, J., J.T. Buboltz, and G.W. Feigenson. 1999. Maximum solubility of cholesterol in phosphatidylcholine and phosphatidylethanolamine bilayers. Biochim. Biophys. Acta. 1417: 89–100.

32. Mukherjee, S., and F.R. Maxfield. 2004. Membrane domains. Annu. Rev. Cell Dev. Biol. 20: 839–866.

33. Huang, J., and G.W. Feigenson. 1999. A microscopic interaction model of maximum solubility of cholesterol in lipid bilayers. Biophysj. 76: 2142–2157.

34. Feigenson, G.W. 1989. Calcium ion binding between lipid bilayers: the four-component system of phosphatidylserine, phosphatidylcholine, calcium chloride, and water. Biochemistry. 28: 1270–1278.

35. Huang, J., J.E. Swanson, A.R. Dibble, A.K. Hinderliter, and G.W. Feigenson. 1993. Nonideal mixing of phosphatidylserine and phosphatidylcholine in the fluid lamellar phase. Biophysj. 64: 413–425.

36. Denisov, G., S. Wanaski, P. Luan, M. Glaser, and S. McLaughlin. 1998. Binding of basic peptides to membranes produces lateral domains enriched in the acidic lipids phosphatidylserine and phosphatidylinositol 4,5-bisphosphate: an electrostatic model and experimental results. Biophysj. 74: 731–744.

37. Iglič, A., T. Slivnik, and V. Kralj-Iglič. 2007. Elastic properties of biological membranes influenced by attached proteins. Journal of Biomechanics. 40: 2492–2500.

38. Murray, D., A. Arbuzova, G. Hangyás-Mihályné, A. Gambhir, N. Ben-Tal, et al. 1999. Electrostatic properties of membranes containing acidic lipids and adsorbed basic peptides: theory and experiment. Biophysj. 77: 3176–3188.

39. Mbamala, E.C., A. Ben-Shaul, and S. May. 2005. Domain Formation Induced by the Adsorption of Charged Proteins on Mixed Lipid Membranes. Biophysj. 88: 1702–1714.

CHAPTER 6
Conclusions and Future Directions

6.1 Modulated phase studies in DSPC/DOPC/POPC/CHOL

6.1.1 Summary of findings

Fluorescence microscopy imaging of GUVs has been useful in studying phase behavior of multicomponent lipid mixtures (1-4). Taking careful precautions to avoid artifacts, we employed this method to examine the nature of domain size change in the coexisting fluid region of DSPC/DOPC/POPC/CHOL, a model for the PM outer leaflet. As the ratio of DOPC/POPC is changed, we observed that the transition from nanoscopic to macroscopic domains goes through a modulated phase regime, where patterned domains are found. The compositional width of this "modulated phase window" and the ρ values at which patterned domains occur vary depending on the composition within the two-phase region. One key experimental observation is that modulated phase patterns along the same tieline follow the lever arm rule, indicating that modulated phases are governed by the rules that describe phase separation along a thermodynamic tieline. A competing interactions model of line tension and curvature energies faithfully reproduced experimental results, consistent with the various morphologies still corresponding to equilibrium phase separation. Importantly, we found that line tension exerts the main control over the majority of the trends observed in GUV experiments.

In temperature dependent studies of modulated phases, FRET was employed to study GUVs. Energy transfer between two different probe pairs revealed: 1) phase

boundaries along a tieline as a function of temperature, and 2) the miscibility transition temperature of the Ld + Lo modulated phase region (at ρ = 20%). Consistent with other miscibility transition studies (5-7), the Ld + Lo region narrowed towards higher χ_{DSPC} as temperature increased, with the miscibility transition temperature depending on the Tm of the high Tm lipid: in our mixtures, the temperature of complete miscibility occurred at 45°C < T ≤ 50°C.

We have performed both *in situ* and bulk studies on the reversibility of modulated phase patterns on GUVs. In the Lo-rich composition examined, we observed a disappearance of patterns when GUVs were heated to ~35°C; FRET indicated that nanoscopic domains are still present at 35°C. Patterns typically reappeared after brief cooling to ambient temperature, implying that at physiological temperature, the morphologies of the nanoscopic Ld + Lo phases could resemble patterns similar to those observed at the micron-size regime. However, due to some discrepancies in GUV results relating to temperature cycles performed at 50°C, the reversibility and the thermal stability of modulated phases warrant more thorough investigations.

6.1.2 Future directions

The discovery of coexisting fluid bilayer phases that form patterned domains is intriguing. In our system, we obtained modulated phases when we used DOPC as the "titration lipid" to replace the more biologically relevant POPC in the four-component mixture DSPC/DOPC/POPC/CHOL. It would be valuable to extend this type of investigation to a more biologically relevant Type I mixture, such as SM/POPC/CHOL, where all the components in the system are naturally found in

mammalian cell PM. DOPC can be used as the standard lipid to find the ρ values at which modulated phases occur in the new mixtures. Based on studies in the DSPC/DOPC/POPC/CHOL system, if a ρ value where modulated phases appear corresponds to a specific line tension value, then modulated phases that occur at higher ρ values in a new system could indicate that the mixtures probably have lower line tension than DSPC/POPC/CHOL at ρ = 0%. These mixtures could be better models for understanding the nature of domain size transition of nanoscopic rafts in cells.

The partitioning of what are thought to be raft-preferring transmembrane peptides *out of* the Lo phase in model membrane mixtures has prompted questions of the relevance of model membrane phase studies to the nonrandom mixing occurring in actual cell PM. However, all of the peptide partitioning studies was performed using Type II lipid mixtures that exhibit macroscopic fluid phase separation driven by large line tension at domain boundaries (8-10). The Ld + Lo region in the four-component DSPC/DOPC/POPC/CHOL outer leaflet model could be better mixtures for examining transmembrane peptide partitioning behavior. In particular, the mixtures within the modulated phase regime offer a range of sufficiently low line tension values that still allow micron-size domains to form. The closer properties of the coexisting Lo + Lo phases could change the preferred phase location of transmembrane peptides, mimicking their affinities for rafts in cells.

Comparisons of experimental observations with theoretical models have been extremely useful in understanding the multiple interactions in play to produce phase separation in model membrane mixtures. At the micron-size scale, where modulated

phases are observed in DSPC/DOPC/POPC/CHOL mixtures, line tension dominates in controlling domain size and morphology, in the presence of competing curvature energies. However, it is still unclear whether the same two interactions are maintaining the formation of domains at the nanoscopic scale. Other factors such as dipole repulsions, entropy or special properties of the Lo phase could play an important role in stabilizing nanodomains. To more accurately model intermolecular interactions at the nanoscopic level, it will be extremely helpful if actual values of line tension as a function of ρ can be measured in DSPC/DOPC/POPC/CHOL mixtures. Since visible round domains can be observed in several Ld + Lo phase separated mixtures from ρ = 100% to as low as ρ = ~ 30%, a relatively wide range of line tension values can be experimentally determined. This will allow better extrapolation of line tension in the nanoscopic regime, and provide good estimates for theoretical simulations to explore possible parameters that can maintain stable nanodomains.

The thermal stability and reversibility of modulated phase patterns on GUVs are not well described. Our studies suggested that glass adhesion could affect the reappearance of patterned morphologies after a temperature cycle on the microscope stage, indicating that a better way of performing the experiment, perhaps via tethered GUVs, is needed. On the other hand, FRET has proven to be useful in determining phase boundaries and miscibility transition temperature along a tieline that traverses the Ld + Lo region at ρ = 20% in DSPC/DOPC/POPC/CHOL mixtures. This line of experiments should be continued to obtain a more complete miscibility map of the Ld + Lo volume of this four-component system, which could be important to relate phase

behavior of this outer leaflet model to nonrandom mixing in cell PM at physiologically relevant temperatures.

6.2 Membrane binding and remodeling studies

6.2.1 Pacsin-mediated membrane deformation: summary of findings

Pacsin-1 is a versatile membrane remodeler within the F-BAR domain sub-family. Using liposome binding assays and *in vitro* membrane deformation assays (observed via EM), we found that activated pacsin-1 can induce vesiculation under certain experimental conditions. Activation of pacsin-1 requires key arginine residues in the binding motif of the PRD domain of dynamin-1; the resulting pacsin-PRD complex showed enhanced recruitment to liposomes and increased membrane deformation activity compared to the isolated F-BAR domains of pacsin-1. Similar elevated membrane remodeling activity (vesiculation) was also observed in PRD-bound endophilin-A1, suggesting a more general mode of activation by dynamin-1 PRD to its SH3 domain interacting partners.

The versatility of pacsin-1 at the membrane was also observed using liposomes prepared from various protocols, where distinct properties of the liposomes influenced the *in vitro* membrane sculpting abilities of pacsin-1, pacins-$1^{F\text{-}BAR}$, and the pacsin-PRD complex. While the intrinsic structural characteristics of pacsin-1 are main determinants of its activity, membrane properties still play an important role. Altogether, our *in vitro* studies illustrate a synergistic relationship between pacsin and dynamin in membrane remodeling, and highlight the functional versatility of pacsin-1, which could be important in its role in endocytotic pathways *in vivo*.

6.2.2 HIV-1 Gag membrane binding: summary of findings

The hypothesis that HIV-1 buds from rafts was examined by investigating the preference of HIV-1 Gag for lipid compositions that are "raft-like". Using an *in vitro* reticulocyte translation system and liposome flotation assays, membrane affinity of HIV-1 Gag to lipid compositions varying in cholesterol, negatively charged lipids, and acyl chain saturation was examined. While Gag responded to increasing net negative charge, as expected from previous studies (11), Gag also exhibited more affinity towards liposomes containing high cholesterol content. However, ESR-determined order parameters indicated that Gag-membrane association does not correlate directly with increasing membrane order. Instead, details in acyl chain saturation and the type of PS species contribute towards Gag-membrane binding in a more complicated manner that is not yet fully understood.

6.2.3 Future directions

Studies on membrane binding and remodeling, mediated by BAR domains and HIV-1 Gag, indicated a strong dependence on lipid composition and membrane properties. In pacsin-driven membrane deformation studies, membrane curvature and bending rigidity as imposed by the size and lamellarity of the liposomes affected the types of morphologies generated by pacsin-1 constructs. On the other hand, lipid composition such as cholesterol content and particular PS species influenced Gag-membrane association. The integral role played by lipids in these processes is still unclear, and requires a better understanding of nonrandom mixing behavior of inner leaflet model membrane mixtures.

Commonly used methods in studying phase behavior in outer leaflet model mixtures (ie. GUV imaging, FRET) may not be applied to inner leaflet models, mainly because inner leaflet lipid mixtures do not tend to phase-separate (12). However, since the processes that are of interest involve binding to negatively charged lipids (PS), the thermodynamic activity of PS, a_{PS}, in various inner leaflet mixtures can be examined. a_{PS} describes the availability of PS molecules in a mixture for binding to Gag or BAR domains, and is strongly influenced by how well PS molecules mix with other lipids in the mixture. Even in simple binary mixtures of PS/PC, a_{PS} does not correlate linearly with PS mole fraction, and can differ depending on the acyl chain compositions in the mixture (13, 14). Hence, systematic determination of a_{PS} in mixtures varying in cholesterol concentrations or acyl chain saturations could be a better way to examine the active role played by lipids in membrane binding and remodeling processes.

While inner leaflet lipids alone may exist as one-phase mixtures, this does not mean that addition of BAR domain or Gag proteins will not induce phase separation. Many studies have shown that the Ld phase is always preferred at regions of narrow curvature (15-17). Moreover, Gag multimerization (18) and formation of higher-order BAR oligomers (19, 20) on the membrane surface are required during membrane deformation. Hence, it is reasonable to expect that protein mediated membrane remodeling (possibly via scaffolding) could result in lipid sorting, where the more fluid and disordered lipids are found in the more highly curved areas on the membrane: this could be a mechanism of driving phase separation in the inner leaflet.

Since membrane remodeling is an active process, the effects of protein binding and protein-mediated membrane deformation should be observed *in situ* using fluorescence imaging of GUVs. Ideally, GUVs would be tethered to the glass surface, while protein solution is locally injected to the surface of a GUV. Pseudo inner leaflet model mixtures derived from outer leaflet models can first be employed since the phase behavior of the resulting mixtures may be better estimated. For example, DOPS can be used to partially replace DOPC in the four-component DSPC/DOPC/DOPS/CHOL mixture, where phase boundaries are expected to be largely unchanged with this replacement. Once the preliminary effects of protein addition to lipid phase behavior are established, then mixtures that better mimic the inner leaflet composition may be used. Particularly, in studies of HIV-1 Gag assembly and budding, the role played by $PI(4,5)P_2$ should be investigated.

The determinations of protein structures have identified key features that drive membrane interaction. In addition, investigations using simple model membrane systems revealed that small changes in membrane properties such as lipid composition, phase behavior, and bending rigidity strongly affect protein mediated membrane remodeling. The complex nature of the cell PM poses a major challenge for researchers in this field. While a better understanding of the lipid matrix, especially of the PM inner leaflet-, is needed, a thorough description of protein-mediated membrane remodeling processes would require a meaningful marriage of the two fields: protein structural studies and model membrane studies.

References

1. Korlach, J., P. Schwille, W.W. Webb, and G.W. Feigenson. 1999. Characterization of lipid bilayer phases by confocal microscopy and fluorescence correlation spectroscopy. Proc. Natl. Acad. Sci. U.S.A. 96: 8461–8466.

2. Veatch, S.L., and S.L. Keller. 2005. Seeing spots: Complex phase behavior in simple membranes. Biochimica et Biophysica Acta (BBA) - Molecular Cell Research. 1746: 172–185.

3. Zhao, J., J. Wu, F.A. Heberle, T.T. Mills, P. Klawitter, et al. 2007. Phase studies of model biomembranes: Complex behavior of DSPC/DOPC/Cholesterol. Biochimica et Biophysica Acta (BBA) - Biomembranes. 1768: 2764–2776.

4. Morales-Penningston, N.F., J. Wu, E.R. Farkas, S.L. Goh, T.M. Konyakhina, et al. 2010. GUV preparation and imaging: minimizing artifacts. Biochim. Biophys. Acta. 1798: 1324–1332.

5. Veatch, S., and S. Keller. 2005. Miscibility Phase Diagrams of Giant Vesicles Containing Sphingomyelin. Phys. Rev. Lett. 94.

6. Buboltz, J. 2007. Steady-state probe-partitioning fluorescence resonance energy transfer: A simple and robust tool for the study of membrane phase behavior. Phys. Rev. E. 76.

7. Farkas, E.R., and W.W. Webb. 2010. Precise and millidegree stable temperature control for fluorescence imaging: application to phase transitions in lipid membranes. Rev. Sci. Instrum. 81: 093704.

8. Fastenberg, M.E., H. Shogomori, X. Xu, D.A. Brown, and E. London. 2003. Exclusion of a transmembrane-type peptide from ordered-lipid domains (rafts) detected by fluorescence quenching: extension of quenching analysis to account for the effects of domain size and domain boundaries. Biochemistry. 42: 12376–12390.

9. Shogomori, H., A.T. Hammond, A.G. Ostermeyer-Fay, D.J. Barr, G.W. Feigenson, et al. 2005. Palmitoylation and intracellular domain interactions both contribute to raft targeting of linker for activation of T cells. J. Biol. Chem. 280: 18931–18942.

10. de Planque, M.R.R., and J.A. Killian. 2003. Protein-lipid interactions studied with designed transmembrane peptides: role of hydrophobic matching and interfacial anchoring. Mol. Membr. Biol. 20: 271–284.

11. Dalton, A.K., D. Ako-Adjei, P.S. Murray, D. Murray, and V.M. Vogt. 2007. Electrostatic interactions drive membrane association of the human immunodeficiency virus type 1 Gag MA domain. Journal of Virology. 81: 6434–6445.

12. Wang, T.Y., and J.R. Silvius. 2001. Cholesterol does not induce segregation of liquid-ordered domains in bilayers modeling the inner leaflet of the plasma membrane. Biophysj. 81: 2762–2773.

13. Feigenson, G.W. 1989. Calcium ion binding between lipid bilayers: the four-component system of phosphatidylserine, phosphatidylcholine, calcium chloride, and water. Biochemistry. 28: 1270–1278.

14. Huang, J., J.E. Swanson, A.R. Dibble, A.K. Hinderliter, and G.W. Feigenson. 1993. Nonideal mixing of phosphatidylserine and phosphatidylcholine in the fluid lamellar phase. Biophysj. 64: 413–425.

15. Roux, A., D. Cuvelier, P. Nassoy, J. Prost, P. Bassereau, et al. 2005. Role of curvature and phase transition in lipid sorting and fission of membrane tubules. EMBO J. 24: 1537–1545.

16. Manneville, J.B., J.F. Casella, E. Ambroggio, P. Gounon, J. Bertherat, et al. 2008. COPI coat assembly occurs on liquid-disordered domains and the associated membrane deformations are limited by membrane tension. Proc. Natl. Acad. Sci. U.S.A. 105: 16946–16951.

17. Parthasarathy, R., C.-H. Yu, and J.T. Groves. 2006. Curvature-Modulated Phase Separation in Lipid Bilayer Membranes. Langmuir. 22: 5095–5099.

18. Ono, A. 2010. Relationships between plasma membrane microdomains and HIV-1 assembly. Biol. Cell. 102: 335–350.

19. Frost, A., R. Perera, A. Roux, K. Spasov, O. Destaing, et al. 2008. Structural Basis of Membrane Invagination by F-BAR Domains. Cell. 132: 807–817.

20. Mim, C., H. Cui, J. Gawronski-Salerno, A. Frost, E. Lyman, et al. 2012. Structural Basis of Membrane Bending by the N-BAR Protein Endophilin. Cell. 149: 137–145.

APPENDIX A

Investigating macroscopic fluid phase separation in inner leaflet model membranes

Without fully understanding how canonical inner leaflet lipids mix, systematic studies on the roles played by lipids in these processes cannot be deciphered properly. Initially, we had set out to first determine the phase behavior of a three-component inner leaflet model membrane mixture consisting of PE, PS, and cholesterol, since previous studies only examined limited number of inner leaflet lipid mixtures (1). We intended to use the phase diagram, which we predicted to display regions of liquid immiscibility, for selecting suitable mixtures to examine the effects of lipid phase behavior on BAR domain protein mediated membrane deformation activity.

Using fluorescence microscopy imaging of GUVs, various PE- and PS-containing mixtures were examined, including POPC/POPE/POPS, POPE/POPS/CHOL, and stearyl-oleoyl-PE (SOPE)/DOPS/CHOL. Monounsaturated lipids were chosen based on their abundance found in the inner leaflet of the PM, based on mass spectrometry studies (2). Figure A.1 summarizes the data collected for POPC/POPE/POPS and SOPE/DOPS/CHOL mixtures. Unfortunately, we observed only uniform GUVs or else gel-fluid (Ld + Lβ) phase coexistence at limited regions of the phase diagrams in the mixtures examined. Even in mixtures where the two phospholipids have a large difference in Tm's, SOPE at ~30°C (3) and DOPS at -11°C (4), we observed only a very limited region of gel-fluid coexistence (Fig. A.1 *B*).

No Ld + Lo regions were detected, in line with previous predictions (1) and more recent reports (5, 6), suggesting that inner leaflet lipids (including cholesterol) alone may not display phase separation.

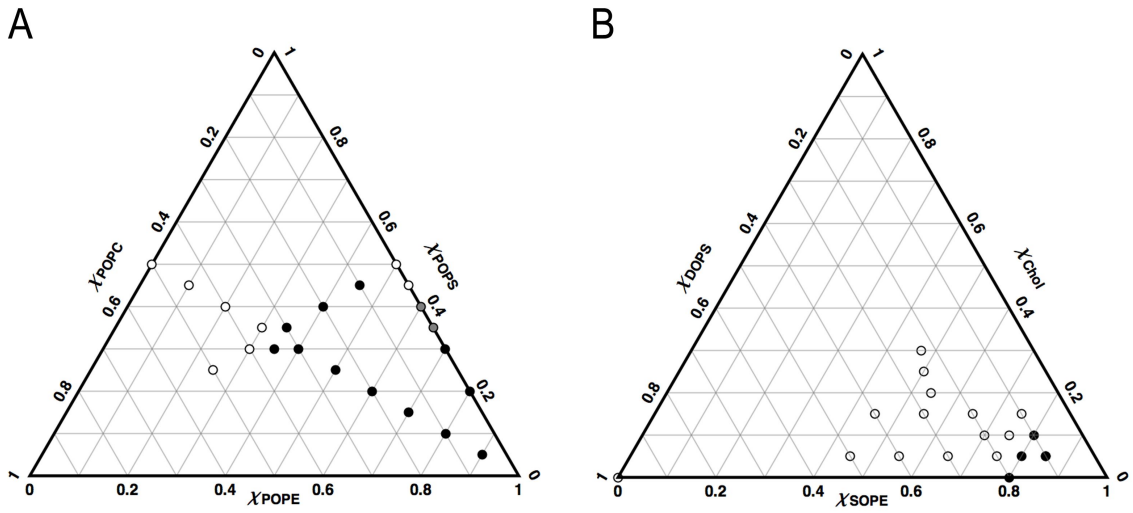

Figure A.1 GUV compositions examined in inner leaflet model membrane mixtures display only uniform and Ld + Lβ coexisting domains. Compositions that display uniform (*white circles*), Ld + Lβ (*black circles*) and unknown (*grey circles*) morphologies are plotted onto the Gibbs triangle of POPE/POPC/POPS (A) and SOPE/DOPS/CHOL (B) systems. Temperature, 20-21°C.

Materials and Methods

Materials

All phospholipids were purchased from Avanti Polar Lipids (Alabaster, AL), and cholesterol was purchased from Nu Chek Prep (Elysian, MN). Purity (to >99%) was determined via TLC for all phospholipids, using 60/30/6 = chloroform/methanol/water as the developing solvent. Concentration of lipid stocks were determined to <1% using inorganic phosphate assay (7). Cholesterol stock was prepared gravimetrically to ~ 0.2%. Fluorescent dye C12:0-DiI (1,1′-didodecyl-3,3,3′,3′-tetramethylindocarbocyanine perchlorate) was purchased from Invitrogen (Carlsbad, CA). C12:0-DiI stocks were prepared in absolute ethanol, and concentration determined by absorption spectroscopy on an HP 8452A spectrophotometer (Hewlett-Packard, Palo Alto, CA)

Preparation of GUVs

GUVs were prepared following the gentle hydration method described in (8), and modified in (9). Briefly, 500 nmoles of lipids and 0.03% C12:0-DiI were dissolved in a 98/2 = chloroform/methanol solution. The organic solvent was removed via rotary evaporation at ~50°C to produce a thin even film, followed by incubation under high vacuum for 1-2 hours. The dried lipid film was then gently hydrated under wet nitrogen gas at ~ 40°C for 30 min. Pre-warmed buffer (100 mM sucrose, 2 mM KCl, 0.2 mM EDTA, pH7.0) was added to the film and the samples were hydrated at ~ 40°C for 12 hours, followed by cooling to room temperature in 10-12 hours. GUVs were then harvested into harvesting buffer (100 mM glucose, 2 mM KCl, 0.2 mM EDTA, pH7.0), let settle for ~ 1hour before microscopy observations.

Fluorescence microscopy

Grease-sealed chambers were made using type L Apiezon vacuum grease, where 2-5 μL sample was sandwiched in between a glass slide and cover slip. Wide-field fluorescence imaging was conducted on an inverted Nikon Diaphot-TMD using a 60X 1.4NA oil immersion objective. C12:0-DiI was imaged using 535-550 nm excitation and 565-610 nm emission.

References

1. Wang, T.Y., and J.R. Silvius. 2001. Cholesterol does not induce segregation of liquid-ordered domains in bilayers modeling the inner leaflet of the plasma membrane. Biophysj. 81: 2762–2773.

2. Ejsing, C.S., E. Duchoslav, J. Sampaio, K. Simons, R. Bonner, et al. 2006. Automated Identification and Quantification of Glycerophospholipid Molecular Species by Multiple Precursor Ion Scanning. Anal. Chem. 78: 6202–6214.

3. Lohner, K., G. Degovics, P. LAGGNER, E. Gnamusch, and F. Paltauf. 1993. Squalene promotes the formation of non-bilayer structures in phospholipid model membranes. Biochim. Biophys. Acta. 1152: 69–77.

4. CAFFREY, M. 1987. The combined and separate effects of low temperature and freezing on membrane lipid mesomorphic phase behavior: relevance to cryobiology. Biochim. Biophys. Acta. 896: 123–127.

5. Shimokawa, N., M. Hishida, H. Seto, and K. Yoshikawa. 2010. Phase separation of a mixture of charged and neutral lipids on a giant vesicle induced by small cations. Chemical Physics Letters. 496: 59–63.

6. Vequi-Suplicy, C.C., K.A. Riske, R.L. Knorr, and R. Dimova. 2010. Vesicles with charged domains. Biochim. Biophys. Acta. 1798: 1338–1347.

7. Kingsley, P.B., and G.W. Feigenson. 1979. Synthesis of a Perdeuterated Phospholipid - 1,2-Dimyristoyl-Sn-Glycero-3-Phosphocholine-D72. Chemistry and Physics of Lipids. 24: 135–147.

8. Akashi, K., H. Miyata, H. Itoh, and K. Kinosita. 1996. Preparation of giant liposomes in physiological conditions and their characterization under an optical microscope. Biophysj. 71: 3242–3250.

9. Zhao, J., J. Wu, F.A. Heberle, T.T. Mills, P. Klawitter, et al. 2007. Phase studies of model biomembranes: Complex behavior of DSPC/DOPC/Cholesterol. Biochimica et Biophysica Acta (BBA) - Biomembranes. 1768: 2764–2776.

APPENDIX B

Energy calculations and estimations for protein-mediated membrane deformation[††]

Section 1 (by Qi Wang)

The overall radius of a curved bilayer, considering the asymmetry of surface area of the two leaflets, is given by (1):

$$R = d \times \frac{A^{out} + A^{in}}{A^{out} - A^{in}}$$

Reformulation of this equation gives the relationship between A^{out} and A^{in}:

$$\frac{A^{out}}{A^{in}} = 1 + \frac{2d}{R - d} = 1 + \varepsilon$$

where ε is the excess surface ratio of the two leaflets. This equation indicates that a more curved surface is accompanied by a higher degree of surface expansion at the outer-leaflet of the membrane. The table below lists the dependence of ε on the membrane curvature.

R (nm)	5	10	15	20	25	30	35	40	45	50	55	60
ε	1.33	0.50	0.31	0.22	0.17	0.14	0.12	0.11	0.09	0.08	0.08	0.07

[††] The following sections are reproduced from the Supporting Text S1 in: Goh, S.L.,[1] Wang, Q.,[1] Byrnes, L.J., and Sondermann, H. 2012. Versatile membrane deformation potential of activated pacsin. PLoS ONE 7(12): e51628. doi:10.1371/ journal.pone.0051628 ([1]co-first authors), with modifications to conform to the required format.

For a 10 nm tubular structure, the surface area of the outer-leaflet membrane is twice that of the inner-leaflet.

Section 2 (by Qi Wang)

The energy cost to generate a tube of diameter $2R_t$ and length L from a flat membrane can be described as:

$$E_t = \pi\kappa \frac{L}{R_t}$$

where κ is the membrane bending rigidity, generally estimated as 20 k_BT for a plasma membrane. Therefore, the energy cost per unit area (energy density) will be:

$$\rho_t = \frac{E_t}{2\pi R_t L} = \frac{\kappa}{2} \times \frac{1}{R_t^2}$$

Similarly, the energy density to generate a spherical vesicle with a radius R_s nm from a flat membrane can be estimated as:

$$\rho_v = 2\kappa \times \frac{1}{R_v^2}$$

At the isoenergy density point $\rho_v = \rho_t$ the following relation may apply:

$$R_v = 2R_t$$

This relationship implies that a tubular structure of radius R has the same surface energy density as a vesicle with radius 2R, which forms the basis for our discussion on tubule-vesicle bimodality.

Section 3

The energy required to bend a flat symmetric bilayer into a sphere (E_{sph}) is $8\pi\kappa$, independent of the size (radius) of the sphere (2). Hence, the energy needed to make N_f number of spheres is

$$E = N_f x\, E_{sph}$$

If the initial state contains N_i spheres, then the energy needed to make N_f spheres is the difference between the energies of the two states:

$$\Delta E = N_f * E_{sph} - N_i * E_{sph} = (N_f - N_i)\, E_{sph}$$

The process is more favorable if the difference between N_i and N_f is small. Hence, if two systems have the same total number of lipids, where system A is made up of larger liposomes (e.g. >1 micron), and system B consists of smaller liposomes (e.g. <1 micron), it will require more energy to generate the same final number of 30 nm diameter vesicles from system A than from system B.

References

1. Campelo, F., H.T. McMahon, and M.M. Kozlov. 2008. The Hydrophobic Insertion Mechanism of Membrane Curvature Generation by Proteins☆. Biophys. J. 95: 2325–2339.

2. Zimmerberg, J., and M.M. Kozlov. 2005. How proteins produce cellular membrane curvature. Nat Rev Mol Cell Biol. 7: 9–19.